JSCSEN 79(2)115–276(2014)

ISSN 1820-7421(Online)

Journal of the Serbian Chemical Society

Electronic Version

VOLUME 79

No 2

BELGRADE 2014

Available on line at

www.shd.org.rs/JSCS/

J. Serb. Chem. Soc. Vol. 79, No. 2 (2014)

CONTENTS

Published by the Serbian Chemical Society
Karnegijeva 4/III, 11000 Belgrade, Serbia
Printed by the Faculty of Technology and Metallurgy
Karnegijeva 4, P.O. Box 35-03, 11120 Belgrade, Serbia

Journal of the Serbian Chemical Society
JSCS-info@shd.org.rs • www.shd.org.rs/JSCS
J. Serb. Chem. Soc. 79 (2) 115–123 (2014) UDC 547.53.024+547.78+547–316:615.281/.282
JSCS–4569 *Original scientific paper*

Synthesis and antimicrobial activity of some new *N*-(aryloxoalkyl)-5-arylidene-thiazolidine-2,4-diones

ANCA STANA[1]*, BRÎNDUȘA TIPERCIUC[1], MIHAELA DUMA[2], ADRIAN PÎRNĂU[3], PHILIPPE VERITÉ[4] and OVIDIU ONIGA[1]

[1]Department of Pharmaceutical Chemistry, "Iuliu Haţieganu" University of Medicine and Pharmacy, 12 Ion Creangă Street, 400010 Cluj Napoca, Romania, [2]State Veterinary Laboratory for Animal Health and Food Safety, 400572 Cluj-Napoca, Romania, [3]National Institute for Research and Development of Isotopic and Molecular Technologies, 400293 Cluj Napoca, Romania and [4]University of Medicine and Pharmacy Rouen, Faculty of Pharmacy, Department of Analytical Chemistry, 22 Boulevard Gambetta, F-76183 Rouen Cedex, France

(Received 13 January, revised 2 July 2013)

Abstract: A series of new 5-(2,6-dichlorobenzylidene)thiazolidine-2,4-dione and 5-(4-methoxybenzylidene)thiazolidine-2,4-dione derivatives (**3a–h** and **5a–h**, respectively) were synthesized starting from 5-arylidenethiazolidine--2,4-dione and *α*-halo-ketones. The structural elucidation of the newly synthesized compounds was based on elemental analysis and spectroscopic data (MS, ^{1}H-NMR and ^{13}C-NMR). The synthesized compounds were screened *in vitro* for their antimicrobial activities against several pathogenic strains of Gram-positive and Gram-negative bacteria and one fungal strain (*Candida albicans*), as growth inhibition diameters. Some of the compounds displayed better inhibitory activities than that of the reference drug against the Gram--positive *Staphylococcus aureus*, *Bacillus cereus* and *Listeria monocytogenes* bacterial strains, and showed good antifungal activity against *C. albicans*, while the antibacterial activity against the Gram-negative *Escherichia coli* and *Salmonella typhimurium* bacterial strains was moderate.

Keywords: 5-arylidenethiazolidine-2,4-dione; *α*-haloketone; antibacterial; antifungal.

INTRODUCTION

Heterocyclic compounds have long been recognized in the field of synthetic organic chemistry as a very important class. Nitrogen-, oxygen- and sulphur--containing heterocyclic compounds are known to exhibit a large variety of biological activities and are used in various fields of pharmacy.[1]

* Corresponding author. E-mail: teodora_anca@yahoo.com
doi: 10.2298/JSC130114078S

Especially great attention has been given to thiazolidine-2,4-dione derivatives as they posses a diverse array of pharmacological activities, such as antidiabetic,[2] antioxidant, analgesic, anti-arthritic,[3] anti-inflammatory,[4] anticancer,[5] antibacterial and antifungal.[6] Besides showing a remarkable antidiabetic activity by binding with PPARγ, heterocyclic compounds bearing thiazolidine-2,4-dione moiety with substitution at the fifth position can reduce oxidative stress and inhibit intracellular free radical overproduction.[7] They also have inhibitory effects on monocyte/macrophage activation, the expression of inflammatory molecules[8] and tyrosinase activity.[9] It was reported that 5-arylidene-2,4-thiazolidinediones can act as potentially promising 15-hydroxyprostaglandin dehydrogenase inhibitors,[10] inhibitors of MurD ligase[11] and antimicrobial agents.[12–14]

The search for new high-effective antimicrobial drugs is a very important issue because of the appearance of a large group of antibiotic and antifungal resistant strains.[15]

In view of these facts and in continuation of efforts to discover potentially active new antimicrobial agents,[16] the synthesis of two series of various N-substituted 5-arylidene-thiazolidine-2,4-diones and an evaluation of their antibacterial and antifungal activities are reported herein.

RESULTS AND DISCUSSION

Chemistry

The synthetic strategy for the target compounds, *N*-(aryloxoalkyl)-5-(2,6-dichlorobenzylidene)thiazolidine-2,4-diones (**3a**–**h**) and *N*-(aryloxoalkyl)-5-(4-methoxybenzylidene)thiazolidine-2,4-diones (**5a**–**h**) is illustrated in Scheme 1.

The general method known as the Knoevenagel condensation was used to synthesize the *N*-unsubstituted 5-arylidene-thiazolidine-2,4-diones (**2** and **4**) in good yields (94–95 %). 5-(2,6-Dichlorobenzylidene)thiazolidine-2,4-dione (**2**) and 5-(4-methoxybenzylidene)thiazolidine-2,4-dione (**4**) were prepared by the condensation of thiazolidine-2,4-dione with the appropriate arylaldehyde, according to procedures reported in the literature.[17,18]

In order to accomplish *N*-substitution, the 5-arylidenethiazolidine-2,4-diones (**2** and **4**) were first converted into potassium salts at the nitrogen atom of the thiazolidine-2,4-dione ring with the help of anhydrous potassium hydroxide in dimethylformamide (DMF) under continuous stirring at room temperature. The treatment of the obtained potassium salts with various α-halo-ketones in DMF under continuous stirring at room temperature afforded the target compounds, *N*-(aryloxoalkyl)-5-arylidene-thiazolidine-2,4-diones (**3a**–**h** and **5a–h**, respectively) in 45–95 % yields.

The newly synthesized *N*-substituted 5-arylidenethiazolidine-2,4-diones (**3a**–**h** and **5a–h**) were characterized by melting point, elemental analysis and spectro-

scopic data (^{1}H-NMR, ^{13}C-NMR and MS). All compounds gave good CHNS quantitative elemental analysis results, in agreement with the calculated values**.** All spectral and analytical data were consistent with the assumed structures. Details of the synthetic procedures and the yields are presented in the Experimental while the physical, analytical and spectral data for the synthesized compounds are given in the Supplementary material to this paper.

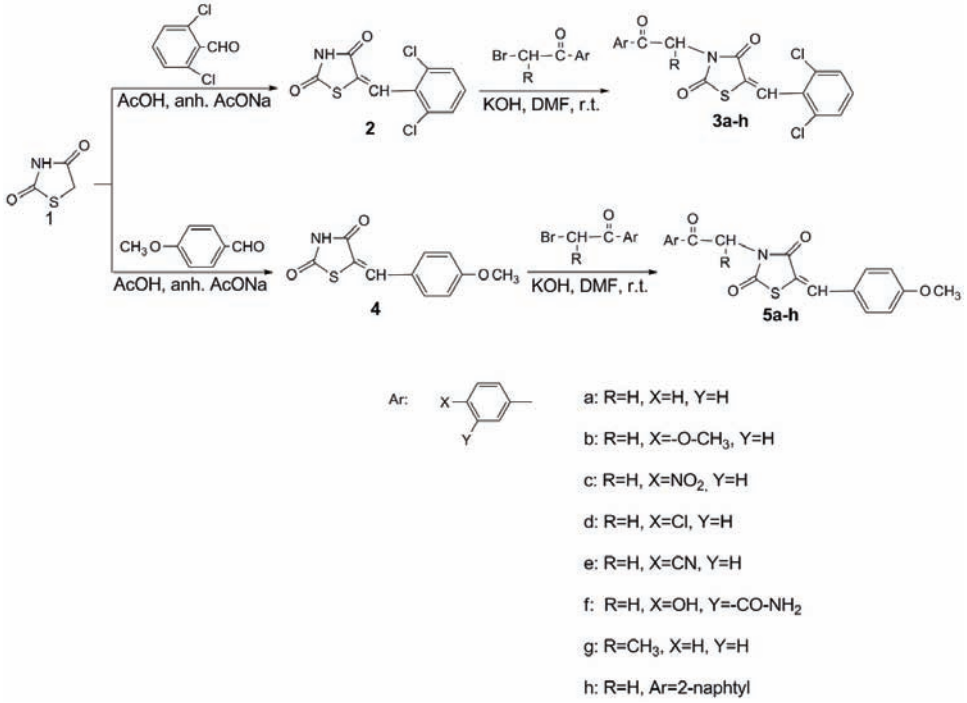

Scheme 1. General synthetic route for the synthesis of the compounds **3a**–**h** and **5a**–**h**.

The IR spectra of the synthesized compounds **3a**–**h** and **5a**–**h** displayed three strong absorption peaks at 1749–1731 cm^{-1}, 1705–1692 cm^{-1} and 1687–1668 cm^{-1} due to C=O stretching of the thiazolidine-2,4-dione ring and the arylalkylketone, respectively. The absence of absorption bands corresponding to the –NO group of the thiazolidine-2,4-dione moiety in the IR spectra of all the newly synthesized compounds confirmed the formation of *N*-substituted derivatives. Compounds **3b** and **5a**–**h** give two strong bands at 1043–1031 cm^{-1} and 1258––1248 cm^{-1} due to the presence of phenyl methyl ether group. The absorption bands at 1521–1517 cm^{-1} and 1331–1324 cm^{-1} in the IR spectra of compounds **3c** and **5c** are due to the asymmetric and symmetric stretch of the –NO_2 group. The IR spectra of compounds **3e** and **5e** exhibited one sharp absorption at 2235––2231 cm^{-1} due to the –C≡N stretch. In the IR spectra of compounds **3f** and **5f**,

the C=O stretch of the amide group appeared at 1635–1628 cm^{-1} and the phenol group presented an absorption band at 1233–1231 cm^{-1} due to the C–O stretching vibration and an absorption band at 3417–3411 cm^{-1} due to the intramolecular hydrogen-bonded OH stretch.

The ^{1}H-NMR spectra of the synthesized compounds **3a**–**h** and **5a**–**h** showed one signal for the methylidene proton, as a singlet at 7.879–7.991 ppm, which supported the occurrence of the Knoevenagel condensation between the thiazolidine-2,4-dione and aromatic aldehydes. The absence of a singlet signal corresponding to the NH proton from the thiazolidine-2,4-dione ring in the 12.50–12.52 ppm region[16] in the ^{1}H-NMR spectra of all compounds confirmed the formation of *N*-substituted derivatives. The $-OCH_3$ protons resonated as singlets at 3.822––3.896 ppm and the aromatic protons appeared as characteristic doublets, triplets or multiplets in the 7.043–8.902 ppm region of the ^{1}H-NMR spectra. ^{13}C-NMR spectra of the synthesized compounds were in accordance with the assumed structures.

The mass spectra of the synthesized compounds gave idea about the fragmentation of the final compounds with their corresponding mass and revealed the correct molecular ion peaks (M^+ or M+1), as suggested by their molecular formulas.

Antibacterial/antifungal activity

All compounds were tested for their antibacterial activity against two Gram--negative (*Salmonella typhimurium* ATCC 13311 and *Escherichia coli* ATCC 25922) and three Gram-positive (*Listeria monocytogenes* ATCC 35152, *Staphylococcus aureus* ATCC 25923 and *Bacillus cereus* ATCC 13061) bacterial strains. The antifungal activity of the compounds was evaluated against a strain of *Candida albicans* ATCC 90028.

The results of the antifungal and antibacterial activity of the *N*-(aryloxoalkyl)-5-arylidenethiazolidine-2,4-diones **3a**–**h** and **5a**–**h** in comparison with those of reference drugs are presented in Table I.

All the tested compounds presented modest to good inhibitory activity against the Gram-positive and the Gram-negative bacteria, compared to ciprofloxacin (50 μg $well^{-1}$), employed as a standard drug. All of the synthesized compounds were active and showed moderate activity against *E. coli* and *S. typhimurium* (10–18 mm inhibition zone). The 5-(4-methoxybenzylidene)thiazolidine-2,4-diones (**5a**–**h**) were generally more active than the 5-(2,6-dichlorobenzylidene)thiazolidine-2,4-diones (**3a**–**h**), suggesting that substitution of the thiazolidine-2,4-dione ring with a methoxybenzylidene moiety in the fifth position rather than with a 2,6-dichlorobenzylidene moiety favoured the antibacterial activity of the compounds against Gram-negative bacteria. On the contrary, the 5-(2,6-dichlorobenzylidene)thiazolidine-2,4-diones **3a**–**h** exhibited better anti

-bacterial properties than the 5-(4-methoxybenzylidene)thiazolidine-2,4-diones (**5a**–**h**) did against the Gram-positive bacteria. Compounds **3a,c,e** and **f** and **5a**–**c** displayed similar or better inhibitory activities than that of the reference drug ciprofloxacin against *S. aureus*, while compounds **3e–f** were more active than ciprofloxacine against *L. monocytogenes*, and compound **3f** was more active than the standard against *B. cereus*. The antibacterial activity of compounds **3a, 3c** and **3e**–**f** and **5a**–**c** was generally better than that of the other *N*-(aryloxoalkyl)--5-arylidenethiazolidine-2,4-diones, suggesting that the presence of an electron withdrawing group, such as nitro, nitrile or carbonyl, on the aromatic ring plays an important role in enhancing the antibacterial properties of the titled compounds. Regarding the antifungal activity, most of the synthesized compounds showed moderate to good inhibition (14–24 mm inhibition zone) against *C. albicans*, at the test concentrations.

TABLE I. Antimicrobial activity of the synthesized compounds **3a**–**h** and **5a**–**h**; inhibition zone, mm; (–) no activity

Compound	Gram-positive bacteria			Gram-negative bacteria		Fungi
	S. aureus	*L. monocytogenes*	*B. cereus*	*E. coli*	*S. typhimurium*	*C. albicans*
3a	20	18	20	16	14	14
3b	18	16	12	12	12	18
3c	28	16	18	14	16	16
3d	18	16	16	12	14	18
3e	22	28	20	12	12	22
3f	20	22	24	10	16	22
3g	18	18	16	10	14	24
3h	18	16	14	10	14	18
5a	20	18	14	14	18	18
5b	20	18	14	14	18	18
5c	24	16	12	12	18	16
5d	18	16	12	12	18	16
5e	18	18	12	14	16	14
5f	18	18	14	14	18	14
5g	18	16	12	18	18	16
5h	18	16	12	16	18	16
Ciprofloxacin[a]	20	22	22	24	22	–
Fluconazole[a]	–	–	–	–	–	25

[a]Ciprofloxacin and fluconazole (50 μg well^{-1}) were used as standard drugs

EXPERIMENTAL

Chemistry

All chemicals and reagents were obtained from commercial sources and were used as supplied, without further purification. Compounds **2** and **4** were previously reported in the literature.[16-18]

Melting points were determined with an electrothermal melting point meter in open glass capillary method and are uncorrected. The reaction progress and purity of the synthesized

compounds were monitored by analytical thin layer chromatography (TLC) using Merck pre-coated Silica Gel $60F_{254}$ sheets (Darmstadt, Germany), a heptane–ethyl acetate 3:7 elution system and UV light for visualization. The IR spectra were recorded on a JASCO FT-IR-4100 spectrometer (Cremella, Italy) using the ATR technique (Attenuated Total Reflectance). The nuclear magnetic resonance (^{1}H-NMR) spectra were recorded at room temperature on Bruker Avance NMR spectrometer (Karlsruhe, Germany) operating at 500 and 125 MHz for ^{1}H- and ^{13}C-NMR, respectively, using tetramethylsilane (TMS) as an internal standard (chemical shifts, δ, in ppm). The spectra were in accordance with the assigned structures. The samples were prepared by dissolving the compounds in DMSO-d_6 (δ_H = 2.51 ppm) as solvent and the spectra were recorded using a single excitation pulse of 12 μs (^{1}H-NMR). Spin multiplets are given as *s* (singlet), *d* (doublet), *t* (triplet) and *m* (multiplet). The ^{13}C-NMR spectra were recorded on a Bruker Avance NMR spectrometer (Karlsruhe, Germany) operating at 125 MHz in DMSO-d_6, using a waltz-16 decoupling scheme. The MS analyses were performed at 70 eV with an Agilent gas chromatograph 6890 (Darmstadt, Germany) equipped with an apolar Macherey Nagel Permabond SE 52 capillary column (Dueren, Germany) and with an LCMS--2020 Shimadzu mass spectrometer (Shimadzu Corporation, North America). Elemental analyses were realized using a Vario El CHNS instrument (Hanau, Germany). Physical, analytical and spectral data of the prepared compounds are given in Supplementary material to this paper.

*5-(2,6-Dichlorobenzylidene)-3-(2-oxo-2-phenylethyl)thiazolidine-2,4-dione (**3a**)*. 1 mmol (273 mg) of **2** was dissolved in dimethylformamide (DMF) (3.5 mL) and finely dispersed anhydrous potassium hydroxide (84 mg, 1.5 mmol) was added. The mixture was stirred for 30 min at room temperature to give the potassium salt of 5-(2,6-dichlorobenzylidene)thiazolidine-2,4-dione. To the resulting suspension was added 2-bromo-1-phenylethanone (199 mg, 1 mmol) for *N*-substitution. The mixture was stirred at room temperature for 8 h. The reaction was monitored by TLC. After completion of the reaction, the reaction mass was poured into ice-cold water. The resulting precipitate was filtered, washed with water and ethanol, dried and then recrystallized from absolute ethanol. Yellow solid; yield: 85 %.

*5-(2,6-Dichlorobenzylidene)-3-[2-(4-methoxyphenyl)-2-oxoethyl]thiazolidine-2,4-dione (**3b**)*. Using 2-bromo-1-(4-methoxyphenyl)ethanone (229 mg, 1 mmol), the compound was prepared according to the procedure described for **3a**. White solid; yield: 93 %.

*5-(2,6-Dichlorobenzylidene)-3-[2-(4-nitrophenyl)-2-oxoethyl]thiazolidine-2,4-dione (**3c**)*. The compound was prepared according to the procedure for **3a** using 2-bromo-1-(4--nitrophenyl)ethanone (244 mg, 1 mmol). Dark brown solid; yield: 69 %.

*3-[2-(4-Chlorophenyl)-2-oxoethyl]-5-(2,6-dichlorobenzylidene)thiazolidine-2,4-dione (**3d**)*. The title compound was prepared according to the procedure described for **3a** using 2-bromo--1-(4-chlorophenyl)ethanone (233.5 mg, 1 mmol). Brown solid; yield: 74 %.

*4-{2-[5-(2,6-Dichlorobenzylidene)-2,4-dioxothiazolidin-3-yl]acetyl}benzonitrile (**3e**)*. The title compound was prepared following the procedure presented for **3a** using 4-(2-bromo-acetyl)benzonitrile (224 mg, 1 mmol) and was recrystallized from absolute ethanol. Yellow solid; yield: 51 %.

*5-{2-[5-(2,6-Dichlorobenzylidene)-2,4-dioxothiazolidin-3-yl]acetyl}-2-hydroxybenzamide (**3f**)*. The compound was prepared using 5-(2-bromoacetyl)-2-hydroxybenzamide (258 mg, 1 mmol) following the synthetic procedure described for **3a**. Brown solid; yield: 53 %.

*5-(2,6-Dichlorobenzylidene)-3-(1-methyl-2-oxo-2-phenylethyl)thiazolidine-2,4-dione (**3g**)*. The title compound was prepared following the procedure presented for **3a** using 2-bromo-1-phenylpropan-1-one (213 mg, 1 mmol). Yellow liquid; yield: 45 %.

*5-(2,6-Dichlorobenzylidene)-3-[2-(naphthalen-2-yl)-2-oxoethyl]thiazolidine-2,4-dione (**3h**)*. The title compound was prepared using 2-bromo-1-(naphthalen-2-yl)ethanone (249 mg, 1 mmol) according to the procedure described for **3a**. White solid; yield: 78 %.

*5-(4-Methoxybenzylidene)-3-(2-oxo-2-phenylethyl)thiazolidine-2,4-dione (**5a**)*. To a solution of **4** (235 mg, 1 mmol) in DMF (3.5 mL) was added finely dispersed anhydrous potassium hydroxide (84 mg, 1.5 mmol). The mixture was stirred for 30 min at room temperature to give the potassium salt of 5-(4-methoxybenzylidene)thiazolidine-2,4-dione. To the resulting suspension was added 2-bromo-1-phenylethanone (199 mg, 1 mmol) and then the reaction mixture was stirred at room temperature for 8 h. TLC was used to monitor the reaction progress. After completion of the reaction, the mass was poured into ice-cold water under continuous stirring. The resulting compound was washed with water and ethanol, dried and then recrystallized from absolute ethanol. White solid; yield: 79 %.

*5-(4-Methoxybenzylidene)-3-(2-(4-methoxyphenyl)-2-oxoethyl)thiazolidine-2,4-dione (**5b**)*. Using 2-bromo-1-(4-methoxyphenyl)ethanone (229 mg, 1 mmol), the title compound was prepared according to the procedure described for **5a**. White solid; yield: 95 %.

*5-(4-Methoxybenzylidene)-3-[2-(4-nitrophenyl)-2-oxoethyl]thiazolidine-2,4-dione (**5c**)*. The title compound was prepared according to the procedure for **5a** but using 2-bromo-1-(4--nitrophenyl)ethanone (244 mg, 1 mmol). Pale yellow solid; yield: 92 %.

*3-[2-(4-Chlorophenyl)-2-oxoethyl]-5-(4-methoxybenzylidene)thiazolidine-2,4-dione (**5d**)*. The title compound was prepared according to the procedure described for **5a** but using 2-bromo-1-(4-chlorophenyl)ethanone (233.5 mg, 1 mmol). White solid; yield: 78 %.

*4-{2-[5-(4-methoxybenzylidene)-2,4-dioxothiazolidin-3-yl]acetyl}benzonitrile (**5e**)*. Following the procedure presented for **5a**, the title compound was prepared using 4-(2-bromoacetyl)benzonitrile (224 mg, 1 mmol) and was recrystallized from absolute ethanol. Light brown solid; yield: 53 %;

*2-Hydroxy-5-{2-[5-(4-methoxybenzylidene)-2,4-dioxothiazolidin-3-yl]acetyl}benzamide (**5f**)*. The compound was prepared using 5-(2-bromoacetyl)-2-hydroxybenzamide (258 mg, 1 mmol) according to the synthetic procedure described for **5a**. Yellow solid; yield: 62 %.

*5-(4-Methoxybenzylidene)-3-(1-methyl-2-oxo-2-phenylethyl)thiazolidine-2,4-dione (**5g**)*. Following the procedure presented for **5a** but using 2-bromo-1-phenylpropan-1-one (213 mg, 1 mmol), the title compound was prepared. White solid; yield: 64 %.

*5-(4-Methoxybenzylidene)-3-[2-(naphthalen-2-yl)-2-oxoethyl]thiazolidine-2,4-dione (**5h**)*. The title compound was prepared using 2-bromo-1-(naphthalen-2-yl)ethanone (249 mg, 1 mmol) according to the procedure described for **5a**. White solid; yield: 81 %.

Antibacterial/antifungal activity

The *in vitro* antimicrobial activity was determined using the cup-plate agar diffusion method according to the Clinical and Laboratory Standards Institute (CLSI) guidelines.[19]

For antibacterial testing, Mueller–Hinton agar medium was used whereas for antifungal testing, Mueller–Hinton medium supplemented with 2 % glucose (providing adequate growth of yeasts) and 0.5 mg mL^{-1} methylene blue (providing a better definition of the inhibition zone diameter) was used. The inoculum was prepared by suspending five representative colonies, obtained from an 18–24 h culture on non-selective nutritive agar medium, in sterile distilled water. The cell density was adjusted to the density of 0.5 McFarland standard by measuring the absorbance in a spectrophotometer at a wavelength of 530 nm and adding sterile distilled water as required (corresponding to a population of $(1–5)\times10^6$ CFU mL^{-1}). A sterile swab was soaked in suspension and then the Mueller–Hinton agar plates were inoculated by streaking the entire surface. After drying for 10–15 min, six mm-diameter wells were cut from the agar

using a sterile cork-borer, and a volume of 10 μL of each compound solution (5 mg mL^{-1} in DMSO) were delivered into the wells (50μg $well^{-1}$). Ciprofloxacin (50 μg $well^{-1}$) and fluconazole (50 μg $well^{-1}$) were used as standard drugs. The controls were performed with only sterile broth, overnight culture and 10 μL DMSO. The plates were incubated at 35 °C. The inhibition zone diameters were measured to the nearest whole millimetre where there was no visible growth after 24–48 h. The results were obtained in triplicate. The solvent used for the preparation of each compound stock solution (5 mg ml^{-1}), DMSO (Merck, Germany) exhibited no inhibitory activity against the tested bacterial and fungal strains.

CONCLUSIONS

In conclusion, a series of new 5-(2,6-dichlorobenzylidene)thiazolidine-2,4--dione and 5-(4-methoxybenzylidene)thiazolidine-2,4-dione derivatives were synthesized by Knoevenagel condensation of thiazolidine-2,4-dione with the required aromatic aldehyde, followed by N_3-substitution with various α-halo--ketones. Their structures were confirmed by analytical techniques: ^{1}H-NMR, ^{13}C-NMR, mass and elemental analysis. The synthesized compounds were evaluated for their antibacterial and antifungal activities against several Gram-positive, Gram-negative bacteria and *Candida albicans*. The results of the antimicrobial screening revealed that all of the tested compounds have antibacterial and antifungal properties, while some showed promising antimicrobial activities: compounds **3c**, **3e** and **5c** displayed better inhibitory activities than ciprofloxacin against *S. aureus*, compounds **3e** and **3f** were more active against *L. monocytogenes* and compound **3f** was more active against *B. cereus* than ciprofloxacin.

SUPPLEMENTARY MATERIAL

Physical, analytical and spectral data of the prepared compounds are available electronically from http://www.shd.org.rs/JSCS/, or from the corresponding author on request.

ИЗВОД

СИНТЕЗА И АНТИМИКРОБНА АКТИВНОСТ НОВИХ *N*-(АРИЛОКСОАЛКИЛ)-5--АРИЛИДЕНТИАЗОЛИДИН-2,4-ДИОНА

ANCA STANA[1], BRÎNDUȘA TIPERCIUC[1], MIHAELA DUMA[2], ADRIAN PÎRNĂU[3], PHILIPPE VERITÉ[4] и OVIDIU ONIGA[1]

[1]Department of Pharmaceutical Chemistry,"Iuliu Haţieganu" University of Medicine and Pharmacy, 12 Ion Creangă Street, 400010 Cluj Napoca, Romania, [2]State Veterinary Laboratory for Animal Health and Food Safety, 400572 Cluj-Napoca, Romania, [3]National Institute for Research and Development of Isotopic and Molecular Technologies, 400293 Cluj Napoca, Romania и [4]University of Medicine and Pharmacy Rouen, Faculty of Pharmacy, Department of Analytical Chemistry, 22 Boulevard Gambetta, F-76183 Rouen Cedex, France

Синтетисана је серија нових деривата 5-(2,6-дихлоробензилиден)тиазолидин-2,4--диона и 5-(4-метоксибензилиден)тиазолидин-2,4-диона (**3a**–**h** и **5a**–**h**) полазећи од 5-арилидентиазолидин-2,4-диона и α-халоген-кетона. Структура нових једињења одређена је на основу елементалне анализе и спектроскопских података (IR, MS, ^{1}H-NMR и ^{13}C-NMR). Одређена је антимикробна активност синтетисаних једињења према неко-

лико сојева грам-позитивних и грам-негативних бактерија и сoју гљивица (*Candida albicans*). Нека од синтетисаних једињења показују добру активност према *C. albicans*, док је активност према сојевима грам-негативних бактерија *Escherichia coli* и *Salmonella typhimurium* умерена.

(Примљено 13. јануара, ревидирано 2. јула 2013)

REFERENCES

1. R. Murugan, S. Anbazhagan, S. S. Narayanan, *Eur. J. Med. Chem.* **44** (2009) 3272
2. A. K. M. Iqbal, A. Y. Khan, M. B. Kalashetti, N. S. Belavagi, Y.-D. Gong, I. A. M. Khazi, *Eur. J. Med. Chem.* **53** (2012) 308
3. M. Koufany, D. Moulin, A. Bianchi, M. Muresan, S. Sebillaud, P. Netter, G. Weryha, J.-Y. Jouzeau, *Arthritis Res. Ther.* **10** (2008) R6
4. A. Ialenti, G. Grassia, P. Di Meglio, P. Maffia, M. Di Rosa, A. Ianaro, *Mol. Pharmacol.* **67** (2005) 1620
5. D. Havrylyuk, N. Kovach, B. Zimenkovsky, O. Vasylenko, R. Lesyk, *Arch. Pharm.* **344** (2011) 514
6. M. Tuncbilek, N. Altanlar, *Arch. Pharm.* **33** (2006) 213
7. S. K. Hossain, S. Bhattacharya, *Bioorg. Med. Chem. Lett.* **17** (2007) 1149
8. L. A. Faine, M. Rudnicki, F. A. César, B. L. Heras, L. Boscá, E. S. Souza, M. Z. Hernandes, S. L. Galdino, M. C. Lima, I. R. Pitta, D. S. Abdalla, *Curr. Med. Chem.* **18** (2011) 3351
9. T. Mendgen, C. Steuer, C. D. Klein, *J. Med. Chem.* **55** (2012) 743
10. Y. Wu, S. Karna, C. H. Choi, M. Tong, H. H. Tai, D. H. Na, C. H. Jang, H. Cho, *J. Med. Chem.* **54** (2011) 5260
11. N. Zidar, T. Tomasic, R. Sink, V. Rupnik, A. Kovac, S. Turk, D. Patin, D. Blanot, C. C. Martel, A. Dessen, M. M. Premru, A. Zega, S. Gobec, L. P. Masic, D. Kikelj, *J. Med. Chem.* **53** (2010) 6584
12. O. Zvarec, S. W. Polyak, W. Tieu, K. Kuan, H. Dai, D. S. Pedersen, R. Morona, L. Zhang, G. W. Booker, A. D. Abell, *Bioorg. Med. Chem. Lett.* **22** (2012) 2720
13. O. Bozdağ-Dündar, O. Ozgen, A. Menteşe, N. Altanlar, O. Atli, E. Kendi, R. Ertan, *Bioorg. Med. Chem. Lett.* **15** (2007) 6012
14. T. Tomašic, N. Zidar, V. Rupnik, A. Kovac, D. Blanot, S. Gobec, D. Kikelj, L. P. Mašic, *Bioorg. Med. Chem. Lett.* **19** (2009) 153
15. I. Chopra, C. Schofield, M. Everett, K. O'Neill, K. Miller, M. Wilcox, *Lancet Infect. Dis.* **8** (2008) 133
16. A. Stana, B. Tiperciuc, M. Duma, L. Vlase, O. Crişan, A. Pîrnău, O. Oniga, *J. Heterocyclic Chem.*, in press, doi: 10.1002/jhet.1726
17. Y. Hu, T. Xie, K.-M. Fu, H. Kang, P. Wei, H. Huang, *Heterocycles* **78** (2009) 757
18. H. B. Olsen, N. C. Kaarsholm, P. Madsen, S. Ostergaard, S. Ludvigsen, P. Jakobsen, A. K. Petersen, D. B. Steensgaard, US Pat. 789893 B2 (2011)
19. CLSI, *Performance Standards for Antimicrobial Susceptibility Testing*, Seventeenth Informational Supplement M100-S17, Clinical and Laboratory Standards Institute, Wayne, PN, 2007.

Journal of the Serbian Chemical Society
JSCS@tmf.bg.ac.rs • www.shd.org.rs/JSCS
J. Serb. Chem. Soc. 79 (2) S12–S17 (2014) *Supplementary material*

SUPPLEMENTARY MATERIAL TO

Synthesis and antimicrobial activity of some new *N*-(aryloxoalkyl)-5-arylidenethiazolidine-2,4-diones

ANCA STANA[1]*, BRÎNDUŞA TIPERCIUC[1], MIHAELA DUMA[2], ADRIAN PÎRNĂU[3], PHILIPPE VERITÉ[4] and OVIDIU ONIGA[1]

[1]*Department of Pharmaceutical Chemistry, "Iuliu Haţieganu" University of Medicine and Pharmacy, 12 Ion Creangă Street, 400010 Cluj Napoca, Romania,* [2]*State Veterinary Laboratory for Animal Health and Food Safety, 400572 Cluj-Napoca, Romania,* [3]*National Institute for Research and Development of Isotopic and Molecular Technologies, 400293 Cluj Napoca, Romania and* [4]*University of Medicine and Pharmacy Rouen, Faculty of Pharmacy, Department of Analytical Chemistry, 22 Boulevard Gambetta, F-76183 Rouen Cedex, France*

J. Serb. Chem. Soc. 79 (2) (2014) 115–123

PHYSICAL, ANALYTICAL AND SPECTRAL DATA OF THE PREPARED COMPOUNDS

*5-(2,6-Dichlorobenzylidene)-3-(2-oxo-2-phenylethyl)thiazolidine-2,4-dione (**3a**)*. Yield: 85 %; yellow solid; m.p.: 128–130 °C; Anal. Calcd. for $C_{18}H_{11}Cl_2NO_3S$: C, 55.12; H, 2.83; N, 3.57; S, 8.17 %. Found: C, 55.23; H, 2.91; N, 3.48; S, 8.05 %; IR (ATR, cm^{-1}): 1673 ($C=O_{ketone}$), 1695 ($C=O_{thiazolidinedione}$), 1738 ($C=O_{thiazolidinedione}$); ^{1}H-NMR (500 MHz, DMSO-d_6, δ / ppm): 7.97 (1H, *s*, CH=), 7.76 (2H, *d*, *J* = 7.8 Hz, Ar-H), 7.65 (2H, *d*, *J* = = 8.7 Hz, Ar-H), 7.62 (1H, *t*, *J* = 7.8 Hz, Ar-H), 7.55 (1H, *t*, *J* = 8.7 Hz, Ar-H), 7.53 (2H, *t*, *J* = 7.8 Hz, Ar-H), 5.29 (2H, *s*, CH_2); ^{13}C-NMR (125 MHz, DMSO-d_6, δ / ppm): 185.88 (C=O), 170.13 (C=O), 164.98 (C=O), 133.67 (2C), 132.34 (C), 131.96 (C), 131.73 (CH), 131.23 (CH), 130.63 (C), 129.16 (2CH), 127.52 (2CH), 127.08 (2CH), 123.89 (CH), 50.98 (CH_2); MS (*m*/*z* (relative abundance, %)): 392 (M+1, 100), 393 (M+2, 19.8), 394 (M+3, 62.4), 286 (15.3), 274 (22.7), 233 (39.1), 169 (69.9).

*5-(2,6-Dichlorobenzylidene)-3-[2-(4-methoxyphenyl)-2-oxoethyl]thiazolidine--2,4-dione (**3b**)*. Yield: 93 %; white solid; m.p.: 165–166 °C; Anal. Calcd. for $C_{19}H_{13}Cl_2NO_4S$: C, 54.04; H, 3.10; N, 3.32; S, 7.59 %. Found: C, 54.30; H, 2.98; N, 3.58; S, 7.26 %; IR (ATR, cm^{-1}): 1038, 1254 ($C–O_{methoxy}$), 1676 ($C=O_{ketone}$), 1698 ($C=O_{thiazolidinedione}$), 1735 ($C=O_{thiazolidinedione}$); ^{1}H-NMR (500 MHz, DMSO-d_6, δ / ppm): 8.08 (2H, *d*, *J* = 9.0 Hz, Ar-H), 7.97 (1H, *s*,

* Corresponding author. E-mail: teodora_anca@yahoo.com

CH=), 7.66 (2H, *d*, *J* = 8.7 Hz, Ar-H), 7.55 (1H, *t*, *J* = 8.7 Hz, Ar-H), 7.13 (2H, *d*, *J* = 9.0 Hz, Ar-H), 5.29 (2H, *s*, CH_2), 3.89 (3H, *s*, OCH_3); ^{13}C-NMR (125 MHz, DMSO-d_6, δ / ppm): 185.66 (C=O), 170.32 (C=O), 165.41 (C), 164.76 (C=O), 133.87 (2C), 132.62 (C), 131.86 (C), 131.65 (CH), 129.74 (2CH), 129.12 (2CH), 128.34 (C), 123.44 (CH), 111.15 (2CH), 55.69 (CH_3), 50.84 (CH_2); MS (*m*/*z* (relative abundance, %)): 423 (M+1, 100), 424 (M+2, 76), 425 (M+3, 12.1), 391 (39), 316 (18.4), 288 (8.1), 286 (9.2), 260 (45.9).

*5-(2,6-Dichlorobenzylidene)-3-[2-(4-nitrophenyl)-2-oxoethyl]thiazolidine--2,4-dione (**3c**)*. Yield: 69 %; dark brown solid; m.p.: 172–175 °C; Anal. Calcd. for $C_{18}H_{10}Cl_2N_2O_5S$: C, 49.44; H, 2.31; N, 6.41; S, 7.33. Found: C, 49.54; H, 2.12; N, 6.59; S, 7.25; IR (ATR, cm^{-1}): 1324 (NO_2, sym.), 1521 (NO_2, asym.), 1671 ($C{=}O_{ketone}$), 1692 ($C{=}O_{thiazolidinedione}$), 1733 ($C{=}O_{thiazolidinedione}$); ^{1}H-NMR (500 MHz, DMSO-d_6, δ / ppm): 8.41 (2H, *d*, *J* = 9.0 Hz, Ar-H), 8.32 (2H, *d*, *J* = 9.0 Hz, Ar-H), 7.99 (1H, *s*, CH=), 7.67 (2H, *d*, *J* = 8.7 Hz, Ar-H), 7.55 (1H, *t*, *J* = 8.7 Hz, Ar-H), 5.42 (2H, *s*, CH_2); ^{13}C-NMR (125 MHz, DMSO-d_6, δ / / ppm): 186.21 (C=O), 170.12 (C=O), 164.84 (C=O), 150.42 (C), 140.57 (C), 133.66 (2C), 132.44 (C), 131.81 (CH), 129.89 (2CH), 129.18 (2CH), 128.57 (C), 123.34 (CH), 123.15 (2CH), 50.72 (CH_2); MS (*m*/*z* (relative abundance, %)): 437 (M+1, 100), 438 (M+2, 43.1) 439 (M+3, 25.2), 391 (13), 315 (11.8), 291 (37.5), 286 (9.6), 280 (8.3).

*3-[2-(4-Chlorophenyl)-2-oxoethyl]-5-(2,6-dichlorobenzylidene)thiazolidine--2,4-dione (**3d**)*. Yield: 74 %; brown solid; m.p.: 106–108 °C; Anal. Calcd. for $C_{18}H_{10}Cl_3NO_3S$: C, 50.67; H, 2.36; N, 3.28; S, 7.51 %. Found: C, 50.88; H, 2.22; N, 3.42; S, 7.65 %; IR (ATR, cm^{-1}): 1674 ($C{=}O_{ketone}$), 1696 ($C{=}O_{thiazolidinedione}$), 1731 ($C{=}O_{thiazolidinedione}$); ^{1}H-NMR (500 MHz, DMSO-d_6, δ / ppm): 7.98 (1H, *s*, CH=), 7.83 (2H, *d*, *J* = 8.9 Hz, Ar-H), 7.68 (2H, *d*, *J* = 8.9 Hz, Ar-H), 7.55 (1H, *t*, *J* = 8.7 Hz, Ar-H), 7.54 (2H, *d*, *J* = 8.7 Hz, Ar-H), 5.32 (2H, *s*, CH_2); ^{13}C-NMR (125 MHz, DMSO-d_6, δ / ppm): 186.34 (C=O), 169.98 (C=O), 164.76 (C=O), 138.34 (C), 133.69 (2C), 133.01 (C), 132.41 (C), 131.60 (CH), 130.38 (C), 130.07 (2CH), 129.32 (2CH), 128.76 (2CH), 123.38 (CH), 50.77 (CH_2); MS (*m*/*z* (relative abundance, %)): 428 (M+1, 100), 429 (M+2, 6.3), 430 (M+3, 32.2), 391 (25.7), 314 (5.9), 288 (18.4), 260 (58.6), 233 (20.6), 168 (72.2).

*4-{2-[5-(2,6-Dichlorobenzylidene)-2,4-dioxothiazolidin-3-yl]acetyl}benzonitrile (**3e**)*. Yield: 51 %; yellow solid; m.p.: 163–164 °C; Anal. Calcd. for $C_{19}H_{10}Cl_2N_2O_3S$: C, 54.69; H, 2.42; N, 6.71; S, 7.68 %. Found: C, 54.98; H, 2.17; N, 6.87; S, 7.77 %; IR (ATR, cm^{-1}): 1681 ($C{=}O_{ketone}$), 1699 ($C{=}O_{thiazolidinedione}$), 1745 ($C{=}O_{thiazolidinedione}$), 2235 (C≡N); ^{1}H-NMR (500 MHz, DMSO-d_6, δ / ppm): 8.01 (2H, *d*, *J* = 8.6 Hz, Ar-H), 7.99 (2H, *d*, *J* = 8.6 Hz, Ar-H), 7.97 (1H, *s*, CH=), 7.66 (2H, *d*, *J* = 8.7 Hz, Ar-H), 7.54 (1H, *t*, *J* = 8.7 Hz, Ar-H), 5.41 (2H, *s*, CH_2); ^{13}C-NMR (125 MHz, DMSO-d_6, δ / ppm): 186.54

(C=O), 170.89 (C=O), 164.98 (C=O), 135.74 (C), 133.83 (2C), 132.49 (C), 132.01 (2CH), 131.24 (CH), 130.32 (C), 129.19 (2CH), 128.76 (2CH), 123.22 (CH), 116.66 (C≡N), 116.13 (C), 50.79 (CH_2); MS (*m*/*z* (relative abundance, %)): 418 (M+1, 100), 419 (M+2, 23.4), 420 (M+3, 34.1), 391 (11.5), 288 (39.7), 274 (15.6), 161 (44.1).

*5-{2-[5-(2,6-Dichlorobenzylidene)-2,4-dioxothiazolidin-3-yl]acetyl}-2-hydroxybenzamide (**3f**)*. Yield: 53 %; brown solid; m.p.: 116–118 °C; Anal. Calcd. for $C_{19}H_{12}Cl_2N_2O_5S$: C, 50.57; H, 2.68; N, 6.21; S, 7.11 %. Found: C, 50.37; H, 2.61; N, 6.49; S, 7.28 %; IR (ATR, cm^{-1}): 1231 ($C–O_{phenol}$), 1628 ($C=O_{amide}$), 1668 ($C=O_{ketone}$), 1695 ($C=O_{thiazolidinedione}$), 1749 ($C=O_{thiazolidine-dione}$), 3417 (OH); ^{1}H-NMR (500 MHz, DMSO-d_6, δ / ppm): 13.87 (1H, *s*, OH), 8.65 (1H, *d*, *J* = 1.1 Hz, Ar-H), 8.44 (1H, *s*, NH amide), 8.11 (1H, *s*, NH amide), 8.03 (1H, *dd*, J_1 = 8.8 Hz, J_2 = 1.1 Hz, Ar-H), 7.98 (1H, *s*, CH=), 7.69 (2H, *d*, *J* = = 8.7 Hz, Ar-H), 7.54 (1H, *t*, *J* = 8.7 Hz, Ar-H,), 7.09 (1H, *d*, *J* = 8.8 Hz, Ar-H), 5.29 (2H, *s*, CH_2); ^{13}C-NMR (125 MHz, DMSO-d_6, δ / ppm): 191.88 (C=O), 175.12 (C=O), 170.45 (C=O), 164.91 (C=O), 157.66 (C–OH), 133.97 (2C), 132.58 (C), 132.09 (CH), 131.67 (CH), 129.99 (C), 129.31 (2CH), 128.77 (CH), 128.22 (C), 123.59 (CH), 122.41 (C), 117.24 (CH), 51.03 (CH_2); MS (*m*/*z* (relative abundance, %)): 452 (M+1, 100), 453 (M+2, 95.9), 454 (M+3, 21), 392 (8.1), 304 (4.8), 289 (3.1).

*5-(2,6-Dichlorobenzylidene)-3-(1-methyl-2-oxo-2-phenylethyl)thiazolidine--2,4-dione (**3g**)*. Yield: 45 %; yellow liquid; m.p.: 16 °C; Anal. Calcd. for $C_{19}H_{13}Cl_2NO_3S$: C, 56.17; H, 3.23; N, 3.45; S, 7.89 %. Found: C, 56.26; H, 3.05; N, 3.72; S, 7.97 %; IR (ATR, cm^{-1}): 1678 ($C=O_{ketone}$), 1702 ($C=O_{thiazolidinedione}$), 1743 ($C=O_{thiazolidinedione}$); ^{1}H-NMR (500 MHz, DMSO-d_6, δ / ppm): 7.98 (1H, *s*, CH=), 7.78 (2H, *d*, *J* = 7.8 Hz, Ar-H), 7.67 (2H, *d*, *J* = 8.7 Hz, Ar-H), 7.61 (1H, *t*, *J* = 7.8 Hz, Ar-H), 7.55 (1H, *t*, *J* = 8.7 Hz, Ar-H), 7.50 (2H, *t*, *J* = 7.8 Hz, Ar-H), 5.58 (1H, *q*, *J* = 6.9 Hz, CH), 1.53 (3H, *d*, *J* = 6.9 Hz, CH_3); ^{13}C-NMR (125 MHz, DMSO-d_6, δ / ppm): 193.24 (C=O), 171.05 (C=O), 163.88 (C=O), 136.80 (C), 133.61 (2C), 132.75 (C), 131.43 (CH), 130.84 (2CH), 129.97 (2CH), 128.56 (C), 126.88 (2CH), 124.78 (CH), 123.12 (CH), 54.13 (CH), 20.92 (CH_3); MS (*m*/*z* (relative abundance, %)): 407 (M+1, 100) 408 (M+2, 90.9), 409 (M+3, 5.5), 391 (14.7), 302 (67.4), 274 (44.2), 231 (56.9), 261 (11.5), 168 (62.9).

*5-(2,6-Dichlorobenzylidene)-3-[2-(naphthalen-2-yl)-2-oxoethyl]thiazolidine--2,4-dione (**3h**)*. Yield: 78 %; white solid; m.p.: 176–178 °C; Anal. Calcd. for $C_{22}H_{13}Cl_2NO_3S$: C, 59.74; H, 2.96; N, 3.17; S, 7.25 %. Found: C, 60.05; H, 2.81; N, 3.25; S, 7.32 %; IR (ATR, cm^{-1}): 1672 ($C=O_{ketone}$), 1705 ($C=O_{thiazolidinedione}$), 1741 ($C=O_{thiazolidinedione}$); ^{1}H-NMR (500 MHz, DMSO-d_6, δ / ppm): 8.90 (1H, *s*, Ar-H), 8.18 (1H, *d*, *J* = 8.0 Hz, Ar-H), 8.10 (1H, *d*, *J* = 8.0 Hz, Ar-H), 8.04 (2H, *t*, *J* = 8.6 Hz, Ar-H), 7.89 (1H, *s*, CH=), 7.74 (1H, *t*, *J* = 8.6

Hz, Ar-H), 7.69 (1H, *t*, *J* = 8.6 Hz, Ar-H), 7.65 (2H, *d*, *J* = 8.7 Hz, Ar-H), 7.55 (1H, *t*, *J* = 8.7 Hz, Ar-H), 5.50 (2H, *s*, CH_2); ^{13}C-NMR (125 MHz, DMSO-d_6, δ / / ppm): 191.79 (C=O), 170.45 (C=O), 164.83 (C=O), 136.68 (C), 135.72 (C), 133.85 (2C), 133.44 (CH), 132.78 (C), 130.25 (CH), 130.11 (CH), 129.77 (CH), 129.17 (2CH), 128.71 (CH), 128.30 (CH), 128.15 (C), 127.74 (CH), 127.68 (CH), 125.27 (CH), 123.29 (CH), 50.39 (CH_2); MS (*m*/*z* (relative abundance, %)): 443 (M+1, 100), 444 (M+2, 43.9), 445 (M+3, 27.4), 297 (21.1), 274 (45.1), 288 (67.4), 168 (33.5).

*5-(4-Methoxybenzylidene)-3-(2-oxo-2-phenylethyl)thiazolidine-2,4-dione (**5a**)*. Yield: 79 %; white solid; m.p. 239–240 °C; Anal. Calcd. for $C_{19}H_{15}NO_4S$: C, 64.58; H, 4.28; N, 3.96; S, 9.07 %. Found: C, 64.73; H, 4.32; N, 4.07; S, 9.41 %; IR (ATR, cm^{-1}): 1031, 1257 ($C–O_{methoxy}$), 1675 ($C=O_{ketone}$), 1693 ($C=O_{thiazolidinedione}$), 1739 ($C=O_{thiazolidinedione}$); ^{1}H-NMR (500 MHz, DMSO-d_6, δ / ppm): 7.95 (1H, *s*, CH=), 7.73 (2H, *d*, *J* = 7.8 Hz, Ar-H), 7.6 (2H, *d*, *J* = 9.0 Hz, Ar-H), 7.61 (1H, *t*, *J* = 7.8 Hz, Ar-H), 7.52 (2H, *t*, *J* = 7.8 Hz, Ar-H), 7.14 (2H, *d*, *J* = 9.0 Hz, Ar-H), 5.33 (2H, *s*, CH_2), 3.82 (3H, *s*, OCH_3); ^{13}C-NMR (125 MHz, DMSO-d_6, δ / ppm): 189.85 (C=O), 170.33 (C=O), 163.76 (C=O), 162.65 (C), 136.53 (C), 135.87 (C), 131.96 (C), 131.34 (CH), 129.34 (CH), 129.23 (2CH), 127.52 (2CH), 127.04 (2CH), 118.32 (2CH), 56.18 (CH_3), 49.78 (CH_2); MS (*m*/*z* (relative abundance, %)): 354 (M+1, 100), 355 (M+2, 4.1), 356 (M+3, 6), 249 (5.7), 236 (4.9), 165 (60.5), 150 (16.5).

*5-(4-Methoxybenzylidene)-3-(2-(4-methoxyphenyl)-2-oxoethyl)thiazolidine-2,4--dione (**5b**)*. Yield: 95 %; white solid; m.p.: 223–224 °C; Anal. Calcd. for $C_{20}H_{17}NO_5S$: C, 62.65; H, 4.47; N, 3.65; S %, 8.36. Found: C, 62.82; H, 4.27; N, 3.88; S, 8.23 %; IR (ATR, cm^{-1}): 1036, 1255 ($C–O_{methoxy}$), 1683 ($C=O_{ketone}$), 1701 ($C=O_{thiazolidinedione}$), 1742 ($C=O_{thiazolidinedione}$); ^{1}H-NMR (500 MHz, DMSO-d_6, δ / ppm): 8.05 (2H, *d*, *J* = 9.0 Hz, Ar-H), 7.96 (1H, *s*, CH=), 7.65 (2H, *d*, *J* = 9.0 Hz, Ar-H), 7.14 (2H, *d*, *J* = 9.0 Hz, Ar-H), 7.12 (2H, *d*, *J* = 9.0 Hz, Ar-H), 5.29 (2H, *s*, CH_2), 3.90 (3H, *s*, OCH_3), 3.86 (3H, *s*, OCH_3); ^{13}C-NMR (125 MHz, DMSO-d_6, δ / ppm): 191.09 (C=O), 170.54 (C=O), 163.89 (C=O), 162.42 (C), 160.56 (C), 134.57 (C), 132.47 (C), 130.95 (C), 130.63 (2CH), 129.45 (CH), 129.31 (2CH), 118.62 (2CH), 116.43 (2CH), 56.11 (CH_3), 55.78 (CH_3), 49.95 (CH_2); MS (*m*/*z* (relative abundance, %)): 384 (M+1, 100), 385 (M+2, 2.6), 386 (M+3, 1.7), 277 (95), 269 (84), 250 (2.2).

*5-(4-Methoxybenzylidene)-3-(2-(4-nitrophenyl)-2-oxoethyl)thiazolidine-2,4--dione (**5c**)*. Yield: 92 %; pale yellow solid; m.p.: 227–229 °C; Anal. Calcd. for $C_{19}H_{14}N_2O_6S$: C, 57.28; H, 3.54; N, 7.03; S, 8.05 %. Found: C, 57.03; H, 3.32; N, 7.34; S, 8.22 %; IR (ATR, cm^{-1}): 1037, 1251 ($C–O_{methoxy}$), 1331 (NO_2, *sym*.), 1517 (NO_2, *asym*.), 1687 ($C=O_{ketone}$), 1704 ($C=O_{thiazolidinedione}$), 1747 ($C=O_{thiazolidinedione}$); ^{1}H-NMR (500 MHz, DMSO-d_6, δ / ppm): 8.41 (2H, *d*, *J* = = 9.0 Hz, Ar-H), 8.34 (2H, *d*, *J* = 9.0 Hz, Ar-H), 7.98 (1H, *s*, CH=), 7.66 (2H, *d*,

J = 9.0 Hz, Ar-H), 7.15 (2H, *d*, *J* = 9.0 Hz, Ar-H), 5.44 (2H, *s*, CH_2), 3.86 (3H, *s*, OCH_3); ^{13}C-NMR (125 MHz, DMSO-d_6, δ / ppm): 186.79 (C=O), 170.53 (C=O), 164.92 (C=O), 162.33 (C), 151.61 (C), 140.77 (C), 133.26 (C), 132.24 (C), 129.81 (2CH), 129.44 (CH), 129.29 (2CH), 123.76 (2CH), 114.99 (2CH), 56.01 (CH_3), 49.98 (CH_2); MS (*m*/*z* (relative abundance, %)): 399 (M+1, 100), 400 (M+2, 9.7), 401 (M+3, 5.7), 276 (3.4), 236 (7.4), 193 (84), 150 (30.3).

*3-[2-(4-Chlorophenyl)-2-oxoethyl]-5-(4-methoxybenzylidene)thiazolidine--2,4-dione (**5d**)*. Yield: 78 %; white solid; m.p.: 239–241 °C; Anal. Calcd. for $C_{19}H_{14}ClNO_4S$: C, 58.84; H, 3.64; N, 3.61; S, 8.27 %. Found: C, 60.12; H, 3.87; N, 3.44; S, 8.46 %; IR (ATR, cm^{-1}): 1041, 1248 ($C–O_{methoxy}$), 1681 ($C=O_{ketone}$), 1697 ($C=O_{thiazolidinedione}$), 1744 ($C=O_{thiazolidinedione}$); ^{1}H-NMR (500 MHz, DMSO-d_6, δ / ppm): 7.98 (1H, *s*, CH=), 7.70 (2H, *d*, *J* = 8.9 Hz, Ar-H), 7.67 (2H, *d*, *J* = 9.0 Hz, Ar-H), 7.51 (2H, *d*, *J* = 8.9 Hz, Ar-H), 7.14 (2H, *d*, *J* = = 9.0 Hz, Ar-H), 5.34 (2H, *s*, CH_2), 3.83 (3H, *s*, OCH_3); ^{13}C-NMR (125 MHz, DMSO-d_6, δ / ppm): 186.97 (C=O), 169.84 (C=O), 164.63 (C=O), 160.46 (C), 138.65 (C), 133.99 (C), 133.19 (C), 132.58 (C), 130.25 (2CH), 129.32 (CH), 129.12 (2CH), 128.64 (2CH), 118.06 (2CH), 55.87 (CH_3), 50.23 (CH_2); MS (*m*/*z* (relative abundance, %)): 388 (M+1, 100), 389 (M+2, 18.6), 390 (M+3, 53.3), 266 (48.8), 248 (55.7), 236 (9.6), 178 (27.9), 166 (55.1).

*4-{2-[5-(4-methoxybenzylidene)-2,4-dioxothiazolidin-3-yl]acetyl}benzonitrile (**5e**)*. Yield: 53 %; light brown solid; m.p.: 212–214 °C; Anal. Calcd. for $C_{20}H_{14}N_2O_4S$: C, 63.48; H, 3.73; N, 7.40; S, 8.47 %. Found: C, 63.29; H, 3.51; N, 7.48; S, 8.69 %; IR (ATR, cm^{-1}): 1043, 1253 ($C–O_{methoxy}$), 1679 ($C=O_{ketone}$), 1698 ($C=O_{thiazolidinedione}$), 1748 ($C=O_{thiazolidinedione}$), 2231 (C≡N); ^{1}H-NMR (500 MHz, DMSO-d_6, δ / ppm): 8.02 (2H, *d*, *J* = 8.6 Hz, Ar-H), 7.99 (2H, *d*, *J* = 8.6 Hz, Ar-H), 7.96 (1H, *s*, CH=), 7.61 (2H, *d*, *J* = 9.0 Hz, Ar-H), 7.15 (2H, *d*, *J* = 9.0 Hz, Ar-H), 5.41 (2H, *s*, CH_2), 3.84 (3H, *s*, OCH_3); ^{13}C-NMR (125 MHz, DMSO-d_6, δ / ppm): 186.97 (C=O), 170.34 (C=O), 164.23 (C=O), 160.30 (C), 135.43 (C), 134.08 (C), 132.38 (C), 132.27 (2CH), 129.69 (2CH), 129.41 (CH), 128.99 (2CH), 116.65 (C≡N), 116.14 (C), 114.51 (2CH), 55.89 (CH_3), 50.11 (CH_2); MS (*m*/*z* (relative abundance, %)): 379 (M+1, 100), 380(M+1, 10.1), 381 (M+2, 5.4), 274 (3.8), 193 (87.3), 165 (71.8), 150 (28.5), 121 (12.7).

*2-Hydroxy-5-{2-[5-(4-methoxybenzylidene)-2,4-dioxothiazolidin-3-yl]acetyl}benzamide (**5f**)*. Yield: 62 %; yellow solid; m.p.: 295–296 °C; Anal. Calcd. for $C_{20}H_{16}N_2O_6S$: C, 58.25; H, 3.91; N, 6.79; S, 7.77 %. Found: C, 58.38; H, 3.59; N, 6.69; S, 7.91 %; IR (ATR, cm^{-1}): 1040, 1252 ($C–O_{methoxy}$), 1233 ($C–O_{phenol}$), 1635 ($C=O_{amide}$), 1677 ($C=O_{ketone}$), 1694 ($C=O_{thiazolidinedione}$), 1741 ($C=O_{thiazolidinedione}$), 3411 (OH); ^{1}H-NMR (500 MHz, DMSO-d_6, δ / ppm): 14.01 (1H, *s*, OH), 8.81 (1H, *s*, NH amide), 8.67 (1H, *d*, *J* = 1.1 Hz, Ar-H), 8.20 (1H, *s*, NH amide), 8.07 (1H, *dd*, J_1 = 8.8 Hz, J_2 = 1.1 Hz, Ar-H), 7.98 (1H, *s*,

CH=), 7.66 (2H, *d*, *J* = 9.0 Hz, Ar-H), 7.15 (2H, *d*, *J* = 9.0 Hz, Ar-H), 7.05 (1H, *d*, *J* = 8.8 Hz, Ar-H), 5.28 (2H, *s*, CH_2), 3.86 (3H, *s*, OCH_3); ^{13}C-NMR (125 MHz, DMSO-d_6, δ / ppm): 191.66 (C=O), 174.78 (C=O), 170.23 (C=O), 164.94 (C=O), 160.44 (C), 157.78 (C–OH), 133.98 (C), 132.74 (C), 132.22 (CH), 129.96 (C), 129.63 (CH), 129.35 (2CH), 128.46 (CH), 122.34 (C), 117.71 (CH), 116.38 (2CH), 55.78 (CH_3), 50.03 (CH_2); MS (*m*/*z* (relative abundance, %)): 413 (M+1, 100), 414 (M+2, 13.9), 415 (M+3, 8.8), 391 (10.8), 276 (30.7), 248 (10.1), 266 (37.4), 177 (16.8).

*5-(4-Methoxybenzylidene)-3-(1-methyl-2-oxo-2-phenylethyl)thiazolidine-2,4--dione (**5g**)*. Yield: 64 %; white solid; m.p.: 146–148 °C; Anal. Calcd. for $C_{20}H_{17}NO_4S$: C, 65.38; H, 4.66; N, 3.81; S, 8.73 %. Found: C, 65.56; H, 4.61; N, 3.70; S, 8.87 %; IR (ATR, cm^{-1}): 1035, 1250 ($C–O_{methoxy}$), 1686 ($C=O_{ketone}$), 1703 ($C=O_{thiazolidinedione}$), 1736 ($C=O_{thiazolidinedione}$); ^{1}H-NMR (500 MHz, DMSO-d_6, δ / ppm): 7.88 (1H, *s*, CH=), 7.70 (2H, *d*, *J* = 7.8 Hz, Ar-H), 7.59 (1H, *t*, *J* = 7.8 Hz, Ar-H), 7.56 (2H, *d*, *J* = 9.0 Hz, Ar-H), 7.49 (2H, *t*, *J* = 7.8 Hz, Ar-H), 7.09 (2H, *d*, *J* = 9.0 Hz, Ar-H), 5.88 (1H, *q*, *J* = 6.9 Hz, CH), 3.82 (3H, *s*, OCH_3), 1.54 (3H, *d*, *J* = 6.9 Hz, CH_3); ^{13}C-NMR (125 MHz, DMSO-d_6, δ / ppm): 188.34 (C=O), 170.95 (C=O), 163.76 (C=O), 160.37 (C), 137.89 (C), 136.46 (C), 132.39 (C), 129.99 (2CH), 129.61 (2CH), 129.43 (CH), 126.67 (2CH), 124.89 (CH), 116.22 (2CH), 56.03 (CH_3), 52.46 (CH), 20.79 (CH_3); MS (*m*/*z* (relative abundance, %)): 368 (M+1, 100), 369 (M+2, 1.4), 370 (M+3, 1.4), 290 (14), 262 (97.9), 237 (17.3), 167 (11.7).

*5-(4-Methoxybenzylidene)-3-[2-(naphthalen-2-yl)-2-oxoethyl]thiazolidine-2,4--dione (**5h**)*. Yield: 81 %; white solid; m.p.: 265–267 °C; Anal. Calcd. for $C_{23}H_{17}NO_4S$: C, 68.47; H, 4.25; N, 3.47; S, 7.95 %. Found: C, 68.61; H, 4.31; N, 3.29; S, 8.12 %; IR (ATR, cm^{-1}): 1038, 1258 ($C–O_{methoxy}$), 1673 ($C=O_{ketone}$), 1700 ($C=O_{thiazolidinedione}$), 1746 ($C=O_{thiazolidinedione}$); ^{1}H-NMR (500 MHz, DMSO-d_6, δ / ppm): 8.90 (1H, *s*, Ar-H), 8.17 (1H, *d*, *J* = 8.0 Hz, Ar--H), 8.11 (1H, *d*, *J* = 8.0 Hz, Ar-H), 8.03 (2H, *t*, *J* = 8.6 Hz, Ar-H), 7.89 (1H, *s*, CH=), 7.74 (1H, *t*, *J* = 8.6 Hz, Ar-H), 7.69 (1H, *t*, *J* = 8.6 Hz, Ar-H), 7.59 (2H, *d*, *J* = 9.0 Hz, Ar-H), 7.12 (2H, *d*, *J* = 9.0 Hz, Ar-H), 5.45 (2H, *s*, CH_2), 3.85 (3H, *s*, OCH_3); ^{13}C-NMR (125 MHz, DMSO-d_6, δ / ppm): 190.89 (C=O), 170.24 (C=O), 164.88 (C=O), 160.54 (C), 136.57 (C), 135.31 (C), 134.46 (C), 133.40 (C), 132.61 (C), 130.13 (CH), 129.69 (2CH), 129.30 (CH), 129.24 (CH), 128.81 (CH), 128.54 (CH), 128.18 (CH), 127.68 (CH), 124.50 (CH), 116.27 (2CH), 55.29 (CH_3), 50.12 (CH_2); MS (*m*/*z* (relative abundance, %)): 404 (M+1, 100), 405 (M+2, 24.6), 406 (M+3, 10.8), 373 (5.4), 286 (32.4), 250 (7.9), 237 (19.5).

Journal of the Serbian Chemical Society
JSCS-info@shd.org.rs • www.shd.org.rs/JSCS
J. Serb. Chem. Soc. 79 (2) 125–132 (2014)
JSCS–4570
UDC 547.759.32+547.233+547.251.1+542.913+543.42:615.281/.282
Original scientific paper

Synthesis, characterization and biological evaluation of some newer carbazole derivatives

DIVYANSHU SHARMA, NITIN KUMAR and DEVENDER PATHAK*

Rajiv Academy for Pharmacy, Delhi-Mathura Highway, Chhattikara, Mathura - 281001, India

(Received 23 January, revised 16 June 2013)

Abstract: A series of novel 5-[(9*H*-carbazol-9-yl)methyl]-*N*-[(substituted phenyl)(piperazin-1-yl)methyl]-1,3,4-oxadiazol-2-amines (**4a**–**o**) derivatives was synthesized by starting with carbazole, which on reaction with ethyl chloroacetate yielded ethyl 2-(9*H*-carbazole-9-yl)acetate (**1**). Compound **1** on reaction with semicarbazide followed by cyclisation with sulphuric acid gave 5-((9*H*-carbazole-9-yl)-1,3,4-oxadiazol-2-amine (**3**), which through Mannich reaction with piperazine and a variety of aromatic aldehydes in the presence of acetic acid yielded the titled compounds (**4a**–**o**). The structures of compounds were characterized by UV, FT-IR, ^{1}H-NMR and MS spectral studies, and by elemental analysis. All the derivatives were evaluated for their antibacterial, antifungal and anticancer activities. Among the tested compounds, **4a**, **4d**, **4e** and **4n** exhibited significant antibacterial and antifungal activity, while the compounds **4a**, **4d**, **4k** and **4n** were found to be active on the human breast cancer cell line MCF7.

Keywords: Mannich reaction; antibacterial activity; antifungal activity; MCF7; synthesis; spectroscopy.

INTRODUCTION

Carbazole derivatives are well known for their pharmacological activities. It is evident from the literature that the derivatives of carbazole moiety possess a wide spectrum of pharmacological activities, such as antibacterial,[1–3] antifungal,[4,5] antitumour, antineoplastic,[6–10] anticonvulsant,[11] antioxidant,[12] antidiabetic,[13] antipsychotic[14] and larvicidal activity.[15]

Various heteroannulated carbazole derivatives have drawn attention because of their natural occurrence and the broad spectrum of biological activity associated with these compounds. The carbazole moiety is a frequent moiety of numerous drugs, such as olivacine, ondansetron, rimcazole, stauroapirone, carbazolol, carvedilol, carprofen, cacotheline, rebaccamycin, ellipticine and various

* Corresponding author. E-mail: dev_15@rediffmail.com
doi: 10.2298/JSC130123069S

naturally occurring carbazole alkaloids.[16] Carbazole derivatives have documented consistent advances in the design of novel antipsychotic, neuroleptic and anticonvulsant agents.[17] Furthermore, various congeners of oxadiazole, thiadiazole, azetidinone and thiazolidinone have also been reported to exhibit potential antimicrobial, anticancer, antipsychotic, antidepressant and anticonvulsant activity.[18–21] In view of broad biological activity of carbazole derivatives, in this study it was planned to synthesize new carbazole derivatives and by incorporation of new pharmacophores, such as oxadiazole at position 9 of carbazole nucleus, with the hope of obtaining better pharmacologically active drugs as anticancer and antimicrobial agents. In the same direction, a one pot method was developed to synthesize a series of 5-[(9*H*-carbazol-9-yl)methyl]-*N*-[(substituted--phenyl)(piperazin-1-yl)methyl]-1,3,4-oxadiazol-2-amine derivatives (**4a**–**o**) as Mannich bases.

EXPERIMENTAL

The purity of all the newly synthesized compounds were checked by TLC on silica gel--protected aluminium sheets (type 60 F_{254}, Merck) and the spots were detected by exposure to iodine vapour and a UV-lamp at λ 254 nm. The melting points were determined in open capillary tubes and are uncorrected. The infrared (FT-IR) spectra were recorded on a 470--Shimadzu infrared spectrophotometer using the KBr pressed pellet technique and the result are expressed in cm^{-1}. The ^{1}H- and ^{13}C-NMR spectra were recorded on a Bruker DRX-300 instrument using $CDCl_3$ as a solvent. The chemical shifts, δ, are given in ppm downfield from the internal standard tetramethylsilane (TMS). The splitting patterns are designated as follows; *s*: singlet; *d*: doublet and *m*: multiplet. The mass spectra were obtained on a Shimadzu 2010A LC-MS spectrometer. Elemental analyses were realised on an Elemental Vario EL III Carlo Erba 1108 instrument and the obtained values were within ±0.04 % of the theoretical values.

*Synthesis of ethyl 2-(9*H*-carbazol-9-yl)acetate (**1**)*

To a solution of carbazole (2.01 g, 0.012 mol) in 18 mL of dry acetone, ethyl chloroacetate (1.472 g, 0.012 mol) was added dropwise in the presence of anhydrous potassium carbonate (0.09 g) and the resultant mixture refluxed for 22 h. Then the mixture was cooled and the thus obtained solid was filtered, dried and recrystallized from methanol to give compound **1**.[17] Yield: 59.44 %; m.p.: 240–241 °C

*Synthesis of 1-[2-(9*H*-carbazol-9-yl)acetyl]semicarbazide (**2**)*

Compound **1** (2.53 g, 0.01 mol) was dissolved in 90 mL of acetone (solution A) and semicarbazide (0.62 g, 0.01 mol) was dissolved in 20 mL of water (solution B). Solution B was poured into solution A and the mixture was refluxed for 28 h. On cooling, the solid product that separated out was filtered, dried and recrystallized from methanol to give compound **2**.[17] Yield: 70.40 %; m.p.: 184–185 °C.

*Synthesis of 5-[(9*H*-carbazol-9-yl)methyl]-1,3,4-oxadiazol-2-amine (**3**)*

A solution of compound **2** (2.83 g, 0.01 mol) with 25 mL of conc. H_2SO_4 was kept overnight at room temperature, then the reaction mixture was poured into ice-cold water, neutralized with ammonia and extracted with ether. The ethereal solution was distilled off and the product obtained was recrystallized from acetone to give compound **3**.[17] Yield: 65.9 %; m.p.: 161–162 °C.

*General synthetic procedure for the synthesis of 5-[(9*H*-carbazol-9-yl)methyl]*-N-*[(substituted phenyl)(piperazin-1-yl)methyl]-1,3,4-oxadiazol-2-amines (**4a**–**o**)*

A mixture of equimolar quantity (0.01 mol) of compound (**3**), derivative of aromatic aldehydes and piperazine along with few drops of glacial acetic acid was refluxed in 15 mL of methanol for 8–13 h. The hot solution was poured onto crushed ice and the thus obtained solid mass was filtered, dried and recrystallized from acetone to give compounds **4a**–**o**.

Antibacterial activity

The antibacterial activities of the newly synthesized compounds were tested by the disc diffusion method on nutrient agar medium against the bacterial strains *Staphylococcus aureus* ATCC 6538 and *Bacillus subtilis* ATCC 6633 (Gram-positive), and *Escherichia coli* ATCC 35210 and *Pseudomonas aeruginosa* ATCC 27853 (Gram-negative).

In the disc diffusion method, a paper disc (6 mm in diameter) was impregnated with the test compounds dissolved in DMSO at concentrations of 25, 50 and 100 μg mL^{-1}. A disc impregnated with DMSO was used as the solvent control because of the free solubility of the test compounds. The nutrient agar medium in Petri dishes was inoculated with bacterial strains and the discs impregnated with the solutions of different concentrations of the compounds were placed over it. The plates were incubated at 35 °C for 24 h. The zone of inhibition indicating the inhibited growth of microorganism around the discs was observed. Ciprofloxacin was used as the standard (50 μg mL^{-1}) to compare the efficacy of tested compounds. Each testing was performed in triplicate. The results were interpreted in terms of diameter (mm) of the zone of inhibition.

Antifungal activity

The antifungal activity of the newly synthesized compounds was tested on the fungal strains *Candida albicans* ATCC 10261 and *Aspergillus niger* ATCC 9643 using the paper disc diffusion method by using agar medium.

The procedure for the activity testing was similar to that described above for the antibacterial testing and the same concentrations of the tested compounds were employed. The results were recorded and reported after incubation for 48 h at 25 °C for the fungal strains and fluconazole was used as the standard (50 μg mL^{-1}). The zones of inhibition indicating the inhibited growth of microorganism by the prepared compounds around the discs was observed and reported. Each experiment was performed in triplicate.

Anticancer activity

The newly synthesized compounds were evaluated for their anticancer activity by determining the percentage control growth of human breast cancer cell lines MCF7 by the *in vitro* sulforhodamine B assay (SRB assay) method.[22] The cell lines were grown in Roswell Park Memorial Institute (RPMI) 1640 medium containing 10 % foetal bovine serum and 2 mM L-glutamine. The tested compounds were solubilised in appropriate solvent at 400-fold the desired final maximum test concentration and stored frozen prior to use. At the time of drug addition, an aliquot of frozen concentrate was thawed and diluted to 10 times the desired final maximum test concentration with complete medium containing the test article at a concentration of 10^{-3} μg ml^{-1}. Additional three 10-fold serial dilutions were made to provide a total of four drug concentrations plus control. Aliquots of 10 μL of these different drug dilutions were added to the appropriate microtitre wells already containing 90 μL of medium, resulting in the required final drug concentrations, *i.e.*, 10, 20, 40 and 80 μg mL^{-1}. The absorbance was read on a plate reader at a wavelength of 540 nm with 690 nm reference wavelength. The percent growth was calculated on a plate-by-plate basis for the test wells relative to the control wells.

The percent growth was expressed as the ratio of the average absorbance of the test well to the average absorbance of the control wells×100. Using the six absorbance measurements (time zero (T_z), control growth (C), and test growth in the presence of drug at the four concentration levels (T_i)), the percentage growth was calculated at each of the drug concentration levels. Percentage growth inhibition was calculated as: $((T_i - T_z)/(C - T_z))\times100$ for concentrations for which $T_i \geq T_z$ ($T_i - T_z$ is positive or zero) or $((T_i - T_z)/T_z)\times100$ for concentrations for which $T_i < T_z$ ($T_i - T_z$ is negative). The dose response parameters, *i.e.*, growth inhibition of 50 % (GI_{50}), total growth inhibition (*TGI*) and killing of 50 % of the cells (LC_{50}), were calculated for each test substance.

RESULTS AND DISCUSSION

The reaction sequences leading to different carbazole derivatives are outlined in Scheme 1. The carbazole derivatives were synthesized by incorporating new pharmacophores, such as oxadiazole, at position 9 of the carbazole nucleus by a conventional method in which carbazole was taken as a starting material to produce the corresponding 5-[(9*H*-carbazol-9-yl)methyl]-*N*-[(substituted-phenyl)(piperazin-1-yl)methyl]-1,3,4-oxadiazol-2-amines (**4a**–**o**). Synthesized compounds were identified based on their physical parameters, *i.e.*, solubility, melting point, chromatographic methods (TLC). The data is given in Table I and spectroscopic methods (UV, IR, ^{1}H-NMR, MS and elemental analysis are given in the Supplementary material to this paper. The ^{1}H-NMR spectra showed a peak between δ 6.00–7.00 ppm, which was assigned to the N–H (aliphatic) proton. A peak characteristic of –CH– appeared between δ 4.00–5.00 ppm. The peaks at δ 6.00–8.00 ppm showed the presence of aromatic protons. In the FT-IR spectra, a peak characteristic of N–H (aliphatic) appeared at 3200–3450 cm^{-1} and a peak for C=N was observed at 1500–1600 cm^{-1}.

Pharmacological screening

All the newly synthesized compounds **4a**–**o** were screened for their antibacterial and antifungal activity (Table II). The results revealed that among the synthesized compounds tested, **4a**, **4d** and **4n** were found to be more potent against all the bacterial and fungal strains at a concentration 50 μg mL^{-1}

Anticancer screening. All the synthesized compounds **4a**–**o** were evaluated for their anticancer activity against the human breast cancer cell line MCF7 by the SRB assay The *in vitro* anticancer study was realised at the Tata Memorial Centre, Advanced Centre for Treatment Research and Education in Cancer (ACTREC), Navi Mumbai, India. The obtained data are given in Table III. Among all the synthesized compounds tested, **4a**, **4d**, **4k**, **4m** and **4n** were found to be most active against human breast cancer cell lines. It was found that for a large variety of polycyclic compounds, basic moieties attached to the ring system not only improve the solubility under physiological conditions, but also lead to an increase in anticancer activity.[1] In the present study, it was established that presence of an electronegative atom on the benzene ring makes MCF7 cell lines

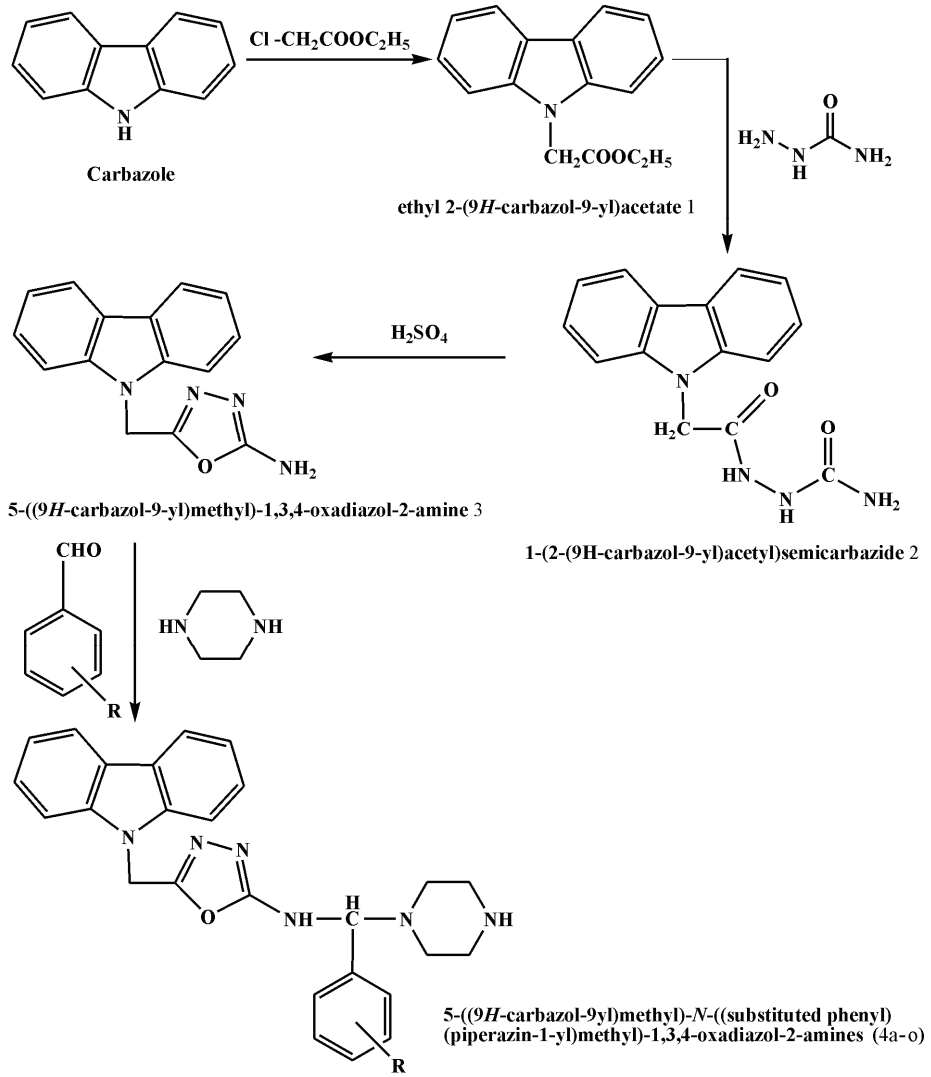

Scheme 1. Synthesis of carbazole derivatives **4a**–**o**.

TABLE I. Physical data of the synthesized compounds **4a**–**o**

Compound	R	Yield, %	Reaction time, h	M.p. range, °C	R_f value[a]
4a	*p*-Nitro	82.55	4.0	236–237	0.73
4b	*p*-Hydroxy	79.69	5.0	208–209	0.62
4c	3,4,5-Trimethoxy	61.5	4.3	184–185	0.69
4d	*p*-Chloro	73.22	6.0	221–222	0.75
4e	*p*-(Dimethylamino)	53.78	5.5	202–203	0.59
4f	*o*-Nitro	63.96	4.4	225–226	0.65
4g	*m*-Hydroxy	72.71	5.2	213–214	0.56

TABLE I. Continued

Compound	R	Yield, %	Reaction time, h	M.p. range, °C	R_f value[a]
4h	*m*-Nitro	69.98	6.8	229–230	0.71
4i	*o*-Hydroxy	59.33	5.0	218–219	0.60
4j	*m*-Chloro	67.07	4.4	231–232	0.67
4k	*o*-Chloro	56.45	6.2	237–238	0.66
4l	*m*-Methoxy	52.54	4.5	192–193	0.77
4m	*p*-Methoxy	58.75	7.0	189–190	0.79
4n	*p*-Fluoro	55.0	6.0	234–235	0.54
4o	H	51.23	5.2	176–177	0.63

[a]Solvent system: benzene:chloroform:methanol (4:3:2)

TABLE II. Antibacterial and antifungal activity of compounds **4a**–**o**; diameter of zone of inhibition at 50 μg mL^{-1}, mm (mean±*SD* (*n* = 3))

Compound	Bacteria				Fungi	
	B. subtilis	*S. aureus*	*E. coli*	*P. aeruginosa*	*C. albicans*	*A. niger*
4a	16.2±0.3	16.1±0.3	22.0±0.2	24.0±0.1	16.3±0.3	11.1±0.2
4b	12.6±0.1	14.6±0.1	20.2±0.1	19.5±0.2	13.1±0.1	9.9±0.1
4c	10.1±0.3	12.8±0.3	17.1±0.1	17.1±0.2	10.1±0.4	8.1±0.5
4d	15.6±0.1	16.2±0.1	21.8±0.1	24.1±0.1	16.1±0.1	11.7±0.2
4e	14.1±0.3	15.9±0.1	22.3±0.5	22.7±0.3	15.3±0.2	10.5±0.2
4f	13.6±0.2	14.8±0.2	21.6±0.2	23.0±0.4	14.9±0.1	10.2±0.1
4g	11.3±0.1	13.6±0.2	19.4±0.2	18.0±0.1	12.2±0.3	9.5±0.4
4h	15.4±0.1	15.2±0.1	21.9±0.2	22.4±0.1	15.1±0.4	10.9±0.1
4i	10.8±0.2	11.4±0.1	18.6±0.1	19.1±0.4	14.9±0.2	10.3±0.3
4j	14.3±0.3	13.7±0.2	20.8±0.1	23.7±0.2	15.6±0.3	10.8±0.4
4k	13.5±0.1	12.4±0.3	21.0±0.3	21.5±0.3	15.1±0.1	10.4±0.3
4l	10.1±0.4	8.8±0.1	15.8±0.1	15.6±0.1	8.9±0.4	7.1±0.2
4m	9.9±0.1	10.3±0.1	16.7±0.3	17.2±0.2	9.5±0.1	8.3±0.1
4n	16.8±0.2	16.5±0.1	22.6±0.1	23.6±0.1	15.9±0.3	11.4±0.4
4o	8.2±0.1	9.9±0.3	14.5±0.1	15.9±0.2	8.1±0.2	5.8±0.1
Ciprofloxacin[a]	15.5±0.2	17.8±0.6	22.2±0.4	26.5±0.5	–	–
Fluconazole[a]	–	–	–	–	16.9±0.5	11.8±0.3

[a]Standards – ciprofloxacin and fluconazole at 50 μg mL^{-1} concentrations. Statistical analysis of the data was performed by one way ANOVA

TABLE III. Anticancer activity of compounds **4a**–**o** against human breast cancer cell line MCF7

Compound	Control growth %	Drug concentration μg mL^{-1}			Drug concentration, μg mL^{-1}		
	10	20	40	80	GI_{50}[a]	*TGI*	LC_{50}
4a	40.4	27.4	10.3	2.1	<10	34.4	60.6
4b	58.5	45.3	38.2	30.8	<20	>80	>80
4c	52.4	40.9	34.7	29.2	<20	>80	>80
4d	43.7	19.1	10.0	2.8	<10	35.2	60.2
4e	59.6	41.5	30.2	22.6	<20	>80	>80

TABLE III. Continued

Compound	Control growth %	Drug concentration μg mL^{-1}			Drug concentration, μg mL^{-1}		
	10	20	40	80	GI_{50}[a]	*TGI*	LC_{50}
4f	53.4	38.7	27.2	13.3	<20	>80	>80
4g	61.6	50.2	41.9	36.0	<40	>80	>80
4h	51.9	33.7	28.5	16.4	<20	68.4	>80
4i	58.2	49.3	37.0	31.3	<20	>80	>80
4j	55.8	38.5	27.6	18.1	<20	72.9	>80
4k	46.9	31.5	11.8	3.4	<10	26.5	53.6
4l	50.6	37.3	29.7	20.2	<20	>80	>80
4m	49.2	34.6	18.3	13.9	<10	60.3	>80
4n	35.4	11.3	8.4	1.2	<10	16.5	35.6
4o	66.4	53.7	45.2	39.4	<40	>80	>80
ADR[b]	0.3	–10.7	–33.6	–59.7	<10	11.6	23.2

[a]A GI_{50} value of < 10 μg mL^{-1} is considered to demonstrate activity in the case of a pure compound; [b]standard – adriamycin (ADR), positive control compound

more susceptible towards the compound. The results revealed that the substitution is more effective at position 4 than at position 2.

SUPPLEMENTARY MATERIAL

Analytic and spectral data for the prepared compounds are available electronically from http://www.shd.org.rs/JSCS/, or from the corresponding author on request.

Acknowledgements. The authors are thankful to the management of Rajiv Academy for Pharmacy, Mathura for providing research facilities and the Tata Memorial Centre, Mumbai for determining the anticancer activity of the synthesized compounds.

ИЗВОД

СИНТЕЗА, КАРАКТЕРИЗАЦИЈА И ИСПИТИВАЊЕ БИОЛОШКЕ АКТИВНОСТИ НОВИХ ДЕРИВАТА КАРБАЗОЛА

DIVYANSHU SHARMA, NITIN KUMAR и DEVENDER PATHAK

Rajiv Academy for Pharmacy, Delhi-Mathura Highway, Chhattikara, Mathura - 281001, India

Синтетисана је серија нових деривата 5-[(9*H*-карбазол-9-ил)метил]-*N*-[(супституисани фенил)(пиперазин-1-ил)метил]-1,3,4-оксадиазол-2-амина (**4a**–**o**), полазећи од карбазола. У реакцији карбазола и етил-хлорацетата добијен је етил-2-(9*H*-карбазол-9-ил)ацетат (**1**), који у реакцији са семикарбазолом и након циклизације у присуству сумпорне киселине даје 5-(9*H*-карбазол-9-ил)-1,3,4-оксадиазол-2-амин (**3**). Амин **3** у Маниковој реакцији са пиперазином и различитим ароматичним алдехидима, у присуству сирћетне киселине, даје циљане деривате **4a**–**o**. Једињења су окарактерисана UV, FT-IR, ^{1}H-NMR, MS спектрима и елементалном анализом. Испитане су антибактеријске, антифунгална и антиканцерска активност свих добијених дервата. Деривати **4a**, **4d**, **4e** и **4n** погазују значајну антибактеријску и антифунгалну активност, док деривати **4a**, **4d**, **4k** и **4n** показују активност и према хуманим ћелијским линијама рака дојке MCF7.

(Примљено 23. јануара, ревидирано 16. јуна 2013)

REFERENCES

1. C. Asche, W. Frank, A. Antje, U. Kucklaender, *Bioorg. Med. Chem.* **13** (2005) 819
2. R. B. Bedford, M. Betham, *J. Org. Chem.* **71** (2006) 9403
3. R. B. Bedford, M. Betham, J. P. H. Charmant, A. L. Weeks, *Tetrahedron* **64** (2008) 6038
4. A. Bombrun, G. Casi, *Tetrahedron Lett.* **43** (2002) 2187
5. A. Bombrun, P. Gerber, G. Casi, O. Terradillos, B. Antonsson, S. Halazy, *J. Med. Chem.* **46** (2003) 4365
6. A. Carsuo, A. S. V. Chiret, J. C. Lancelot, M. S. Sinicropi, A. Garofalo, S. Rault, *Molecules* **13** (2008) 1312
7. A. Caruso, J. C. Lancelot, H. El. Kashef, M. S. Sinicropi, R. Legay, A. Lesnard, S. Rault, *Tetrahedron* **65** (2009) 1040
8. M. Chakrabarty, N. Ghosh, Y. Harigaya, *Tetrahedron Lett.* **45** (2004) 4955
9. E. Conchon, F. Anizon, B. Aboab, M. Golsteyn, S. Leonce, B. Pfeiffer, M. Prudhomme, *Eur. J. Med. Chem*. **43** (2008) 282
10. E. Conchon, F. Anizon, R. M. Golsteyn, S. Leonce, B. Pfeiffer, N. Prudhonne, *Tetrahedron* **62** (2006) 11136
11. A. I. Danish, K. J. R. Prasad, *Indian J. Heterocycl. Chem.* **14** (2006) 19
12. C. Guillonneau, A. Pierre, Y. Charton, N. Guilbard, L. K. Berthier, S. Leonce, A. Michael, E. Bisagni, G. Atassi, *J. Med. Chem.* **42** (1999) 2191
13. T. Indumati, F. R. Fronczek, K. J. R. Prasad, *J. Mol. Struct.* **1016** (2012) 134
14. S. Issa, N. Walchshofer, I. Kassab, H. Termoss, S. Chamat, A. Geahchan, Z. Bouaziz, *Eur. J. Med. Chem*. **45** (2010) 2567
15. S. Kantevari, T. Yempala, G. Surineni, B. Sridhar, D. Sriram, *Eur. J. Med. Chem*. **46** (2011) 4827
16. http://pharma.financialexpress.com/ (accessed in Feb, 2014)
17. H. Kaur, S. Kumar M. Sharma, K. K. Saxena, A. Kumar, *Eur. J. Med. Chem*. **45** (2010) 2777
18. R. Kumar, U. Ramchandran, K. Srinivasan, P. Ramarao, S. Raichur, R. Chakrabati, *Bioorg. Med. Chem*. **13** (2005) 4279
19. V. V. Mulwad, C. A. Patil, *Indian J. Chem*., *B* **44** (2005) 2355
20. M. Laronze, M. Boisburn, S. Leonce, P. Renard, O. Lozach, L. Meijer, A. Lansiaux, C. Bailly, J. Sapi, J. Y. Laronze, *Bioorg. Med. Chem.* **13** (2005) 2263
21. R. V. Patel, P. K. Patel, P. Kumari, D. P. Rajani, K. H. Chikhalia, *Eur. J. Med. Chem*. **53** (2012) 41
22. P. Skehn, R. Storeng, A. Scudiero, J. Monks, D. McMohan, D. Vistica, T. W. Jonathan, H. Bokesch, *J. Natl. Cancer Inst.* **82** (1990) 1107.

Journal of the Serbian Chemical Society
JSCS@tmf.bg.ac.rs • www.shd.org.rs/JSCS
J. Serb. Chem. Soc. 79 (2) S18–S23 (2014) *Supplementary material*

SUPPLEMENTARY MATERIAL TO

Synthesis, characterization and biological evaluation of some newer carbazole derivatives

DIVYANSHU SHARMA, NITIN KUMAR and DEVENDER PATHAK*

Rajiv Academy for Pharmacy, Delhi-Mathura Highway, Chhattikara, Mathura - 281001, India

J. Serb. Chem. Soc. 79 (2) (2014) 125–132

ANALYTIC AND SPECTRAL DATA FOR THE PREPARED COMPOUNDS

*5-[(9*H*-Carbazol-9-yl)methyl]*-N-*[(4-nitrophenyl)(piperazin-1-yl)methyl]--1,3,4-oxadiazol-2-amine (**4a**)*. Anal. Calcd. for $C_{26}H_{25}N_7O_3$: C, 64.58; H, 5.21; N, 20.28 %. Found: C, 64.57; H, 5.19; N, 20.25 5; IR (KBr, cm^{-1}) 3415, 3049, 2927, 2846, 1674, 1606, 1533, 1340, 1291, 1112, 837; ^{1}H-NMR (300 MHz, $CDCl_3$, δ / ppm): 1.89 (1H, *s*, NH, D_2O exchangeable), 2.49 (4H, *t*, *J* = 4.5 Hz, CH_2), 2.67 (4H, *t*, *J* = 7.5 Hz, CH_2), 3.97 (1H, *s*, NH, D_2O exchangeable), 4.98 (1H, *s*, CH), 5.16 (2H, *s*, CH_2), 7.10 (2H, *d*, *J* = 6.0 Hz, Ar-H), 7.26 (3H, *t*, *J* = = 9.0 Hz, Ar-H), 7.46 (3H, *t*, *J* = 7.5 Hz, Ar-H), 7.71 (2H, *d*, *J* = 15 Hz, Ar-H), 8.06 (2H, *d*, *J* = 6.0 Hz, Ar-H); ^{13}C-NMR (75 MHz, $CDCl_3$, δ / ppm): 146.9, 144.4, 130.9, 129.8, 122.2, 120.8, 118.9, 111.1, 77.9, 50.0, 46.3; MS-ESI (*m*/*z* (relative abundance, %)): 483.24 (M^+, 100), 437.21 (29.9), 361.18 (22.2), 263.09 (16.6), 248.08 (38.0), 180.08 (14.4), 166.06 (13.3), 115.03 (6.0). UV (DMSO, λ_{max} / nm): 356.

*4-[[(5-[(9*H*-Carbazol-9-yl)methyl]-1,3,4-oxadiazol-2-yl)amino](piperazin-1-yl)methyl]phenol (**4b**)*. Anal. Calcd. for $C_{26}H_{26}N_6O_2$: C, 68.70; H, 5.77; N, 18.49 %. Found: C, 68.66; H, 5.75; N, 18.46 %; IR (KBr, cm^{-1}) 3642, 3414, 3046, 2921, 2856, 1670, 1600, 1335, 1155, 844; ^{1}H-NMR (300 MHz, $CDCl_3$, δ / ppm): 1.97 (1H, *s*, NH, D_2O exchangeable), 2.45 (4H, *t*, *J* = 9.0 Hz, CH_2), 2.69 (4H, *t*, *J* = 6.0 Hz, CH_2), 4.09 (1H, *s*, NH, D_2O exchangeable), 4.91 (1H, *s*, OH, D_2O exchangeable), 5.15 (1H, *s*, CH), 5.29 (2H, *s*, CH_2), 6.74 (2H, *d*, *J* = 9.0 Hz, Ar-H), 6.95 (3H, *t*, *J* =7.5 Hz, Ar-H), 7.14 (3H, *t*, *J* = 9.0 Hz, Ar-H), 7.37 (2H, *d*, *J* = 6.0 Hz, Ar-H), 7.56 (2H, *d*, *J* = 15 Hz, Ar-H); ^{13}C-NMR (75 MHz, $CDCl_3$, δ / ppm): 157.0, 130.9, 122.2, 120.1, 115.6, 111.1, 77.9, 58.1, 50.0, 46.3; MS-ESI (*m*/*z* (relative abundance, %)): 454.21 (M^+, 100), 437.36 (27.8), 361.25 (21.7), 263.17 (17.1), 248.01 (40.3), 180.05 (13.8), 166.10 (14.1), 115.85 (4.2); UV (DMSO, λ_{max} / nm): 353.

* Corresponding author. E-mail: dev_15@rediffmail.com

*5-[(9*H*-Carbazol-9-yl)methyl]*-N-*[(piperazin-1-yl)(3,4,5-trimethoxyphenyl)-methyl]-1,3,4-oxadiazol-2-amine (**4c**).* Anal. Calcd. for $C_{29}H_{32}N_6O_4$: C, 65.89; H, 6.10; N, 15.90 %. Found: C, 65.86; H, 6.07; N, 15.88 %; IR (KBr, cm^{-1}): 3413, 3047, 2908, 2812, 1661, 1601, 1323, 1236, 1166, 1068; ^{1}H-NMR (300 MHz, $CDCl_3$, δ / ppm): 1.96 (1H, *s*, NH, D_2O exchangeable), 2.44 (4H, *t*, *J* = 7.5 Hz, CH_2), 2.68 (4H, *t*, *J* = 6.0 Hz, CH_2), 3.73 (9H, *s*, $(OCH_3)_3$), 4.13 (1H, *s*, NH, D_2O exchangeable), 4.99 (1H, *s*, CH), 5.18 (2H, *s*, CH_2), 6.06 (2H, *d*, *J* = 12 Hz, Ar-H), 6.10 (2H, *d*, *J* = 9.0 Hz, Ar-H), 6.96 (2H, *d*, *J* = 6.0 Hz, Ar-H), 7.19 (3H, *t*, *J* = 4.5 Hz, Ar-H), 7.46 (3H, *t*, *J* = 7.5 Hz, Ar-H); ^{13}C-NMR (75 MHz, $CDCl_3$, δ / ppm): 150.5, 137.7, 132.6, 130.9, 122.2, 120.1, 119.0, 111.1, 106.2, 78.5, 58.1, 56.23, 50.0, 46.3; MS-ESI (*m*/*z* (relative abundance, %)): 528.25 (M^+, 100), 513.22 (34.2), 497.23 (30.6), 361.32 (24.3), 263.29 (15.9), 248.36 (36.6), 180.11 (15.8), 166.01 (13.1), 115.43 (3.9); UV (DMSO, λ_{max} / nm): 360.

*5-[(9*H*-Carbazol-9-yl)methyl]*-N-*[(4-chlorophenyl)(piperazin-1-yl)methyl]--1,3,4-oxadiazol-2-amine (**4d**).* Anal. Calcd. for $C_{26}H_{25}ClN_6O$: C, 66.03; H, 5.33; N, 17.77 %. Found: C, 66.01; H, 5.32; N, 17.74 %; IR (KBr, cm^{-1}) 3417, 3053, 2920, 2854, 1660, 1601, 1330, 1147, 1063, 852; ^{1}H-NMR (300 MHz, $CDCl_3$, δ / ppm): 2.01 (1H, *s*, NH, D_2O exchangeable), 2.45 (4H, *t*, *J* = 6.0 Hz, CH_2), 2.63 (4H, *t*, *J* = 6.0 Hz, CH_2), 4.12 (1H, *s*, NH, D_2O exchangeable), 4.95 (1H, *s*, CH), 5.09 (2H, *s*, CH_2), 7.08 (2H, *d*, *J* = 9.0 Hz, Ar-H), 7.21 (3H, *t*, *J* = = 7.5 Hz, Ar-H), 7.32 (3H, *t*, *J* = 9.0 Hz, Ar-H), 7.42 (2H, *d*, *J* = 6.0 Hz, Ar-H), 7.68 (2H, *d*, *J* = 6.0 Hz, Ar-H); ^{13}C-NMR (75 MHz, $CDCl_3$, δ / ppm): 136.4, 130.3, 122.2, 120.1, 118.9, 111.1, 77.9, 58.1,50.0, 46.3; MS-ESI (*m*/*z* (relative abundance, %)): 472.18 (M^+, 100), 437.12 (26.2), 361.22 (23.5), 263.18 (18.4), 248.17 (38.0), 180.33 (14.2), 166.23 (12.8), 115.33 (5.2); UV (DMSO, λ_{max} / / nm): 338.

*5-[(9*H*-Carbazol-9-yl)methyl]*-N-*[(4-(dimethylamino)phenyl)(piperazin-1-yl)-methyl]-1,3,4-oxadiazol-2-amine (**4e**).* Anal. Calcd. for $C_{28}H_{31}N_7O$: C, 69.83; H, 6.49; N, 20.36 %. Found: C, 69.81; H, 6.46; N, 20.32 %; IR (KBr, cm^{-1}): 3412, 3040, 2919, 2851, 1666, 1598, 1323, 1159, 817; ^{1}H-NMR (300 MHz, $CDCl_3$, δ / / ppm): 1.90 (1H, *s*, NH, D_2O exchangeable), 2.32 (4H, *t*, *J* = 9.0 Hz, CH_2), 2.58 (4H, *t*, *J* = 7.5 Hz, CH_2), 2.85 (6H, *s*, $N(CH_3)_2$), 4.01 (1H, *s*, NH, D_2O exchangeable), 4.89 (1H, *s*, CH), 5.08 (2H, *s*, CH_2), 6.45 (2H, *d*, *J* = 6.0 Hz, Ar-H), 6.68 (3H, *t*, *J* = 10.5 Hz, Ar-H), 6.90 (3H, *t*, *J* = 3.0 Hz, Ar-H), 7.02 (2H, *d*, *J* = 6.0 Hz, Ar-H), 7.37 (2H, *d*, *J* = 6.0 Hz, Ar-H); ^{13}C-NMR (75 MHz, $CDCl_3$, δ / ppm): 148.1, 130.9, 129.8, 127.8, 122.2, 120.1, 118.9, 111.1, 58.1, 50.0, 46.3, 40.3; MS-ESI (*m*/*z* (relative abundance, %)): 481.25 (M^+, 100), 466.23 (30.6), 437.20 (28.7), 361.14 (22.6), 263.22 (16.3), 248.13 (40.3), 180.23 (15.2), 166.05 (13.8), 115.28 (6.6); UV (DMSO, λ_{max} / nm): 351.

*5-[(9*H*-Carbazol-9-yl)methyl]*-N-*[(2-nitrophenyl)(piperazin-1-yl)methyl]--1,3,4-oxadiazol-2-amine (**4f**).* Anal. Calcd. for $C_{26}H_{25}N_7O_3$: C, 64.58; H, 5.21;

N, 20.28 %. Found: C, 64.54; H, 5.20; N, 20.27 %; IR (KBr, cm^{-1}) 3417, 3055, 2923, 2855, 1659, 1610, 1525, 1343, 1296, 1153, 740; ^{1}H-NMR (300 MHz, $CDCl_3$, δ / ppm): 2.08 (1H, *s*, NH, D_2O exchangeable), 2.37 (4H, *t*, *J* = 7.5 Hz, CH_2), 2.66 (4H, *t*, *J* = 7.5 Hz, CH_2), 4.06 (1H, *s*, NH, D_2O exchangeable), 4.84 (1H, *s*, CH), 5.03 (2H, *s*, CH_2), 7.03 (2H, *d*, *J* = 9.0 Hz, Ar-H), 7.35 (3H, *t*, *J* = = 7.5 Hz, Ar-H), 7.67 (3H, *t*, *J* = 7.5 Hz, Ar-H), 7.77 (2H, *d*, *J* = 9.0 Hz, Ar-H), 8.00 (2H, *d*, *J* = 6.0 Hz, Ar-H); ^{13}C-NMR (75 MHz, $CDCl_3$, δ / ppm): 148.9, 131.4, 130.9, 122.2, 119.0, 118.9, 111.1, 69.3, 58.1, 50.1, 46.3; MS-ESI (*m*/*z* (relative abundance, %)): 483.78 (M^+, 100), 437.21 (30.6), 361.26 (22.3), 263.01 (18.3), 248.02 (39.1), 180.14 (14.3), 166.26 (13.6), 115.13 (4.6); UV (DMSO, λ_{max} / nm): 352.

*3-[[(5-[(9*H*-Carbazol-9-yl)methyl]-1,3,4-oxadiazol-2-yl)amino](piperazin-1--yl)methyl]phenol (**4g**).* Anal. Calcd. for $C_{26}H_{26}N_6O_2$: C, 68.70; H, 5.77; N, 18.49 %. Found: C, 68.69; H, 5.76; N, 18.48 %; IR (KBr, cm^{-1}): 3671, 3416, 3051, 2925, 2860, 1689, 1603, 1330, 1157, 738; ^{1}H-NMR (300 MHz, $CDCl_3$, δ / ppm): 2.01 (1H, *s*, NH, D_2O exchangeable), 2.38 (4H, *t*, *J* = 7.5 Hz, CH_2), 2.68 (4H, *t*, *J* = 6.0 Hz, CH_2), 4.02 (1H, *s*, NH, D_2O exchangeable), 4.92 (1H, *s*, OH, D_2O exchangeable), 5.14 (1H, *s*, CH), 5.28 (2H, *s*, CH_2), 6.42 (2H, *d*, *J* = 6.0 Hz, Ar-H), 6.57 (3H, *t*, Ar-H, *J* = 7.5 Hz), 6.87 (3H, *t*, Ar-H, *J* = 10.5 Hz), 7.06 (2H, *d*, Ar-H, *J* = 6.0 Hz), 7.37 (2H, *d*, *J* = 6.0 Hz, Ar-H); ^{13}C-NMR (75 MHz, $CDCl_3$, δ / ppm): 158.2, 139.7, 130.9, 122.2, 120.1, 118.9, 111.1, 78.2, 58.1, 46.3; MS-ESI (*m*/*z* (relative abundance, %)): 454.63 (M^+, 100), 437.31 (31.2), 361.19 (20.4), 263.24 (14.2), 248.09 (35.8), 180.27 (19.2), 166.02 (12.6), 115.15 (7.1); UV (DMSO, λ_{max} / nm): 346.

*5-[(9*H*-Carbazol-9-yl)methyl]-*N*-[(3-nitrophenyl)(piperazin-1-yl)methyl]--1,3,4-oxadiazol-2-amine (**4h**).* Anal. Calcd. for $C_{26}H_{25}N_7O_3$: C, 64.58; H, 5.21; N, 20.28 %. Found: C, 64.55; H, 5.17; N, 20.24 %; IR (KBr, cm^{-1}) 3415, 3053, 2925, 2858, 1672, 1602, 1518, 1348, 1302, 1157, 676; ^{1}H-NMR (300 MHz, $CDCl_3$, δ / ppm): 1.97 (1H, *s*, NH, D_2O exchangeable), 2.35 (4H, *t*, *J* = 10.5 Hz, CH_2), 2.66 (4H, *t*, *J* = 7.5 Hz, CH_2), 4.08 (1H, *s*, NH, D_2O exchangeable), 4.94 (1H, *s*, CH), 5.19 (2H, *s*, CH_2), 7.13 (2H, *d*, *J* = 6.0 Hz, Ar-H), 7.36 (3H, *t*, *J* = = 10.5 Hz, Ar-H), 7.56 (3H, *t*, *J* = 7.5 Hz, Ar-H), 7.66 (2H, *d*, *J* = 6.0 Hz, Ar-H), 8.09 (2H, *d*, *J* = 6.0 Hz, Ar-H); ^{13}C-NMR (75 MHz, $CDCl_3$, δ / ppm): 148.1, 139.3, 130.9, 124.1, 122.2, 120.1, 119.0, 111.1, 76.3, 58.1, 50.0, 46.3; MS-ESI (*m*/*z* (relative abundance, %)): 483.59 (M^+,100), 437.18 (27.4), 361.07 (21.6), 263.06 (18.3), 248.09 (38.3), 180.12 (13.4), 166.05 (12.2), 115.68 (6.8); UV (DMSO, λ_{max} / nm): 350.

*2-[[(5-[(9*H*-Carbazol-9-yl)methyl]-1,3,4-oxadiazol-2-yl)amino](piperazin--yl)methyl]phenol (**4i**).* Anal. Calcd. for $C_{26}H_{26}N_6O_2$: C, 68.70; H, 5.77; N, 18.49 %. Found: C, 68.68; H, 5.74; N, 18.47 %, IR (KBr, cm^{-1}): 3691, 3415, 3053, 2924, 2853, 1668, 1606, 1333, 1149, 740; ^{1}H-NMR (300 MHz, $CDCl_3$, δ /

/ ppm): 2.01 (1H, *s*, NH, D_2O exchangeable), 2.46 (4H, *t*, *J* = 7.5 Hz, CH_2), 2.67 (4H, *t*, *J* = 6.0 Hz, CH_2), 4.02 (1H, *s*, NH, D_2O exchangeable), 4.99 (1H, *s*, OH, D_2O exchangeable), 5.10 (1H, *s*, CH), 5.29 (2H, *s*, CH_2), 6.64 (2H, *d*, *J* = 9.0 Hz, Ar-H), 6.86 (3H, *t*, *J* = 6.0 Hz, Ar-H), 7.05 (3H, *t*, *J* = 12.0 Hz, Ar-H), 7.19 (2H, *d*, *J* = 9.0 Hz, Ar-H), 7.50 (2H, *d*, *J* = 9.0 Hz, Ar-H); ^{13}C-NMR (75 MHz, $CDCl_3$, δ / ppm): 136.8, 130.9, 119.0, 111.1, 79.3, 50.0, 46.3; MS-ESI (*m*/*z* (relative abundance, %)): 454.02 (M^+, 100), 437.31 (25.3), 361.23 (21.5), 263.12 (16.1), 248.06 (41.3), 180.31 (13.2), 166.08 (11.4), 115.06 (3.5); UV (DMSO, λ_{max} / nm): 340.

*5-[(9*H*-Carbazol-9-yl)methyl]*-N-*[(3-chlorophenyl)(piperazin-1-yl)methyl]-1,3,4-oxadiazol-2-amine (**4j**).* Anal. Calcd. for $C_{26}H_{25}ClN_6O$: C, 66.03; H, 5.33; N, 17.77 %. Found: C, 65.99; H, 5.31; N, 17.75 %; IR (KBr, cm^{-1}): 3415, 3050, 2912, 2827, 1649, 1581, 1307, 1151, 1080, 661; ^{1}H-NMR (300 MHz, $CDCl_3$, δ / / ppm): 2.10 (1H, *s*, NH, D_2O exchangeable), 2.35 (4H, *t*, *J* = 7.5 Hz, CH_2), 2.58 (4H, *t*, *J* = 6.0 Hz, CH_2), 4.07 (1H, *s*, NH, D_2O exchangeable), 4.95 (1H, *s*, CH), 5.01 (2H, *s*, CH_2), 6.97 (2H, *d*, *J* = 9.0 Hz, Ar-H), 7.07 (3H, *t*, *J* = 6.0 Hz, Ar-H), 7.16 (3H, *t*, *J* = 7.5 Hz, Ar-H), 7.25 (2H, *d*, *J* = 6.0 Hz, Ar-H), 7.40 (2H, *d*, *J* = = 6.0 Hz, Ar-H); ^{13}C-NMR (75 MHz, $CDCl_3$, δ / ppm): 139.4, 134.0, 130.9, 118.9, 111.1, 77.4, 58.3, 50.0, 46.3; MS-ESI (*m*/*z* (relative abundance, %)): 472.91 (M^+,100), 437.16 (26.9), 361.29 (23.0), 263.13 (16.5), 248.23 (38.6), 180.38 (14.9), 166.20 (13.1), 115.13 (7.2); UV (DMSO, λ_{max} / nm): 333.

*5-[(9*H*-Carbazol-9-yl)methyl]*-N-*[(2-chlorophenyl)(piperazin-1-yl)methyl]-1,3,4-oxadiazol-2-amine (**4k**).* Anal. Calcd. for $C_{26}H_{25}ClN_6O$: C, 66.03; H, 5.33; N, 17.77 %. Found: C, 66.02; H, 5.30; N, 17.76 %; IR (KBr, cm^{-1}): 3428, 3056, 2941, 2847, 1652, 1580, 1348, 1148, 1056, 756; ^{1}H-NMR (300 MHz, $CDCl_3$, δ / ppm): 1.99 (1H, *s*, NH, D_2O exchangeable), 2.38 (4H, *t*, *J* = 7.5 Hz, CH_2), 2.60 (4H, *t*, *J* = 4.5 Hz, CH_2), 4.06 (1H, *s*, NH, D_2O exchangeable), 5.01 (1H, *s*, CH), 5.20 (2H, *s*, CH_2), 7.01 (2H, *d*, *J* = 6.0 Hz, Ar-H), 7.12 (3H, *t*, *J* = = 4.5 Hz, Ar-H), 7.25 (3H, *t*, *J* = 7.5 Hz, Ar-H), 7.33 (2H, *d*, *J* = 6.0 Hz, Ar-H), 7.44 (2H, *d*, *J* = 9.0 Hz, Ar-H); ^{13}C-NMR (75 MHz, $CDCl_3$, δ / ppm): 138.4, 133.0, 129.9, 118.9, 111.1, 77.4, 58.3, 50.0, 46.3; MS-ESI (*m*/*z* (relative abundance, %)): 472.59 (M^+ ,100), 437.14 (30.6), 361.34 (22.5), 263.20 (16.9), 248.11 (41.1), 180.46 (18.6), 166.12 (14.1), 115.06 (5.7); UV (DMSO, λ_{max} / / nm): 330.

*5-[(9*H*-Carbazol-9-yl)methyl]*-N-*[(3-methoxyphenyl)(piperazin-1-yl)methyl]-1,3,4-oxadiazol-2-amine (**4l**).* Anal. Calcd. for $C_{27}H_{28}N_6O_2$: C, 69.21; H, 6.02; N, 17.94 %. Found: C, 69.20; H, 6.00; N, 17.91 %; IR (KBr, cm^{-1}): 3415, 3060, 2931, 2844, 1639, 1579, 1320, 1242, 1124, 1037, 667; ^{1}H-NMR (300 MHz, $CDCl_3$, δ / ppm): 2.06 (1H, *s*, NH, D_2O exchangeable), 2.46 (4H, *t*, *J* = 6.0 Hz, CH_2), 2.70 (4H, *t*, *J* = 6.0 Hz, CH_2), 3.73 (3H, *s*, OCH_3), 4.06 (1H, *s*, NH, D_2O exchangeable), 4.95 (1H, *s*, CH), 5.15 (2H, *s*, CH_2), 6.61 (3H, *t*, *J* = 6.0 Hz,

Ar-H), 6.81 (2H, *d*, *J* = 3.0 Hz, Ar-H), 6.99 (2H, *d*, *J* = 6.0 Hz, Ar-H), 7.08 (2H, *d*, *J* = 6.0 Hz, Ar-H), 7.32 (3H, *t*, *J* = 13.5 Hz, Ar-H). ^{13}C-NMR (75 MHz, $CDCl_3$, δ / ppm): 160.4, 130.5 129.9, 118.9, 111.1, 77.4, 58.3, 55.9, 50.0, 46.3; MS-ESI (*m*/*z* (relative abundance, %)): 468.23 (M^+ ,100), 453.20 (31.3), 437.48 (26.1), 361.10 (22.9), 263.25 (15.4), 248.29 (37.7), 180.14 (15.1), 166.19 (12.1), 115.11 (5.2); UV (DMSO, λ_{max} / nm): 328.

*5-[(9*H*-Carbazol-9-yl)methyl]*-N-*[(4-methoxyphenyl)(piperazin-1-yl)methyl]--1,3,4-oxadiazol-2-amine (**4m**).* Anal. Calcd. for $C_{27}H_{28}N_6O_2$: C, 69.21; H, 6.02; N, 17.94 %. Found: C, 69.18; H, 6.01; N, 17.93 %; IR (KBr, cm^{-1}): 3416, 3053, 2935, 2839, 1645, 1595, 1323, 1251, 1161, 1016, 854; ^{1}H-NMR (300 MHz, $CDCl_3$, δ / ppm): 1.95 (1H, *s*, NH, D_2O exchangeable), 2.45 (4H, *t*, *J* = 12.0 Hz, CH_2), 2.64 (4H, *t*, *J* = 6.0 Hz, CH_2), 3.73 (3H, *s*, OCH_3), 4.08 (1H, *s*, NH, D_2O exchangeable), 4.89 (1H, *s*, CH), 5.20 (2H, *s*, CH_2), 6.67 (3H, *t*, *J* = 6.0 Hz, Ar-H), 6.89 (2H, *d*, *J* = 6.0 Hz, Ar-H), 7.05 (2H, *d*, *J* = 6.0 Hz, Ar-H), 7.14 (2H, *d*, *J* = 9.0 Hz, Ar-H), 7.34 (3H, *t*, *J* = 10.5 Hz, Ar-H); ^{13}C-NMR (75 MHz, $CDCl_3$, δ / ppm): 158.4, 131.9 129.9, 118.9, 111.1, 77.4, 58.3, 55.9, 50.0, 46.3; MS-ESI (*m*/*z* (relative abundance, %)): 468.73 (M^+ ,100), 453.20 (31.3), 437.48 (26.1), 361.10 (22.9), 263.25 (15.4), 248.29 (37.7), 180.14 (15.1), 166.19 (12.1), 115.11 (5.2); UV (DMSO, λ_{max} / nm): 330 nm.

*5-[(9*H*-Carbazol-9-yl)methyl]*-N-*[(4-fluorophenyl)(piperazin-1-yl)methyl]--1,3,4-oxadiazol-2-amine (**4n**).* Anal. Calcd. for $C_{26}H_{25}FN_6O$: C, 68.40; H, 5.52; N, 18.41 %. Found: C, 68.39; H, 5.49; N, 18.38 %; IR (KBr, cm^{-1}): 3417, 3051, 2933, 2843, 1653, 1575, 1334, 1257, 1151, 860; ^{1}H-NMR (300 MHz, $CDCl_3$, δ / / ppm): 2.05 (1H, *s*, NH, D_2O exchangeable), 2.38 (4H, *t*, *J* = 7.5 Hz, CH_2), 2.63 (4H, *t*, *J* = 6.0 Hz, CH_2), 4.15 (1H, *s*, NH, D_2O exchangeable), 4.89 (1H, *s*, CH), 5.10 (2H, *s*, CH_2), 6.84 (2H, *d*, *J* = 9.0 Hz, Ar-H), 6.93 (3H, *t*, *J* = 7.5 Hz, Ar-H), 7.08 (3H, *t*, *J* = 6.0 Hz, Ar-H), 7.13 (2H, *d*, *J* = 6.0 Hz, Ar-H), 7.34 (2H, *d*, *J* = = 9.0 Hz, Ar-H); ^{13}C-NMR (75 MHz, $CDCl_3$, δ / ppm): 161.4, 130.9 120.9, 118.9, 111.1, 77.4, 58.3, 55.9, 50.0, 46.3; MS-ESI (*m*/*z* (relative abundance, %)): 456.21 (M^+ ,100), 437.04 (27.3), 361.06 (22.1), 263.19 (15.4), 248.16 (39.3), 180.02 (16.3), 166.09 (12.8), 115.18 (7.6); UV (DMSO, λ_{max} / nm): 342.

*5-[(9*H*-Carbazol-9-yl)methyl]*-N-*(phenyl(piperazin-1-yl)methyl)-1,3,4-oxadiazol-2-amine (**4o**).* Anal. Calcd. for $C_{26}H_{26}N_6O$: C, 71.21; H, 5.98; N, 19.16 %. Found: C, 71.19; H, 5.95; N, 19.15 %; IR (KBr, cm^{-1}): 3410, 3045, 2931, 2832, 1678, 1604, 1325, 1157; ^{1}H-NMR (300 MHz, $CDCl_3$, δ / ppm): 2.08 (1H, *s*, NH, D_2O exchangeable), 2.42 (4H, *t*, *J* = 6.0 Hz, CH_2), 2.63 (4H, *t*, *J* = 7.5 Hz, CH_2), 4.08 (1H, *s*, NH, D_2O exchangeable), 5.01 (1H, *s*, CH), 5.21 (2H, *s*, CH_2), 7.02 (2H, *d*, *J* = 6.0 Hz, Ar-H), 7.17 (3H, *t*, *J* = 6.0 Hz, Ar-H), 7.24 (3H, *t*, *J* = 6.0 Hz, Ar-H), 7.32 (2H, *d*, *J* = 6.0 Hz, Ar-H), 7.41 (2H, *d*, *J* = 6.0 Hz, Ar-H); ^{13}C--NMR (75 MHz, $CDCl_3$, δ / ppm): 138.6, 130.9 128.9, 120.5, 118.9, 111.1, 77.4, 58.3, 55.9, 50.0, 46.3; MS-ESI (*m*/*z* (relative abundance, %)): 438.22 (M^+, 100),

361.40 (22.4), 263.01 (16.5), 248.10 (38.0), 180.05 (17.4), 166.06 (13.2), 115.71 (5.5); UV (DMSO, λ_{max} / nm): 320.

Journal of the Serbian Chemical Society
JSCS-info@shd.org.rs • www.shd.org.rs/JSCS
J. Serb. Chem. Soc. 79 (2) 133–150 (2014)
JSCS–4571
UDC 612.398+544.022:659.24:57
Original scientific paper

A bioinformatics study concerning the structural and functional properties of human caveolin proteins

ADRIANA ISVORAN[1,2]*, DANA CRACIUN[3], ALECU CIORSAC[4], NAHUEL PERROT[5], VERONICA BESWICK[5,6], PIERRE NEDELLEC[5], ALAIN SANSON[5] and NADEGE JAMIN[5]

[1]Department of Biology–Chemistry, West University of Timisoara, 16 Pestalozzi, 300316 Timisoara, Romania, [2]Laboratory of Advanced Researches in Environmental Protection, West University of Timisoara, 4 Oituz, 300086 Timisoara, Romania, [3]Teacher training Department, West University of Timisoara, 4 V. Pirvan, 300223 Timisoara, Romania, [4]Department of Physical Education and Sport, Politehnica University of Timisoara, 2 P-ta Victoriei, 300306 Timisoara, Romania, [5]Commissariat à l'Energie Atomique (CEA), Institute of Biology and Technologies of Saclay (iBiTecS) 91191 Gif-sur-Yvette Cedex, France and [6]Department of Physics, Université d'Evry-val-d'Essonne, 91025 Evry Cedex, France

(Received 16 July, revised 21 September 2013)

Abstract: A bioinformatics study was performed to predict and compare the structural and functional properties of human caveolins: caveolin-1, -2 and -3. The computed local physicochemical properties, predictions of their secondary structure elements and interacting partners of caveolin-2 and -3 were compared to the experimentally determined structural and functional properties of caveolin-1. These data combined with sequence alignments of the three caveolins allowed the functional domains of caveolin-2 and -3 to be predicted and characterised. The hydrophobic regions of these proteins are highly similar in sequences and physicochemical properties, which is in good agreement with their known membrane locations and functions. The most divergent in terms of sequences and properties are the C-terminal regions of the caveolins, suggesting that they might be responsible for their distinct predicted interactions, with direct consequences on signalling processes.

Keywords: secondary structure; disordered regions; functional domains.

INTRODUCTION

Caveolins belong to a family of small (around 20 kDa) integral membrane proteins with both N- and C-termini facing the cytoplasm.[1] This family comprises three members in vertebrates: caveolin-1 (cav1), caveolin-2 (cav2) and caveolin-3 (cav3). Cav1 and cav2 are ubiquitously co-expressed, while cav3 is muscle specific. Caveolins play essential structural roles in the organisation of

* Corresponding author. E-mail: adriana.isvoran@cbg.uvt.ro
doi: 10.2298/JSC130716100I

the caveolae and also participate in many important cellular processes, such as vesicular transport, signal transduction, cholesterol homeostasis and tumour suppression.[2]

Cav1 is the most studied member of the caveolin family. It is oligomeric and is a cholesterol and fatty acid binding protein. There are two isoforms of cav1: the α- and the β-isoform. The β-isoform lacks the first 32 amino acid residues of the α-isoform.[3,4] Two types of post-translational modifications have been shown to affect cav1, *i.e.*, palmitoylation and phosphorylation, both of which are important for its functions.[5,6] Three palmitoylation sites at cysteine 133, 143 and 156 and two phosphorylation sites at tyrosine 14 and serine 80 have been identified.

Caveolin-1 is expressed in most types of cells, whereby adipocytes, endothelial cells, fibroblasts and type I pneumocytes have the highest levels of its expression.[7] It is found only in vertebrates and has been the subject of numerous research studies, the data of which provide the basis of the present knowledge regarding the interactions of these proteins with their cellular environment. A structural bioinformatics analysis of cav1 revealed its highly conserved sequence among vertebrate organisms (more than 64 % for vertebrates and 99 % for mammals), its high similarity with cav2 and cav3 and enabled to its structural organization and functional regions to be predicted.[8] The functional regions of Cav1 are the hydrophobic domain (HD), composed of residues 102 to 134, and two adjacent regions flanking the HD: the N-terminal attachment domain (N-MAD, residues 82–101) and the C-terminal attachment domain (C-MAD, residues 135–150), which were found to bind to membrane with high affinity.[7,9] The C-terminal domain of cav1 contains three cysteine residues that are modified by palmitoylation and are supposed to be involved in caveolin–caveolin and caveolin–lipids interactions.[7] The N-MAD domain, also known as the scaffolding domain (CSD) of cav1, has been shown to act both as an anchor for different proteins within caveolae and as a regulatory element able to activate or inhibit the signalling activity of a given protein.[10,11] Moreover, the interactions of cav1 with other proteins may also be mediated by other regions.[12] The CSD includes a short amino acid sequence, residues 94–101, known as the CRAC (cholesterol recognition/interaction amino acid consensus) motif,[13] which is involved in the membrane interaction of cav1.[14] It was proposed that the CSD has two functional regions: the CRAC region responsible for interactions with cholesterol and its first segment (residues 82–93) being involved in a signal transduction process.[8]

Earlier studies considered that proteins interacting with caveolin have a specific "caveolin binding domain" (CBD), ψXψXXXψ or ψXXXXψXXψ, where ψ is an aromatic residue (Trp, Tyr or Phe)[15] that interacts with the CSD *via* their aromatic residues.[9,16] However, recent studies argue against the role of this motif in caveolin interactions and involvement in signalisation processes.[8,10,12,17] Tyrosine and serine phosphorylation of cav1, as well as cysteine

palmitoylation also seem to be involved in caveolin–protein interactions. Tyrosine phosphorylation of cav1 occurs at its N-terminal domain (Tyr14) and phosphorylated cav1 serves as a scaffolding protein to recruit SH2-domain containing proteins.[18] Serine phosphorylation occurs at Ser80 and is responsible for the topology change of cav1 from a membrane protein to a secreted protein.[7] Cav1 palmitoylation has been proposed to play a role in the interaction of cav1 with lipids,[16] in cholesterol binding and transport and for the assembly of signalling molecules in caveolae.[5,6]

Caveolin-2 exists as a homo-dimer[19] and acts as a scaffolding protein within caveolar membranes directly interacting with cav1 to form a stable hetero-oligomeric complex that is required for targeting to lipid rafts and for caveolae formation.[20] It has three isoforms: α, β and γ. The α- and β-isoforms differ in their subcellular locations and the β-isoform does not interact with cav1.[21] Cav2 is phosphorylated at tyrosine residues 19 and 27.[22] Phosphocaveolin-2 (Tyr(P)19) is localized near focal adhesions, remains associated with lipid rafts/caveolae, but no longer forms a high molecular mass hetero-oligomer with caveolin-1.[23–25] Information about the γ-isoform of cav2 is lacking.

Caveolin 3 (also known as M-caveolin) is the muscle-specific member of caveolin family being the only member of the family that is present in striated muscle. It shares 65 % sequence identity and 85 % sequence similarity with cav1,[2] it also forms a large homo-oligomeric complex of 350–400 kDa molecular weight[26] and appears to have similar cellular functions, such as caveolae formation and cellular signalling. It is a modulator of the function of the dystrophin––glycoproteins complex with consequences for muscle diseases.[27]

Caveolins cellular functions ascribed to caveolae are endocytocis, transcytosis and signal transduction. Caveolins also play a role in some diseases:[26,28] cancer (they are implicated in both tumour suppression and oncogenesis), cardiovascular diseases, lung diseases and muscular dystrophy.

The structural and functional characteristics of caveolin proteins have not yet been well defined, but some useful information can be obtained through sequence based predictions using structural bioinformatics tools. In the present study, a bioinformatics investigation was performed in which, to the best of our knowledge, all the three human caveolins were considered for the first time in order to predict and compare their structural and functional properties. The sequence identity, hydrophobicity, alpha-helix and beta-turn profiles were analysed and the secondary structure elements, the disordered regions and the interacting partners were predicted. Comparing the obtained results with known structural and functional data concerning caveolin 1, the functional domains of caveolin 2 and caveolin 3 were predicted and characterized.

EXPERIMENTAL

Within this study, bioinformatics tools were employed to analyse and predict structural and physicochemical properties of the family of human caveolin proteins starting from sequence information retrieved from SwissProt data base.[29] Sequence analysis relating to the sequence identity of the vertebrate caveolins was performed using the BLAST tool.[30] The sequence similarity between the human caveolins was studied using multiple sequence analysis performed with the CLUSTALW2 on-line tool.[31]

The ProtParam tool[32] was used to compute the global physicochemical properties of the caveolins and of their predicted functional regions, *i.e.*, the molecular weight, GRAVY index, net charge and aliphatic index. GRAVY is the grand average of hydropathicity and indicates the solubility of the protein. It is computed using the Kyte and Doolittle hydrophobicity scale.[33] A positive value of GRAVY reveals a hydrophobic protein and a negative value, a hydrophilic one.

The aliphatic index is a measure of the relative volume occupied by the amino acids with aliphatic side chains. This parameter is usually computed for globular proteins but it has also been used for proteins containing membrane regions.[34,35]

The ProtScale tool[32] was also used to obtain the hydrophobicity, membrane tendency and the alpha helix and beta-turn profiles for caveolins. The hydrophobicity shows the degree of hydrophobicity of each amino acid in the protein chain *versus* its position in the chain. For the hydrophobicity profiles, the Kyte and Doolittle hydrophobicity scale[32] was used. Prediction of the secondary structural elements of caveolins was performed using GOR,[36] Jpred3,[37] PsiPred,[38] CFSSP[39] and ProtPred[40] on-line tools and their results were compared. Moreover, prediction of disordered regions of caveolins was obtained using ProtPred[40], RONN[41] and GlobPlot[42] tools.

Caveolins are predicted to have an unusual membrane topology. They do not cross the membrane, but they are anchored to one of its layers. A few computational tools for predicting the re-entrant loops of membrane proteins can be found: OCTOPUS[43] and SPOCTOPUS[44] and they were employed to predict the re-entrant loops of the caveolins.

In order to obtain the membrane tendency (MT), the transmembrane tendency indexes introduced by Zhao and London in 2006[45] were used, and for the alpha-helix and beta-turn profiles, the alpha-helix and beta-turn propensities indexes introduced by Deleage and Roux in 1987[46] were employed. The MT sequence prediction scale shows the propensity of each amino acid in the protein chain to participate in transmembrane helices[45] and the alpha--helix/beta-turn propensity is a measure of the tendency of an amino acid to adopt an alpha helix/beta-turn structure.[46] All these profiles take into account the physicochemical background for every amino acid in the sequence, the average values of each considered property being computed using a window of 21 amino acids with the considered amino acid at its centre. The large window of 21 amino acids used for computation of profiles has been proven to be good for membrane proteins[32] and the profiles that were computed in the present study with windows of 9 and 13 residues did not significantly differ from the profiles computed with a window of 21 residues (see Figs. S-1 and S-2 of the Supplementary material to this paper). In the profiles computed with a window of 21 residues, predictions for the first 10 and the last 10 amino acids of the sequence are lacking.

A short region of 8 amino acids was identified as identical in all three proteins, FEDVIAEP, and it is named as the "caveolin signature sequence" (CSS).[2] Therefore, for cav2 and cav3, the profiles were translated in comparison to the cav1 profile such that the caveolin

signature amino acid sequence corresponds for all caveolins: 14 positions for cav2 and 28 positions for cav3.

STRING software[47] was used to predict the interacting partners of the family of caveolin proteins. STRING is based on both experimental and predicted interaction information and it reports a network containing the highest scoring interacting partners and specifies if the interaction has been proved experimentally. As parameters setting for using STRING, a medium confidence score (*i.e.*, higher than 0.400) was chosen and the following active prediction methods: experiments, databases and text mining.

Cav1 and cav2 have two and three identified isoforms, respectively. If not specified further in the text, the cav1 and cav2 notation will refer to the alpha isoforms.

RESULTS AND DISCUSSION

No three dimensional structure of caveolin proteins have been yet determined. Homology modelling using the Geno3D tool[48] revealed that no satisfactory template could be found for their sequences (see Fig. S-3 of the Supplementary material to this paper).

The BLAST tool[30] revealed that caveolin amino acid sequences have been highly conserved throughout evolution, the sequence identity for vertebrates being higher than 47 %. The members of the human caveolin family share high sequence similarity: cav1 and cav2 are 58 % similar, cav1 and cav3 are 85 % similar and cav2 and cav3 are 39.0 % similar. The sequence alignment was performed using CLUSTALW2 software[31] and the results are shown in Fig. 1, the highly conserved regions being highlighted.

```
sp|Q03135|CAV1_HUMAN      -MSGGKYVDSEGHLYTVPIREQGNIYKPNNKAMADELSEKQVYDAHTKEIDLVNRDPKHL 59
sp|P56539|CAV3_HUMAN      -MMAEEHTD----------------------------LEAQIVKDIHCKEIDLVNRDPKNI 32
sp|P51636|CAV2_HUMAN      MGLETEKADVQLFMD---------------DDSYSHHSGLEYADPEKFADSDQDRDPHRL 45
                               : .*                          .    * .    .  :***:.:

                                     --CSS---                ----CRAC---------HD-------
sp|Q03135|CAV1_HUMAN      NDDVVKIDFEDVIAEPEGTHSFDGIWKASFTTFTVTKYWFYRLLSALFGIPMALIWGIYF 119
sp|P56539|CAV3_HUMAN      NEDIVKVDFEDVIAEPVGTYSFDGVWKVSYTTFTVSKYWCYRLLSTLLGVPLALLWGFLF  92
sp|P51636|CAV2_HUMAN      NS-HLKLGFEDVIAEPVTTHSFDKVWICSHALFEISKYVMYKFLTVFLAIPLAFIAGILF 104
                          *.  :*:.******** *:*** :*  *.: * ::**  *:.*:.::.:*:*:: *: *

                           ---HD----------
sp|Q03135|CAV1_HUMAN      AILSFLHIWAVVPICKSFLIEIQCISRVYSIYVHTVCDPLFEAVGKIFSNVRINLQKEI 178
sp|P56539|CAV3_HUMAN      ACISFCHIWAVVPCIKSYLIEIQCISHIYSLCIRTFCNPLFAALGQVCSSIKVVLRKEV 151
sp|P51636|CAV2_HUMAN      ATLSCLHIWILMPFVKTCLMVLPSVQTIWKSVTDVIIAPLCTSVGRCFSSVSLQLSQD- 162
                           * :*  *** ::* :*: *: : .:. ::.    ..  **  ::*:  *.: : * ::
```

Fig. 1. Sequence alignment of the alpha isoforms of cav1, cav2 and cav3; * (asterisk) indicates positions that have a single, fully conserved residue; colon indicates conservation between groups of very similar properties; period indicates conservation between groups of weakly similar properties. The single-letter amino acid code is used. The caveolin signature sequence (CSS) and the hydrophobic domain (HD) are highlighted in dark grey. The cholesterol recognition/interaction amino acid consensus (CRAC) sequences of caveolins are highlighted in light grey.

Being membrane proteins, it is expected that caveolins possess highly hydrophobic amino acid domains. The hydrophobicity profiles of the caveolin proteins obtained using the ProtScale tool[32] and the Kyte & Doolittle hydrophobicity scale[33] are shown in Fig. 2, in which the hydrophobic residues have positive indexes.

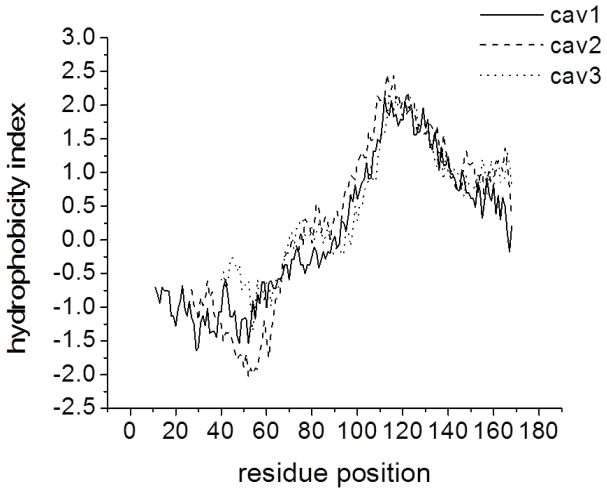

Fig. 2. Hydrophobicity profiles of cav1, cav2 and cav3 obtained using the ProtScale tool. For cav2 and cav3 proteins, the residue position was translated so as the caveolin signature sequence correspond for all caveolins.

The hydrophobicity profiles divide the amino acid sequences of caveolins in two different regions: a hydrophilic region (residues 1–93 for cav1, 1–60 for cav2 and 1–50 for cav3) and a hydrophobic region (residues 94–178 for cav1, 61–162 for cav2 and 51–151 for cav3). Figure 2 also reflects that the known hydrophobic domain of cav1 (residues 102–134) and a part of its adjacent regions are highly hydrophobic. Using this profile, it is suggested that the hydrophobic domains of cav2 and cav3 proteins are composed of the amino acid sequences 87–119 and 75–107, respectively, and this suggestion is in good agreement with the sequence alignment presented in Fig. 1.

The membrane tendency profiles were also analysed (see Fig. S-4 of the Supplementary material to this paper). The profiles are very similar for the three caveolins and, as expected, they are also similar to the hydrophobicity profiles. Moreover, both tools, OCTOPUS[43] and SPOCTOPUS,[44] did not predict any re--entrant loops for the caveolins.

The alpha-helix and beta-turn profiles obtained using the ProtScale tool are presented in Fig. 3.

Alpha-helix profiles show the high probability for the following amino acid sequences to form helical regions: 29–60 and 94–140 for cav1, 84–125 for cav2

and 77–141 for cav3. Except for cav1, these profiles are in reasonable agreement with the predicted membrane helices. The beta-turn profiles depict the probable regions adopting beta-structures, *i.e.*, amino acid sequences 1–38 for cav1, 20–50 for cav2 and 25–41 for cav3.

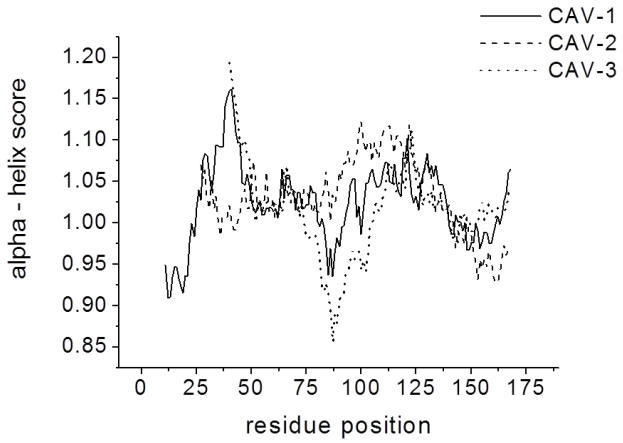

(a)

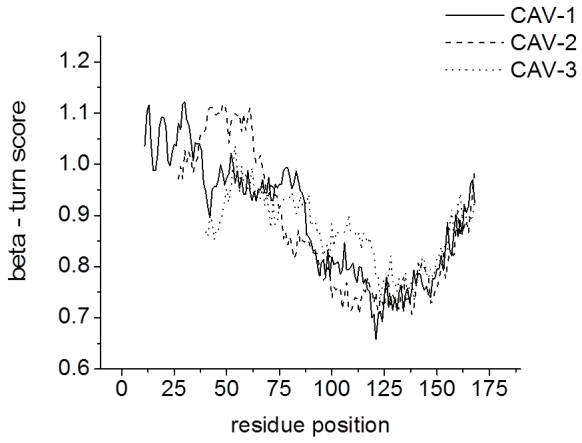

(b)

Fig. 3. Alpha-helix (a) and beta-turn (b) profile for caveolin proteins obtained using the ProtScale tool. For cav2 and cav3, the residue position was translated so that the caveolin signature sequence corresponds for all caveolins.

The alpha helix and beta-turn profiles obtained using the ProtScale tool were not fully confirmed by the prediction of the secondary structure elements using the GOR, Jpred, PsiPred, CFSSP and ProtPred tools (Fig. 4), by the predictions using RONN, GlobPlot, ProtPred of their disordered regions (Fig. 5) nor by other published data concerning their structural properties.

```
         1         10         20         30         40         50         60
cav1     MSGGKYVDSE GHLYTVPIRE QGNIYKPNNK AMADELSEKQ VYDAHTKEID LVNRDPKHLN
GOR      ccccceeccc cceeeeeccc ccccccccch hhhhhhhhhh hhhhchhhhh hccccccccc
Jpred    ---------- -eeeee---- ---------- ---------- ---------- ----------
PsiPred  cccccccccc cceecccccc cccccccccc cchhhhcccc cccccccccc cccccccccc
CFSSP    ccttcccctt cceeeeeect ctcccctcth hhhhhhhhhh hhhhhhhhhh hcctctcchh
ProtPred ---------- ---------- ---------- ---------- ---------- ----------

         61         70         80         90         100        110    120
cav1     DDVVKIDFED VIAEPEGTHS FDGIWKASFT TFTVTKYWFY RLLSALFGIP MALIWGIYFA
GOR      cceeeeeccc eecccccccc ccceeeeece eeeeccchhh hhhhhhhccc chhhhhhhhh
Jpred    ---eee---- eee------- ---hehhhh eeeeehhhhh hhhhhhhhhh hhhhhhhhhh
PsiPred  cccccccccc eecccccccc ccceeeeeee eeeeeeeehh hhhhhhhhhh hhhhhhhhhh
CFSSP    hhheeehhhh hhhttcccch hhhhheeeee eeeeeeeeee hhhhhhhhhh hhhhhhhhhh
ProtPred ---eeeeeee ee-------- ---eeeee-e eeeeehhhhh hhhhhhhhhh hhhhhhhhhh

         121        130        140        150        160        170    178
cav1     ILSFLHIWAV VPCIKSFLIE IQCISRVYSI YVHTVCDPLF EAVGKIFSNV RINLQKEI
GOR      hhceeceeee ecccccceec ccccceeeee eeeeccccce cccchhhhhh hhhhceec
Jpred    hhhhhhhhhh hhhhhheeee -hhhhhhhhh hhhhhhhhhh hhhhhh-ee eee-----
PsiPred  hhhhceeeee chhhhhhhhh hhhhhhhhhh hhhhhhhhhh hhhhhcccee eeeecccc
CFSSP    hhhhhheeee eeehhhhhhe eeeeeeeeee eeeeehhhh hhhhheeeee eehhhhhc
ProtPred hhhhhheeee ehhheeeehh hhhhhhhhhh hhhhh--hhh hhhhhhh ee eeeeee--
```

(a)

```
         1          10         20         30         40         50         60
cav2     MGLETEKADV QLFMDDDSYS HHSGLEYADP EKFADSDQDR DPHRLNSHLK LGFEDVIAEP
GOR      ccccccchhh hhhccccccc cccccccccc cccccccccc cchhhhhhhh cccccceccc
Jpred    ---------e eeee------ ---------- ---------- ---------e e--eeeee--
PsiPred  cccccccccc eeeeccccccc cccccccccc cccccccccc cccccccccc eeeeeeeccc
CFSSP    hhhhhhhhhe hhhhhttccc cctccchhhh hhhhtthhcc tcccchhhh hhhhhhhhee
ProtPred ---------e eeee------ ---------- ----------  hhhhhhhee eeeeeee---

         61         70         80         90         100        110    120
cav2     VTTHSFDKVW ICSHALFEIS KYVMYKFLTV FLAIPLAFIA GILFATLSCL HIWILMPFVK
GOR      ceeeeeceee ecccceeecc hhhhhhhhhh hhhchhhhhh hhhhhccccc ceeeeeceec
Jpred    -------heh hhh-eeeeh hhhhhhhhhh hhhhhhhhhh hhhhhhhhhh hhhhhhhhhh
PsiPred  ccccccccce eecceeeeee eeeeeehhhh hhhhhhhhhh hhhhhhhhhc eeeeehhhhh
CFSSP    eeeeeeeeee hhhhhheeee hhhhhhhhhh hhhhhhhhhh hhhhhhhhhh hhhhhhhhhh
ProtPred ---------e ehhheeeeee hhhhhhhhhh hhhhhhhhhh hhhhhhhhh- eeeeee-hhh

         121        130        140        150        160
cav2     TCLMVLPSVQ TIWKSVTDVI IAPLCTSVGR CFSSVSLQLS QD
GOR      cceeeeeccc cccccccccee eecccccccc ccccceecee ec
Jpred    eeee-hhhhh hhhhhhhhhh hhhhhhhhhh hh-eeeeee --
PsiPred  hhcccchhhh hhhhhhhhhh hhhhhhhhhh hcccceeeee cc
CFSSP    hhhhhhhhhh hhhhhhhhhh hhhhhhhhhh heeeeeeeee ec
ProtPred hhhhhhhhhh hhhhhhhhhh -hhhhhhhhh hh--eee--- --
```

(b)

Fig. 4. Prediction of the secondary structure elements of human: a) cav1, b) cav2 and c) cav3 using the GOR, Jpred, PsiPred, CFSSP and ProtPred tools (h – helix, e – beta strand, c – coil, t – turn).

```
          1         10         20         30         40         50        60
cav3      MMAEEHTDLE AQIVKDIHCK EIDLVNRDPK NINEDIVKVD FEDVIAEPVG TYSFDGVWKV
gor       ccccccchh hhhhhhhccc eeccccccce ccccceeeec ccceeccccc eeeeceeeee
jpred     ---------- ---------- ---------- -------ee- e--eee---- -----hehhh
psipred   ccccccccch hhhhccccce ccccccccce ccccceeeee cceeeccccc ccccceeeee
CFSSP     hhhhhhhhhh hhhhhhhhhh hhhhctcctc ceeeeeeeee eeeeceeeee eeehhhhhhe
ProtPred  ---------- hhhhhhh--- ---------- ------eeee eeeeee---- -------eee

          61        70         80         90         100        110    120
cav3      SYTTFTVSKY WCYRLLSTLL GVPLALLWGF LFACISFCHI WAVVPCIKSY LIEIQCISHI
gor       eeeeeeeccc ceeeeecccc ccceeeeeee eeeeecccce eeeeccccce ccccceeece
jpred     h-eeeeehhh hhhhhhhhhh hhhhhhhhhh hhhhhhhhhh hhhhhhhhee eee-hhhhhh
psipred   eeeeeeeeee ehhhhhhhhh hhhhhhhhhh hhhhhhhcee eeechhhhhh hhhhhhhhhh
CFSSP     eeeeeeeeee eeehhhhhhh hhhhhhhhhh hhhhhhhhhh hhhhhhhhhh hhhhhheeee
ProtPred ee-eeeeeeh hhhhhhhhhh hhhhhhhhhh hhhhhhhhhh -eeeee---e eeehhhhhhh

          121        130        140     150
cav3      YSLCIRTFCN PLFAALQVCS SIKVVLRKEV
gor       eeeccccccc ccccccccce eeeeeeceec
jpred     hhhhhhhhhh hhhhhhhh- -eeeee----
psipred   hhhhhhhhhh hhhhhhhhhc ccceeeeeec
CFSSP     eeeeeeeeee hhhhhhhhhh hheeeccccc
ProtPred hhhhhhhhhh --hhhhhhhh -eeeeeeee-
```

(c)

Fig. 4. (Continued) Prediction of the secondary structure elements of human: a) cav1, b) cav2 and c) cav3 using the GOR, Jpred, PsiPred, CFSSP and ProtPred tools (h – helix, e – beta strand, c – coil, t – turn).

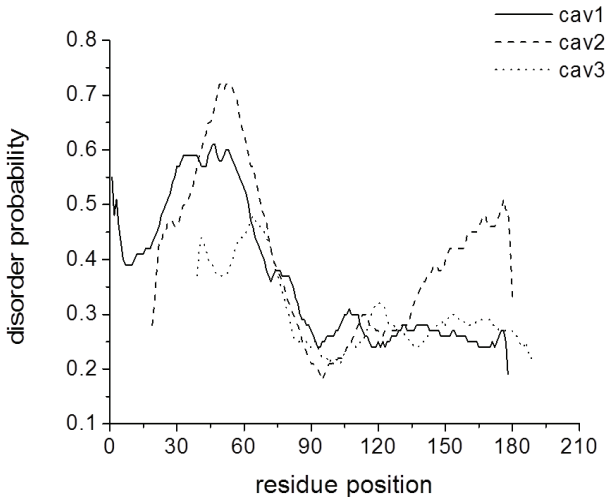

Fig. 5. Prediction of the disordered regions of caveolins using RONN software (regions with probability of disorder higher than 0.5 were predicted as disordered). For cav2 and cav3, the residue position was translated so that the caveolin signature sequence corresponds for all caveolins.

The consensus of the secondary structure predictions made using different bioinformatics tools led to the proposal that for cav1, the most probable helical regions are 98–125 (predicted by all the used tools) and 141–165 (predicted by Jpred, PsiPred and ProtPred).

Moreover, the consensus of the secondary structure predictions reflects that the 86–94 and 126–131 regions of cav1 adopt a beta-strand secondary structure. Furthermore, the prediction of the secondary structural elements of cav1 (Fig. 4) predicts that the first segment of the CSD contains a beta strand structural arrangement rich in hydrophobic amino acids and the segment 94–101 adopts a helical structure. The hydrophobic domain of cav1 is predicted to have a helical structure. The prediction of disordered regions of cav1 obtained using RONN[41] reflects a quite disordered N-terminal domain with a long disordered region, 26–63 (Fig. 5).

The use of GlobPlot software[42] for the same purpose (see Fig. S-5 of the Supplementary material to this paper) predicts the segment 24–47 as disordered and the 102–135 region as hydrophobic. ProtPred tool reflects a disordered N-terminal region (1–56) for cav1. These predictions of the secondary structure and of disordered regions for cav1 indicate that the N-terminal region of cav1 is disordered and lacks secondary structure arrangement. It was also registered that all tools used for secondary structure predictions (GOR, Jpred, PsiPred, CFSSP and ProtPred) agreed in their prediction of a helical structure for the hydrophobic domain, but concerning the prediction of disordered regions, only Jpred and ProtPred tools found the same amino acid sequences.

Comparisons of the computational and experimental data concerning the structural properties of cav1 or its fragments indicate controversial results. Based on the analysis of cav1 amino acids sequence using multiple computational algorithms, a topology model for cav1 was proposed.[49] This model proposes that the entire region of cav1 has a high probability to form helical structural elements and that the highest helical probability is found for the region 113–127. Circular dichroism (CD) and NMR spectroscopic studies of the hydrophobic domain of cav1 (96–136) revealed that this domain has a high α-helical content (57–65 %) and possess a helix-break-helix structure, the helix breaking region being 108––110.[50] Other CD studies have been performed on cav1 fragments in different environments. In particular, a CD study of cav1 fragments demonstrates that peptides 2–20 and 19–40 display 20 % content of alpha-helical structure and peptide 161–160 shows a 43 % content of alpha helix.[51] Furthermore, CD analysis of cav1 (1–101) fragment in solution reflects that the amino acids 79–96 are arranged in an alpha-helix[52]. The same technique applied for the cav1 (83–102) in the presence of 1-palmitoyl-2-oleoyl-*sn*-glycero-3-phosphocholine (POPC) vesicles[53] and for cav1 (82–101) in the presence of dodecylphosphocholine (DPC) micelles[54] revealed only a partially alpha-helical structure of this isolated

domain. For a longer fragment, cav1 (82–109), NMR studies indicate alpha-helical structures for the fragments 83–88 and 93–97 of the CSD domain and a stable helical conformation only for the fragment 102–109 belonging to the first region of the hydrophobic domain.[54] CD, FTIR and NMR experimental studies of cav1 (82–109) and cav1 (83–102) in the presence of a POPC/cholesterol mixture indicated that the CSD region of cav1 contains both alpha- and beta-structures, the content of alpha-helices being higher for the longer fragment.[54] The conformational model built by Hoop *et al.*[55] proposes an anti-parallel beta-strand for the region 84–94, which was also proposed by Spisni *et al.*[8]

For cav2, there is only one helical region in alpha-helix profile, 84–125 which is in quite good agreement with predictions of the secondary structure made using Jpred, PsiPred and CFSSP (Fig. 4) and this predicted helical region also includes the predicted membrane region (87–104). The beta-turn profile indicates that the region 20–50 adopts a beta-turn structure but this was not confirmed by the Jpred algorithm. The predicted disordered regions for cav2 are the amino acid sequences 17–49 using RONN (Fig. 5) and 19–25 and 32–45 using GlobPlot. These predictions are in good agreement with the results of the GOR, Jpred and PsiPred algorithms (Fig. 4). GlobPlot software also predicts the amino acid sequence 90–119 as the membrane domain of cav2 and this prediction should be compared with the predicted helical region, amino acid sequence 84––125, with the proposed hydrophobic domain, 87–119 as well as with the predicted membrane region, 87–104. A CD experimental study of cav2 (1–73) fragment indicated a 25 % helical content of this fragment.[52] Only the CFSSP prediction is in agreement with this experimental result.

Concerning cav3, the different algorithms used for the secondary structure predictions unanimously predict the 77–141 amino acid sequence as helical. A consensus for the membrane domain prediction was also obtained for the amino acid sequence 84–104. No disordered regions of cav3 were identified using RONN (Fig. 5) while the GlobPlot tools predict that the fragment 79–101 of cav3 is a hydrophobic domain and this prediction is in agreement with the hydrophobicity profile and with the membrane domain and secondary structure predictions. An experimental CD study revealed that fragment 1–74 for cav3 contains 25 % of α-helical secondary structure,[56] and the authors proposed that the CSD of cav3 (residues 55–72) forms an alpha-helix and that the remaining region 1–54 lacks a stable secondary structure.[57]

Taking into account the sequence alignments and the analysis presented above, the following functional domains are proposed for cav2 and cav3.

For cav2: N-terminal domain – residues 1–66; CSD – residues 67–86, including the CRAC motif (residues 79–86); HD domain – residues 87–119; C-MAD domain – residues 120–135 and C-terminal domain – residues 136–162.

For cav3: N-terminal domain – residues 1–54; CSD domain – residues 55–74, including the CRAC motif (67–74); HD domain – residues 75–107; C-MAD domain – residues 108–123 and C-terminal domain – residues 124–151.

To the best of our knowledge, no published data concerning the predicted functional domains of cav2 have been published. Concerning cav3, the present predictions are in good agreement with published data of Balijepalli and Kamp, 2009.[57]

The physicochemical properties of the predicted domains of cav1, cav2 and cav3 are reported in Table I.

TABLE I. Physicochemical properties of different functional domains of caveolins

Protein domain	Net charge			GRAVY			Aliphatic index		
	cav1	cav2	cav3	cav1	cav2	cav3	cav1	cav2	cav3
N-TER	–8	–11	–9	–0.858	–0.889	–0.361	74.25	60.61	95.56
CSD	+2	+1	+2	–0.265	0.160	–0.385	39.00	92.50	43.50
HD	0	0	0	2.009	2.218	2.015	171.52	171.52	165.45
C-TER	+2	+3	+3	0.212	0.774	0.796	108.46	118.89	118.21

As expected, the values presented in Table I show that the hydrophobic domains have the highest hydrophobicity reflected by GRAVY and the highest values of the aliphatic indexes. The GRAVY index of the CSD of cav2 strongly differs from the GRAVY index of the CSD of cav1 and cav3 as a result of the different amino acid contents of these domains. The amino acid sequences of cav1 and cav3 CSD differ by 6 residues while cav1 and cav2 CSD amino acid sequences differ by 12 residues. The CSD of cav2 has a higher content of hydrophobic residues: Ile71 in comparison with Lys86 in cav1 and Lys59 in cav3, Ala75 in comparison with Thr90 in cav1 and Thr63 in cav3, Leu76 in comparison with Thr91 in cav1 and Thr64 in cav3 and Val83 in comparison with Trp98 in cav1 and Trp71 in cav3 (Fig. 1). The N-terminal domain of cav2 has a more negative charge in comparison to that of cav1 and cav3. These differences could be responsible for the different folding of these proteins and/or for the different properties of the associations with themselves or with other partners.

The predicted functional partners of human cav2 and cav3 were obtained using STRING software[47] and are compared with those of caveolin-1. There are only a few common interacting partners for all the caveolins (they are presented in Table II), cav1 and cav3 having more common partners than cav1 and cav2 (Table III).

This may be due to the differences in the amino acid sequences of cav1 and cav2, but also to the lack of data concerning these interactions. Some of the predicted interacting partners of cav2 and cav3 do not contain the CBD, which is in good agreement with recent literature data.[12]

TABLE II. Proteins predicted to interact with all human caveolins: cav1, cav2 and cav3 (the interactions that are experimentally proven are marked with an asterisk)

Protein	Interaction with			CBM and/or CBM-like motif containing molecule [17]
	cav1	cav2	cav3	
v-src Sarcoma viral oncogene homolog	X*	X*	X	–
FYN oncogene related to SRC	X*	X	X	–
Nitric oxide synthase 3 (NOS3)	X*	X	X	X
Gap junction protein, alpha 1 (GJA1)	X*	X	X	X
Flotillin 2 (FLOT2)	X*	X*	X*	X
Integrin, beta 4 (ITGB4)	X*	X	X	–
Integrin, beta 5 (ITGB5)	X*	X	X	–
Integrin, beta 6 (ITGB6)	X*	X	X	–
Integrin, beta 7 (ITGB7)	X*	X	X	–
Integrin, beta 3 (ITGB3)	X*	X	X	–
Integrin, beta 8 (ITGB8)	X*	X	X	–
Integrin, beta 1 (ITGB1)	X*	X	X	–

TABLE III. Proteins predicted to interact with cav1 and cav2, respectively with cav1 and cav3 (the experimentally proven interactions are marked with an asterisk)

Protein	Interaction with			CBM and/or CBM-like motif containing molecule[17]
	cav1	cav2	cav3	
Caveolin 2 (CAV2)	X*	–	–	–
Insulin receptor (INSR)	X*	–	X	X
Insulin receptor substrate 1 (ISR1)	X*	–	X	X
Transient receptor potential cation channel, subfamily C	X*	–	X	X
Nitric oxide synthase 3 (NOS3)	X*	X	X	X
Ras-related C3 botulinum toxin substrate 1 (RAC1)	X*	–	X	X
Dystroglycan 1(DAG1)	X*	–	X*	X
Polymerase I and transcript release factor (PTRF)	X*	–	X	–
Phospholipase D1, phosphatidylcholine-specific	X*	–	X	X
Mal (MALL)	X*	X*		X
Platelet-derived growth factor receptor	X*	–	X*	X
Phospholipase D2 (PLD2)	X*	X*		X
Ras homolog gene family, member A (RHOA)	X*	–	X	–
Nitric oxide synthase 2, inducible (NOS2)	X*	–	X*	X
V-Akt murine thymoma viral oncogene homolog 1	X	–	X	–
Calcium channel, voltage-dependent, L type	X	–	X	–
Nitric oxide synthase 1 (NOS1)	X*	–	X*	X
Calcium channel, voltage-dependent, N type	X	X		X
Solute carrier family 2 (SLC2A4)	X	–	X	–
RAS p21 protein activator (RASA1)	X*	X	–	–

TABLE III. Continued

Protein	Interaction with			CBM and/or CBM-like motif containing molecule[17]
	cav1	cav2	cav3	
Syndecan 2 (SDC2)	–	X	–	–
V-Ha-ras Harvey rat sarcoma viral oncogene homolog	X*	X	–	–
Solute carrier family 8, member 1 (SLC8A1)	X*	–	X*	X
Synaptosomal-associated protein (SNAP23)	X*	–	X*	X
SMAD family member 3 (SMAD3)	X*	–	X*	X
Stromal interaction molecule 1 (STIM1)	X*	–	X*	–
Dopamine receptor D1(DRD1)	X*	X*	–	X

CONCLUSIONS

For the first time, a bioinformatics study comparing all the three amino acid sequences of human caveolins is presented. Taking into account the known data about cav1 (the most studied from this family), the functional domains of cav2 and cav3 were predicted and characterised. The predicted functional domains of cav2 are: N-terminal domain – residues 1–66; CSD – residues 67–86, including the CRAC motif (residues 79–86); HD domain – residues 87–119; C-MAD domain – residues 120–135 and C-terminal domain – residues 136–162. Similarly, the predicted functional domains for cav3 are: N-terminal domain – residues 1–54; CDS domain – residues 55–74, including the CRAC motif (67–74); HD domain – residues 75–107; C-MAD domain – residues 108–123 and C-terminal domain residues 124–151.

The amino acid sequence of cav2 differs slightly from that of cav1 and cav3 and its N-terminal is more hydrophilic and has a higher overall negative charge than the N-terminal domains of cav1 and cav3. All the caveolins possess three cysteine residues in the C-terminal domains, their positions being conserved for cav1 and cav3 but not for cav2. Therefore, for cav3, the three cysteine residues are most probably palmitoylated. The oligomerization domain of cav1 contains 41 residues (region 61–101). Sequence alignment revealed that in the homology region of cav3 (residues 34–74), there are only 7 distinct residues (17 %) and in the homology region of cav2 (residues 46–86), there are 17 distinct residues (41 %). This sequence dissimilarity may be responsible for the difference in oligomerization of the three caveolins: cav1 and cav3 being able to form high weight oligomers while cav2 forms only homo-dimers.[19]

The CSD of the three caveolins also differ in sequence: there are 6 distinct residues between the amino acids sequences of cav1 (82–101) and cav3 (55–74), and 12 distinct residues between the amino acids sequences of cav1 (82–101) and cav2 (67–86). These differences may be responsible for the specificity of the interactions of the three caveolins, as the CSD domain has been proposed to be involved in interactions with functional partners.

The amino acid sequences of the hydrophobic domains of the three caveolins are the most similar in sequence, they are highly hydrophobic and are predicted to comprise helical structures. This expected result is in good agreement with experimental data concerning the cav1 (96–136) fragment in the presence of lyso-myristoylphosphatidylglycerol.[50]

The amino acid sequences of the C-terminal domains of the caveolins are the most divergent: there are 18 distinct residues between the amino acid sequences of cav1 (135–178) and cav3 (108–151) and 32 distinct residues between the amino acid sequences of cav1 (135–178) and of cav2 (120–162). The amino acid sequence of the C-terminal segment of cav1 is mostly hydrophilic, and has two proposed functions: membrane anchoring for its first part (C-MAD, residues 135–150) and protein–protein interactions for its last part (residues 168–178), which is also involved in homotypic interactions[58] and contributes to the side-by-side clustering of homo-oligomers of caveolin-1.[7] There are few experimental results concerning the C-terminal region of cav2, but it is known that the Ser154––Val155–Ser156 motif of the C-terminal of cav2 is essential for insulin-induced phosphorylation and nuclear targeting of extracellular signal-regulated kinase;[59,60] this motif being absent in the sequences of cav1 and cav3. In addition, experimental data suggest that the C-terminal domain of cav2 is necessary for targeting cav2 to caveolae.[21] Therefore, the divergence of the amino acid sequences of the C-terminal regions of the three caveolins may also contribute to the different location and distinct interacting partners of these proteins.

The performed bioinformatics analysis of the amino acid sequences of human caveolins highlighted both similar and distinct structural and functional properties of caveolins in correlation with their amino acid sequences. It also highlighted the limitations of the currently existing tools concerning the predictions of structural features of membrane proteins. An agreement between the different experimental structural data, especially obtained for cav1, is lacking. This reflects that the structure adopted by the different regions of caveolin may be distinct as a result of the different lengths of the considered fragments and of the interactions with their environments. It must also be taken into account that the computational tools for the prediction of the structural features of membrane proteins have limitations.

Further research must be realised to elucidate the interaction network of caveolins with physiological implications. From this point of view, knowledge concerning their full length spatial structures would substantially contribute to an understanding of their functions.

SUPPLEMENTARY MATERIAL

Figures S-1–S-5 are available electronically from http://www.shd.org.rs/JSCS/, or from the corresponding author on request.

Aknowledgement. This work is a result of a bilateral collaboration Romania – France project, Programme Brancusi, 492/2011.

И З В О Д

БИОИНФОРМАТИЧКО ИСПИТИВАЊЕ СТРУКТУРЕ И ФУНКЦИОНАЛНИХ СВОЈСТАВА ХУМАНИХ ПРОТЕИНА КАВЕОЛИНА

ADRIANA ISVORAN[1,2], DANA CRACIUN[3], ALECU CIORSAC[4], NAHUEL PERROT[5], VERONICA BESWICK[5,6], PIERRE NEDELLEC[5], ALAIN SANSON[5] и NADEGE JAMIN[5]

[1]Department of Biology–Chemistry, West University of Timisoara, 16 Pestalozzi, 300316 Timisoara, Romania, [2]Laboratory of Advanced Researches in Environmental Protection, West University of Timisoara, 4 Oituz, 300086 Timisoara, Romania, [3]Teacher training Department, West University of Timisoara, 4 V.Pirvan, 300223 Timisoara, Romania, [4]Department of Physical Education and Sport, Politehnica University of Timisoara, 2 P-ta Victoriei, 300306 Timisoara, Romania, [5]Commissariat à l'Energie Atomique (CEA), Institute of Biology and Technologies of Saclay (iBiTecS) 91191 Gif-sur-Yvette Cedex, France и [6]Department of Physics, Université d'Evry-val-d'Essonne, 91025 Evry Cedex, France

Урађена је биоинформатичка студија у циљу предвиђања и упоређивања структуре и функционалних својстава хуманог кавеолина-1, -2 и -3. Компјутерски процењена физичко–хемијска својстава, секундарна структура и интерагујући партнери кавеолина-2 и -3 су упоређивани са експериментално доказаном структуром и својствима кавеолина-1. Ови подаци, заједно са примарном секвенцијом три кавеолина, омогућили су предвиђање и карактеризацију функционалних домена кавеолина-2 и -3. Хидрофобни региони ова три протеина имају веома сличну секвенцију и физичко–хемијска својства, што је у складу са њиховом мембранском локализацијом и функцијама. Највећа разлика у секвенцији и својствима нађена је у С-терминалном региону кавеолина, те се може претпоставити да је он одговоран за различите интеракције које би имале директне последице на пренос сигнала.

(Примљено 16 јула, ревидирано 21. септембра 2013)

REFERENCES

1. A. Schlegel, D. Volonte, J. A. Engelman, F. Galbiati, P. Mehta, X. L. Zhang, P. E. Scherer, M. P. Lisanti, *Cell. Signal.* **10** (1998) 457
2. A. W. Cohen, R. Hnasko, W. Schubert M. P. Lisanti, *Physiol. Rev.* **84** (2004) 134
3. P. E. Scherer, Z. Tang , M. Chun, M. Sargiacomo, H. F. Lodish, M. P. Lisanti, *J. Biol. Chem.* **270** (1995) 16395
4. H. Kogo, T. Fujimoto, *FEBS Lett.* **465** (2000) 119
5. A. Uittenbogaard, E. J. Smart, *J. Biol. Chem.* **275** (2000) 25595
6. M. O. Parat, P. L. Fox, *J. Biol. Chem.* **276** (2001) 15776
7. A. Schlegel, M. P. Lisanti, *J. Biol. Chem.* **275** (2000) 21605
8. E. Spisni, V. Tomasi, A. Cestaro, S. C. E. Tosatto, *Biochem. Biophys. Res. Comm.* **338** (2005) 1383
9. A. Arbuzova, J. Wang, L. Wang, G. Hangyas-Mihalyne, D. Murray, B. Honig, S. McLaughlin, *Biochemistry* **39** (2000) 10330
10. J. Couet, S. Li, T. Okamoto, T. Ikezu, M. P. Lisanti, *J. Biol. Chem.* **272** (1997) 6525
11. J. Couet, M. Sargiacomo, M. P. Lisanti, *J. Biol. Chem.* **272** (1997) 30429
12. B. M. Collins, M. J. Davis, J. F. Hancock, R. G. Parton, *Dev. Cell.* **23** (2012) 11
13. H. Li, V. Papadopoulos, *Endocrinology* **139** (1998) 4991

14. C. Le Lan, J. Gallay, M. Vincent, J. M. Neumann, B. de Foresta, N. Jamin, *Eur. Biophys. J.* **39** (2010) 307
15. M. Sáinz-Jaspeado, J. Martin-Liberal, L. Lagares-Tena, S. Mateo-Lozano, X. G. del Muro, O. M. Tirado, *Oncotarget* **2** (2011) 305
16. R. G. W. Anderson, *Annu. Rev. Biochem.* **67** (1998) 199
17. D. P. Byrne, C. Dart, D. J. Rigden, *PLOS ONE* **7** (2012) e44879
18. H. Lee, D. Volonte, F. Galbiati, P. Iyengar, D. M. Lublin, D. B. Bregman, M. T. Wilson, R. Campos-Gonzales, B. Bouzahzah, R. G. Pestell, P. E. Scherer, M. P. Lisanti, *Mol. Endocrinol.* **14** (2000) 1750
19. P. E. Scherer, T. Okamoto, M. Chun, I. Nishimoto, H. F. Lodish, M. P. Lisanti, *Proc. Natl. Acad. Sci. U.S.A.* **93** (1996) 131
20. P. E. Scherer, R. Y. Lewis, D. Volonte, J. A. Engelman, F. Galbiati, J. Couet, D. S. Kohtz, E. van Donselaar, P. Peters, M. P. Lisanti, *J. Biol. Chem.* **272** (1997) 29337
21. H. Kogo, K. Ishiguro, S. Kuwaki, T. Fujimoto, *Arch. Biochem. Biophys.* **401** (2002) 108
22. H. Lee, D. S. Park, X. B. Wang, P. E. Scherer, P. E. Schwartz, M. P. Lisanti, *J. Biol. Chem.* **277** (2002) 34556
23. X. B. Wang, H. Lee, F. Capozza, S. Marmon, F. Sotgia, J. W. Brooks, R. Campos-Gonzalez, M. P. Lisanti, *Biochemistry* **43** (2004) 13694
24. G. Sowa, M. Pypaert, D. Fulton, W. C. Sessa, *Proc. Natl. Acad. Sci. U.S.A.* **100** (2003) 6511
25. G. Sowa, L. Xie, L. Xu, W. C. Sessa, *Biochemistry* **47** (2008) 101
26. T. M. Williams, M. P. Lisanti, *Ann. Med.* **36** (2004) 584
27. K. S. Song, P. E. Scherer, Z. Tang, T. Okamoto, S. Li, M. Chafel, C. Chu, D. S. Kohtz, M. P. Lisanti, *J. Biol. Chem.* **271** (1996) 15160
28. M. Shatz, M. Liscovitch, *Int. J. Radiat. Biol.* **84** (2008) 177
29. R. Apweiler, A. Bairoch, C. H. Wu, *Curr. Opin. Chem. Biol.* **8** (2004) 76
30. S. F. Altschul, W. Gish, W. Miller, E. W. Myers, D. J. Lipman, *J. Mol. Biol.* **215** (1990) 403
31. M. A. Larkin, G. Blackshields, N. P. Brown, R. Chenna, P. A. McGettigan, H. McWilliam, F. Valentin, I. M. Wallace, A. Wilm, R. Lopez, J. D. Thompson, T. J. Gibson, D. G. Higgins, *Bioinformatics* **23** (2007) 2947
32. E. Gasteiger, C. Hoogland, A. Gattiker, S. Duvaud, M. R. Wilkins, R. D. Appel, A. Bairoch, in *The Proteomics Protocols Handbook*, J. M. Walker, Ed., Humana Press, Totova, NJ, 2005, p. 571
33. J. Kyte, R. F. Doolittle, *J. Mol. Biol.* **157** (1982) 105
34. B. Vaseeharan, S. Valli, *J. Proteomics Bioinform.* **4** (2011) 1
35. R. Mohan, S. Venugopal, *Bioinformation* **8** (2012) 722
36. J. Garnier, J. F Gibrat, B. Robson, in *Methods in Enzymology*, Vol. 266, R. F. Doolittle Ed., Academic Press, Lemoyne, PN, 1996, p. 540
37. C. Cole, J. D. Barber, G. J. Barton, *Nucl. Acids Res.* **36** (2008) W197
38. D. W. Buchan, S. M. Ward, A. E. Lobley, T. C. Nugent, K. Bryson, D. T. Jones, *Nucl. Acids Res.* **38** Suppl. (2010) W563
39. P. Y. Chou, G. D. Fasman, *Biochemistry* **13** (1974) 211
40. B. Rost, G. Yachdav, J. Liu, *Nucl. Acids Res.* **32** (2004) W321
41. Z. R. Yang, R. Thomson, P. McNeil, R. M. Esnouf, *Bioinformatics* **21** (2005) 3369
42. R. Linding, R. B. Russell, V. Neduva, T. J. Gibson, *Nucl. Acids Res.* **31** (2003) 3701
43. H. Viklund, A. Elofsson, *Bioinformatics* **24** (2008) 1662
44. H. Viklund, A. Bernsel, M. Skwark, A. Elofsson, *Bioinformatics* **24** (2008) 2928

45. G. Zhao, E. London, *Protein Sci.* **15** (2006) 1987
46. G. Deleage, B. Roux, *Protein Eng.* **1** (1987) 2890
47. D. Szklarczyk, A. Franceschini, M. Kuhn, M. Simonovic, A. Roth, P. Minguez, T. Doerks, M. Stark, J. Muller, P. Bork, L. J. Jensen, C. von Mering, *Nucl. Acids Res.* **39** (2011) D561
48. C. Combet, M. Jambon, G. Deleage, C. Geourjon, *Bioinformatics* **18** (2002) 213
49. R. G. Parton, M. Hanzal-Bayer, J. F. Hancock, *J. Cell. Sci.* **119** (2006) 787
50. J. Lee, K. J. Glover, *Biochim. Biophys. Acta* **1818** (2012) 1158
51. M. E. Schroeder, H. A. Hostetler, F. Schroeder, J. M. Ball, *J. Amino Acids* (2012) ID 575180
52. I. Fernandez, Y. Ying, J. Albanesi, R. G. Anderson, *Proc. Natl. Acad. Sci. U.S.A.* **99** (2002) 11193
53. R. M. Epand, B. G. Sayer, R. F. Epand, *J. Mol. Biol.* **345** (2005) 339
54. C. Le Lan, J. M. Neumann, N. Jamin, *FEBS Lett.* **580** (2006) 5301
55. C. D. Hoop, V. N. Sivanandam, R. Kodaly, M. N. Srnec, P. C. A. van der Wel, *Biochemistry* **51** (2012) 90
56. S. R. Fuhs, P. A. Insel, *J. Biol. Chem.* **286** (2011) 14830
57. R. C. Balijepalli, T. J. Kamp, *Prog. Biophys. Mol. Biol.* **98** (2009) 149
58. K. S. Song, Z. Tang, S. Li, M. P. Lisanti, *J. Biol. Chem.* **272** (1997) 4398
59. H. Kwon, K. Jeong, E. M. Hwang, J. Y. Park, Y. Pak, *J. Cell. Mol. Med.* **15** (2011) 888
60. K. Jeong, H. Kwon, J. Lee, D. Jang, E. M. Hwang, J. Y. Park, Y. Pak, *Traffic* **13** (2012) 1218.

Journal of the Serbian Chemical Society
JSCS@tmf.bg.ac.rs • www.shd.org.rs/JSCS
J. Serb. Chem. Soc. 79 (2) S24–S26 (2014) *Supplementary material*

SUPPLEMENTARY MATERIAL TO

A bioinformatics study concerning the structural and functional properties of human caveolin proteins

ADRIANA ISVORAN[1,2]*, DANA CRACIUN[3], ALECU CIORSAC[4], NAHUEL PERROT[5], VERONICA BESWICK[5,6], PIERRE NEDELLEC[5], ALAIN SANSON[5] and NADEGE JAMIN[5]

[1]Department of Biology–Chemistry, West University of Timisoara, 16 Pestalozzi, 300316 Timisoara, Romania, [2]Laboratory of Advanced Researches in Environmental Protection, West University of Timisoara, 4 Oituz, 300086 Timisoara, Romania, [3]Teacher training Department, West University of Timisoara, 4 V. Pirvan, 300223 Timisoara, Romania, [4]Department of Physical Education and Sport, Politehnica University of Timisoara, 2 P-ta Victoriei, 300306 Timisoara, Romania, [5]Commissariat à l'Energie Atomique (CEA), Institute of Biology and Technologies of Saclay (iBiTecS) 91191 Gif-sur-Yvette Cedex, France and [6]Department of Physics, Université d'Evry-val-d'Essonne, 91025 Evry Cedex, France

J. Serb. Chem. Soc. 79 (2) (2014) 133–150

HYDROPHOBICITY, ALPHA-HELIX AND BETA-TURN PROFILES FOR CAVEOLIN 1 OBTAINED USING DIFFERENT WINDOW SIZES

The independence of the hydrophobicity, alpha-helix and beta-turn profiles on the window size used to compute them is illustrated in Figs. S-1 and S-2 for caveolin 1. The hydrophobicity profile of caveolin 1 for three different window sizes, *i.e.*, 9, 13 and 21 residues, is illustrated in Fig. S-1. It could be seen that the profiles do not differ significantly.

This is also true for the alpha-helix and beta-turn profiles, presented in Fig. S-2a and b, respectively.

HOMOLOGY MODELLING USING THE GENO3D TOOL

The use of the Geno3D tool is illustrated in Fig. S-3. For any of the human caveolin sequences, the obtained result was the same "No satisfying template found for sequence 1".

* Corresponding author. E-mail: adriana.isvoran@cbg.uvt.ro

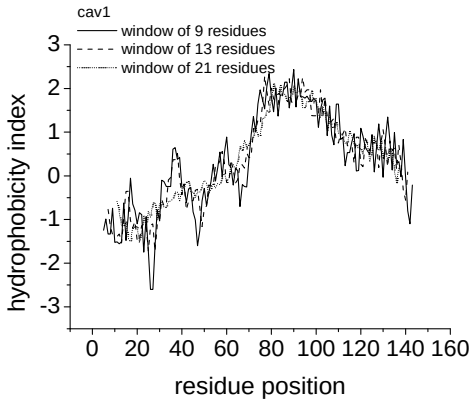

Fig. S-1. The hydrophobicity profile of caveolin 1 for three different window sizes: 9 residues – solid line, 13 residues – dashed line, 21 residues – dotted line.

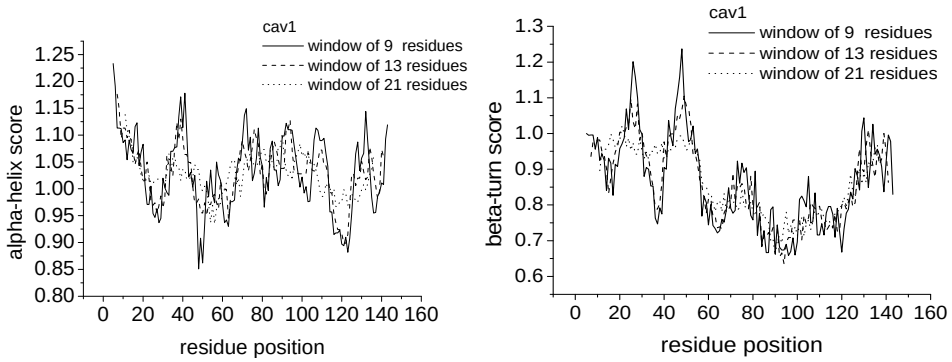

(a) (b)

Fig. S-2. a) Alpha-helix and b) beta-turn profile of caveolin 1 for three different window sizes: 9 residues – solid line, 13 residues – dashed line, 21 residues – dotted line.

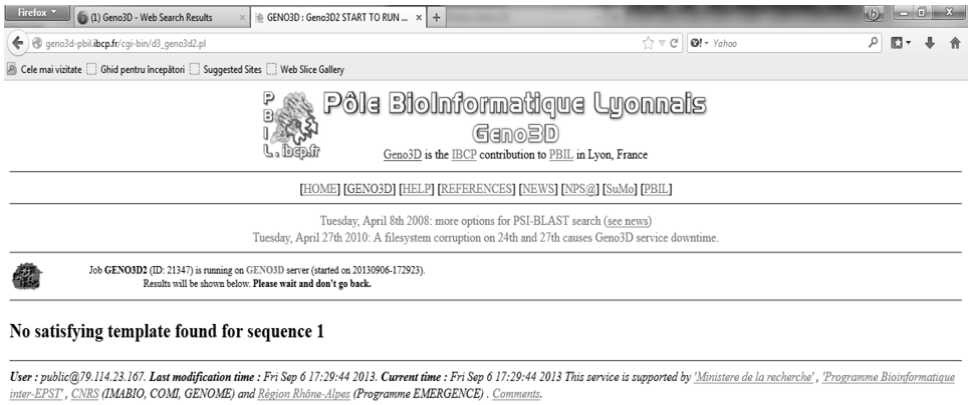

Fig. S-3. Illustration of using Geno3D tool for human caveolin 1.

MEMBRANE TENDENCY PROFILES FOR HUMAN CAVEOLINS

Membrane tendency profiles for the three caveolins are presented in Fig. S-4 in comparison to the hydrophobicity profile of caveolin 1. The similarity between the membrane tendency profiles and their correspondence to the hydrophobicity profile of cav1 could be evidenced.

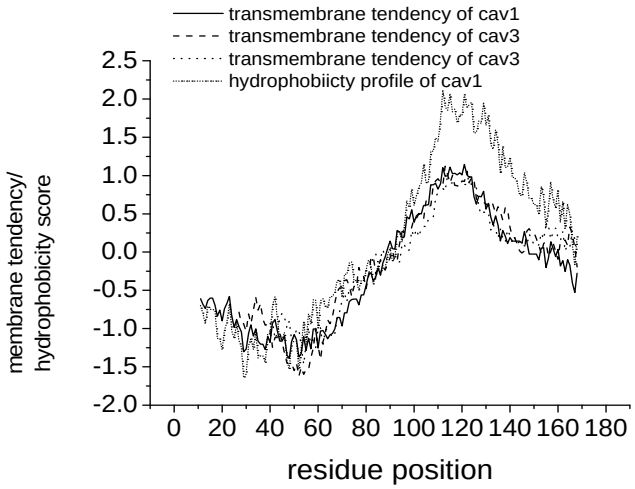

Fig. S-4. Membrane tendency profiles of cav1 (solid line), cav2 (dashed line), cav3 (dotted line) and the hydrophobicity profile of cav1 (short dotted line) obtained using ProtScale tool. For cav2 and cav3 proteins the residue position was translated such as the caveolin signature sequence to correspond for all caveolins. Prediction of disordered regions of cav1 using GlobPlot.

PREDICTION OF DISORDERED REGIONS OF CAV1 USING GLOBPLOT SOFTWARE

Prediction of disordered regions of cav1 using GlobPlot software is presented in Fig. S-5.

Disordered by Russell/Linding definition

>none_Disorder 23-42
spqcavhman cavelinshm sa**PIENSGNC**
AVPESVMSGG KYvdseghly tvpireqgni
ykpnnkamad elsekqvyda htkeidlvnr
dpkhlnddvv kidfedviae pegthsfdgi
wkasfttftv tkywfyrlls alfgipmali
wgiyfailsf lhiwavvpci ksflieiqci
srvysiyvht vcdplfeavg kifsnvrinl
qkei

Fig. S-5. Prediction of the disordered region of human caveolin 1 using the GlobPlot tool.

The predicted disordered region is 23–42.

Journal of the Serbian Chemical Society
JSCS-info@shd.org.rs • www.shd.org.rs/JSCS
J. Serb. Chem. Soc. 79 (2) 151–165 (2014)
JSCS–4572
UDC 577.213.3+546.962+542.9+547.571+547.551:543.42–74
Original scientific paper

Synthesis, spectral, DNA binding and cleavage properties of ruthenium(II) Schiff base complexes containing PPh_3/$AsPh_3$ as co-ligands

SUBBAIYAN SATHIYARAJ, GANESAN AYYANNAN and CHINNASAMY JAYABALAKRISHNAN*

Post Graduate and Research Department of Chemistry, Sri Ramakrishna Mission Vidyalaya College of Arts and Science, Coimbatore – 641 020, Tamil Nadu, India

(Received 1 December 2012, revised 8 May 2013)

Abstract: Dihydroxybenzaldehyde-based Schiff base ligands (L^1–L^3) and their ruthenium(II) complexes were synthesized and characterized by elemental analysis, ^{1}H-, ^{13}C- and ^{31}P-NMR, UV–Vis, IR and mass spectroscopy. The DNA binding of the ruthenium(II) complexes was investigated by UV–Vis absorption spectroscopy. The experiments revealed that all the compounds could bind to DNA through electrostatic interactions and the intrinsic binding constants (K_b) were estimated under similar sets of experimental conditions. The absorption spectral study indicated that the ruthenium(II) complexes had intrinsic binding constants in the range of $(1.6–8.6)\times10^4$ mol^{-1} dm^3. The complex $[Ru(CO)(PPh_3)_2(L^3)]$ bound more strongly than the other complexes. In addition, the DNA cleavage properties for all ruthenium(II) complexes were tested.

Keywords: Schiff base; ruthenium(II) complexes; CT-DNA; nuclease activity.

INTRODUCTION

It is well known that deoxyribonucleic acid (DNA) plays an important role in the life process since it contains all the genetic information for cellular function. However, DNA is the primary intracellular target of anticancer drugs due to the interaction between small molecules and DNA, which cause DNA damage in cancer cells, blocking the division of cancer cells and resulting in cell death. This is due to their possible application as new therapeutic agents and their photochemical properties that make them potential probes of DNA structure and conformation.[1–3] The binding interaction of transition metal complexes with DNA is of interest for both therapeutic and scientific reasons.[4] Many transition metal complexes are known to bind to DNA *via* both covalent and non-covalent interac-

* Corresponding author. E-mail: cjayabalakrishnan@gmail.com
doi: 10.2298/JSC121201073S

tions. In covalent binding, the labile ligand of the complexes is replaced by a nitrogen base of DNA. On the other hand, the non-covalent DNA interactions include intercalative, electrostatic and groove (surface) binding of cationic metal complexes along the outside of the DNA helix, and the major or minor groove. Schiff bases are potential anticancer drugs and when administered as their metal complexes, the anticancer activity of these complexes is enhanced in comparison to that of the free ligand. Schiff base complexes are considered the most important stereochemical models in transition metal coordination chemistry due to their preparative accessibility and structural variety. It was suggested that the azomethine linkage in Schiff bases is responsible for their biological activities, such as antitumour, antibacterial, antifungal and herbicidal activities.[5]

Metal complexes are employed in many fields of drug discovery. Platinum coordination complexes are widely used as antitumour drugs. The first platinum antitumour drug introduced into clinical practice was *cis*-diamminedichloroplatinum(II) (cisplatin), which became the most widely used anticancer drug in the world. However, intrinsic and acquired tumour resistance diminishes the clinical efficacy of cisplatin and other platinum drugs. In addition cisplatin is of high toxicity, leading to side effects that limit the administered dose.[6] These limiting issues have led to an intense effort to design new transition metal-based compounds that are capable of overcoming problems associated with cisplatin while maintaining the same level of activity and broadening the spectrum of the therapeutic effect. In attempts to find a new, metal-based anticancer drug with activity complementary to cisplatin, several ruthenium complexes have recently been investigated for their antitumour activity.[7]

Bearing these facts in mind, our interest was focused on the synthesis of ruthenium(II) complexes containing tridentate Schiff base ligands and triphenylphosphine or triphenylarsine as co-ligands. The Schiff base ligands were derived by the condensation of 2,4-dihydroxybenzaldehyde with 2-aminobenzothiazole, 2-amino-6-methylbenzothiazole or *o*-aminophenol (Scheme 1). Then the new Schiff base ligands and their ruthenium(II) complexes were characterized by elemental analysis, FT-IR, electronic, mass spectra, and ^{1}H-, ^{13}C- and ^{31}P-NMR spectroscopy. Additionally, a comparative study of the interaction of the ruthenium complexes with CT-DNA has been employed in order to investigate the potential mechanism of their biological properties using UV–Vis spectroscopic and gel electrophoresis techniques.

EXPERIMENTAL

Materials and instrumentation

Reagent grade chemicals were used without further purification in all the synthetic work. All solvents were purified by standard methods. $RuCl_3 \cdot 3H_2O$, triphenylphosphine / arsine were purchased from Himedia. Calf thymus DNA (CT-DNA) was purchased from Bangalore Genei, Bangalore, India. Infrared spectra were recorded on a Perkin Elmer FT-IR spectro-

photometer (model RXI) as KBr pellets in the range 4000–400 cm^{-1}. Elemental analyses were performed with a Vario ELIII CHNS instrument at the Sophisticated Test and Instrumentation Centre (STIC), Cochin University, Kerala, India. Electronic spectra were recorded in DMSO solution in a Systronics 2202 double beam spectrophotometer in the 800–200 nm range. The ^{1}H-, ^{13}C- and ^{31}P-NMR spectra were recorded on Bruker WM DCX 500 MHz instrument using TMS and orthophosphoric acid as internal standards at SAIF, Indian Institute of Technology, Chennai. The mass spectra were recorded using a JEOL GC mate instrument at SAIF, Indian Institute of Technology, Chennai, India. The DNA cleavage studies were performed using the gel documentation system, Gelstan. Melting points were recorded on a Veego VMP-DS model heating table and are uncorrected. The metal precursors $[RuHCl(CO)(PPh_3)_3]$,[8] $[RuHCl(CO)(AsPh_3)_3]$,[9] were prepared according to reported procedures.

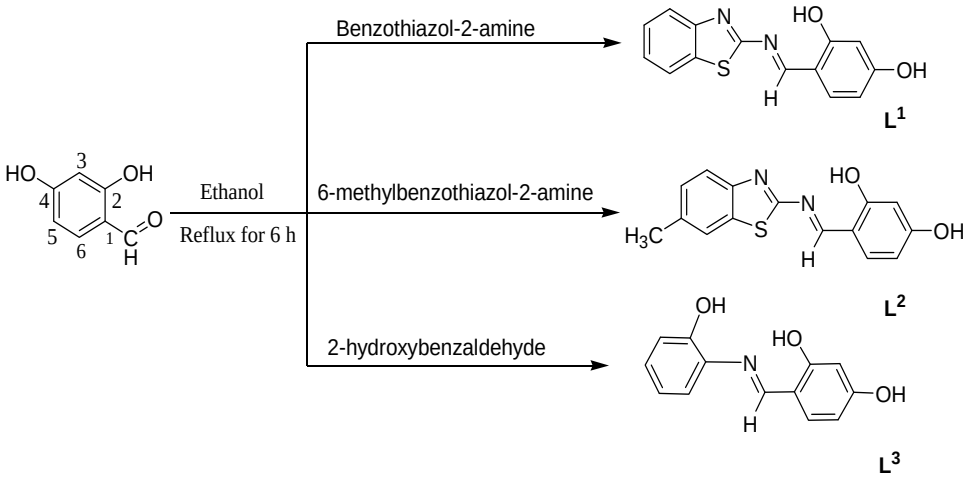

Scheme 1. Preparation of the Schiff base ligands.

Preparation of the Schiff base ligands

A solution of 2,4-dihydroxybenzaldehyde (1.38 g, 10 mmol) in ethanol (15 ml) was added to a stirred solution of 2-aminobenzothiazole/2-amino-6-methylbenzothiazole/*o*-amino phenol (1.09–1.64 g, 10 mmol) in ethanol (20 mL). The mixture was refluxed for 6 h. Upon cooling, a precipitate was formed, which was filtered off, dried and recrystallized from ethanol (Scheme 1).

Preparation of the ruthenium(II) Schiff base complexes

All the new ruthenium(II) complexes were prepared by the following general procedure (Scheme 2). A solution of $[RuHCl(CO)(B)_3]$ (0.190–0.216 g, 0.20 mmol) in benzene (20 mL, B = PPh_3/$AsPh_3$), was added to a stirred solution of Schiff base ligands (0.045–0.056 g, 0.20 mmol) in methanol (15 mL). The mixture was refluxed for 12 h. The solvent was then evaporated under reduced pressure and the solid mass filtered and washed with petroleum ether. The purity of the complexes was checked by thin layer chromatography and was further purified by column chromatography using 1:10 CH_2Cl_2:*n*-hexane as an eluent. This solid was recrystallized from CH_2Cl_2/*n*-hexane mixture. All attempts to obtain single crystals of the complexes were unsuccessful.

DNA-binding and cleavage assay

Electronic absorption spectroscopy. Experiments involving the interaction of the ruthenium(II) complexes with CT-DNA were realized in double distilled water containing tris(hydroxymethyl)aminomethane (Tris, 5 mM) and sodium chloride (50 mM), with the pH adjusted to 7.2 using hydrochloric acid. A solution of CT-DNA in the buffer gave a UV absorbance ratio at 260 to 280 nm of about 1.9, indicating that the DNA was sufficiently free of protein. The DNA concentration per nucleotide was determined by absorption spectroscopy using the molar extinction coefficient value of 6600 dm^3 mol^{-1} cm^{-1} at 260 nm. Electronic absorption titration experiments were performed by maintaining the concentration of the complexes constant (25 μM) but with variable nucleotide concentrations from 0 to 25 μM. While measuring the absorption spectra, equal amounts of DNA were added to both compounds and reference solutions to eliminate the absorbance of DNA itself. The data were then fitted into the following equation and the intrinsic binding constant K_b was calculated in each case:[10]

$$[DNA]/(\varepsilon_a-\varepsilon_f) = [DNA]/(\varepsilon_b-\varepsilon_f) + (1/K_b)(\varepsilon_b-\varepsilon_f) \quad (1)$$

where [DNA] is the concentration of DNA in base pairs. The apparent absorption coefficients ε_a, ε_f and ε_b correspond to A_{obsd}/[complex], the extinction coefficient of the free compound and the extinction coefficient of the compound when fully bound to DNA, respectively. In plots of [DNA]/(ε_a–ε_f) *versus* [DNA], K_b is given by the ratio of the slope to the intercept.

DNA cleavage studies. The DNA cleavage activity of the ruthenium(II) complexes was monitored by agarose gel electrophoresis on CT-DNA. Each reaction mixture contained 30 μM of CT-DNA, 30 and 60 μM of each complex in 50 mM Tris–HCl, (pH 7.1). The reaction was incubated at 37 °C for 2 h. After incubation, 1μL of loading buffer (0.25 % bromophenol blue, 0.25 % xylene cyanol and 60 % glycerol) was added to the reaction mixture and loaded onto a 1 % agarose gel containing 1.0 μg mL^{-1} of ethidium bromide (3,8-diamino-5-ethyl-6--phenylphenanthridinium bromide). The electrophoresis was performed for 2 h at 50 V in Tris–acetic acid–EDTA (ethylenediaminetetraacetic acid) buffer, pH 7.1. The bands were visualized under UV light and photographed.

RESULTS AND DISCUSSION

A new series of ruthenium(II) dihydroxybenzaldehyde Schiff base complexes were synthesized, stable in air at room temperature, non-hygroscopic in nature and soluble in common solvents such as dichloromethane, dimethylformamide and dimethyl sulphoxide. The analytical data (Table I) of the ligands and complexes are in good agreement with the calculated values, thus confirming the proposed molecular formulae (Scheme 2).

IR spectra

The IR spectra of the complexes, in comparison with those of the free ligands, display certain changes, which gives an indication about the mode of coordination and their structure. The significant IR spectral bands of the ligands and the complexes are listed in Table II. The free Schiff bases show a very strong absorption around 1636–1626 cm^{-1}, which is the characteristic of the azomethine (>C=N) group.[11] Coordination of the Schiff bases to the ruthenium ion through the azomethine nitrogen atom is expected to reduce the electron density in the azo

TABLE I. Physicochemical analysis data of the ligands and ruthenium(II) Schiff base complexes

Ligands and complexes	Empirical formula	Colour	Yield, %	M.p. °C	Found (Calcd.), %			
					C	H	N	S
L^1	$C_{14}H_{10}N_2O_2S$	Yellow	82	221	62.56 (62.21)	3.81 (3.73)	10.11 (10.36)	12.14 (11.86)
L^2	$C_{15}H_{12}N_2O_2S$	Yellow	78	212	63.42 (63.34)	4.48 (4.24)	9.44 (9.85)	11.49 (11.28)
L^3	$C_{13}H_{11}NO_3$	Orange	72	245	67.80 (68.11)	4.51 (4.84)	6.37 (6.11)	–
[RuCl(CO)(PPh_3)(L^1)] (**1**)	$C_{33}H_{24}ClN_2O_3PRuS$	Pink	66	285	56.62 (56.94)	4.03 (3.69)	4.28 (3.94)	4.73 (4.52)
[RuCl(CO)(PPh_3)(L^2)] (**2**)	$C_{34}H_{26}ClN_2O_3PRuS$	Pink	62	275	57.12 (57.50)	4.01 (4.15)	4.04 (4.17)	4.42 (4.55)
[Ru(CO)(PPh_3)$_2$(L^3)] (**3**)	$C_{51}H_{41}NO_4P_2Ru$	Green	61	293	68.12 (68.45)	4.51 (4.62)	1.05 (1.57)	–
[RuCl(CO)($AsPh_3$)(L^1)] (**4**)	$C_{33}H_{24}ClN_2O_3AsRuS$	Brown	68	267	53.21 (53.56)	3.70 (3.27)	4.02 (3.79)	4.54 (4.33)
[RuCl(CO)($AsPh_3$)(L^2)] (**5**)	$C_{34}H_{26}ClN_2O_3AsRuS$	Brown	64	271	53.40 (54.15)	3.01 (3.48)	3.92 (3.71)	4.30 (4.25)
[Ru(CO)($AsPh_3$)$_2$(L^3)] (**6**)	$C_{51}H_{41}NO_4As_2Ru$	Black	63	288	62.67 (62.33)	4.42 (4.20)	1.67 (1.43)	–

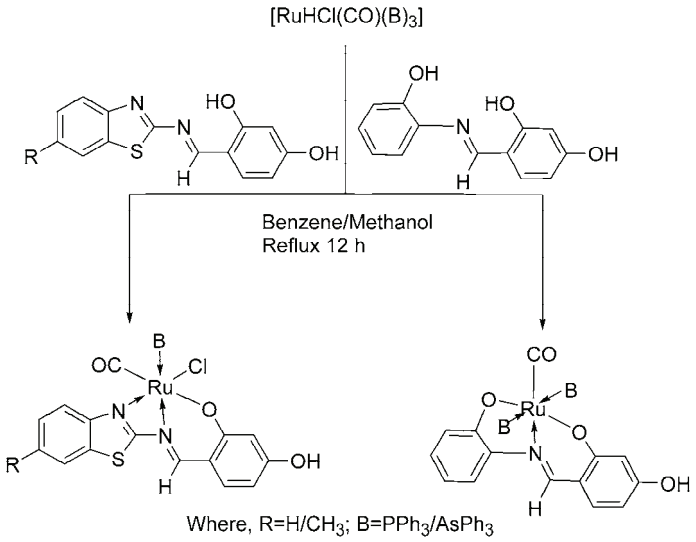

Scheme 2. Formation of the new ruthenium(II) Schiff base complexes.

methine link and thus lower the ν(C=N) absorption frequency. Hence these bands undergo shift to lower frequencies (1621–1594 cm^{-1}) after complexation, indicating coordination of the azomethine nitrogen to ruthenium.[12,13] The IR spectrum of the ligands revealed a medium intensity band at 1599–1598 cm^{-1}

(C=N) of the thiazole ring, which were shifted to lower frequencies (1586–1580 cm^{-1}) after complexation in the spectra of complexes **1**, **2**, **4** and **5**, which also indicated that the thiazole ring was affected upon coordination to the ruthenium metal ion.[14] The free ligands exhibit a broad band at 3426–3370 cm^{-1}, which may be assigned to the phenolic ν(OH) and this band was absent in the spectra of all the complexes, implying deprotonation of the Schiff bases prior to coordination. The hydroxy protons were displaced by the metal leading to higher ν(C–O) values (1285–1252 cm^{-1}) compared to those of the free ligands (1274–1242 cm^{-1}), suggesting that the other coordinating atom was the phenolic oxygen.[15] The binding of the metal to the ligand through nitrogen and oxygen atoms was further supported by the appearance of new bands in the 460–400 cm^{-1} and 540–510 cm^{-1} ranges due to ν(M–N) and ν(M–O),[16] respectively, in the spectra of all the complexes. A strong band for all the complexes in the region 1957–1931 cm^{-1} is due to terminally coordinated carbonyl groups. The ν(C–S–C) at 743 cm^{-1} of the thiazole ring remained unchanged, which demonstrated that the sulphur atom of the thiazole group does not coordinate to the ruthenium metal. In addition, the Schiff base complexes showed strong vibrations near 520, 695, 740 and 1430 cm^{-1}, which are attributed to the triphenylphosphine or triphenylarsine fragments.[17]

TABLE II. FT-IR and electronic spectral data for the ligands and ruthenium(II) Schiff base complexes

Ligands and complexes	FT-IR, ν / cm^{-1}					UV–Vis λ_{max} / nm
	C=N	Ph-OH	Ph-CO	C≡O	C=N thiazole	
L^1	1649	3390	1254	–	1598	309, 368, 416, 448
L^2	1626	3426	1242	–	1599	307, 368, 420, 442
L^3	1651	3370	1274	–	–	310, 366, 392, 435
[RuCl(CO)(PPh_3)(L^1)] (**1**)	1597	–	1285	1941	1573	308, 365, 421, 450, 486
[RuCl(CO)(PPh_3)(L^2)] (**2**)	1597	–	1258	1931	1575	308, 362, 425, 452, 481
[Ru(CO)(PPh_3)$_2$(L^3)] (**3**)	1611	–	1313	1943	–	308, 368, 420, 452, 480
[RuCl(CO)($AsPh_3$)(L^1)] (**4**)	1594	–	1284	1939	1568	306, 368, 416, 441, 481, 524
[RuCl(CO)($AsPh_3$)(L^2)] (**5**)	1594	–	1252	1957	1582	304, 363, 412, 442, 483, 521
[Ru(CO)($AsPh_3$)$_2$(L^3)] (**6**)	1621	–	1309	1943	–	307, 369, 420, 454

Electronic spectra

The electronic spectra of all the ligands and complexes in DMSO showed four to six bands in the 306–524 nm regions as given in Table II. The electronic spectra of all the free ligands showed two types of transitions, the first one appeared in the range 309–368 nm that could be assigned to π–π* transitions,

which were due to transitions involving molecular orbitals located on the phenolic chromophore. These peaks were shifted in the spectra of the complexes. This may be due to the donation of a lone pair of electrons by the oxygen of the phenoxy group to the central metal atom.[18] The second type of transitions appeared at the range 309–448 nm that could be assigned to n–π* transitions, which were due to transitions involving the molecular orbitals of the C=N chromophore. These bands were also shifted upon complexation, indicating that the imine group nitrogen atom could be coordinated to the metal ion.[19]

The ground state of ruthenium(II) in an octahedral environment is $^1A_{1g}$, arising from the t_{2g}^6 configuration. The excited state terms are $^3T_{1g}$, $^3T_{2g}$, $^1T_{1g}$ and $^1T_{2g}$. Hence four bands corresponding to the transition $^1A_{1g}\rightarrow{}^3T_{1g}$, $^1A_{1g}\rightarrow{}^3T_{2g}$, $^1A_{1g}\rightarrow{}^1T_{1g}$ and $^1A_{1g}\rightarrow{}^1T_{2g}$ in order of increasing energy are possible. The bands around 521–524 nm and 392–486 nm are assigned to $^1A_{1g}\rightarrow{}^1T_{1g}$ and charge transfer (CT) transitions, respectively.[12,20] The charge transfer bands observed in all the complexes due to M→L transitions are possible in the visible region. Moreover, the presences of carbonyl, triphenylphosphine/arsine and heterocyclic bases as ligands, which are capable of producing strong ligand field e_g^* levels place these levels relatively high in energy. Therefore, the lowest charge bands due to excitation of an electron from the metal t_{2g} level to an unfilled molecular orbital derived from the π* level of the ligands should appear in the relatively high energy region compared to those due to $t_{2g}\rightarrow e_g^*$ transitions.[20–22] The other high intensity bands in the region 306–369 nm region were assignable to ligand centred (LC) transitions and have been designated as π–π* and n–π* transition. The pattern of the electronic spectra of all the complexes indicated the presence of an octahedral environment around the ruthenium(II) ion, similar to that of other ruthenium(II) octahedral complexes.[23]

Mass spectra

The EI mass spectra of the ligands and complexes were recorded. The maximum peaks are observed at *m*/*z*, 284, 230, 696, 755 for the ligands L^2 and L^3 and for complexes [RuCl(CO)(PPh_3)(L^1)] and [RuCl(CO)($AsPh_3$)(L^2), respectively, which match well with the corresponding calculated masses.

NMR spectra

The ^{1}H-NMR spectra of ligands and complexes were recorded in DMSO-d_6 solution for confirming the binding mode of the Schiff base to ruthenium ion and the values are given in Table III and the spectra are shown in Figs. 1 and 2. The aromatic proton for the ligands appears as a multiplet at δ 6.24–8.03 ppm. On complexation, the protons on the phenyl ring remain more or less unchanged in the complexes, even if there are slight variation in their resonances due to the delocalization of electron density in the system,[24] and these signals in the com-

plexes cannot be distinguished from the aromatic signals of PPh_3/$AsPh_3$ due to their extensive overlap appearing at δ 6.22–8.24 ppm.[25] The protons of the hydroxyl groups appear as broad singlets at δ 11.64–11.98 (2-OH), δ 9.79–9.92 ppm (4-OH) and 14.27 ppm (Ph–OH) for the free Schiff base ligands. In the spectra of the complexes, the resonances arising from the hydroxyl (2-OH) and (Ph–OH) proton were not observed, indicating the coordination of the hydroxyl oxygens to the metal ion.[14] The signal due to the azomethine proton (–HC=N) was found to be considerably deshielded at δ 9.12–9.35 ppm relatively to that of the free Schiff base ligand δ 8.77–9.24 ppm as a consequence of electron donation to the metal centre. The methyl proton for L^2 and its complexes appeared as a singlet at δ 2.90–2.34 ppm.

TABLE III. ^{1}H-NMR data for the ligands and ruthenium(II) Schiff base complexes

Ligands and complexes	^{1}H-NMR data, δ / ppm
L^1	6.39–8.03 (*m*, Ar), 9.24 (*s*, HC=N), 11.98 (*s*, 2-OH), 9.92 (*s*, 4-OH)
L^2	6.20–7.65 (*m*, Ar), 9.07 (*s*, HC=N), 11.90 (*s*, 2-OH), 9.79 (*s*, 4-OH), 2.29 (*s*, CH_3)
L^3	6.24–7.43 (*m*, Ar), 8.77 (*s*, HC=N), 11.60 (*s*, 2-OH), 9.92 (*s*, 4-OH), 14.27 (*s*, OH)
[RuCl(CO)(PPh_3)L^1] (**1**)	7.15–7.67 (*m*, Ar), 9.32 (*s*, HC=N), 9.94 (*s*, 4-OH)
[RuCl(CO)(PPh_3)L^2] (**2**)	7.26–7.70 (*m*, Ar), 9.12 (*s*, HC=N), 9.84 (*s*, 4-OH), 2.34 (*s*, CH_3)
[Ru(CO)(PPh_3)$_2L^3$] (**3**)	6.62–8.23 (*m*, Ar), 9.14 (*s*, HC=N), 9.92 (*s*, 4-OH)
[RuCl(CO)($AsPh_3$)L^1] (**4**)	6.92–7.76 (*m*, Ar), 9.35 (*s*, HC=N), 10.14 (*s*, 4-OH),
[RuCl(CO)($AsPh_3$)L^2] (**5**)	6.26–7.83 (*m*, Ar), 9.32 (*s*, HC=N), 9.91 (*s*, 4-OH), 2.28 (*s*, CH_3)
[Ru(CO)($AsPh_3$)$_2L^3$] (**6**)	6.82–7.66 (*m*, Ar), 9.16 (*s*, HC=N), 9.85 (*s*, 4-OH)

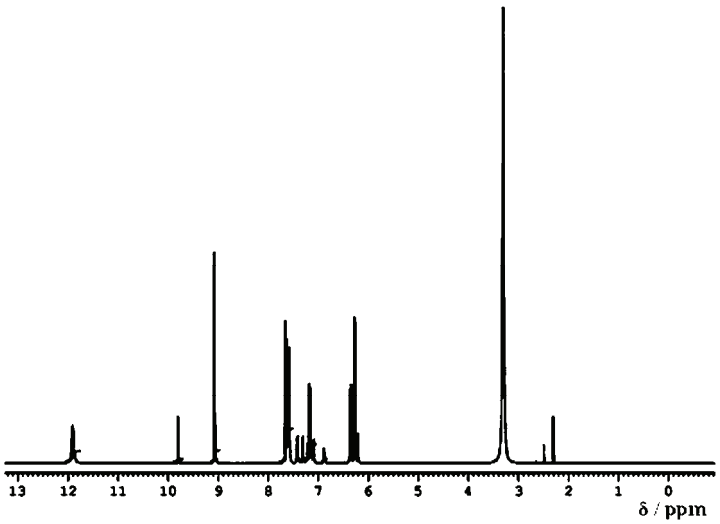

Fig.1. ^{1}H-NMR spectrum of ligand L^2.

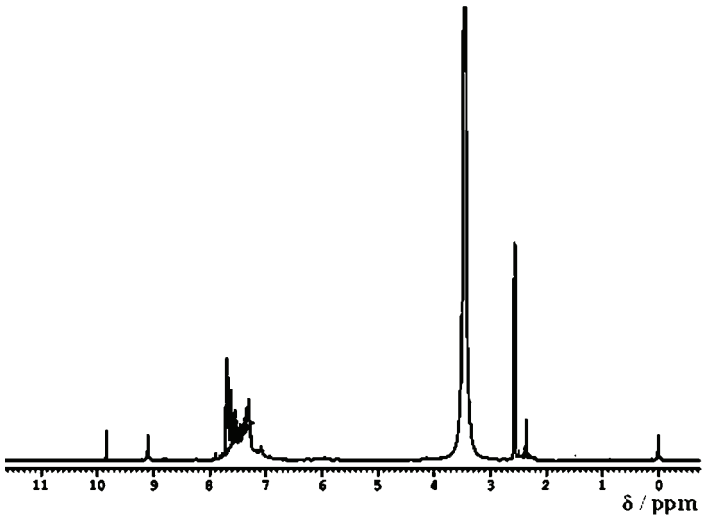

Fig. 2. ^{1}H-NMR spectrum of [RuCl(CO)(PPh_3)L^2].

The ^{13}C-NMR data were recorded in DMSO-d_6 solution and the assignments for the ligands and the complexes are listed in Table IV and a respective spectrum is shown in Fig. 3. The ^{13}C-NMR spectra of all the Schiff base ligands displayed a single resonance at δ 150–152 ppm,[26] showing that the azomethine carbon atoms were equivalent, which also confirms the structure of the ligands. The signal at δ 164–165 ppm corresponds to thiazolic C=N carbon.[27] The downfield shift of these two signals at δ 164–165 and 169–172 ppm clearly indicates that both the C=N carbons were affected by coordination.[28] The aromatic carbons of the free ligands and the corresponding complexes show signals in the region δ 102–139 ppm. The signal due to the methyl carbon of L^2 and the corresponding complexes appeared at δ 21–22 ppm. For all the complexes, the terminal carbonyl carbon appeared in the range δ 191–194 ppm.[29]

TABLE IV. ^{13}C-NMR data for the ligands and ruthenium(II) Schiff base complexes

Ligands and complexes	^{13}C-NMR data, δ / ppm
L^1	117–137 (Ar C), 152 (C=N), 164 (thiazole, C=N)
L^2	102–134 (Ar C), 151 (C=N), 165 (thiazole, C=N), 21 (CH_3)
L^3	107–134 (Ar C), 150 (C=N),
[RuCl(CO)(PPh_3)L^1] (**1**)	128–133 (Ar C), 164 (C=N), 170 (thiazole, C=N), 194 (C≡O)
[RuCl(CO)(PPh_3)L^2] (**2**)	122–134 (Ar C), 165 (C=N), 169 (thiazole, C=N), 191 (C≡O), 21 (CH_3)
[Ru(CO)(PPh_3)$_2L^3$] (**3**)	122–139 (Ar C), 165 (C=N), 191 (C≡O)
[RuCl(CO)($AsPh_3$)L^1] (**4**)	112–134 (Ar C), 165 (C=N), 172 (thiazole, C=N), 191 (C≡O)
[RuCl(CO)($AsPh_3$)L^2] (**5**)	127–133 (Ar C), 164 (C=N), 171 (thiazole, C=N), 192 (C≡O), 22 (CH_3)
[Ru(CO)($AsPh_3$)$_2L^3$] (**6**)	128–139 (Ar C), 164 (C=N), 193 (C≡O)

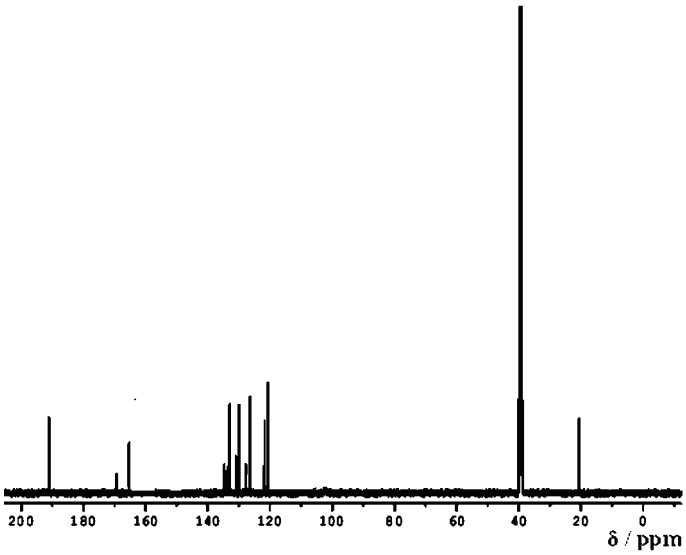

Fig. 3. ^{13}C-NMR spectrum of [RuCl(CO)(PPh_3)L^2].

In order to confirm the presence of triphenylphosphine groups and to determine the geometry of the complexes ^{31}P-NMR spectra were recorded. The ^{31}P--NMR spectra of the complexes [Ru(CO)Cl(PPh_3)L^1] and [Ru(CO)(PPh_3)$_2$L^3] were recorded in DMSO-d_6 solution. The observation of a sharp singlet at δ 28.2 and 32.2 ppm for the complexes [Ru(CO)Cl(PPh_3)L^1] and [Ru(CO)(PPh_3)$_2$L^3], respectively, confirmed the presence of only one triphenylphosphine group. The appearance of only one signal for [Ru(CO)(PPh_3)$_2$L^3] suggests that the two triphenylphosphine groups are magnetically equivalent and hence, they must be *trans* to each other in the complex.

DNA binding study

The interactions of metal complexes with DNA are of interest for the development of effective chemotherapeutic agents. Transition metal centres are particularly attractive moieties for such research since they exhibit well-defined coordination geometries and often possess distinctive electrochemical or photophysical properties, thus enhancing the functionality of the binding agent.[2] Electronic absorption spectroscopy is one of the most useful techniques for DNA-binding studies of metal complexes. The interactions of the ruthenium complexes with CT-DNA were investigated by UV–Vis absorption titrations. The binding of the ruthenium(II) complexes to DNA helices were characterized by following the changes in the absorbance and shift in wavelength on each addition of DNA solution to the complex. Upon addition of increasing amounts of CT-DNA from 0 to 25 μM, a significant “hyperchromic” effect of the intraligand bands at 252–

–323 nm was observed accompanied by a moderate red shift of 2–3 nm, indicative of the breakage of the DNA helix. However, there were no appreciable wavelength shifts in the charge transfer band. These spectral characteristics suggest that the complexes and ligand bind either to the external contact (electrostatic binding) or to the major and minor grooves of DNA. As the concentration of the DNA was increased, the absorption bands of the [RuCl(CO)(PPh_3)L^2] complex initially showed hyperchromism but on further increasing, hypochromism with a blue shift of 5 nm was observed. An isosbestic point was observed at 295 nm. This behaviour reveals an electrostatic association of the complex with the helix surface.[30,31] Generally, hypochromism and hyperchromism are the two spectral features which are closely connected with the double helix structure of DNA. The observation of hypochromism is indicative of intercalative mode of binding of DNA to the complexes along with the stabilization of the DNA double helix structure.[32] On the other hand, the observation of hyperchromism is indicative of breakage of the secondary structure of DNA.[33] The binding constant of the complex [RuCl(CO)(PPh_3)L^2] could not be evaluated due to the random changes in the absorption on the addition of DNA. Hence, the observation of hyperchromism with a red shift for the ligand and complexes showed that they interact with the secondary structure of CT-DNA by breaking its double helix structure.

In order to compare the DNA-binding affinity of the ruthenium(II) complexes quantitatively, their intrinsic binding constants were calculated by monitoring the changes in absorption of the higher energy band with increasing concentration of DNA(Eq. (1) and Fig. 4). The intrinsic binding constants K_b were calculated and were found to be (1.6–8.6)×10^4 mol^{-1} dm^3, for the ruthenium(II) complexes (Fig. 4 and Table V). The magnitude of the binding constant clearly showed that complex [Ru(CO)(PPh_3)$_2$(L^3)] bound more strongly with CT-DNA than the other complexes. The significant difference in DNA-binding affinity of the ruthenium(II) complexes may be a result of the fact that complex with different co-ligands shows different binding affinity with DNA. Interestingly, the K_b values obtained for the above ruthenium(II) complexes are comparable with those for another known complex [Ru(dmp)$_2$(APIP)]$^{2+}$, APIP = 2-(2-aminophenyl)-1*H*-imidazo[4,5-*f*][1,10]phenanthroline, (2.3–3.3)×10^4 mol^{-1} dm^3.[34]

DNA cleavage activity

To assess the DNA cleavage ability of the new ruthenium(II) complexes, calf thymus DNA was incubated with two different concentrations of the complexes in 5 mM Tris–HCl/50 mM NaCl buffer at pH 7.2 for 2 h without the addition of a reductant. Upon gel electrophoresis of the reaction mixture, concentration-dependent DNA cleavage was observed. When the concentration of

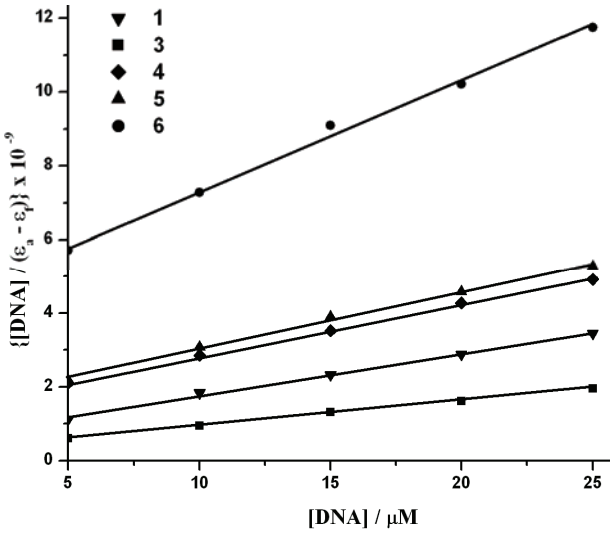

Fig. 4. Plots of [DNA]/(ε_a–ε_f) *versus* [DNA] for the titration of the prepared compounds with CT-DNA.

TABLE V. Binding constant value for interaction of the ruthenium(II) complexes with CT-DNA

Complex	$K_b \times 10^4$ / mol^{-1} dm^3
[RuCl(CO)(PPh_3)(L^1)] (**1**)	8.2
[RuCl(CO)(PPh_3)(L^2)] (**2**)	–
[Ru(CO)(PPh_3)$_2$(L^3)] (**3**)	8.6
[RuCl(CO)($AsPh_3$)(L^1)] (**4**)	5.6
[RuCl(CO)($AsPh_3$)(L^2)] (**5**)	3.3
[Ru(CO)($AsPh_3$)$_2$(L^3)] (**6**)	1.6

the complexes **1**–**6** was increased from 30 to 60 μM, the production of Form II of DNA increased, (Fig. 5 for complexes **1**–**3**, and Fig. 6 for complexes **4**–**6**). No DNA cleavage was observed for the control in which metal complex was absent (Fig. 5, lane 1, and Fig 6, lane 8). With increasing concentration of the ruthenium(II) complexes (Fig. 5, lanes 2 and 3 for complex **1**; lanes 4 and 5 for complex **2**; lanes 6 and 7 for complex **3** and Fig. 6, lanes 9 and 10 for complex **4**; lanes 11 and 12 for complex **5**; lanes 13 and 14 for complex **6**) the amount of Form I of CT-DNA diminished gradually and the amount of the nicked circular DNA (Form II) increased remarkably. When the concentration was increased to 60 μM for all the complexes, the DNA was completely converted from Form I to Form II, showing the potential chemical nuclease activity of the complexes. Moreover, complex [RuCl(CO)(PPh_3)(L^1)] (**1**) exhibited greater cleavage efficiency than other complexes, which could be attributed to the longer metal-to-ligand charge transfer (MLCT) excited state lifetime of [RuCl(CO)(PPh_3)(L^1)].

Fig. 5. Gel electrophoresis showing the chemical nuclease activity of CT-DNA incubated at 37 °C for 2 h with different concentrations of complexes **1**–**3**; lane 1, DNA control; lane 2, DNA + complex **1** (30 μM); lane 3, DNA + complex **1** (60 μM); lane 4, DNA + complex **2** (30 μM); lane 5, DNA + complex **2** (60 μM); lane 6, DNA + complex **3** (30 μM); lane 7, DNA + complex **3** (60 μM).

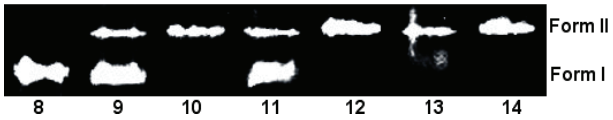

Fig. 6. Gel electrophoresis showing the chemical nuclease activity of the CT-DNA incubated at 37 °C for 2 h with different concentrations of complexes **4**–**6**; lane 8, DNA control; lane 9, DNA + complex **4** (30 μM); lane 10, DNA + complex **4** (60 μM); lane 11, DNA + complex **5** (30 μM); lane 12, DNA + complex **5** (60 μM); lane13, DNA + complex **6** (30 μM); lane 14, DNA + complex **6** (60 μM).

CONCLUSION

Three novel Schiff base ligands and their ruthenium(II) complexes were designed, synthesized and characterized by elemental analyses, stoichiometric and spectroscopic studies. Based on the characterization, an octahedral geometry was tentatively proposed for all the new ruthenium(II) complexes. Furthermore, *in vitro* DNA binding studies were performed for complexes **1**–**6** using the absorption titration technique. These complexes are unique and act synergistically at the molecular level but with different binding modes. This study revealed that the complexes bind electrostatically to the DNA double helix surface. The binding constants were found to be $(1.6–8.6)\times10^4$ mol^{-1} dm^3 for complexes **1** and **3**–**6**. Interestingly, the K_b values obtained for the above ruthenium(II) complexes were comparable to those for other known $[Ru(dmp)_2(APIP)]^{2+}$ complexes (APIP = 2-(2-aminophenyl)-1*H*-imidazo[4,5-*f*][1,10]phenanthroline), $(2.3–3.3)\times10^4$ mol^{-1} dm^3. From the values of the binding constant, it was inferred that the triphenylphosphine complexes bind more with CT-DNA than the corresponding triphenylarsine complexes. The DNA cleavage study revealed that all ruthenium complexes had the ability to cleave nucleic acids and the extent of the cleavage was found to be dose dependent. The information obtained in this study could be helpful in the understanding of the mechanism of interactions of ruthenium(II) complexes with nucleic acids and should be useful in the development of potential probes for investigation of the structure and conformation of DNA, or new therapeutic agents for some diseases.

Acknowledgement. We sincerely thank the University Grants Commission (UGC), New Delhi, India, for financial support (MRP Scheme, No. 38-222/2009 (SR)).

ИЗВОД

СИНТЕЗА И СПЕКТРАЛНА КАРАКТЕРИЗАЦИЈА КОМПЛЕКСА РУТЕНИЈУМА(II) СА ШИФОВИМ БАЗАМА КОЈИ САДРЖЕ PPh_3/$AsPh_3$ ЛИГАНДЕ И ИСПИТИВАЊЕ ЊИХОВИХ ИНТЕРАКЦИЈА СА ДНК

SUBBAIYAN SATHIYARAJ, GANESAN AYYANNAN и CHINNASAMY JAYABALAKRISHNAN

Post Graduate and Research Department of Chemistry, Sri Ramakrishna Mission Vidyalaya College of Arts and Science, Coimbatore - 641 020, Tamil Nadu, India

У овом раду су синтетизоване Шифове базе полазећи од дихидроксибензалдехида (L^1–L^3), као и одговарајући рутенијум(II) комплекси. Сва једињења су окарактерисана применом елементалне микроанализе, ^{1}H-, ^{13}C- и ^{31}P-NMR, и IR спектроскопије, UV–Vis спектрофотометрије и масене спектрометрије. Применом UV–Vis спектрофотометрије испитиване су интеракције комплекса рутенијума(II) и ДНК. На основу добијених резултата, закључено је да се сви комплекси електростатички везују за ДНК, при чему су одговарајуће константе везивања (K_b) у опсегу $(1{,}6–8{,}6)\times10^4$ mol^{-1} dm^3. Додатно је испитивано раскидање веза у молекулу ДНК помоћу комплекса рутенијума(II).

(Примљено 1. децембра 2012, ревидирано 8. маја 2013)

REFERENCES

1. M. Navarro, E. J. Cisneros-Fajardo, A. Sierralta, M. Fernández-Mestre, P. Silva, D. Arrieche, E. Marchán, *J. Biol. Inorg. Chem.* **4** (2003) 401
2. C. Metcalfe, J. A. Thomas, *Chem. Soc. Rev.* **32** (2003) 215
3. S. Arturo, B. Giampaolo, R. Giuseppe, L. G. Maria, T. J. Salvatore, *J. Inorg. Biochem.* **98** (2004) 589
4. L. R. Kelland, *Eur. J. Cancer* **41** (2005) 971
5. S. Rekha, K. R. Nagasundara, *Indian J. Chem., A* **45** (2006) 2421
6. M. A. Fuertes, C. Alonso, J. M. Perez, *Chem. Rev.* **103** (2003) 645
7. C. P. Tan, S. Hu, J. Liu, L. N. Ji. *Eur. J. Med. Chem.* **46** 1555 (2011)
8. K. Natarajan, U. Agarwala, *Inorg. Nucl. Chem. Lett.* **14 (**1978) 7
9. R. A. Sanchez-Delgado, W. Y. Lee, S. R. Choi, Y. Cho, M. J. Jun, *Transition Met. Chem.* **16** (1991) 241
10. A. Wolf, G. H. Shimer, T. Meehan, *Biochemistry* **26** (1987) 6392
11. K. Naresh Kumar, R. Ramesh, *Spectrochim. Acta, A* **60** (2004) 2913
12. R. Ramesh, M. Sivagamasundari, *Synth. React. Inorg. Met-Org. Chem.* **33** (2003) 899
13. S. N. Pal, S. Pal, *J. Chem. Soc., Dalton Trans.* (2002) 2102
14. A. E. M. Ouf, M. S. Ali, M. S. Soliman, A. M. El-Defrawy, S. I. Mostafa, *J. Korean Chem. Soc.* (2010) 54
15. R. C. Maurya, P. Patel, S. Rajput, *Synth. React. Inorg. Met-Org. Chem.* **23** (2003) 817
16. K. Nakamoto, *Infrared and Raman spectra of Inorganic and Coordination compounds*, Wiley Interscience, New York, 1971
17. A. K. Das, S. M. Peng, S. Bhattacharya, *J. Chem. Soc. Jpn.* **49** (1976) 287
18. R. K. Sharma, R. V. Singh, J. P. Tandon, *J. Inorg. Nucl. Chem.* **42** (1980) 1382
19. M. J. M. Cambell, *Coord. Chem. Rev.* **15** (1975) 279
20. K. Natarajan, R. K. Poddar, C. Agarwala, *J. Inorg. Nucl. Chem.* **39** (1977) 431
21. A. B. P. Lever, *Inorganic Electronic Spectroscopy*, 2nd ed., Elsevier, New York, 1984

22. K. Chichak, U. Jacquenard, N. R. Branda, *Eur. J. Inorg. Chem*. (2002) 357
23. P. Sengupta, R. Dinda, S. Ghosh, *Transition Met. Chem.* **27** (2002) 665
24. M. Maji, S. Ghosh, S. K. Chattopaghyay, T. C. W. Mak, *Inorg. Chem.* **36** (1997) 2938
25. R. V. Singh, S. C. Joshi, A. Gajraj, P. Nagpal, *Appl. Organomet. Chem.* **16** (2002) 713
26. J. T. Desai, C. K. Desai, K. R. Desai, *J. Iran. Chem. Soc.* **5** (2008) 67
27. S. Pérez, C. López, A. Caubet, X. Solans, M. Font-Bardía, M. Gich, E. Molins, *J. Organomet. Chem*. **692** (2007) 2402
28. K. Shankera, R. Rohinia, V. Ravindera, P. M. Reddy, Y.-P. Ho, *Spectrochim. Acta, A* **73** (2009) 205
29. M. H. Desbosis, D. Astruc, *Organometallics* **8** (1989) 1841
30. D. Herebian, W. S. Sheldrick, *J. Chem. Soc., Dalton Trans.* (2002) 966
31. M. Asadi, E. Safaei, B. Ranjbar, L. Hasani, *New J. Chem.* **28** (2004) 1227
32. E. C. Long, J. K. Barton, *Acc. Chem. Res*. **23** (1990) 271
33. N. Chitrapriya, V. Mahalingam, M. Zeller, K. Natarajan, *Inorg. Chim. Acta* **363** (2010) 3685
34. Z. H. Liang, Z. Z. Li, H. L. Huang, Y. J. Liu. *J. Coord. Chem*. **64** (2011) 3342.

Journal of the Serbian Chemical Society
JSCS-info@shd.org.rs • www.shd.org.rs/JSCS
J. Serb. Chem. Soc. 79 (2) 167–173 (2014)
JSCS–4573
UDC 546.11'116'17:546.11'17'46:
544.022:519.216
Original scientific paper

Theoretical prediction on the structures of the $HMgN^-$ and $HNMg^-$ using multiconfigurational methods

CUI-PING XIAO, WEN-ZUO LI*, QING-ZHONG LI and JIAN-BO CHENG

The Laboratory of Theoretical and Computational Chemistry, College of Chemistry and Chemical Engineering , Yantai University, Yantai 264005, China

(Received 12 April, revised 23 April 2013)

Abstract: The nine-valence-electron $HMgN^-$ and $HNMg^-$ have been investigated for the first time theoretically using complete active space self-consistent field (CASSCF) and multiconfiguration second-order perturbation theory (CASPT2) methods in conjunction with the contracted atomic natural orbital (ANO) basis sets. The structures of the low-lying electronic states of $HMgN^-$ and $HNMg^-$ were predicted. The possible unimolecular conversions between $HMgN^-$ and $HNMg^-$ were discussed. The calculated results indicated that the ground-state of $HMgN^-$ is linear, while the ground-state $HNMg^-$ is bent, which is in contradiction to the Walsh rules, which predict linear structures for HXY systems containing 10 or fewer valence electrons.

Keywords: $HMgN^-$; $HNMg^-$; complete active space self-consistent field; multiconfiguration second-order perturbation theory.

INTRODUCTION

One of the predictions of the Walsh rules is that molecules of the class HXY containing 10 or fewer valence electrons should be linear in their ground electronic states.[1] However, some ten-valence-electron HXY systems,[2] such as HSB, HSAl, HOAl, and HOB, and some nine-valence-electron systems, such as HSB^+,[3] $HSAl^+$,[4] HPB,[5] and HNAl[6] have been predicted to be bent in their ground states using theoretical calculations.

$HMgN^-$ and its tautomer $HNMg^-$ are iso-electronic species with HMgO, HOMg, HAlN and HNAl, which all have nine valence electrons. The high-level *ab initio* theoretical calculations indicated that the ground states of HMgO,[7] HOMg[7] and HAlN[6] are linear, which obey the Walsh rules. However, the ground state of HNAl[6] is bent, which is in contradiction to the Walsh rules. $HMgN^-$ and $HNMg^-$have not hitherto been studied by any experimental and theoretical works. What are the structures of the $HMgN^-$ and $HNMg^-$? Are their ground

* Corresponding author. E-mail: liwenzuo2004@126.com
doi: 10.2298/JSC130412044X

states linear or bent? Do the two anions obey the Walsh rules or not? What are the unimolecular conversions between the low-lying states of two anions? All of the above questions inspired the present large-scale theoretical studies on $HMgN^-$ and $HNMg^-$. In the present paper, calculated results are reported, which include the geometries, energies and the frequencies of the low-lying states of $HMgN^-$ and $HNMg^-$, and the potential energy curves (PECs) for the isomerization reactions between the two anions.

COMPUTATIONAL DETAILS

The low-lying states of $HMgN^-$ and $HNMg^-$ were calculated using the complete active space self-consistent field (CASSCF)[8] and the multiconfiguration second-order perturbation theory (CASPT2)[9,10] methods. The CASSCF and CASPT2 calculations were performed using MOLCAS 7.4 quantum chemistry software.[11] In the CASSCF and CASPT2 calculations, the atomic natural orbital basis setswere used:[12-14] [3s2p1d] for H, [5s3p2d1f] for N and [6s4p3d1f] for Mg, denoted as ANO. All stationary points along the potential energy surfaces (PESs) of the $HMgN^-$ and $HNMg^-$ isomerization reactions were optimized at the CASSCF/ /ANO level. To confirm the stationary points as minima or transition states, the vibrational frequencies of all stationary points were calculated at the same level. The CASPT2/ANO energies were calculated at the respective CASSCF/ANO optimized geometries. Nevertheless, for the method of CASSCF does not contain dynamic electron correlation, the CASSCF optimized geometries might not be sufficiently accurate. Therefore, CASPT2/ANO geometry optimization calculations on all stationary points were also performed. The potential energy curves (PECs) for the isomerization reaction between $HMgN^-$ and $HNMg^-$ were computed as functions of the HMgN bond angle at the CASPT2/ANO level. In the point-wise calculations of the surfaces, the HMgN bond angle (denoted as θ, ranging from 0 to 180°) was fixed and other geometric parameters were optimized at the CASSCF/ANO level. In the CASSCF calculation, full-valence space was selected as the active space: nine electrons were active and the active space included nine orbitals [CASSCF (9,9)]. For the linear isomers, the calculations were performed in the C_{2v} subgroup of $C_{\infty v}$, where Σ^+ corresponds to the A_1 irreducible representation, Σ^- to A_2, and Π to $B_1 + B_2$. Labeling the orbital within the C_{2v} point group in the order of a_1, a_2, b_2 and b_1, the active space was identified as (5022). Labeling the orbitals within the C_s point group (in the calculation for the PECs) in the order a' and a'', the active space was identified as (72).

Throughout this article, CASSCF/ANO is referred to as CAS and CASPT2/ANO// //CASSCF/ANO as CASPT2.

RESULTS AND DISCUSSIONS

The CAS optimized geometries and the CASPT2 energies of all stationary points along the $HMgN^- \leftrightarrow HNMg^-$ PECs are listed in Table I. The CASSCF/ /ANO calculated frequencies are listed in Table II. The CASPT2 PECs calculated as functions of the HMgN bond angle for the $HMgN^- \leftrightarrow HNMg^-$ system are shown in Fig. 1.

TABLE I. CAS optimized geometries and CASPT2 relative energies for all stationary points of the $1^2A'$, $1^2A''$ and $2^2A'$ surfaces of the $HMgN^- \leftrightarrow HNMg^-$ system; data in brackets were calculated using the CASPT2 [c] method (CASPT2/ANO optimized geometries and CASPT2/ /ANO//CASPT2/ANO energies

Stationary point	R_{Mg-N} / Å	R_{H-Mg} / Å	R_{H-N} / Å	∠HMgN / °	ΔE^a / kcal* mol^{-1}
$HNMg^-$ ($X^2\Sigma^+$)	1.821 [1.816]	–	1.016 [1.013]	0.0	0.00 [0.00]
M1 ($1^2A'$)	1.892 [1.903]	–	1.032 [1.029]	19.2 [19.7]	–1.25 [–1.26]
TS1 ($1^2A'$)	1.944 [1.912]	1.807 [1.797]	–	69.9 [67.1]	65.59 [67.43]
$HMgN^-$ ($X^2\Pi$)	1.957 [1.955]	1.785 [1.779]	–	180.0	41.40 [41.41]
$HNMg^-$ ($A^2\Pi$)	2.000 [1. 990]	–	1.024 [1.022]	0.0	2.81 [2.81]
M2 ($1^2A''$)	2.048 [2.038]	–	1.031 [1.030]	15.7 [16.5]	2.46 [2.45]
TS2 ($1^2A''$)	2.052 [2.024]	1.859 [1.824]	1.982 [1.992]	60.7 [62.1]	64.26 [64.16]
TS3($2^2A'$)	1.962 [1.892]	1.750 [1.755]	–	89.4 [92.5]	88.19 [89.56]
$HMgN^-$ ($A^2\Sigma^+$)	1.845 [1.838]	1.751 [1.740]	–	180.0	52.12 [52.11]

[a]Relative energy to the $X^2\Sigma^+$ state of $HNMg^-$

TABLE II. The CASSCF/ANO calculated frequencies (in cm^{-1}) of the stationary points

Stationary point	ν(H–Mg)[a]	ν(H–N)[a]	ν (Mg–N)[a]	ν(HMgN/HNMg)[b]
$HNMg^-$ ($X^2\Sigma^+$)	–	3546	798	93i
M1 ($1^2A'$)	–	3515	646	97
TS1 ($1^2A'$)	1335	–	613	1693i
$HMgN^-$ ($X^2\Pi$)	1409	–	638	300
$HNMg^-$ ($A^2\Pi$)	–	3441	522	176i
M2 ($1^2A''$)	–	3358	503	294
TS2 ($1^2A''$)	1156	–	518	1254i
TS3($2^2A'$)	1237	–	580	1469i
$HMgN^-$ ($A^2\Sigma^+$)	1504	–	742	452

[a]Stretching vibration; [b]bending vibration

Geometries for stationary points

Based on the CASPT2 calculations, it is predicted that the ground and first excited states of the linear structure of $HMgN^-$ are the $X^2\Pi$ and $A^2\Sigma^+$ states, respectively. At the CASPT2 level, the $A^2\Sigma^+$ state is about 10.72 kcal mol^{-1} higher in energy than the $X^2\Pi$ state. The CAS frequency calculations indicated that the $X^2\Pi$ and $A^2\Sigma^+$ states of $HMgN^-$ have no imaginary frequency and there should be minima on the PESs.

The CASPT2 calculations indicated that the energy of the $A^2\Pi$ state for the linear $HNMg^-$ is about 2.81 kcal mol^{-1} higher than the $X^2\Sigma^+$ state. Therefore, the ground and first excited states of the linear $HNMg^-$ were predicted to be the $X^2\Sigma^+$ and $A^2\Pi$ states. However, the CAS frequency calculations showed the $X^2\Sigma^+$ and $A^2\Pi$ states both have a unique imaginary frequency. Therefore, the $X^2\Sigma^+$ and $A^2\Pi$ states of the linear $HNMg^-$ should be first-order saddle points. In other words, the ground-state $HNMg^-$ should not be linear.

* 1 kcal = 4.184 kJ

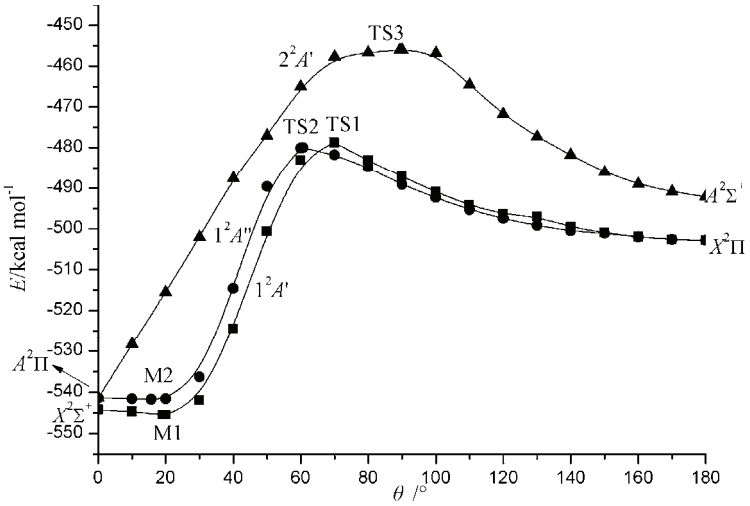

Fig. 1. The CASPT2/ANO potential energy curves as functions of HMgN angle (θ) for the $HMgN^- \leftrightarrow HNMg^-$ system calculated at the CASSCF/ANO partly optimized geometries.

There is a bent equilibrium conformation M1 on the $1^2A'$ potential energy surface (see Fig. 1). The energy of M1 is about 1.25 kcal mol^{-1} lower than the $X^2\Sigma^+$ state of $HNMg^-$ and about 42.65 kcal mol^{-1} lower than the $X^2\Pi$ state of $HMgN^-$ at the CASPT2 level (see Table I). The CAS frequency calculation indicated that M1 has no imaginary frequency (see Table II). Therefore, M1 is a global minimum and the $X^2\Sigma^+$ state of $HNMg^-$ should be the transition state of the isomerization reactions of M1 ↔ M1. At the CAS level, the Mg–N and H–N bond lengths of M1 are 1.892 and 1.032 Å, respectively, and the HMgN bond angle is 19.2° (the HNMg bond angle is about 123.7°).

There is a bent equilibrium conformation M2 on the $1^2A''$ potential energy surface (see Fig. 1). The energy of M2 is about 0.35 kcal mol^{-1} lower than the $A^2\Pi$ state of $HNMg^-$ and about 38.94 kcal mol^{-1} lower than the $X^2\Pi$ state of $HMgN^-$ at the CASPT2 level (see Table I). The CAS frequency calculation indicated that M2 has no imaginary frequency (see Table II). Therefore, the M2 is also a global minimum and the $A^2\Pi$ state of $HNMg^-$ should be the transition state of the isomerization reactions of M2↔M2. At the CAS level, the Mg–N and H–N bond lengths of M2 are 2.048 and 1.031 Å, respectively, and the HMgN bond angle is 15.7° (the HNMg bond angle is about 131.8°).

There are three bent transition states TS1, TS2, and TS3 along the PECs at the CAS geometry optimization level (see Fig. 1). They are all in C_s symmetry and in A', A'' and A' states, respectively. The CAS calculations indicated that they have a unique imaginary frequency. The CAS calculated HMgN bond angles of TS1, TS2 and TS3 are 69.9, 60.7 and 89.4°, respectively. In the next section, "Potential energy curves", it will be shown that the three transition states should

be the transition states for the three different PECs of the isomerization reactions of $HMgN^- \leftrightarrow HNMg^-$.

CASPT2/ANO geometry optimization calculations were also performed on all the stationary points (see Table I). The results showed that the CASPT2 optimized geometries of the stationary points are different from the CASSCF optimized geometries though the CASPT2//CASPT2 and CASPT2//CASSCF calculated relative energies are almost equal. The difference in the optimized bond lengths between the two methods is not larger than 0.07 Å and the difference in the bond angles is not larger than 3.1°. This is due to the absence of a dynamic electron correlation with the CASSCF method. The CASSCF calculated frequency results, which give the theoretical evidence for future analysis of the infrared spectrum of $HMgN^-$ and $HNMg^-$, are listed in Table II.

Potential energy curves

It was found that there are three surfaces ($1^2A'$, $1^2A''$ and $2^2A'$) on the isomerization reaction of the $HMgN^- \leftrightarrow HNMg^-$ system. From Fig. 1, it can be seen that the shape of the $1^2A'$ curve is the same as that of the $1^2A''$ curve, *i.e.*, there is one minimum and one saddle point connecting the two linear structures. Along the $1^2A'$ curve, M1 connects with the $X^2\Pi$ state of $HMgN^-$ *via* the transition state TS1. The $X^2\Sigma^+$ state of $HNMg^-$ should be the transition state between the two same M1 structures. Along the $1^2A''$ curve, M2 connects with the $X^2\Pi$ state of $HMgN^-$ *via* the transition state TS2. The $A^2\Pi$ state of $HNMg^-$ should be the transition state between the two same M2 structures. On the $2^2A'$ curve, the $A^2\Pi$ state of $HNMg^-$ connects with the $A^2\Sigma^+$ state of $HMgN^-$ *via* the transition state TS3.

Based on the CASPT2 calculations, M1 is the mot stable conformation among all the stationary points; therefore, it is the global minimum. According to the CASPT2 calculated relative energies listed in Table I, the energy barrier for isomerization from M1 to the $X^2\Pi$ state of $HMgN^-$ on the $1^2A'$ curve is 66.84 kcal mol^{-1}, whereas the energy barrier in the reverse order is 24.19 kcal mol^{-1}. The CASPT2 energy barrier for isomerization from M1 to M1 is 1.25 kcal mol^{-1}.

Along the $1^2A''$ curve, the CASPT2 calculated energy barrier for isomerization from M2 to the $X^2\Pi$ state of $HMgN^-$ is 61.80 kcal mol^{-1}, whereas the energy barrier in the reverse order is 22.86 kcal mol^{-1}. The CASPT2 energy barrier for isomerization from M2 to M2 is 0.35 kcal mol^{-1}.

Along the $2^2A'$ curve, the CASPT2 calculated energy barrier for isomerization from the $A^2\Pi$ state of $HNMg^-$ to the $A^2\Sigma^+$ state of $HMgN^-$ is 85.38 kcal mol^{-1}, whereas the energy barrier in the reverse order is 36.07 kcal mol^{-1}. Therefore, the isomerization of the $A^2\Sigma^+$ state of $HMgN^-$ to the $A^2\Pi$ state of $HNMg^-$ is easier than in the reverse order.

As shown in Fig. 1 for the $HMgN^- \leftrightarrow HNMg^-$ system, $1^2A'$ and $1^2A''$ are the two components of the Renner-splitting of the $X^2\Pi$ state of $HMgN^-$, and $1^2A''$

and $2^2A'$ are the two components of the Renner-splitting of the $A^2\Pi$ state of $HNMg^-$. The Renner-splitting pattern for the $X^2\Pi$ state of $HMgN^-$ is pattern (a) of the Pople and Longuet–Higgins Scheme,[15] and the Renner-splitting pattern for the $A^2\Pi$ state of $HNMg^-$ is pattern (b) of the Pople and Longuet–Higgins Scheme.[15]

CONCLUSIONS

$HMgN^-$ and $HNMg^-$ were studied for the first time by large-scale theoretical calculations using the CASSCF and CASPT2 methods in conjunction with the contracted atomic natural orbital (ANO) basis sets. The possible unimolecular conversions between $HMgN^-$ and $HNMg^-$ were discussed.

The geometries of all stationary points along the potential energy surfaces were optimized at the CASSCF/ANO level. The CASPT2/ANO potential energy curves of the isomerization reactions were calculated as functions of the HMgN bond angle. The CASPT2 calculations indicated that the ground and the first excited states of the linear $HMgN^-$ are the $X^2\Pi$ and $A^2\Sigma^+$ states, respectively; the ground and the first excited states of the linear $HNMg^-$ are the $X^2\Sigma^+$ and $A^2\Pi$ states, respectively. The $X^2\Sigma^+$ and $A^2\Pi$ states of $HNMg^-$ are first-order saddle points because they have a unique imaginary frequency. Two bent structures M1 and M2 were found along the $1^2A'$ and $1^2A''$ curves respectively. In addition, M1 and M2 are two global minima. The $X^2\Sigma^+$ state of $HNMg^-$ should be the transition state of the isomerazation reactions for M1 ↔ M1 and the $A^2\Pi$ state of $HNMg^-$ should be the transition state of the isomerazation reactions for M2 ↔ M2. Based on the calculated results, it was concluded that the ground-state of $HMgN^-$ is linear, while $HNMg^-$ is strongly bent in the ground state, which is in contradiction to the Walsh rules that predict linear structures for HXY systems containing 10 or less valency electrons.

Acknowledgements. This research was supported by the National Natural Science Foundation Committee of China (No. 21103145), the Natural Science Foundation of Shandong Province (No. ZR2009BQ006) and the Fund for Doctor of Yantai University (No. HY05B30). Professor Cheng acknowledges support by the Open Project of State Key Laboratory of Supramolecular Structure and Materials (sklssm201418), Jilin University.

ИЗВОД

ТЕОРЕТСКО ПРЕДВИЂАЊЕ СТРУКТУРЕ $HMgN^-$ И $HNMg^-$ МУЛТИКОНФИГУРАЦИЈСКИМ МЕТОДАМА

CUI-PING XIAO, WEN-ZUO LI, QING-ZHONG LI и JIAN-BO CHENG

The Laboratory of Theoretical and Computational Chemistry, College of Chemistry and Chemical Engineering, Yantai University, Yantai 264005, China

$HMgN^-$ и $HNMg^-$ са девет валентних електрона испитивани су по први пут теоретски, применом метода CASSCF і CASPT2 повезаним са ANO базичним сетом. Одређене су структуре најнижих електронских стања за $HMgN^-$ и $HNMg^-$. Разматрана је могућност унимолекулске конверзије $HMgN^-$ и $HNMg^-$. Резултати израчунавања указују на то да је

основно стање $HMgN^-$ линеарно док је $HNMg^-$ савијен, што је супротно Walsh правилима која предвиђају да су сви HXY системи са 10 или мање валентних електрона линеарни.

(Примљено 12. априла, ревидирано 23. априла 2013)

REFERENCES

1. A. D. Walsh, *J. Chem. Soc.* (1953) 2288
2. E. R. Talaty, Y. Huang, M. E. Zler, *J. Am. Chem. Soc.* **113** (1991) 779
3. W.-Z. Li, Y.-W. Pei, H.-J. Zhu, J.-B. Cheng, Q.-Z. Li, *Mol. Phys.* **109** (2011) 2671
4. W.-Z. Li, Y.-W. Pei, F.-F. Geng, J.-B. Cheng, Q.-Z. Li, B.-A. Gong, *Int. J. Quantum Chem.* **112** (2012) 2499
5. W.-Z. Li, Y.-W. Pei, C.-X. Sun, Q.-Z. Li, J.-B. Cheng, *Chem. Phys. Lett.* **532** (2012) 36
6. Y.-W. Pei, W.-Z. Li, Q.-Z. Li, J.-B. Cheng, *Comput. Theor. Chem.* **999** (2012) 126
7. W.-Z. Li, F.-F. Geng, Y.-W. Pei, J.-B. Cheng, Q.-Z. Li, B.-A. Gong, *Int. J. Quantum Chem.* **112** (2012) 1209
8. B. O. Roos, in *Advances in Chemical Physics: Ab Initio Methods in Quantum Chemistry*, Part 2, Vol. 69, K. P. Lawley, Ed., Wiley, Hoboken, NJ, 2007, p. 399
9. K. Andersson, P.-A. Malmqvist, B. O. Roos, A. J. Sadley, K. Wolinski, *J. Phys. Chem.* **94** (1990) 5483
10. K. Andersson, P.-A. Malmqvist, B. O. Roos, *J. Chem. Phys.* **96** (1992) 1218
11. F. Aquilante, L. De. Vico, N. Ferré, G. Ghigo, P-Å. Malmqvist, P. Neogrády, T. B. Pedersen, M. Pitoňák, M. Reiher, B. O. Roos, L. Serrano-Andrés, M. Urban, V. Veryazov, R. Lindh, *J. Comput. Chem.* **31** (2010) 224
12. J. Almlof, P. R. Taylor, *J. Chem. Phys.* **86** (1987) 4070
13. P. O. Widmark, P. A. Malmqvist, B. O. Roos, *Theor. Chim. Acta* **77** (1990) 291
14. P. O. Widmark, B. J. Persson, B. O. Roos, *Theor. Chim. Acta* **79** (1991) 419
15. J. A. Pople, H. C. Longuet-Higgins, *Mol. Phys.* **1** (1958) 372.

Journal of the Serbian Chemical Society
JSCS-info@shd.org.rs • www.shd.org.rs/JSCS
J. Serb. Chem. Soc. *79* (2) 175–183 (2014) UDC 547.233–304.2+544.723.232:66.011:615
JSCS–4574 *Original scientific paper*

Modeling of ligand binding to the dopamine D2 receptor

LILIANA OSTOPOVICI-HALIP* and RAMONA RAD-CURPAN

Romanian Academy, Institute of Chemistry Timişoara, Computational Chemistry Department, 24 Mihai Viteazul Av., 300223-Timişoara, Romania

(Received 8 February, revised 4 April 2013)

Abstract: The dopaminic receptors for a long time have been major targets for the development of new small molecules with high affinity and selectivity to treat psychiatric disorders, neurodegeneration, and drug abuse, and in other therapeutic areas. In the absence of a 3D structure for the human dopamine D2 (HDD2) receptor, the efforts for the discovery and design of new potential drugs rely on comparative models generation, docking and pharmacophore development studies. To obtain a better understanding of the HDD2 receptor binding site and the ligand–receptor interactions, a homology model of the HDD2 receptor based on the X-ray structure of the *β*2-adrenergic receptor was built and used to dock a set of partial agonists of the HDD2 receptor. The main characteristics of the binding mode for the HDD2 partial agonists set are given by the particular folding of a ligand and a complex network of contacts represented by stacking interactions, salt bridge and hydrogen bond formation. The characterization of the binding mode of the partial agonists at the HDD2 receptor provides the information required to generate pharmacophore models, which represent essential information for future virtual screening studies in order to identify new potential HDD2 partial agonists.

Keywords: GPCR; homology modeling; D2 receptor; molecular docking.

INTRODUCTION

Once the link between psychosis and dopamine was established, the modulation of dopaminergic activity intermediated by the dopamine D2 receptors as a possible treatment for schizophrenia continues to remain a challenging research problem. Based on their impact on diagnosis and treatment, the symptoms of schizophrenia are separated into positive symptoms that involve an excess or distortion of normal functions and negative symptoms that are given by a reduction or loss of normal functions. The negative symptoms are present during episodes of low (or absent) positive symptoms and are related with hypoactive

* Corresponding author. E-mail: lili.ostopovici@acad-icht.tm.edu.ro
doi: 10.2298/JSC130208046O

prefrontal cortex whereas the positive ones are associated with hyperactive dopaminergic transmission in the mesolimbic brain region.

Dopamine D2 receptor antagonists were initially used to treat schizophrenia and related psychiatric disorders. Traditional D2 antagonist antipsychotics have good results in the treatment of the positive symptoms since they block the D2 receptors but an excessive attenuation of brain dopamine neuronal activity is comparable to the neuronal activity recorded in Parkinson's disease. Thus, normalization of dopaminergic activity can be achieved by using dopamine D2 partial agonists. An effective D2 partial agonist would be very efficient in treating the positive symptoms by selectively activating the inhibitory presynaptic D2 autoreceptors while weakly antagonizing the postsynaptic D2 receptors. A partial D2 agonist is theoretically effective in the treatment of positive symptoms based on hyperactivity and in the treatment of negative symptoms based on hypoactivity.

Among the synthesized partial D2 ligands, compounds having Ki_{high} and Ki_{low} values determined for both high- and low-affinity agonist states of the HDD2 receptor ($D2_{high}$ and $D2_{low}$) were selected for this study.[1–3] The set of ligands was docked at the agonist site of the homology model of HDD2 receptor in order to explore the pharmacophoric requirements of HDD2 receptor and to identify the features of the pharmacophore models for HDD2 receptor ligands.

METHODS

Sequence alignment

The sequence of the HDD2 receptor was extracted in Fasta format from the UniProt/Swiss-Prot database[4,5] (P14416) and was automatically aligned using the T-coffee server[6,7] with the sequence of human β2-adrenergic receptor (β2-AR) taken from the RSCB Protein Data Bank (accession code: 2RH1). The resulting alignment was further manually refined according to the template structure. The lysosome T4 fragment was removed from the sequence of the crystal structure of the β2-AR.

Model building

The homology modeling package Modeller[8,9] (version 9v6) was used to generate ten homology models for the HDD2 receptor based on the X-ray structure of β2-AR using the sequence alignment presented in Fig. 1. The C- and N-terminal parts were not modeled. The obtained models were energy-minimized using the standard AMBER99 force field implemented in the HyperChem7.52 package.[10] In the minimization process, the Polak–Ribiere conjugate gradient was used as the optimization algorithm, the stop criterion for the optimization was set to a RMS gradient equal or less than 0.01 kcal/Å·mol. The refined models were stereochemically validated using PROCHECK software.[11,12]

Ligand docking

Ligand setup. A set of previously synthesized and evaluated ligands[1-3] for their affinity and selectivity for high- and low-affinity agonist state of the D2 receptor were chosen for this study (Table I). The structures of the ligands were generated with ISIS Draw[13] and converted into 3D-structures with the Model Builder module of the HyperChem7.52 program.[10] All

ligands were considered in the protonated form and Gasteiger–Marsili atomic partial charges were computed for all of them. The Polak–Ribiere conjugate gradient was used as the optimization algorithm, the stop criteria for the optimization step was set up to a RMS gradient equal or less than 0.01 kcal $Å^{-1}·mol^{-1}$.

TABLE I. General structures **1** and **2** for the selected set of ligands taken in this study

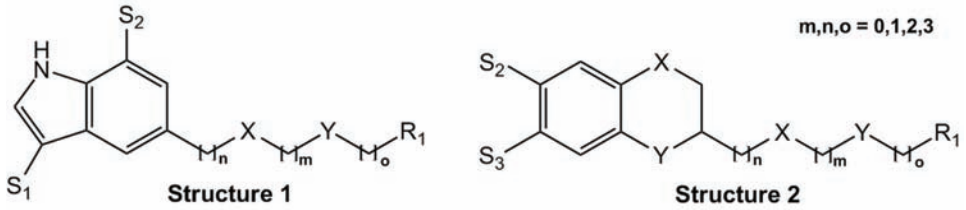

Substituent	Structure
X/Y	CH_2; O; NH
S1	H; Cl; CO–CF_3
S2	H; Cl; OH
S3	H; OH
Ring R1	2-thienyl; 3-thienyl; 2-furyl;3-furyl; cyclohexyl; 4-pyridyl; 4-hydroxyphenyl; 4-fluorophenyl; 4-chlorophenyl; 3-aminophenyl; 1-naphthyl; 2-naphthyl; 1-biphenyl; 1,2,3,4-tetrahydroisoquinoline; 2-indolinyl; 2-indolyl; 2-benzoxazolyl; 3-methyl-1,2-benzo[*d*]isoxazolyl; 3-amino-1-methylphenyl; 3-amino-1-methylphenyl-5-yl; 3-amino-2-chlorophenyl; 2-amino-4-pyrimidinyl

Receptor setup. The 3D structure of the HDD2 receptor was used in the docking process with all the polar hydrogen atoms included. The Kollman united atom charges were also computed.

Docking protocol. The molecular docking was performed with the AutoDock 3.0.5 software package.[14] During the docking simulations, the protein is required to be rigid but the ligands are flexible. The ligand torsional flexibility depends on the number of rotatable bonds from each molecule and it does not apply to bonds in the rings, amide or guanidinium bonds, *etc*. Docking was performed applying a standard protocol, with an initial population of 10 randomly placed individuals, a maximum number of $1.5×10^6$ energy evaluations, a mutation rate of 0.02, a crossover rate of 0.8, and an elitism value of 1. Ten independent docking runs were computed for each ligand. Results differing by less than 0.5 Å in the positional root--mean-square deviation (rmsd) were clustered together and represented by the result with the most favorable free energy of binding. The initial charges were kept and solvation parameters were added to the final protein using the ADDSOL utility of AutoDock 3.0.5.

The grid maps representing the protein in the actual docking process were calculated with AutoGrid. The grids were chosen to be sufficiently large to include not only the active site but also significant portions of the surrounding surface. Thus, the dimensions of the grids were set to 2.44 nm×2.44 nm×2.44 nm, with a spacing of 0.0375 nm between the grid points.

RESULTS AND DISCUSSION

The recently solved structure of the human β2 adrenergic receptor structure (PDB code: 2RH1) was selected as the structural template to model the three-dimensional structure of the HDD2 receptor. The sequence alignment generated with T-coffee server was manually refined using as a guide the three dimensional structure of the template. The refinements were conducted in order to avoid deletions or insertions in the transmembrane domain and to preserve the highly conserved amino acid motifs specific for each transmembrane helix identified based on the conserved residues within the GPCR amino acid sequences. The deletions and insertions were merged into a single piece per loop and moved to the most adequate point according to the template structure. A structural feature common to many GPCR receptors, the formation of a conserved disulfide bond between two cysteine residues placed at the beginning of TM3 and the middle of the second extracellular loop was taken into consideration. The C-terminal part and the second intracellular loop (IL2) were not modeled because these fragments do not have a correspondent in the template structure. The lysosome T4 fragment was removed from the initial structure for ease of use.

The alignment shown in Fig. 1 was used to generate ten 3D models of the HDD2 receptor using the MODELLER software package.[8,9] Each model was further refined with the help of the HyperChem7.52 program as described elsewhere.[15] Shortly, the torsion angles, bond lengths, and peptide-bond planarity were checked with the PROCHECK program and were found to be within the interval of the standard values for nine out of the ten models.

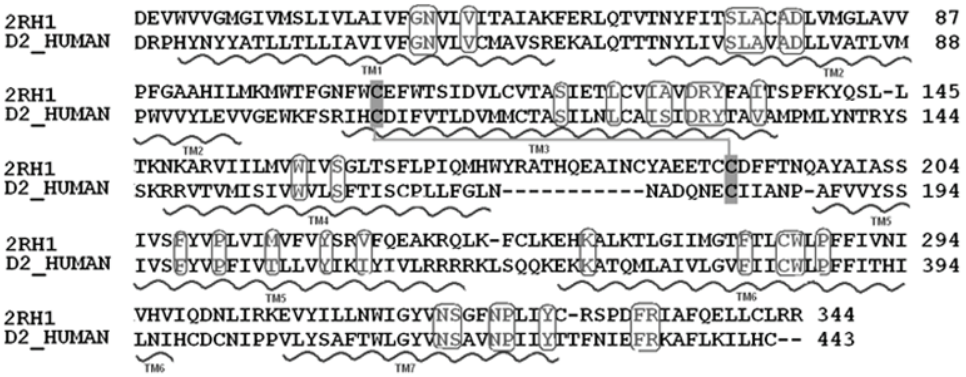

Fig. 1. Sequence alignment of the human beta2-adrenergic receptor and the HDD2 receptor showing a sequence similarity of 59.8 %. The seven transmembranes are underlined with a curved line; the highly conserved residues in the GPCR family are shown in grey and are enclosed in rounded rectangles; the residues involved in the sulfur bridge formation have a grey background.

Site-directed mutagenesis studies showed that Asp114, Ser193, Ser194 and Ser 197 are the most important residues involved in dopamine binding at the active site of the HDD2 receptor.[16] Mutation of Asp114, a highly conserved residue that has been studied in a number of GPCRs, resulted in a marked reduction of ligand binding, emphasizing its importance at the binding site for the agonists and antagonists containing ammonium groups. The serine residues of helix 5: Ser193, Ser194 and Ser 197 are important for binding catechol hydroxyl groups. To check if the present models confirm and support this essential information, docking tests using the endogenous ligand of the HDD2 receptor, dopamine and the nine homology models were performed.

The docking results of two models confirmed the involvement of the previously mentioned residues in the binding of dopamine and the model showing the best stereochemical quality was chosen to be used in further docking experiments (Fig. 2). The three-dimensional coordinates of the final model are provided as Supplemental material to this paper.

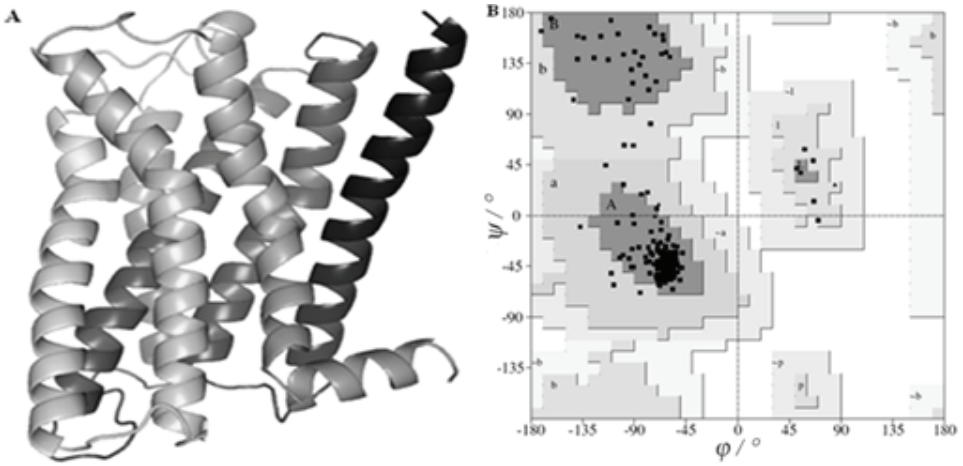

Fig. 2. A) 3D structure of the human dopamine D2 receptor. B) Ramachandran plot for the human dopamine D2 receptor. The final model has 93.6 % amino acids in the most favorable regions, while the other 6.4 % amino acids are placed in the additional allowed regions of the Ramachandran plot.

The positively charged nitrogen atom of dopamine forms a salt bridge with the carboxylate group of the Asp114 residue from helix 3, the distance between the two charged functional groups being 4.26 Å. The *meta*- and *para*-OH groups of the ligand interact with the side-chains of the Ser193 and Ser197 residues, respectively, *via* the formation of two hydrogen bonds. The aromatic ring of dopamine is accommodated in a hydrophobic pocket defined by several aromatic residues found on helix 6: Trp245, Phe248 and Phe249 (Fig. 3).

In order to highlight the molecular characteristics of the active site, a combined docking and pharmacophoric approach was performed using the 3D structure of the HDD2 receptor and a set of HDD2 partial agonists.

The molecular mechanics minimized conformation of each ligand was placed and oriented in the binding site by superposition to the docked dopamine as reference agonist. The rotatable bonds and the torsion angles of the ligands were set up using the AutoDock Tools package. The docking results were analyzed based on their ligand–receptor free binding energies and population clusters. The prediction of the binding affinity for each compound was not very accurate, with a difference of two-log units seen in some cases. Still, the correlation with the experimental results is reasonable if one keeps in mind the dynamics of the binding site and the fact that a homology model was used.

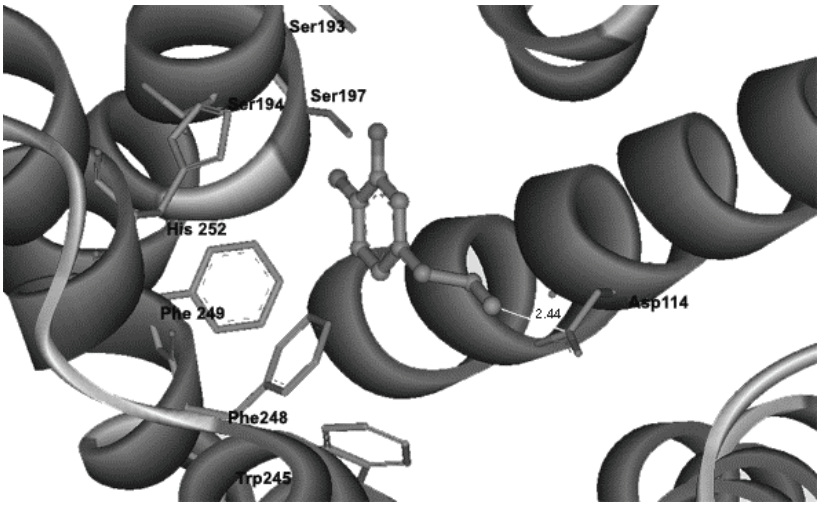

Fig. 3. Molecular model of dopamine in the binding site of the HDD2 receptor.

Analyzing each lowest binding-energy conformation in the binding site, it was observed that the ligands, depending on their size, adopt an L- or a U-shape folded conformation. This folding seems to be very important for biological activity since it allows the formation of one salt bridge between the aspartic acid residue on helix 3, Asp114 and the positively charged nitrogen atoms of the ligands (Fig. 4). Depending on the ligand size, the distance between the two charged functional groups (the carboxyl group from the D2 receptor and the amino function from the ligands) varies between 2.9 and 4.8 Å.

Many compounds showing high affinities against the HDD2 receptor display another important contact, namely a π–π interaction resulting from the stacking of the chromane ring of the ligands on the benzene ring of the Phe248 side-chain. Thanks to this stacked arrangement of the two aromatic rings, another important

interaction for ligand binding could be established. This interaction refers to the formation of a hydrogen bond between the hydroxyl group of one serine residue of helix 5 (usually Ser194) and the hydroxyl group from the chromane ring (Fig. 4). This hydrogen bond seems to be essential for the biological activity of these derivatives against the D2 receptor, being only observed for the *R*-diastereoisomers of the chiral compounds from this set.

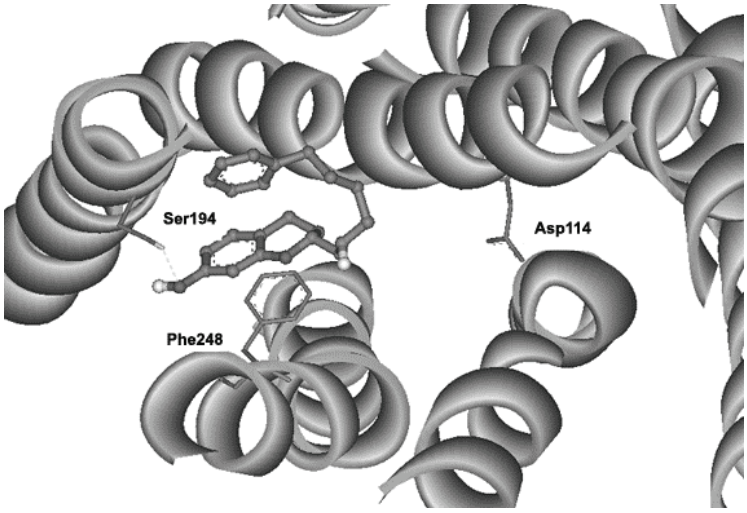

Fig. 4. The best docking pose of a partial D2 agonist in the binding site of the D2 receptor.

According to the experimental data (Table II), the *R*-diastereoisomers are more potent compounds than the *S*-diastereoisomers, allowing the conclusion that substitution at position 2 of the chromane ring is specifically stereoselective (Fig. 5A and B).

TABLE II. Inhibition constants for the R- and S-diastereoisomers

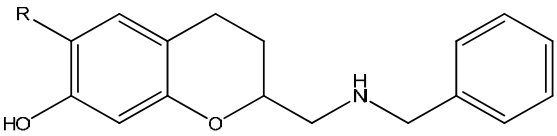

Compound	R	Stereochemistry	Ki_{exp} [a] / nM	Ki_{obs} / μM
1	H	*R*	0.2	1.3
1	H	*S*	12	68.2
2	Cl	*R*	0.6	1
2	Cl	*S*	32	49.6

[a]The values were taken from the literature[1]

The most relevant features that define the binding mode of the studied HDD2 partial agonists are described by the ligand folding and a complex net-

work of interactions represented by stacking interactions, a salt bridge and hydrogen bond formation.

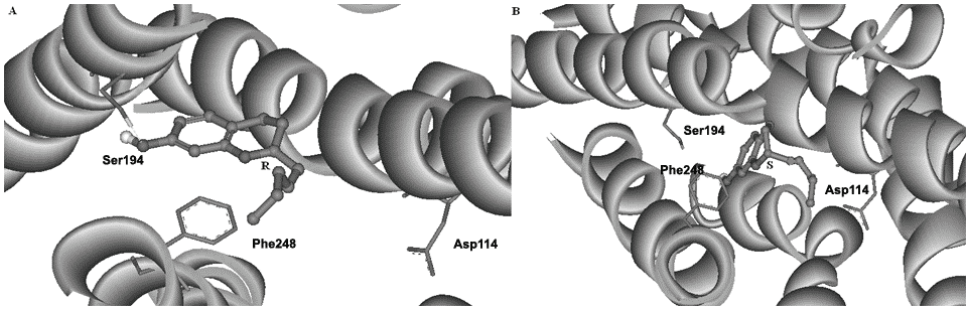

(A) (B)

Fig. 5. View of the *R*-stereoisomer (A) and *S*-stereoisomer (B) in the binding site of the D2 receptor.

CONCLUSIONS

A homology model of the HDD2 receptor based on the X-ray structure of the *β*2-adrenergic receptor was built using comparative modeling. The model has all steric and topologic parameters within the normal range and its accuracy was confirmed by docking experiments using endogenous ligands. In addition, the importance of Asp114, Ser193 and Ser197 residues in ligand binding and affinity at the HDD2 receptor, according to experimental data, was explained *via* docking experiments.

The binding mode of 2-aminochromane derivatives acting as partial agonists against HDD2 receptor is characterized by the following key interactions: 1) a salt bridge formed between Asp114 and one positively charged nitrogen atom of the ligand; 2) one or two hydrogen bonds between the Ser193, Ser194 and/or Ser197 side-chains and hydroxyl group of the chromane ring; 3) a π–π interaction between chromane ring and Phe248. These features of the binding mode of partial agonists at the HDD2 receptor provide the required information to generate pharmacophore models, which represents essential information for future virtual screening studies aimed at identifying new potential HDD2 receptor partial agonists.

Acknowledgements. This work was supported by CNCSIS-UEFISCSU Project No. PN-II-RU No. 500/Agreement 119/2010 to LOH and the Romanian Academy-Institute of Chemistry, Timisoara, Romania, Project No. 1.2/2011 to RC.

ИЗВОД

МОДЕЛОВАЊЕ ВЕЗИВАЊА ЛИГАНДА НА ДОПАМИНСКИ D2 РЕЦЕПТОР

LILIANA OSTOPOVICI-HALIP и RAMONA RAD-CURPAN

Romanian Academy, Institute of Chemistry Timi oara, Computational Chemistry Department, 24 Mihai Viteazul Av., 300223-Timi oara, Romania

Допамински рецептори већ дуже време су главна мета при развоју нових малих молекула који имају велики афинитет и селективност за тај рецептор, а могли би да се примењују за третирање психијатријских сметњи, неуродегенерације, наркоманије и др. Будући да 3D структура хуманог D2 допаминског рецептора (HDD2) није позната, истраживања се заснивају на компаративним моделима. Да би се боље разумело место везивања на HDD2 рецептор, и лиганд–рецептор интеракцоје, конструисан је хомологни модел HDD2. рецептора заснован на рендгенској структури β2-адренергичног рецептора. Одређене су главне карактеристике везивања на HDD2 парцијалних агониста. То даје потребне информације да се добије фармакофорски модел за будућа истраживања и за идентификацију нових потенцијалних HDD2 парцијалних агониста.

(Примљено 8. фебруара, ревидирано 4. априла 2013)

REFERENCES

1. R. E Mewshaw, J. Kavanagh, G. Stack, K. L. Marquis, X. Shi, M. Z. Kagan, M. B. Webb, A. H. Katz, A. Park, Y. H. Kang, M. Abou-Gharbia, R. Scerni, T. Wasik, L. Cortes-Burgos, T. Spangler, J. A. Brennan, M. Piesla, H. Mazandarani, M. I. Cockett, R. Ochalski, J. Coupet, T. H. Andree, *J. Med. Chem.* **40 (**1997) 4235
2. R. E. Mewshaw, M. B. Webb, K. L. Marquis, G. B. McGaughey, X. Shi, T. Wasik, R. Scerni, J. A. Brennan, T. H. Andree, *J. Med. Chem*. **42** (2007) 2007
3. H. Hubner, C. Haubmann, W. Utz, P. Gmeiner, *J. Med. Chem*. **43** (2000) 756
4. B. Boeckmann, A. Bairoch, R. Apweiler, M. C. Blatter, A. Estreicher, E. Gasteiger, M. J. Martin, K. Michoud, C. O'Donovan, I. Phan, S. Pilbout, M. Schneider, *Nucleic Acids Res.* **31** (2003) 365
5. E. Boutet, D. Lieberherr, M. Tognolli, M. Schneider, A. Bairoch, *Methods Mol. Biol.* **406** (2007) 89
6. C. Notredame, D. G. Higgins, J. Heringa, *J. Mol. Biol*. **302** (2000) 205
7. O. Poirot, E. O'Toole, C. Notredame, *Nucleic Acids Res*. **31** (2003) 3503
8. A. Sali, T. L. Blundell, *J. Mol. Biol.* **234** (1993) 779
9. N. Eswar, M. A. Marti-Renom, B. Webb, M. S. Madhusudhan, D. Eramian, M. Shen, U. Pieper, A. Sali, *Curr. Protoc. Bioinformatics* **15** (2007) 561
10. HyperChem 7.52 release for Windows; HyperCube, Inc., Gainesville, FL
11. R. W. W. Hooft, C. Sander, G. Vriend, *Proteins* **26** (1996) 363
12. L. A. Laskowski, M. W. MacArthur, D. S. Moss, J. M. Thornton, *J. Appl. Crystallogr.* **26** (1993) 283
13. ISISTM/Base2.4, UB7K, Information Systems, Inc.
14. G. M. Morris, D. S. Goodsell, R. S. Halliday, R. Huey, W. A. Hart, R. K. Belew, A. J. Olsoni, *J. Comput. Chem.* **19** (1998) 1639
15. L. Ostopovici, R. Rad, M. Mracec, M. Mracec, *Rev. Chim (Bucharest)* **58 (**2007) 273
16. A. Mansour, F. Meng, J. H. Meador-Woodruff, L. P. Taylor, O. Civelli, H. Akil, *Eur. J. Pharmacol.* **227** (1992) 205.

Journal of the Serbian Chemical Society
JSCS-info@shd.org.rs • www.shd.org.rs/JSCS
J. Serb. Chem. Soc. 79 (2) 185–198 (2014)
JSCS–4575
UDC 579.8:544.537:543.426.1
Original scientific paper

Investigation and detection of cyanobacterial Cr-phycoerythrin by laser-based techniques

BRATISLAV P. MARINKOVIĆ[1], AMBRA DELNERI[2], MAJA S. RABASOVIĆ[1], MIRA TERZIĆ[3], MLADEN FRANKO[2] and DRAGUTIN ŠEVIĆ[1]*

[1]*Institute of Physics, Belgrade, P. O. Box 68, University of Belgrade, Serbia,* [2]*Laboratory for Environmental Research, University of Nova Gorica, Slovenia and* [3]*Faculty of Science, University of Novi Sad, Serbia*

(Received 17 April 2013)

Abstract: The application of the high-sensitivity method of time resolved laser induced fluorescence (TR-LIF) and a flow-injection system by thermal lens spectrometry (FIA-TLS) for the analysis of Cr-phycoerythrin (Cr-PE) isolated from a proprietary cyanobacterium is presented. In the excitation wavelength range (340–470 nm), the fluorescence spectra exhibited a pronounced maximum at 575 nm. Another maximum at about 600 nm could also be observed. The obtained results were used to verify the technical parameters of the employed thermal lens technique, which is complementary to spectrofluorimetry and subject to lower sensitivity in the case of high fluorescence quantum yields and photolability of the measured compounds.

Keywords: time resolved laser induced fluorescence spectroscopy; thermal lens spectroscopy; phycoerythrin; cyanobacteria.

INTRODUCTION

Cyanobacteria are photosynthetic microorganisms that are worldwide distributed in marine and fresh waters. During their ageing and decay, they release secondary metabolites (cyanotoxins) that are toxic to the environment and humans. Cyanotoxins have dermatotoxic, hepatotoxic and neurotoxic effects[1] and can also lead to death.[2] Moreover they are tumor promoters and recently they have been related to neurodegenerative diseases, such as amyotrophic lateral sclerosis and Alzheimer's disease.[3] Under particular conditions (for example eutrophication and rising temperature), cyanobacteria can grow abnormally, leading to so called harmful algal blooms (HABs) with a consequent release of large amounts of cyanotoxins during their senescence and death.[4] During such events, the mass of cyanobacteria in water can reach over 100 g m^{-3}.[5] Concern

* Corresponding author. E-mail: sevic@ipb.ac.rs
doi: 10.2298/JSC130417088M

about HABs has grown in the last decades due to their increase in occurrence and severity and because cyanotoxins are not efficiently removed by conventional water treatment technologies; hence, they can be found in recreational and drinking waters. In 2004, the World Health Organization (WHO) set a provisional limit of 1 μg L^{-1} for the presence of microcystin-LR (the most harmful among the cyanotoxins) in drinking water.[6] Cyanobacteria represent a serious threat to the environment and human health, and therefore, the development of sensitive and rapid analytical tools that could be used in early warning systems for the detection of cyanobacteria is of high interest.

Phycoerythrin (PE), isolated from cyanobacteria, is a highly fluorescent pigment with a broad and high absorption of light over a wide range of the visible spectrum. Its content in cyanobacteria is about one percent dry weight, but in some species, up to 8 % PE can be found.[7] The spectral properties of PE depend on the native structure of the polypeptide and interaction with different chromophores. PE was among the first molecules to be observed at the single-molecule level using laser-induced fluorescence.[8] PE fluoresces in a spectral region that is distinct from the region of emission of the simple organic dyes commonly used as fluorescent indicators. Therefore, PE is commonly used for fluorescent immuno-labeling, particularly in applications involving fluorescent-activated cell sorting.[9,10] Sometimes, the relatively high-molecular weight of PE may be problematic in a spectrofluorimetric detection system, due to steric hindrance caused by conjugation to other proteins.[11]

Among the PEs, Cr-phycoerythrins (Cr-PE) provide additional spectral characteristics that can complement the common phycoerythrins (B-PE and R-PE). Besides this, the Cr-PEs have a lower molecular weight (around 40 kDa). Due to these features, Cr-PEs can provide additional functionality to the phycobiliprotein pigments when multiplexing assays or the introduction of the dye into cells is concerned. In addition Cr-PE could find many applications in cellular analysis, flow and laser scanning cytometry.[11,12] Similarly, PEs and other cyanobacterial pigments could serve as early indicators of the presence of cyanobacteria and of the associated risk of cyanotoxins in water, as was shown for phytoplankton cell lysis based on release of carotenoids and the application of thermal lens spectrometry.[13,14]

According to literature data, three different Cr-PE types (Fig. 1) are recognized. They are designated based on their characteristic absorption maxima, λ_{max}.[15–17]

In the present study, a commercially available Cr-PE, a low molecular weight phycobiliprotein (40 kDa) with an absorption maximum at 550 nm, was examined. The characteristics of this Cr-PE, *i.e.*, high extinction coefficient and high fluorescence quantum yield, make it an ideal fluorophore for use in immunoassays.[10,18] To date, not much data for this phycoerythrin type has been pub-

lished. However, information on the fluorescence quantum yield would be valuable for the development of an alternative method for detection of PEs in water, such as, for example, thermal lens spectrometry (TLS). In such a case, however, higher fluorescence quantum yields result in lower sensitivity of the method, which is based on the indirect measurement of absorbance through radiationless de-excitation processes. It is therefore important to estimate eventual differences in the fluorescence quantum yields for excitation in the main PE absorption peak at 550 nm, which is accessible by Ar-ion laser lines (458.9–514.5 nm) and the PE absorption peak at 375 nm, reachable by Kr laser lines (406.7 and 413.1 nm) in the visible spectral range, which are the most frequently used in TLS spectrometry.[19]

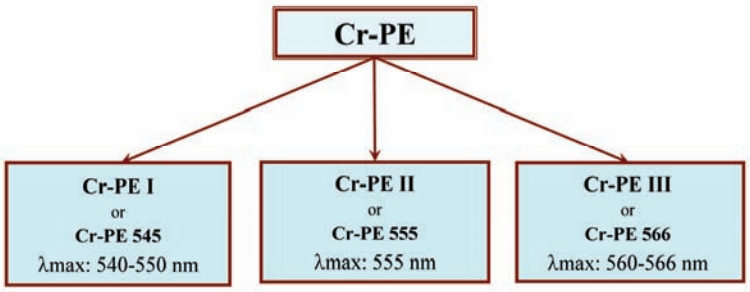

Fig. 1. Schematic illustration of Cr-PE types, modified from the literature.[15-17]

Two laser-based techniques were used for the characterization and detection of Cr-PE: laser-induced fluorescence (LIF)[20] and flow-injection analysis with thermal lens spectrometric detection (FIA-TLS).[21] The fluorescence technique is based on measurement of photons emitted by the excited fluorophore. Detection of absorbed energy by thermal lens techniques is achieved by measurement of heat released by non-radiative relaxation of the excited fluorophore.

The obtained results were used to verify the technical parameters of the employed thermal lens technique, which is complementary to spectrofluorimetry and subject to lower sensitivity in the case of high fluorescence quantum yields and photolability of measured compounds under irradiation by intensive light sources such as lasers.

EXPERIMENTAL

The study was realized using phycobiliprotein Cr-PE I type with a molecular weight of 40 kDa, isolated from a proprietary cyanobacterium. The pigment Flogen® Cr-PE was supplied by FEBICO Taipei (Taiwan) in: 100 mM potassium phosphate buffer, pH 7.0, with 60 %, saturated $(NH_4)_2SO_4$, 1 mM EDTA and 1 mM sodium azide. The absorption spectrum of Cr-PE was characterized by an absorbance maximum at 550 nm. The purity ratios $A_{550}/A_{280} \geq$ $\geq$ 5.5 correspond to pure Cr-PE and $A_{620}/A_{550} \leq 0.005$ demonstrates the absence of phycocyanin contamination.

Time resolved laser-induced fluorescence

The TR-LIF experimental setup used in this work, shown on Fig. 2, was described previously.[22] Solutions of Cr-PE in quartz cuvette were illuminated using a tunable Nd:YAG laser system (Vibrant model 266-I, Opotek, Inc.). This system includes an optical parametric oscillator (OPO) that is pumped by the fourth harmonic of the Nd:YAG Brilliant laser at 266 nm and control electronics. The output of the OPO can be continuously tuned over a spectral range from 320 nm to 475 nm, providing pulses of 5.4 ns and an energy per pulse of between 5.5 and 4 mJ at a 10 Hz repetition rate.

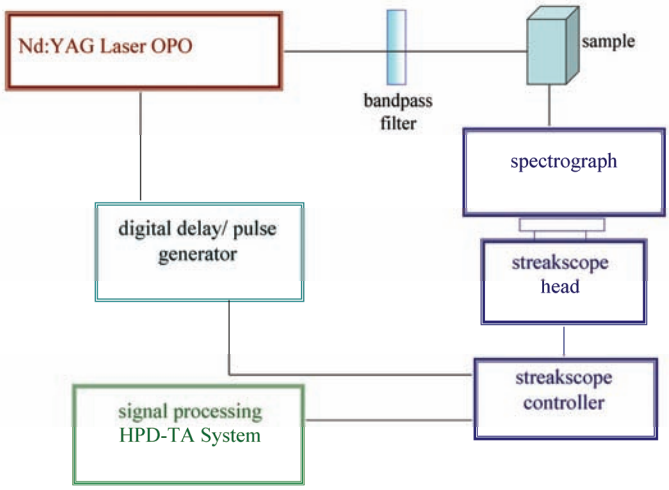

Fig. 2. Experimental set for TR-LIF spectrometry.

The fluorescence signals from Cr-PE solution were measured using a streakscope (Hamamatsu model C4334-01) with an integrated video streak camera. For all measurements of the Cr-PE spectra, the emission was collected in the right angle arrangement and dispersed by a 0.3 m focal length triple grating imaging spectrograph (SpectraPro-2300i). The fluorescence data was acquired in the photon-counting mode using Hamamatsu HPD-TA software. All the measurements were performed at room temperature.

Flow-injection system with thermal lens spectrometric detection

The FIA-TLS experimental set-up used in this work is shown in Fig. 3. The sample is injected into the stream of carrier buffer pumped at 1 mL min^{-1} by an HPLC pump (Knauer Smartline pump 1000). A Knauer injector (Knauer A1358) equipped with a 200 μL injection loop was used for this purpose. The detection was realized in an 8 μL flow-through sample cell (Hellma 176.050-QS) by a dual-beam (pump/probe) thermal lens spectrometer.[19] The pump beam (514.5 nm) was derived from an Ar-ion laser (Inova 90, Coherent) with 100 mW power measured at the laser head. A helium–neon laser (632.8 nm, 2 mW) (Meles Griot, 1103P) was used as a source of the probe beam. The pump and probe beams were properly focused with respect to the sample cell by a set of lenses and their collinear propagation through the sample cell was assured by a dichroic mirror. The pump beam, modulated by a mechanical chopper (Scitec Instruments) at 40 Hz, induces the photo-thermal effect, consisting of periodic changes in the refractive index gradient in the sample, which is related to the

concentration of the sample. The refractive index gradient causes defocusing of the probe beam, resulting in changes of the probe beam intensity at its axis, which can be sensed by a PIN photodiode connected to a lock-in amplifier (Stanford Research, SR830). The signal from the lock-in amplifier is then recorded, stored and later elaborated by a computer.

For batch mode measurements, a 1 mL cuvette (1 cm path length) (Hellma 101-QS) was used, and was placed at the position of the flow-through cell in the FIA-TLS system.

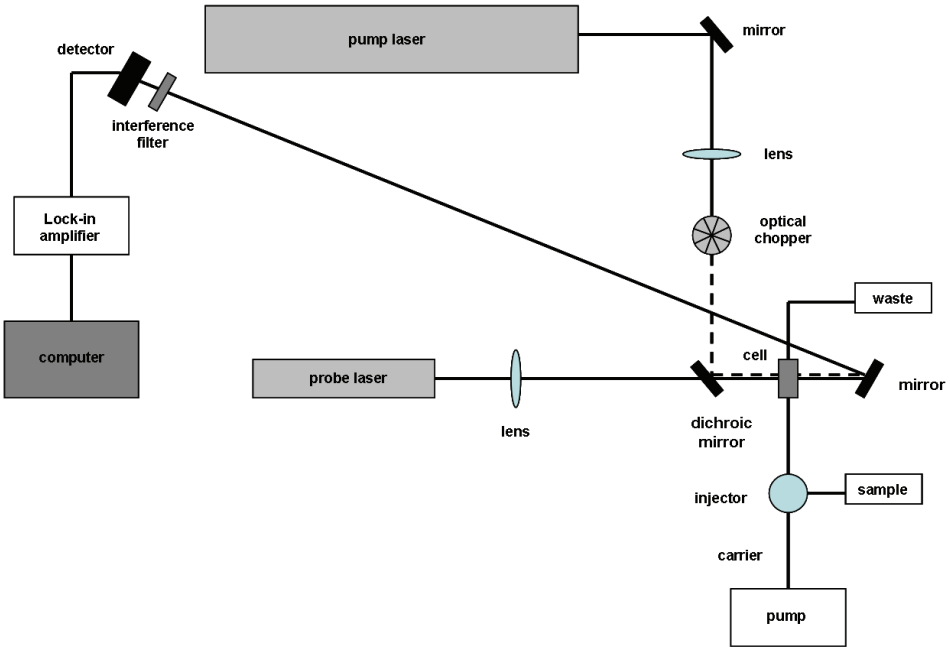

Fig. 3. Experimental set-up for FIA-TLS.

RESULTS AND DISCUSSION

TR-LIF

The fluorescence spectra of Cr-PE (50 μg mL^{-1}) excited at 400 nm are presented in Fig. 4. The spectra exhibit a strong emission maximum around 575 nm, which is expected for this phycoerythrin. Two additional maxima located below and above 575 nm could also be observed. Similar behavior was found for other phycoerythrins.[7,23,24] In order to locate the position of the maximum and their relative contribution in a fluorescence spectrum, the spectra were analyzed by the Gauss peak spectrum (GPS) method[25] for pigment quantification. The method is based on the description of each pigment spectrum by a series of Gaussian peaks. The experimental data were deconvoluted into three emission bands (Fig. 4). A high correlation (R^2 = 0.93) was observed. The three overlapping Gaussians were resolved at 530.2, 575.9 and 592 nm. The two most dominating peak were at 575.9(3) nm (full width at half maximum (FWHM) about 27 nm)

and a shoulder at 592.5(18) nm (FWHM about 115 nm). These components contributed 34.5 and 63.8 % to the total area of the fluorescence emission spectrum, respectively. The third, minor peak at 530.2(18) nm (FWHM about 13 nm) is actually the second harmonic of the laser, not attenuated enough in this measurement.

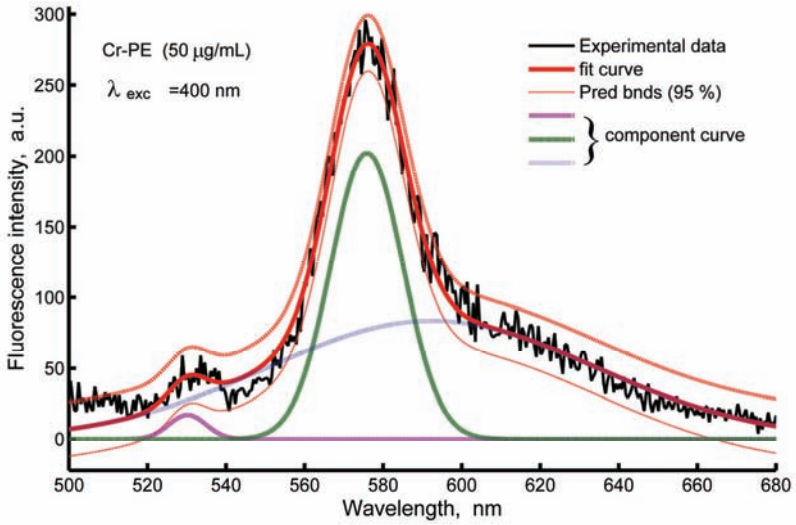

Fig. 4. Emission spectra of Cr-PE (50 µg mL^{-1}) at 400 nm OPO excitation and deconvolution of the emission spectra.

The emission spectrum of the R-PE subunit also showed a maximum at 575 nm and a shoulder at 593 nm.[26] Noticeably, the difference between these two peaks for Cr-PE and R-PE is nearly the same (about 17 nm). Chekalyk and Hafe[27] found a peak at 589 nm for phycoerythrin. An additional fluorescence peak (at 511 nm) before the main peak (555 nm) for PE2b was also detected.[28] The authors indicated that a PE isoform might have been present. The difference between these two fluorescence peaks for PE2b was about 44 nm. A somewhat larger difference between the two peaks was measured for Cr-PE (585 nm and 675 nm for absorption maximum at 550 nm).[15]

In solutions at 25 µg mL^{-1} (diluted in potassium phosphate (KPi), 0.1 M, pH 7), fluorescence spectra were induced by varying the excitation wavelength in 10 nm steps between 340 and 470 nm to obtain the corresponding excitation–emission matrixes (EEMs). The absorption of Cr-PE in this excitation wavelength range is weak. For lower excitation wavelengths (λ_{exc} < 44 nm), an emission maximum appears at about 576 nm and shoulder at about 599 nm. Hence, the fluorescence spectra for 340 ≤ λ_{exc} ≤ 430 nm were deconvoluted into two overlapping Gaussian peaks (Fig. 5), which were resolved at 575.9 nm (FWHM about

34 nm) and 600 nm (FWHM about 109 nm). These components contributed 41 and 59 % to the total area of the fluorescence emission spectrum, respectively. A third peak in the fluorescence spectra appeared at longer excitation wavelengths ($\lambda_{exc} \geq 440$ nm. The position of this peak is at about 520 nm.

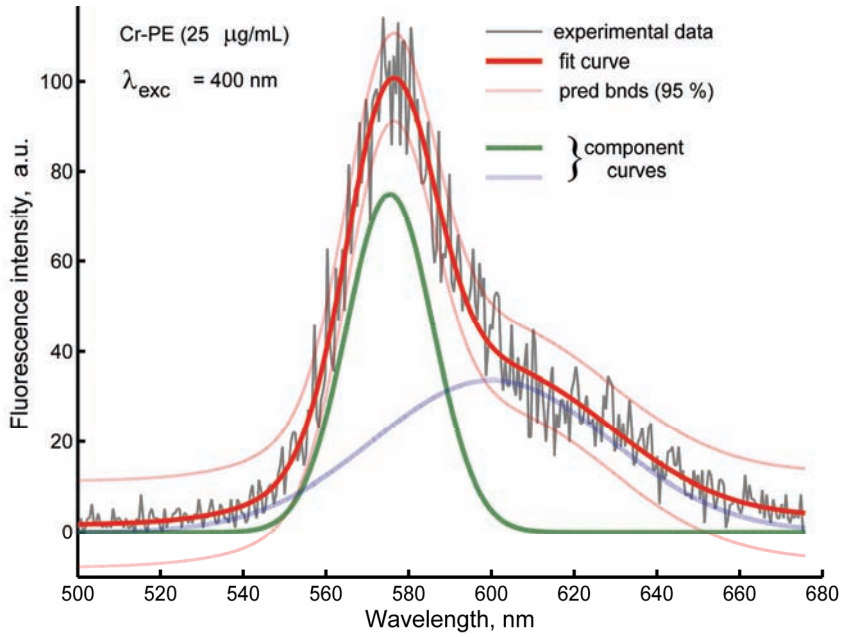

Fig. 5. Emission spectra of Cr-PE (25 μg mL^{-1}) at 400 nm OPO excitation and deconvolution of the emission spectra.

The main advantage of EEMs is that more information about the fluorescent species can be extracted, because the bands arising over a wider area are considered. The three-dimensional EEM of Cr-PE (25 μg mL^{-1}) recorded by measuring the samples within the spectral excitation and emission ranges 340–470 nm and 500–660 nm, respectively, are shown in Fig. 6.

HPD-TA software was applied to determine the fluorescence lifetime of Cr-PE (λ_{exc} = 400 nm, 50 μg mL^{-1}). The best exponential fit deconvoluted with OPO gave a fluorescence lifetime of 2.44 ns. This is in good accordance with literature data for PE, where values in the range of 1.7–4.0 ns were reported.[26]

To the best of our knowledge, the value of the fluorescence quantum yield of Cr-PE has not been published. A simple indirect method was used to determine the fluorescence quantum yield of Cr-PE. Rhodamine B has similar wavelengths for absorption and emission maxima as Cr-PE. The second harmonic of a Nd:YAG laser (532 nm, close enough to absorption maxima of both pigments) was used as an excitation source. An ethanolic solution of rhodamine B and a buffered solu-

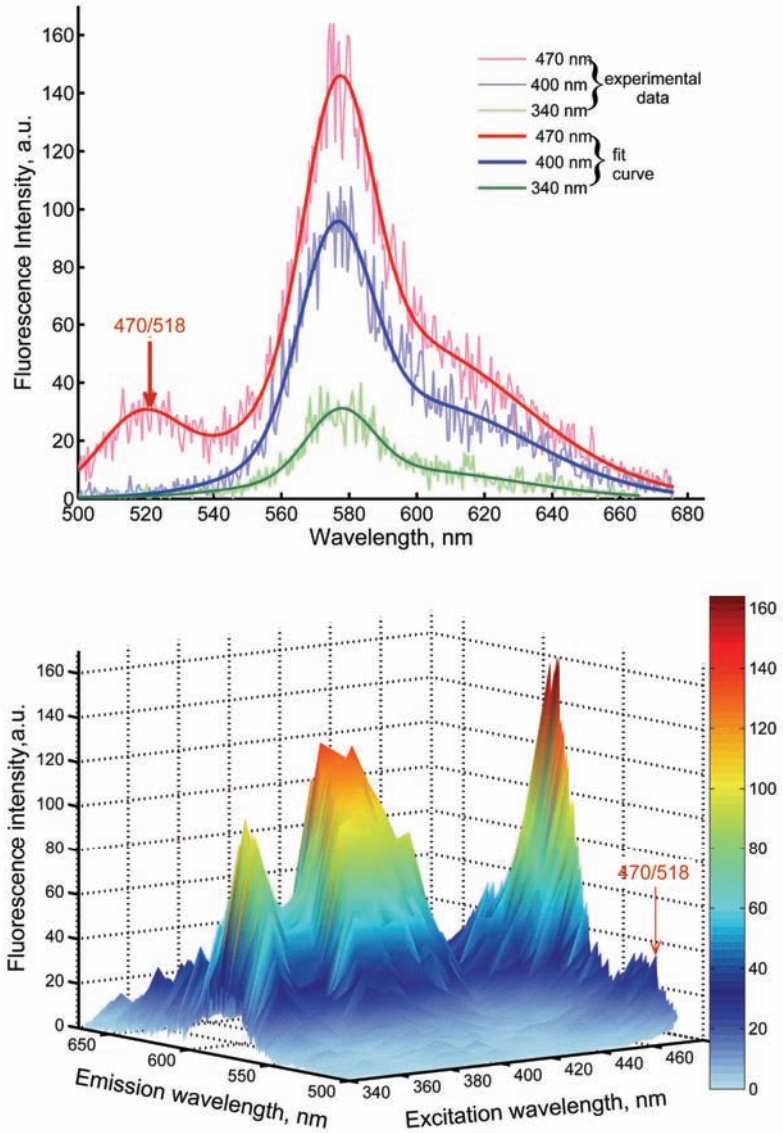

Fig. 6. Emission–excitation spectra of Cr-PE (25 μg mL^{-1}), bottom part. The top part shows the recorded fluorescence spectra, curve fitted spectra at 470, 400 and 340 nm OPO excitation. As an example, the third emission/excitation peak for excitation at 470 nm is marked.

tion of PE were diluted in 10 mm cuvettes until the absorption values measured with an Ocean Optics spectrometer at 532 nm were about 0.2. After that, streak images of both solutions were obtained using 532 nm excitation. The obtained

images are shown in Fig. 7. As can be seen, the streak images of both pigments look very similar, so it seems that an appropriate reference standard for the indirect measurement of the quantum yield of Cr-PE was chosen. Taking into account the value of the quantum yield of an ethanolic rhodamine B solution of 0.7,[29] and comparing the integrated areas of fluorescence on both images, the fluorescence quantum yield of Cr-PE was estimated to be 0.68.

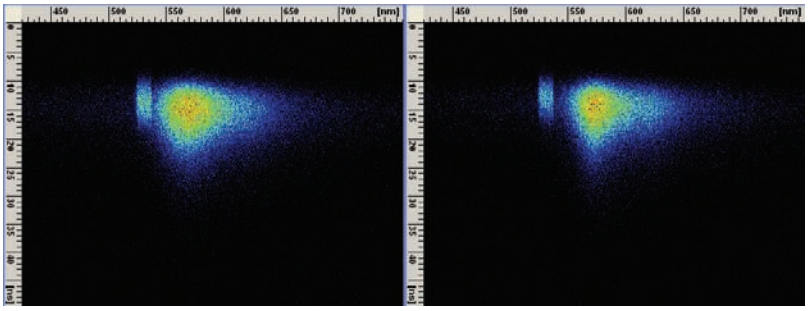

Fig. 7. Streak images of an ethanolic rhodamine B solution (left) and a buffered phycoerithrin solution (right), excitation at 532 nm (second harmonic of the Nd:YAG laser).

Most importantly, by comparison of fluorescence resulting from excitation at selected wavelengths in the two absorption maxima (375 and 550 nm), the ratio of the fluorescence quantum yields for various excitation wavelengths was calculated. For the wavelengths of interest for TLS reachable by the used lasers (458.9, 476.0 nm and 514.5, 406.7 and 413.1 nm) the ratio of the fluorescence quantum yields for excitation at 470 and 410 nm was found to be F_{470}/F_{410} = = 1.6±0.2. Assuming a similar fluorescence quantum yield for Cr-PE when excited at 550 nm as when excited at 532 nm (0.68), it was calculated that the conversion of absorbed energy into heat could be by a factor of 1.8 higher (58 compared to 32 %) when exciting in the 375 nm absorption band (Kr laser emission lines) instead of in the 550 nm absorption band (Ar lasers emission lines). However, the sensitivity of TLS measurement can not be improved due to lower absorbances at the Kr laser lines as compared to the 476 nm ($A_{476.0}/A_{406.7}$ = = 1.86) and particularly the 514.5 nm Ar laser line ($A_{514.5}/A_{406.7}$ = 12.57). It was therefore decided that the Ar laser would be used for excitation in the FIA-TLS system for the detection of phycoerythrin.

FIA-TLS

Batch mode measurements of phycoerythrin showed a considerable degree of photodegradation of the pigment under the intensive irradiation by the tightly focused pump laser beam. As can be observed in Fig. 8, the TLS signal decreases by 0.48 mV over a period of 400 s. Taking into account the 0.22 mV background signal, this represents a 72.4 % decrease of the signal from phycoerythrin. This

can affect the sensitivity as well as the reproducibility of the method, therefore all further measurements were performed in a flow injection mode to reduce the exposure of the pigment to the intense laser light (Fig. 9). The residence time of the sample (8 μL) within the flow through the cell under the given experimental conditions was only 480 ms. Under such conditions, a limit of detection (*LOD*) of 81 μg mL^{-1} was obtained for phycoerythrin.

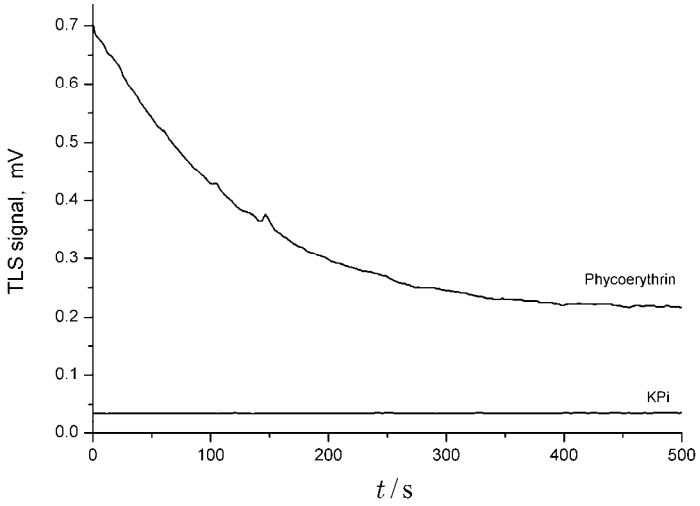

Fig. 8. Batch mode experiments showing photodegradation of phycoerythrin (20 μg mL^{-1}) which resulted in a decrease of the thermal lens signal as opposed to the stable signal of the blank (phosphate buffer-KPi).

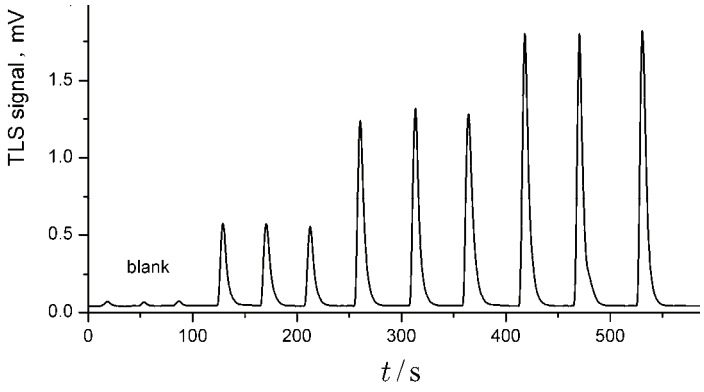

Fig. 9. Thermal lens signal in a flow injection system. Signals corresponding to injection of the blank, and of 5, 10 and 15 μg mL^{-1} of phycoerythrin are shown.

To reduce the loss of absorbed energy and therefore to increase the degree of radiationless de-excitation processes, which are directly related to the magnitude

of thermal lens effect, the effect of KI as a fluorescence quencher was tested. An obvious decrease in fluorescence efficiency was observed (Fig. 10) and a 1.7-fold decrease in the fluorescence intensity at the emission maximum (580 nm, excitation at 540 nm) was calculated. Assuming again that the fluorescence quantum yield was 0.68, it was calculated that 59.5 % of the absorbed energy was converted to heat in the presence of KI. Based on this, an increase in sensitivity of 1.9 times is expected in comparison to phycoerythrin in buffer solution (32 % of the absorbed energy was released as heat). As calculated from the ratio of slopes of calibration curves for phycoerythrin in 0.5 M potassium iodide solution and in buffer (Fig. 11), the sensitivity of phycoerythrin determination by TLS increased by 2.25 times, lowering the *LOD* to 36 μg mL^{-1} which exceeds the predicted increase of 1.9 times by 18 %. This additional increase could be attributed to an increase in the thermal lens enhancement factor (increase in the temperature coefficient of the refractive index and a decrease in thermal conductivity) due to the high concentration of KI, as could be extrapolated from literature data where a 2.6 times enhancement of the thermal lens signal, as compared to water, was reported for 2.5 M KI.[21,30,31] It was also interesting to observe, that the photodegradation of the pigment in batch mode measurements was reduced in the presence of KI (as demonstrated by a constant value of the TLS signal over 75 s, Fig. 8).

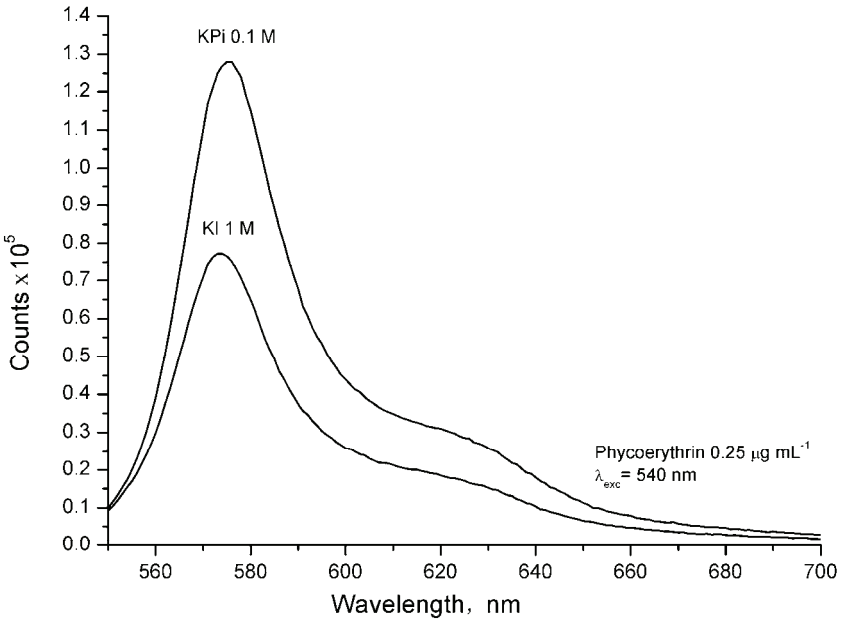

Fig. 10. Fluorescence spectra of Cr-PE in phosphate buffer and in 1 M KI.

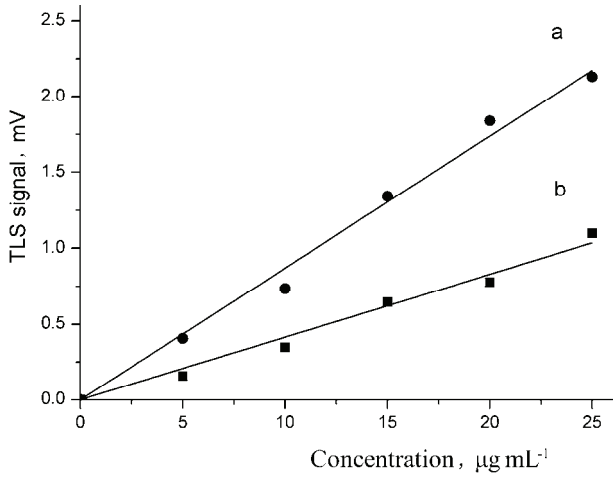

Fig. 11. Calibration curves for phycoerythrin in a) 0.5 M potassium iodide (k = 0.09 VL g^{-1}, R^2 = 0.9846) and b) in phosphate buffer – KPi, 0.1M (k = 0.04 VL g^{-1}, R^2 = 0.9734).

Currently, *LOD*s achieved by FIA-TLS compare favorably with recently reported techniques,[32] which could be used as early warning systems for microcystins and are based on detection of cyanopigments. Taking into account that on average one cyanobacterial cell (60 μm^3) produces about 0.2 pg of microcystin,[33] then 5000 cells mL^{-1} are required to reach the limit of 1 μg L^{-1} for microcystin in water. Using a conservative estimation of 1 % PE in the dry weight of cyanobacterial cells, which can actually reach up to 8 %,[7] and accepting that on average cyanobacteria contain 264 g dry weight μm^{-3},[34] then a comparable concentration of 0.8 μg L^{-1} PE for the maximum contaminant level (*MCL*) of microcystin could be calculated.

As demonstrated in this work, such low concentrations of PE are within the reach of FIA-TLS, which can easily detect early onsets of massive HABs in natural waters, where concentrations of cyanobacteria can peak at up to 1000 times higher levels as required to reach the *MCL* for microcystin.

It is however expected that further improvements in the sensitivity of phycoerythrin detection by TLS could be achieved by using higher concentrations of KI or other compounds for fluorescence quenching and to improve the thermo-optical properties of the analyzed samples, which will be the focus of future research. The achieved *LOD*s already indicate that TLS could represent a powerful tool for the detection of cyanobacteria in water.

CONCLUSIONS

The performances of two laser-based systems: TR-LIF and FIA-TLS for the detection of Cr-PE are presented. The fluorescence and thermal lens signals are complementary. The first one is generated *via* radiation relaxation and the second

via nonradiative relaxation. Hence, the combination of these two laser-based techniques could be suitable for the measurement of various physical quantities of phycobiliproteins with the aim of detecting the presence of cyanobacteria in water.

Acknowledgment. This work was realized within the projects MES RS OI 171020 and COST Action FA0906 "UV-B radiation: A specific regulator of plant growth and food quality in a changing climate (UV4growth)".

И З В О Д

ИСПИТИВАЊЕ И АНАЛИЗА Cr-ФИКОЕРИТРИНА ИЗ ЦИЈАНОБАКТЕРИЈЕ ЛАСЕРСКИМ ТЕХНИКАМА

БРАТИСЛАВ П. МАРИНКОВИЋ[1], AMBRA DELNERI[2], МАЈА С. РАБАСОВИЋ[1], МИРА ТЕРЗИЋ[3], MLADEN FRANKO[2] и ДРАГУТИН ШЕВИЋ[1]

[1]Институт за физику, Београд, п. пр. 68, Универзитет у Београду, [2]Laboratory for Environmental Research, University of Nova Gorica, Slovenia и [3]Природно–математички факултет, Универзитет у Новом Саду

Представљена је примена метода велике осетљивости – временски разложена ласерски индукована флуоресценција (TR-LIF) и систем за убризгавање у проток са спектрометријом термичког сочива (FIA-TLS) – на анализу Cr-фикоеритрина (Cr-PE) изолованог из посебне врсте цијанобактерије. У опсегу побуде таласних дужина (340––470 nm) флуоресцентни спектри показују изразит максимум на 575 nm. Запажен је такође и други максимум, на око 600 nm. Добијени резултати се користе за проверу техничких параметара за употребљену технику термичког сочива. Она је комплементарна спектрофлуорометрији, са мањом осетљивошћу у случају високих флуоресцентних квантних приноса и фотолабилних једињења.

(Примљено 17. априла 2013)

REFERENCES

1. M. E. van Apeldoorn, H. P. van Egmond, G. J. A. Speijers, G. J. I. Bakker, *Mol. Nutr. Food Res.* **51** (2007) 7
2. W. W. Carmichael, S. M. Azevedo, J. S. An, R. J. Molica, E. M. Jochimsen, S. Lau, K. L. Rinehart, G. R. Shaw, G. K. Eaglesham, *Environ. Health Perspect.* **109** (2001) 663
3. J. Pablo, S. A. Banack, P. A. Cox, T. E. Johnson, S. Papapetropoulos, W. G. Bradley, A. Buck, D. C. Mash, *Acta Neurol. Scand.* **120** (2009) 216
4. K. G. Sellner, G. J. Doucette, G. J. Kirkpatrick, *J. Ind. Microbiol. Biotechnol.* **30** (2003) 383
5. K. D. Hambright, T. Zohary, *Limnol. Oceanogr.* **45** (2000) 110
6. *Guidelines for drinking-water quality*, 4th ed., World Health Organization, Geneva, 2011
7. H. Rodriguez, J. Rivas, M. G. Guerrero, M. Losada, *Appl. Environ. Microbiol.* **55** (1989) 758
8. D. C. Nguyen, R. A. Keller, J. H. Jett, J. C. Martin, *Anal. Chem.* **59** (1987) 2158
9. S. Sekar, M. Chandramohan, *J. Appl. Phycol*, **20** (2008) 113
10. M. N. Kronick, *J. Immunol. Methods* **92** (1986) 1
11. W. G. Telford, M. W. Moss, J. P. Morseman, F. C. T. Allnutt, *Cytometry* **44** (2001) 16

12. D. A. McCarthy, in *Flow Cytometry: Principles and applications*, M. G. Macey Ed., Humana Press, Totowa, 2007, p. 78
13. M. B. Zrimec, J. Kožar Logar, A. Zrimec, L. Drinovec, M. Franko, A. Malej, *Cent. Eur. J. Biol.* **4** (2009) 313
14. J. K. Logar, A. Malej, M. Franko, *Instrum. Sci. Technol.* **34** (2006) 23
15. D. R. A. Hill, K. S. Rowan, *Phycologia* **28** (1989) 455
16. G. Novarino, *Hydrobiologia* **502** (2003) 225
17. P. Sanchez-Baracaldo, N. A. El Semary, P. K. Hayes, in *Unravelling the algae: the past, present, and future of algal systematics*, J. Brodie, J. Lewis, Eds., CTC Press, New York, 2007, Ch. 5, p. 93
18. L. Sun, S. Wang, L. Chen, X. Gong, *IEEE J. Selec*t. *Top. Quant. Electron.* **9** (2003) 177
19. M. Franko, C. D. Tran, *Rev. Sci. Instrum.* **67** (1996) 1
20. J. L. Lakowicz, *Principles of fluorescence spectroscopy*, 3rd ed., Springer, Berlin, 2006
21. M. Franko, *Appl. Spectrosc. Rev.* **43** (2008) 358
22. M. S. Rabasović, D. Sević, M. Terzić, B. P. Marinković, *Nucl. Instrum. Meth., B* **279** (2012) 16
23. C. H. Mazel, *Mar. Ecol. Prog. Ser.* **120** (1995) 185
24. H. M. Shapiro, *Practical flow cytometry*, 4th ed., Wiley-Liss, Hoboken, New York, 2003
25. H. Küpper, S. Seibert, P. Aravind, *Anal. Chem.* **79** (2007) 7611
26. J. Sepúlveda-Ugarte, J. E. Brunet, A. R. Matamala, J. Martínez-Oyanedel, M. Bunster, *J. Photochem. Photobiol., A* **219** (2011) 211
27. A. Chekalyuk, M. Hafe, *Limnol. Oceanogr-Meth.* **6** (2008) 591
28. H. Küpper, E. Andresen, S. Wiegert, M. Šimek, B. Leitenmaier, I. Šetlík, *Biochim. Biophys. Acta, Bioenerg.* **1787** (2009) 155
29. F. López Arbeloa, I. Urrecha Aguirresacona, I. López Arbelo, *Chem. Phys.* **130** (1989) 371
30. S. E. Bialkowski, *Photothermal Spectroscopy Methods for Chemical Analysis*, Wiley, New York, 1996
31. C. D. Tran, M. Franko, in *Encyclopedia of Analytical Chemistry*, R. A. Meyers, Ed., Wiley, Chichester, 2010
32. W. Schmidt, H. Petzoldt, K. Bornmann, L. Imhof, C. Moldaenke, *Water Sci. Technol.* **59** (2009) 1531
33. W. Hoogenboezem, A. J. Wagenvoort, K. Blaauboer, *The occurrence of toxic cyanobacteria in some Dutch surface waters used for the production of drinking water*, Vereniging van Rivierwaterbedrijven (RIWA), Nieuwegein, 2004
34. D. M. Mahlmann, J. Jahnke, P. Loosen, *Eur. J. Phycol.* **43** (2008) 355.

Journal of the Serbian Chemical Society
JSCS-info@shd.org.rs • www.shd.org.rs/JSCS

J. Serb. Chem. Soc. 79 (2) 199–209 (2014)
JSCS–4576

UDC 547.995.3+546.722'817+
539.196+543.552+66.087
Original scientific paper

A new electrochemical method for the determination of chondroitin sulfate based on its supramolecular interaction with the cupferron–lead(II) complex

XUELIANG NIU[1,2]*, PINGPING ZHANG[1,2], WEILI ZHANG[1,2] and WEI SUN[3]

[1]*Department of Pharmacy, Shangdong Wanjie Medical College, Zibo,255213, China,* [2]*Key Laboratory of Biomedical Engineering and Technology in the Universities of Shandong (Shangdong Wanjie Medical College), 255213, China and* [3]*College of Chemistry and Molecular Engineering, Qingdao University of Science and Technology, Qingdao,266042, China*

(Received 19 February, revised 25 April 2013)

Abstract: In this paper, the interaction of cupferron (Cup) and its lead(II) complex [Cup–Pb(II)] with chondroitin sulfate (CS) was investigated by the linear sweep voltammetric method. In the selected medium of pH 5.5 (acetic acid––hexamine buffer solution), Cup can interact with Pb(II) to form a stable complex of [Cup–Pb(II)], which has a sensitive second order derivative polarographic reductive peak at –0.64 V *vs.* SCE. After the addition of CS into a solution of the Cup–Pb(II) complex, the reductive peak current decreased without any shift of the peak potential and no new peak appeared, which indicated that a non-electroactive supramolecular complex of CS with [Cup–Pb(II)] was formed. The binding reaction conditions were carefully investigated. The interaction mechanism under the optimal conditions was discussed. The decrease of reductive peak current, I_p'', was directly proportional to the CS concentration, thus a new quantitative determination method for CS was established with the linear regression equation as $\Delta I_p''$ / nA =36.97(c / mg L^{-1}) + + 12.45 (n = 10, γ = 0.995). The effects of other substances on the determination were carefully investigated and three synthetic samples were determined with satisfactory results. The binding constant (β_s) and the binding number (m) of CS with [Cup–Pb(II)] complex were calculated from the voltammetric data with the results $\beta_s = 1.89\times10^{10}$ and $m \approx 2.5$.

Keywords: cupferron; lead(II); chondroitin sulfate; linear sweep voltammetry; interaction.

* Corresponding author. E-mail: xueliangniu@163.com
doi: 10.2298/JSC130219048N

INTRODUCTION

Chondroitin sulfate (CS) is a glycosaminoglycan with a disaccharide unit of *β*-D-galactosamine and *β*-D-glucuronic acid.[1] CS was first extracted from cartelage in 1984 and it was reported to have many important biological and pharmacological activities, such as anticoagulant and anticancer properties, anti-inflammatory activity, lipid metabolism promotion, osteoporosis treatment, *etc*.[2,3] Thus, in clinical therapy CS has been used as an effective medicine for the treatment of chronic diseases such as rheumatism, degenerative arthritis, lumbago, gastric ulcer, cirrhosis and chronic photo damage.[4] Recently, more biomedical activities, including drug delivery, tissue engineering, regenerative medicine and surgery, have been reported.[5–7]

The determination of the content of polysaccharide is the most efficient way to inspect the effective components of a product in the quality control of polysaccharide drug, as well as the best stable basis for a study of drug stability. Therefore, it is significant to establish a sensitive method for the determination of CS. Nowadays, many different kinds of analytical methods have been proposed for CS determination, such as the Elson–Morgan method,[8,9] spectrophotometry,[10,11] HPLC[12–14] and electrophoretic methods.[15–17] However, these methods often suffer from some disadvantages, such as low sensitivity, poor selectivity or a complicated procedure. Owing to the advantages of higher sensitivity, wider liner range, faster response and cheaper instrumentation, electrochemical methods have drawn much attention and have been used to determine successfully different kinds of biomolecules, such as DNA,[18,19] RNA,[20] protein,[21,22] heparin[23,24] and chondroitin sulfate.[25] However, most of the papers were based on the interaction of the biomolecules with electroactive substances. To the best of our knowledge, they are seldom based on the interaction of biomolecules with metal complexes.

As a commonly used organic compound, cupferron (Cup) can form stable complexes with many metals, which has been widely applied for the determination of trace metal elements, such as Cr, Al, Pb, Zn, *etc*., by spectrophotometry and electrochemical methods.[26–29] The metal complexes can also form a polarographic adsorption wave on a mercury working electrode, which can be used for the sensitive detection of metal ions.[30] Sun *et al*. studied the interaction between Cup and Cd(II) and a new electrochemical method for determining proteins was established by using the complex of [Cup–Cd(II)] as a voltammetric probe.[31]

In this work, Pb(II) was selected to interact with Cup and a stable electrochemically active complex of [Cup–Pb(II)] was formed, which showed a sensitive and stable voltammetric reductive peak at –0.64 V (*vs*. SCE) on a dropping mercury working electrode. The polarographic behaviors of the [Cup–Pb(II)] complex was carefully investigated on a dropping mercury electrode.[32] Thus, the [Cup–Pb(II)] complex was selected as an electrochemical probe to study the

binding reaction with CS and its further use to determine CS. The addition of CS into a solution of the [Cup–Pb(II)] complex resulted in a decrease in the concentration of the free [Cup–Pb(II)] complex in solution and consequently a decrease in the electrochemical response without any change of the peak potential, which indicated that the [Cup–Pb(II)] complex could interact with CS to form a supramolecular complex. The decrease in the electrochemical response was directly proportional to the CS concentration; thus, a new sensitive analytical method for CS determination was established.

EXPERIMENTAL

Apparatus

The second order derivative linear sweep voltammetric measurements were performed on a model JP-303 polarographic analyzer (Changed Apparatus Factory, China) with a conventional three-electrode system, composed of a dropping mercury electrode as the working electrode (DME), saturated calomel as the reference electrode (SCE) and a platinum wire as the auxiliary electrode. A pHS-25 acidimeter (Shanghai Leici Instrument Factory, China) was used for the pH measurement. All the experiments were performed at 25±1 °C. All potentials in the paper are expressed against SCE.

Reagents

Chondroitin sulfate (CS, 99 %, Shandong Linyitianli Biochemical Company, China) was used as received without further purification. A 1.0 mg mL^{-1} stock solution of CS was prepared by directly dissolving 0.1000 g of CS in water, then diluting to the mark in a 100-mL volumetric flask and stored at 4 °C. The working solutions were obtained by directly diluting the stock solution with water. A 1.0×10^{-3} mol L^{-1} solution of cupferron (Cup, Shanghai Far Navigation Chemical Reagent Factory, China) was prepared by dissolving 0.0155 g Cup in water and diluting to 100 mL. A 1.0×10^{-3} mol L^{-1} solution of lead nitrate (Shanghai Jinshan Chemical Plant, China) was prepared by dissolving 0.0333 g of the substance in water and diluting to 100 mL. A 1.0 mol L^{-1} acetic acid–hexamine buffer solution was used to control the acidity of reaction solutions. The buffer solution was prepared by mixing 34.05 g of hexamine diluted to 250 mL and adjusting the pH to 5.5 by diluting with 1.0 mol L^{-1} acetic acid (HAc). All of other employed reagents were of analytical reagent grade and doubly distilled water was used throughout.

Procedure

Into a dry 10 mL calibrated tube, the following reaction solutions were added in the following order: 1.5 mL of pH 5.5 HAc–hexamine buffer, 0.5 mL of 1.0×10^{-3} mol L^{-1} Cup, 0.25 mL 1.0×10^{-3} mol L^{-1} Pb (II) and an appropriate amount of CS or sample solution. The mixtures were diluted to the mark with water, mixed thoroughly and allowed to stand for 20 min at 25 °C. A blank solution was also prepared by the same procedure but without the addition of CS. Then the solution was transferred to a 10 mL electrochemical cell and the second order derivative linear sweep polarographic curve was recorded over the potential range from –0.3 to –0.8 V *vs.* SCE. The values of peak current of the [Cup–Pb(II)] complex in the presence (I_p'') and absence ($I_{p,0}''$ of CS at –0.64 V were measured, and the difference in the peak currents ($\Delta I_p'' = I_{p,0}'' - I_p''$) was used for CS determination.

RESULTS AND DISCUSSION

Second order derivative linear sweep polarogram

The second order derivative linear sweep polarograms of HAc–hexamine, Cup, Pb(II) and their mixture with CS are shown in Fig. 1. Curve 1 is the polarogram of the HAc–hexamine buffer solution and no polarographic peak appeared, which indicated that no electroactive substances existed in the HAc––hexamine buffer. Curve 2 is the polarogram of the Cup solution; a reductive peak at –0.54 V was obtained, resulting from the reduction of Cup on the mercury electrode. Curve 3 is the polarogram of Pb(II); no peak appeared in the scanned potential range. Curve 4 is the polarogram of the Cup–Pb(II) solution; a new well-defined polarographic reductive peak at –0.64 V was obtained, which was due to the interaction between Cup and Pb(II) and the deoxidization of the newly formed complex [Cup–Pb(II)] on the mercury electrode. Curve 5 and 6 are the polarograms of the mixture of different amount of CS with [Cup–Pb(II)]. Owing to the interaction of CS with [Cup–Pb(II)], the concentration of free [Cup–Pb(II)] in solution decreased, resulting in decreases in the reductive peak current. The decrease in the peak current was proportional to the concentration of CS, which could be further utilized for the determination of CS.

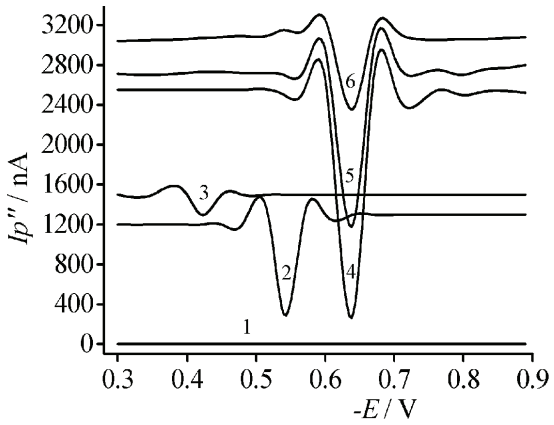

Fig. 1. Second order derivative linear sweep voltammograms of the Cup–Pb(II)–CS interaction system. 1. pH 5.5, HAc–hexamine; 2. 1 + 5.0×10^{-5} mol L^{-1} Cup; 3. 1 + 2.5×10^{-5} mol L^{-1} Pb(II); 4. 1 + 5.0×10^{-5} mol L^{-1} Cup + 2.5×10^{-5} mol L^{-1} Pb(II); 5. 4 + 10.0 mg L^{-1} CS; 6. 4+20.0 mg L^{-1} CS. The potentials are expressed *vs.* SCE.

Optimal reaction conditions

The influence of the reaction conditions, such as the acidity of the buffer solution, the ratio of Cup and Pb(II) concentrations, reaction time, reaction temperature, the instrumental conditions, the ion strength, *etc*., were carefully investigated.

The effect of buffer acidity on the difference of peak current ($\Delta I_p''$) was investigated by keeping the Cup, Pb(II) and CS concentration constant and changing the buffer pH in the range from 3.5 to 6.5. The results are shown in Fig. 2, from which, it can be seen that the value of $\Delta I_p''$ reached its maximum at pH 5.5; hence, pH 5.5 was selected for this assay. The volume of HAc–hexamine buffer solution added into the solution was investigated in the volume range of 1.0–5.0 mL and 1.5 mL was found suitable for the following procedures.

The effect of the ratio of Cup and Pb(II) on the value of $\Delta I_p''$ was studied by keeping CS concentration at 20.0 mg L^{-1}, the Cup concentration at 5.0×10^{-5} mol L^{-1} and changing the Pb(II) concentration. The results showed that the value of $\Delta I_p''$ reached its maximum when the Pb(II) concentration was 2.5×10^{-5} mol L^{-1}. Hence, the ratio of Cup to Pb(II) was kept constant at 2:1 in the following experiments.

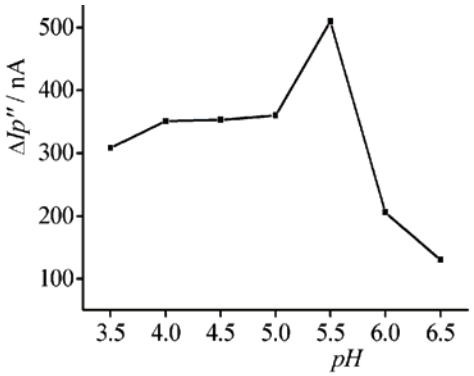

Fig. 2. The influence of pH on the binding interaction; 5.0×10^{-5} mol L^{-1} Cup + 2.5×10^{-5} mol L^{-1} Pb(II) +15.0 mg L^{-1} CS in different pH (HAc–hexamine buffer) solutions.

After mixing Cup, Pb(II) with CS, the value of $\Delta I_p''$ reached the maximum within 20 min and remained constant for about 2 h. Thus, the system gave sufficient time for routine experiments.

The influence of adding order of Cup, Pb(II), CS and buffer on the value of $\Delta I_p''$ was also studied. The order Cup, Pb(II), buffer and CS was selected as the optimal adding order, which indicated that the formation of the [Cup–Pb(II)] complex was the key for the binding reaction.

The effect of the reaction temperature on the interaction was also tested in the range of 10–40 °C. The results showed that there were no obviously differences on $\Delta I_p''$ in the selected temperature range. Therefore, the reaction temperature had little influence on the interaction and 25 °C was used throughout.

The effect of instrumental conditions, such as the scan rate and the dropping mercury standing time (the lifetime of the mercury drop) were tested. As shown in Fig. 3, the results indicated that the value of $\Delta I_p''$ increased with increasing

potential scan rate in the range of 300 to 1000 mV s^{-1} and mercury drop time. However, the mercury drop would fall down naturally when the dropping mercury standing time exceeded 24 s. Hence, the scan rate and the standing time were selected as 1000 mV s^{-1} and 22 s, respectively.

The effect of NaCl concentration on this assay was also examined and the results are shown in Fig. 4, from which it could be seen that the presence of NaCl had a significant influence on the interaction. The value of $\Delta I_p''$ decreased with increasing salt concentration in the range 0.01–0.2 mol L^{-1}, which proved that the interaction of [Cup–Pb(II)] with CS was mainly caused by electrostatic attraction. The electrostatic shielding effect of the charges on binding reaction with the increasing Na^+ concentration was detrimental to the formation of the CS–Cup–Pb(II) complex.

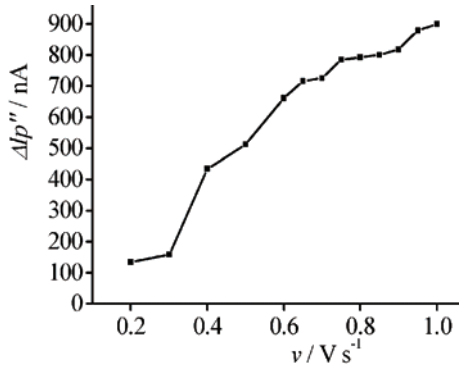

Fig. 3. The influence of scan rate on the binding interaction. 5.0×10^{-5} mol L^{-1} Cup + 2.5×10^{-5} mol L^{-1} Pb(II) + 15.0 mg L^{-1} CS in pH 5.5 HAc–hexamine buffer.

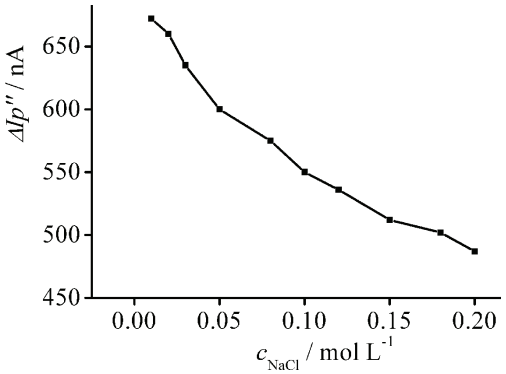

Fig. 4. The effect of NaCl concentration on the binding interaction. 5.0×10^{-5} mol L^{-1} Cup + 2.5×10^{-5} mol L^{-1} Pb(II) + 15.0 mg L^{-1} CS and different amount of NaCl in pH 5.5 HAc–hexamine buffer.

Influences of co-existing substances

The influences of co-existing substances on the determination of 15.0 mg mL^{-1} CS were also tested and the results are listed in Table I. They show that the commonly present substances such as metal ions, amino acids and glucose, had little effects on the determination.

TABLE I. Influence of co-existing substances on the determination of 15.0 mg L^{-1} CS

Co-existing substance	Concentration mg L^{-1}	Relative error, %	Co-existing substance	Concentration mg L^{-1}	Relative error, %
Ni^{2+}	2.0×10^{-6} mol L^{-1}	0.62	L-Glutamate	1.0	–1.55
Zn^{2+}	2.0×10^{-6} mol L^{-1}	–7.57	L-Glutamine	1.0	3.40
SDS	1.0	10.51	L-Valine	1.0	4.02
β-CD	1.0	–10.05	L-Arginine	1.0	1.22
RNA	1.0	–8.04	L-Cysteine	1.0	4.82
HSA	1.0	2.94	L-Leucine	1.0	0.93
DNA	1.0	4.79	Glycin	1.0	–2.78
Glucose	1.0	1.24	L-Tyrosine	1.0	4.50

Calibration curve

Under the optimal conditions, a calibration curve for CS determination, Fig. 5, was obtained in the concentration range of 1.0–25.0 mg L^{-1} with the linear regression equation: $\Delta I_p''$ / nA = 36.97(c / mg L^{-1}) + 12.45 (n = 10, γ = 0.995). The relative standard deviation (*RSD*) for eleven parallel determinations of 15.0 mg L^{-1} CS was 2.59 % and the detection limit was calculated as 0.69 mg L^{-1} (3σ).

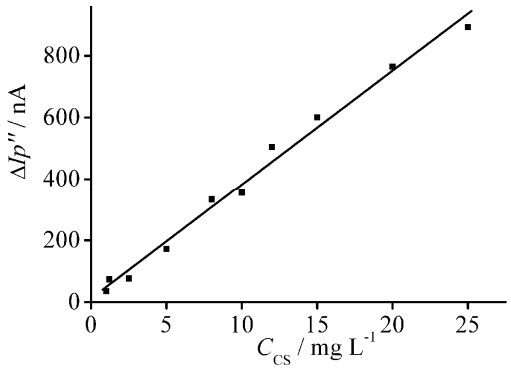

Fig. 5. Relationship between the difference in the peak current and the concentration of CS. 5.0×10^{-5} mol L^{-1} Cup + 2.5×10^{-5} mol L^{-1} Pb(II) and different amount of CS in pH 5.5 HAc–hexamine buffer.

Sample determinations

Three synthetic samples containing CS, metal ions, amino acids, *etc*. were analyzed by the proposed method with the results listed in Table II. It can be seen

that this new method was practical and reliable in the determination of CS in synthetic samples with a recovery in the range of 94.3–105.8 %.

Stoichiometry of CS–Cup–Pb (II) complex

According to a method given in the literature,[33] the binding number and the equilibrium constant of the supramolecular complex were determined. It was presumed that Cup–Pb(II) interacting with CS formed only a single complex of CS–*m*Cup–Pb(II). The binding number (*m*) and the equilibrium constant (β_s) of the binding reaction could be calculated from the following equations:

$$\text{CS}+m\text{Cup–Pb(II)} \rightarrow \text{CS}–m\text{Cup–Pb(II)} \quad (1)$$

The equilibrium constant was deduced as follows:

$$\beta_s = \frac{[\text{CS-}m\text{Cup-Pb}]}{[\text{CS}][\text{Cup-Pb}]^m} \quad (2)$$

Since:

$$\Delta I_{max} = kc_{CS} \quad (3)$$

$$\Delta I = k[\text{CS}–m\text{Cup–Pb(II)}] \quad (4)$$

$$[\text{CS}] + [\text{CS}–m\text{Cup–Pb(II)}] = c_{CS} \quad (5)$$

Therefore:

$$\Delta I_{max}–\Delta I = k(c_{CS}–[\text{CS}–m\text{Cup–Pb(II)}]) = [\text{CS}] \quad (6)$$

Combination of Eqs. (2), (4) and (6) gives:

$$\log [\Delta I / (\Delta I_{max} – \Delta I)] = \log \beta_s + m\log [\text{Cup–Pb(II)}] \quad (7)$$

where ΔI is the difference of the peak current in the presence and absence of CS and ΔI_{max} corresponds to the obtained value when the concentration of [Cup––Pb(II)] is much higher than that of CS. CCS, [CS], [CS–*m*Cup–Pb(II)] correspond to the total, free and bound concentration of CS in the solution, respectively.

TABLE II. Determination results of CS in synthetic samples (n = 5); conditions: L-glutamine, L-leucine, glucose, L-arginine and glutamic acid, 1.0 mg L^{-1}; Ni^{2+}, Mg^{2+} and Ni^{2+}, 2.0×10^{-6} mol L^{-1}

Sample	Foreign co-existing substances	Added mg L^{-1}	Found mg L^{-1}	Recovery %	*RSD* %
1	L-Glutamine, L-leucine, glucose, Mg^{2+}	10.0	9.43	94.3	3.84
2	L-Arginine, glutamic acid, Mg^{2+}, Ni^{2+}	10.0	9.68	96.8	0.51
3	L-Arginine, glutamic acid, Mg^{2+}, Ni^{2+}	20.0	21.16	105.8	1.12

The relationships between I_p'', $\Delta I_p''$ ($I_p1'' – I_p2''$) and the concentration of CS are shown in Fig. 6. The relationship of log [ΔI / ($\Delta I_{max} – \Delta I$)] with log [Cup–

–Pb(II)] is shown in Fig. 7. From the intercept and the slope $m \approx 2.5$ and β_s = = 1.89×10^{10}, respectively, were deduced. The results indicate that a 2:5 complex of 2CS–5Cup–Pb(II) was formed under the selected conditions.

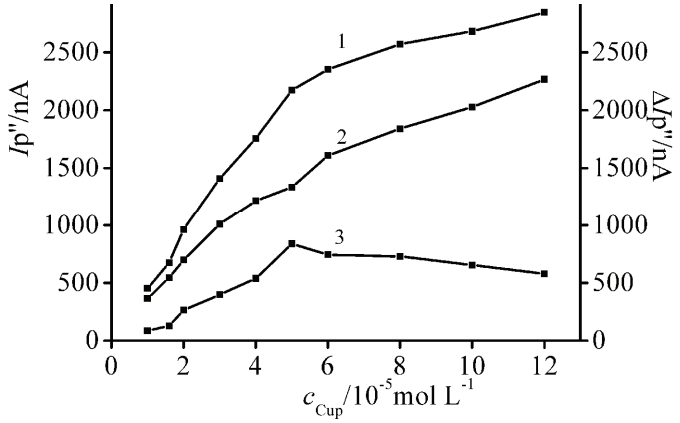

Fig. 6. Relationship between I_p'' and $c_{complex}$ (1 and 2) and $\Delta I_p''$ and $c_{complex}$ (3). 1) $c_{CS} = 0$, 2) $c_{CS} = 15$ mg L^{-1}, 3) $\Delta I_p'' = I_{p1}'' - I_{p2}''$.

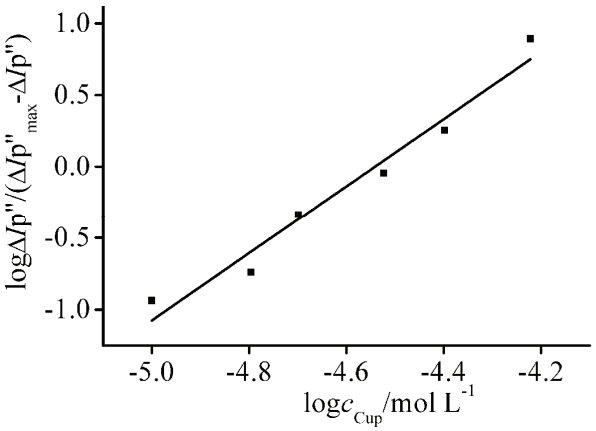

Fig. 7. A plot of log ($\Delta I/(\Delta I_{max} - \Delta I)$) against log [Pb(II)].

CONCLUSIONS

This paper described a new electroanalytical method for the determination of CS by using Cup–Pb(II) as an electrochemical probe. The interaction of Cup with Pb(II) in the solution formed a stable complex, which had a sensitive linear sweep voltammetric peak at –0.64 V *vs.* SCE. The addition of CS into the Cup––Pb(II) solution caused a decrease of the reductive peak current of Cup–Pb(II) without a change in the peak potential, indicating a new supramolecular complex

had been formed. The binding interaction of CS with [Cup–Pb(II)] could be further applied to the determination of micro-amounts of CS with satisfactory results.

Acknowledgements. This work received financial support from the National Natural Science Foundation of China (No. 20635020) and a project of the Shandong Province Higher Educational Science and Technology Program (No. J11LB60).

ИЗВОД

НОВА ЕЛЕКРОХЕМИЈСКА МЕТОДА ЗА ОДРЕЂИВАЊЕ ХОНДРИТИН-СУЛФАТА БАЗИРАНА НА СУПРАМОЛЕКУЛАРНОЈ ИНТЕРАКЦИЈИ СА [КУПФЕРОН– Pb(II)] КОМПЛЕКСОМ

XUELIANG NIU[1,2], PINGPING ZHANG[1,2], WEILI ZHANG[1,2] и WEI SUN[3]

[1]Department of Pharmacy, Shangdong Wanjie Medical College, Zibo,255213, China, [2]Key Laboratory of Biomedical Engineering and Technology in Universities of Shandong (Shangdong Wanjie Medical College), 255213, China и [3]College of Chemistry and Molecular Engineering, Qingdao University of Science and Technology, Qingdao,266042, China

Испитивана је интеракција купферона (Cup) и Pb (II) комплекса [Cup–Pb(II)] са хондритин-сулфатом (CS) помоћу волтаметрије са линеарном променом потенцијала. У медијуму pH 5,5 (пуфер сирћетна киселина–хексамин), Cup реагује са Pb(II) формирајући стабилан комплекс [Cup–Pb(II)], који даје осетљив поларографски редукциони пик другог реда на –0.64 V према ЗКЕ. После додатка CS у раствор комплекса [Cup––Pb(II)], струја редукционог пика се смањује без померања и без појаве новог пика, што указује на формирање електрохемијски неактивног супрамолекуларног комплекса CS са [Cup–Pb(II)]. Услови ове реакције су детаљно испитивани. Дискутован је механизам интеракције под оптималним условима. Смањење струје редукционог пика је директно пропорционално концентрацији CS, па је постављена нова квантитативна метода за одређивање CS, са линеарном регресионом једначином $\Delta Ip''$ / nA = 36,97(c / mg L^{-1}) + + 12,45 (n = 10, γ = 0,995). Испитиван је ефекат утицаја других супстанци на одређивање и анализирана су три синтетичка узорка са задовољавајућим резултатима. Из волтаметријских података израчунати су константа формирања (β_s) и број везаних CS (m) са комплексом [Cup–Pb(II)] и износе $\beta_s = 1{,}89\times10^{10}$ и $m \approx 2{,}5$.

(Примљено 19. фебруара, ревидирано 25. априла 2013)

REFERENCES

1. T. Maruyama, T. Toida, T. Imanari, *Carbohydr. Res.* **306** (1998) 35
2. J. S. Sim, A. R. Im, S. M. Cho, H. J. Jang, J. H. Jo, Y. S. Kim, *Food. Chem.* **101** (2007) 532
3. G. M. Campo, A. Avenoso, S. Campo, A. D. Ascola, P. Traina, D. Sama, *J. Cell. Biochem.* **106** (2009) 83
4. S. L. Xiong, A. L. Li, Z. Jin, M. Chen, *J. Food. Biochem.* **1** (2007) 356
5. R. F, Andre, F. P. Juliana, F. R. Adley, C. M. Edvani, *Carbohydr. Polym.* **80** (2010) 934
6. S. Iossif, N. Zayna, A. Karun, N. Thao, E. Jennifer, *Biomaterials* **31** (2010) 2788
7. S. L. Xiong, A. L. Li, N. Huang, *Adv. Mater. Res.* **152–153** (2011) 399
8. L. Z. Li, Y. J. You, S. H. Lu, *Biopharmaceutics*, Chinese Medical Science Press, Beijing, 1991, p. 295
9. N. Volpi, M. Cusmano, T. Venturelli, *Biochim. Biophys. Acta* **1243** (1995) 49

10. Y. Y. Chen, Z. L. Jiang, Z. Z .Li, S. M. Zhou, S. J. Sun, *Spectrosc. Spect. Anal.* **26** (2006) 1148
11. Z. P. Cui, X. L. Hu, S. P. Liu, Z. F. Liu, *Spectrochim. Acta, A* **83** (2011) 1
12. F. Grøndahl, H. Tveit, L. K. Akslen-Hoel, K. Prydz, *Carbohydr. Res.* **346** (2011) 50
13. N. Volpi, *Anal. Biochem.* **397** (2010) 12
14. P. F. Jin, J. Ma, X. J. Wu, D. Zou, C. H. Sun, X. Hu, *J. Pharmaceut. Biomed.* **50** (2009) 293
15. A. Zinellu, S. Sotgia, M. F. Usai, E. Zinellu, A. J. Lepedda, L. Deiana, M. Formato, C. Carru, *Anal. Bioanal. Chem.* **391** (2008) 2865
16. A. Zinellu, S. Pisanu, E. Zinellu, A. J. Lepedda, G. M. Cherchi, S. Sotgia, C. Carru, L. Deiana, M. Formato, *Electroanalys* **28** (2007) 2439
17. N. Volpi, F. Maccari, R. J. Linhardt, *Anal. Biochem.* **388** (2009) 140
18. M. Kobayashi, T. Kusakawa, M. Saito, S. Kaji, M. Oomura, S. Iwabuchi, Y. Morita, Q. Hasan, E. Tamiya, *Electrochem. Commun.* **4** (2004) 337
19. Q. X. Wang, M. X. Zheng, J. L. Shi, F. Gao, F. Gao, *Electroanalysis* **23** (2012) 915
20. W. L. Zhang, X. L. Niu, N. Zhao, W. Sun, *J. Serb. Chem. Soc.* **74** (2009) 1467
21. W. Sun, N. Zhao, K. Jiao, *Indian J. Chem., A* **46** (2007) 280
22. W. Sun, K. Jiao, X. L. Wang, L. D. Lu, *Electroanalysis* **17** (2005) 162
23. W. Sun, Y. Q. Ding, Q. X. Wang, K. Jiao, *Electroanalysis* **18** (2006) 1114
24. W. Sun, Y. Q. Ding, K. Jiao, *Chem. Res. Chinese. Univ.* **22** (2006) 406
25. W. Sun, N. Zhao, K. Jiao, *J. Indian Chem. Soc.* **84** (2007) 1
26. O. Abollino, M. Aceto, E. Mentasti, C. Sarzanini, C. M. G. Berg, *Electroanalysis* **9** (1997) 444
27. A. I. Popov, W. W. Wendlandt, *Anal. Chem.* **26** (1954) 883
28. M. Yaman, *Mikrochim. Acta* **129** (1998) 115
29. D. Nonova, K. Stoyanov, *Mikrochim. Acta* **74** (1980) 171
30. X. X. Gao, *Polarographic Catalytic Wave*, Scientific Press, Beijing, 1991
31. N. Hui, J. S. Wang, W. Sun, *Electroanalysis* **22** (2010) 536
32. S. Z. Luo, K. Jiao, *J. Qingdao. Univ. Sci-Tech. (Nat. Sci.)* **28** (1992) 527
33. W. Sun, K. Jiao, *Talanta* **56** (2002) 1073.

Journal of the Serbian Chemical Society
JSCS-info@shd.org.rs • www.shd.org.rs/JSCS

J. Serb. Chem. Soc. 79 (2) 211–224 (2014)
JSCS–4577

UDC 678.562+544.773432+
661.717.53:535.65:543.57
Original scientific paper

Preparation and properties of fast temperature-responsive soy protein/PNIPAAm IPN hydrogels

YONG LIU[1]*, YINGDE CUI[2]**, GUOJIE WU[2] and MIAOCHAN LIAO[3]

[1]*School of Chemistry and Chemical Engineering, Zhaoqing University, Zhaoqing 526061, China,* [2]*Institute of Green Chemical Engineering, Zhongkai University of Agriculture and Engineering, Guangzhou 510225, China and* [3]*Department of Logistics Management, Zhaoqing University, Zhaoqing 526061, China*

(Received 19 February, revised 25 April 2013)

Abstract: The interpenetrating polymer network of fast temperature-responsive hydrogels based on soy protein and poly(*N*-isopropylacrylamide) were successfully prepared using sodium bicarbonate ($NaHCO_3$) solutions as the reaction medium. The structure and properties of the hydrogels were characterized by Fourier transform infrared spectroscopy, scanning electron microscopy, differential scanning calorimetry and thermal gravimetric analysis. The swelling and deswelling kinetics were also investigated in detail. The results showed that the proposed hydrogels had a highly porous structure, good miscibility and thermal stability, and a fast temperature response. The presence of $NaHCO_3$ had little effect on the volume phase transition temperature (VPTT) of the hydrogels, and the VPTTs were at about 32 °C. Compared with the traditional hydrogels, the proposed hydrogels had much faster swelling and deswelling rates. The swelling mechanism of the hydrogels was non-Fickian diffusion. These fast temperature-responsive hydrogels may have potential applications in the field of biomedical materials.

Keywords: soy protein; poly(*N*-isopropylacrylamide); hydrogels; fast response.

INTRODUCTION

Stimuli-responsive hydrogels have attracted more and more attention in biomedical and pharmaceutical fields.[1] Increasing interest in a new class of materials based on blends of natural and synthetic polymers has been observed during the last three decades,[2–4] as the blends have the advantages of both natural and synthetic polymers. In recent years, natural polymers due to their renewability, biodegradability and biocompatibility have attracted great interest in blending with stimuli-responsive polymers for biomedical applications.[2,5] An effective

*,** Corresponding authors. E-mail: (*)lygdut@163.com; (**)cuizku@gmail.com
doi: 10.2298/JSC130219047L

method to prepare these blends is the interpenetrating polymer network (IPN) technology.[6,7] Recently, poly(*N*-isopropylacrylamide) (PNIPAAm), a typical temperature-responsive polymer with a volume phase transition temperature (VPTT) around 32 °C, has been utilized to blend with some natural polymers using IPN technology to develop new temperature-responsive hydrogels for biomedical utilization.[8–11]

It is noteworthy that natural proteins have also been the subject of significant interest in the design of biomedical materials in recent years. Some animal proteins, such as collagen, gelatin, casein, albumin and whey protein, have been investigated for drug, nutrient, and bioactive peptide delivery.[12] Soy protein, a very important plant protein, was used to blend with other polymers for drug delivery[13,14] and wound dressing materials.[15] However, plant proteins, particularly soy protein, as new devices for drug delivery have not been fully investigated.

It is well known that the response rate of stimuli-responsive hydrogels is one of the most important parameters for evaluating their performance. Hydrogels with a slow response rate may be limited in their applications. Therefore, various strategies have been proposed to improve the response rate. These strategies include the introduction of comb-type grafted chains,[16,17] the fabrication of microgels[18] or nanogels,[19,20] and the formation of macroporous structures in hydrogel matrices using pore-forming agents,[21,22] foaming agents[23,24] and phase separation technologies.[25,26]

In a previous work, the preparation and properties of soy protein/PNIPAAm IPN hydrogels were discussed.[27] In this work, a new strategy was developed to obtain fast responsive soy protein/PNIPAAm IPN hydrogels using phase separation and foaming agent technologies. The structure and properties of the proposed hydrogels were studied by Fourier transform infrared spectroscopy (FTIR), scanning electron microscopy (SEM), differential scanning calorimetry (DSC) and thermal gravimetric analysis (TGA), and their swelling and deswelling kinetics were also investigated in detail.

EXPERIMENTAL

Materials

Soy protein isolate (SPI, protein content > 95 %) was kindly provided by Dupont Yunmeng Protein Ltd., China. *N*-Isopropylacrylamide (NIPAAm) was purchased from Tokyo Chemical Industry Co. Ltd., Japan. Ammonium persulfate (APS) was obtained from Yongda Chemical Reagent Ltd., China. *N*,*N*′-Methylenebisacrylamide (BIS, a crosslinking agent for NIPAAm), glutaraldehyde (GA, a crosslinking agent for SPI) and sodium bicarbonate ($NaHCO_3$) were supplied by Kermel Chemical Reagent Ltd., China. Tetramethylethylenediamine (TEMED) was purchased from Qianjin Chemical Reagent Ltd., China. All reagents were of analytical grade.

Preparation of hydrogels

A certain amount of $NaHCO_3$ was added into a mixture composed of NIPAAm (2.0 g), SPI (0.4 g) and deionized water (15 mL) and dissolved completely. The mixture was bubbled with nitrogen and then GA (0.2 mL), BIS (0.04 g), APS (0.02 g) and TEMED (20 μL) were added in order. Finally, this mixture was injected immediately into poly(vinyl chloride) tubes (6 mm diameter) to polymerize at 15 °C in a low temperature reactor for 24 h. The hydrogels obtained were cut into pieces of 3 mm in length and put into 0.1 mol L^{-1} HCl solutions until bubble formation ceased. Then, the hydrogels were taken out from HCl solutions and immersed in deionized water for three days. The deionized water was refreshed every 4 h during this period. The swollen hydrogels were dried at room temperature and further dried at 40 °C in a vacuum oven for three days. The sample code, PNS0, PNS1, PNS2 and PNS3 means that the amount of $NaHCO_3$ in the above mixture was 0.0, 0.2, 0.3 and 0.4 g, respectively.

FTIR spectroscopy

The FTIR spectra (Equinox 55, Bruker, Germany) of the vacuum-dried samples were recorded. Each sample was ground with KBr (ratio of sample to KBr 1:100) and compressed into a pellet. The spectra were recorded in the transmission mode as an average of six scans at a resolution of 0.2 cm^{-1}.

Morphology investigation

The hydrogels swollen to equilibrium in deionized water at 25 °C were first frozen at –40 °C for 10 h, and then freeze-dried for 24 h using a SHKY LGJ-18 freeze-dryer (China). Cross-sections of the freeze-dried gels were sputter-coated with gold and the morphologies of the coated gels were examined using an SEM (Quanta 400F, FEI, The Netherlands) operated at an acceleration voltage of 20 kV.

Differential scanning calorimetry investigation

The glass transition temperatures (T_g) of the dried samples were determined by differential scanning calorimetry (DSC 204, Netzsch, Germany). All samples were first heated from room temperature to 120 °C at a rate of 20 °C min^{-1} under a nitrogen atmosphere and then cooled to room temperature. The samples were then reheated to 180 °C at 10 °C min^{-1}. The T_g of the samples was determined from the second cycle. The midpoint of the inflection was taken as the T_g.

Thermal gravimetric measurement

The thermal stability of the hydrogels was examined using a thermal gravimetric analyzer (TG 209, Netzsch, Germany). All vacuum-dried samples were heated from room temperature to 700 °C under a nitrogen atmosphere at a heating rate of 10 °C min^{-1}.

Swelling kinetics measurements

Pre-weighed dried hydrogels were immersed in deionized water to swell. At regular time intervals, the swelling hydrogels were taken out to weigh after removal of the surface water through blotting with filter paper and then put back into the same vials. The swelling ratio (*SR*) was calculated using the following equation:

$$SR = \frac{M_t - M_d}{M_d} \times 100 \quad (0)$$

where M_d is the weight of a dried hydrogel and M_t is the weight of the swollen hydrogel at time *t*.

Measurement of the deswelling kinetics

The swollen hydrogels at equilibrium in deionized water at 25 °C were weighed and then immersed in deionized water at 37 °C to deswell. At regular time intervals, the hydrogels were taken out to weigh and then put back into the same vials. The water retention (*WR*) was defined as the deswelling ratio and was calculated using the following equation:

$$WR = \frac{M_t - M_d}{M_e - M_d} \times 100 \quad (2)$$

where M_d is the weight of a dried hydrogel, M_t is the weight of the swollen hydrogels at the time *t* and M_e is the weight of the swollen hydrogels at the equilibrium state at 25 °C.

RESULTS AND DISCUSSION

Preparation of hydrogels

According to the preparation strategy, fast temperature-responsive soy protein/PNIPAAm IPN hydrogels were obtained through the following two steps. First, the polymerization was performed in $NaHCO_3$ solutions. During the reaction, the presence of $NaHCO_3$ led to phase separation and consequently made the polymer chains curled, intertwisted together and finally agglomerated due to the salt effect,[28] which resulted in the formation of a heterogeneous porous structure.[29] Second, after the polymerization, the $NaHCO_3$ in the hydrogel network was used as a foaming agent. When the hydrogels were removed, cut into pieces and put into HCl solution, carbon dioxide gas was generated due to the reaction between $NaHCO_3$ and HCl, which was released from the hydrogel matrix, resulting in the formation of a highly porous structure. As a result, the proposed hydrogels (PNS1, PNS2 and PNS3) with fast response rates were accordingly achieved.

Structure and morphology analysis

The FTIR spectra of PNS0 (prepared in the absence of $NaHCO_3$) and PNS2 are shown in Fig. 1, and the data of the characteristic absorption bands are listed in Table I. The main characteristic absorption band of PNSO were found at 3434 and 3302 cm^{-1}, due to the stretching vibration of O–H and N–H groups, respectively, and at 1649 and 1543 cm^{-1}, attributed to amide I (C=O group) and amide II (N–H group), respectively. The spectrum of PNS2 was very similar with the respective bands appearing at 3436, 3305, 1652 and 1543 cm^{-1}. This similarity indicates that the $NaHCO_3$ had been completely removed from the PNS2 hydrogel matrix. The presence of soy protein in the hydrogels was hard to evidence because the characteristic absorption bands of soy protein and PNIPAAm are similar.

The morphological images of the cross-sections of the freeze-dried hydrogels are shown in Fig. 2. It was found that the structures of the porous network of

the hydrogels are influenced by the presence of $NaHCO_3$ in the reaction medium. The conventional soy protein/PNIPAAm IPN hydrogel (PNS0) prepared in water had a lower porosity than that of the proposed hydrogels. These porous structures were created during the freeze-drying step, when the ice crystals sublimate and pores are left behind in the hydrogel matrices.[30] Compared with PNS0, the porosity of the proposed hydrogels increased with increasing content of $NaHCO_3$ in the polymerization medium. These results indicate that the presence of $NaHCO_3$ had an effect on the structures of the hydrogel network.

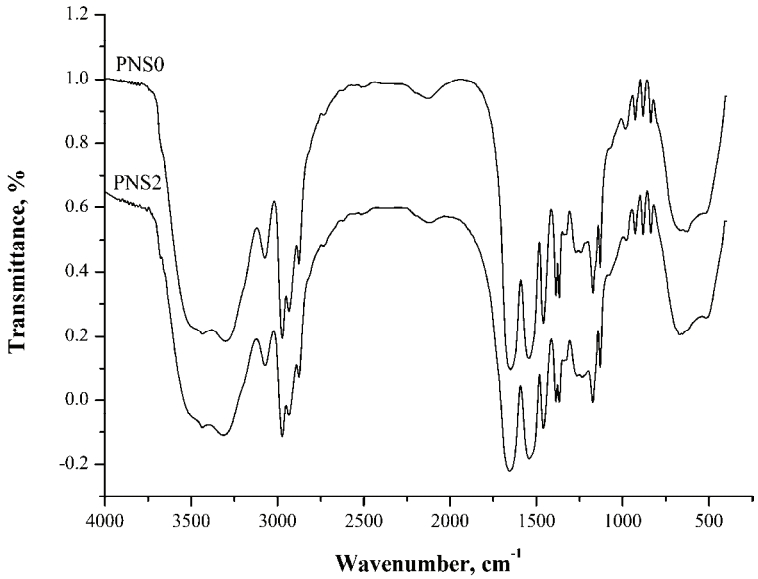

Fig. 1. FTIR spectra of PNS0 and PNS2.

TABLE I. Characteristic absorption bands of the samples

Sample	OH and NH bands, cm^{-1}		Amide I band, cm^{-1}	Amide II band, cm^{-1}
	ν_{O-H}	ν_{N-H}	$\nu_{C=O}$	$\delta_{N-H} + \nu_{C-N}$
PNS0	3434	3302	1649	1543
PNS2	3436	3305	1652	1543

DSC analysis

The glass transition temperature, T_g, is one of the characteristic temperatures for polymer blends. A single T_g means that the blends are miscible. The DSC thermograms of the hydrogels are shown in Fig. 3. All the samples had only a single T_g, which indicates that the samples had good miscibility. The T_g of PNS0, PNS1, PNS2 and PNS3 depicted in Fig. 3 were almost the same, which demonstrates that content of $NaHCO_3$ had almost no effect on the T_g of the proposed hydrogels.

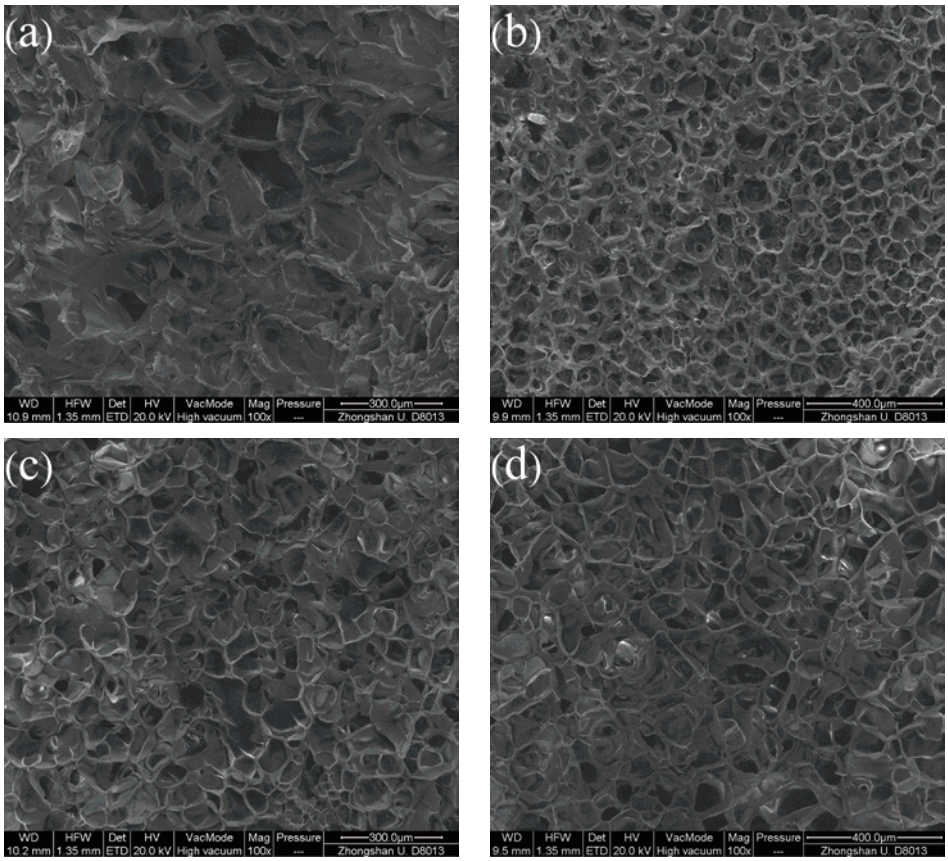

Fig. 2. SEM micrographs of: a) PNS0, b) PNS1, c) PNS2 and d) PNS3.

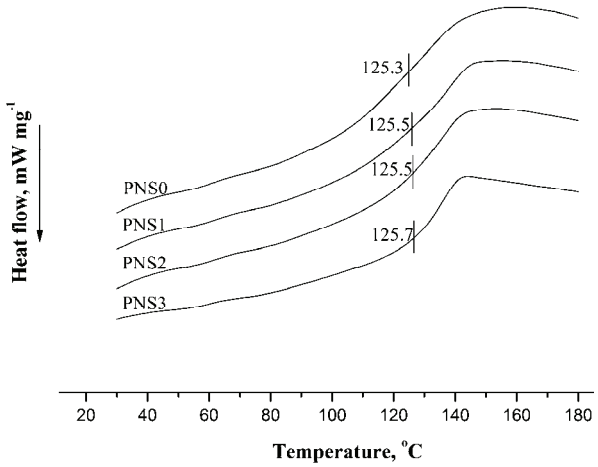

Fig. 3. DSC thermograms of dried hydrogels.

Thermogravimetric analysis

Thermal gravimetric analysis (TGA) is a useful technique to study the thermal stability of composite polymeric materials. The rate of weight loss of the samples as a function of temperature is depicted in Fig. 4. It could be observed that all samples underwent two decomposition stages. The first stage of weight loss for the samples was observed at *ca.* 210 °C (4.65 % weight loss) due to the decomposition of small molecules. In the second stage, the maximum weight loss of the samples was observed. The maximum decomposition temperature of PNS0, PNS1, PNS2 and PNS3 were 419.5 (95.63 % weight loss), 409.4 (88.93 % weight loss), 410.1 (91.01 % weight loss) and 411.6 °C (91.06 % weight loss), respectively. These results show that the hydrogels had good thermal stability for biomaterial applications.

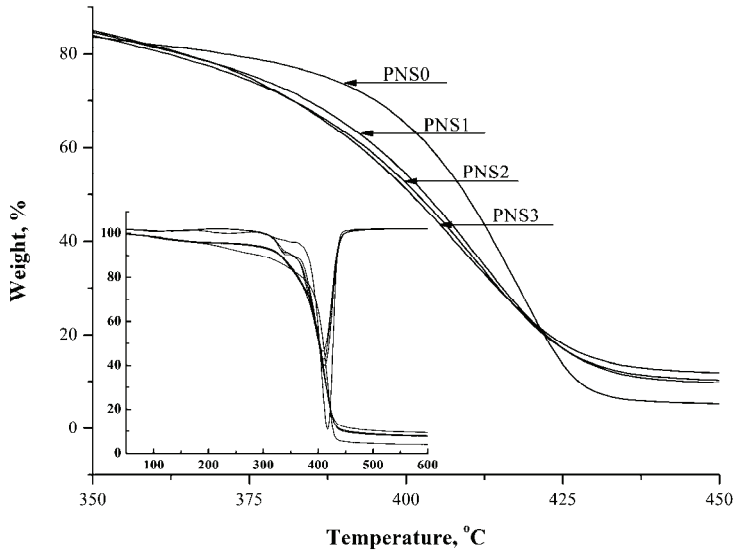

Fig. 4. TGA thermograms of dried hydrogels.

Temperature responsivity

The temperature response of the samples was evaluated by measuring their equilibrium swelling ratios, and the results are shown in Fig. 5. It could be seen that the samples had similar equilibrium swelling ratios and almost the same VPTT (around 32 °C). The equilibrium swelling ratios decreased with increasing temperature. Hydrophobic groups ($–CH(CH_3)_2$) and hydrophilic groups (–CONHR) existed in the hydrogels, which correspond to the hydrophobic and hydrophilic regions, respectively. When the temperature was below the VPTT, hydrogen-bonding interactions between the hydrophilic groups and water molecules were dominant, resulting in high equilibrium swelling ratios, while when

the temperature was above the VPTT, the hydrophobic interactions in the hydrogels become dominant and weakened the hydrophilic interactions, eventually leading to hydrogel shrinkage and the equilibrium swelling ratio decrease markedly. It is noteworthy that the presence of $NaHCO_3$ in the polymerization medium had little effect on the VPTT of the hydrogels.

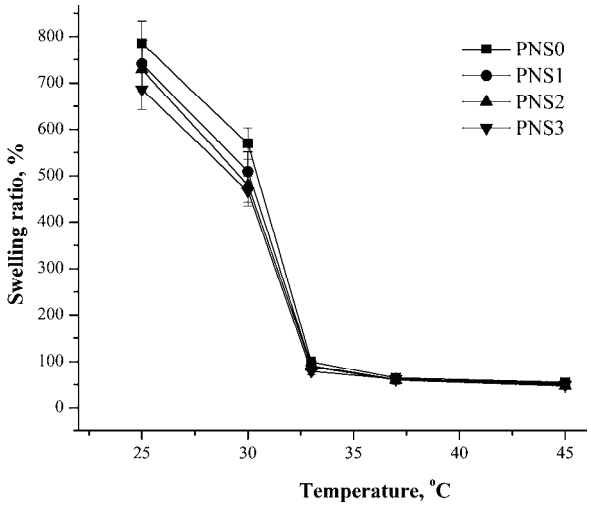

Fig. 5. Equilibrium swelling ratios as a function of temperature.

Swelling kinetics

Pre-weighed dried hydrogels were immersed in deionized water at 25 °C to swell, and the swelling ratios were measured to evaluate their swelling properties. The results are shown in Fig. 6. In the initial swelling stage, the hydrogels had a similar swelling profile. However, as the swelling continued, the swelling rates of PNS1, PNS2 and PNS3 were faster than that of the conventional hydrogel (PNS0). Moreover, the swelling rate increased with increasing amount of $NaHCO_3$. PNS3 hydrogel reached equilibrium swelling first. Initially, the much smaller distance between the polymer chains in the dry hydrogels produced strong interaction forces that prevented the water molecules from diffusing into the hydrogel matrices, which resulted in low swelling rates and similar swelling profiles. As the swelling continued, the polymer chains become stretchable and the porous structures become the dominant factors, which enabled the water molecules to permeate easily into matrices of the hydrogels and resulted in a fast swelling rate. As a result, the higher the content of $NaHCO_3$ in the polymerization mixture, the higher was the achieved swelling rate. It was also found that PNS0 had a higher swelling ratio in the late stages of swelling than those of the proposed hydrogels. As mentioned above, the proposed hydrogels obtained in $NaHCO_3$ solutions had more physical entanglements among the polymer chains

due to the salt effect and consequently had a relatively low swelling ratio in the late stages of swelling.

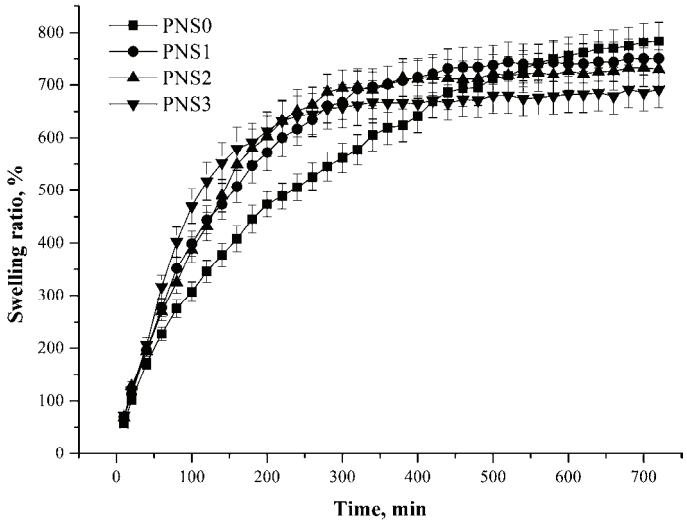

Fig. 6. Swelling kinetics of hydrogels in deionized water at 25 °C.

In order to investigate the swelling mechanism of the hydrogels, a simple and effective method was employed to analyze the swelling data for $M_t/M_\infty < 0.6$, that is:[31–34]

$$M_t / M_\infty = kt^n \quad (3)$$

where M_t and M_∞ are the amount of water absorbed at time t and at equilibrium, respectively; k is a characteristic constant and n is the characteristic exponent of the mode. The exponent n was obtained from the slope of a plot of ln (M_t/M_∞) *versus* ln t (Fig. 7), and the results are given in Table II. The values of n in Table II indicate that the swelling mechanism of the hydrogels was non-Fickian diffusion and the value of n increased with increasing amount of $NaHCO_3$ in the polymerization mixture. Thus, the content of $NaHCO_3$ influenced the swelling kinetics of the hydrogels.

Deswelling kinetics

The hydrogels swollen to equilibrium in deionized water at 25 °C were immersed in deionized water at 37 °C to deswell. The water retention was measured to evaluate their deswelling properties, and the results are shown in Fig. 8. It could be seen that the deswelling rates of the proposed hydrogels were much faster than that of the conventional hydrogel (PNS0). The water retention of PNS1, PNS2 and PNS3 after 30 min were 37.56, 27.70 and 25.72 %, respectively, whereas it was 47.35 % after 300 min for PNS0. When a to equilibrium

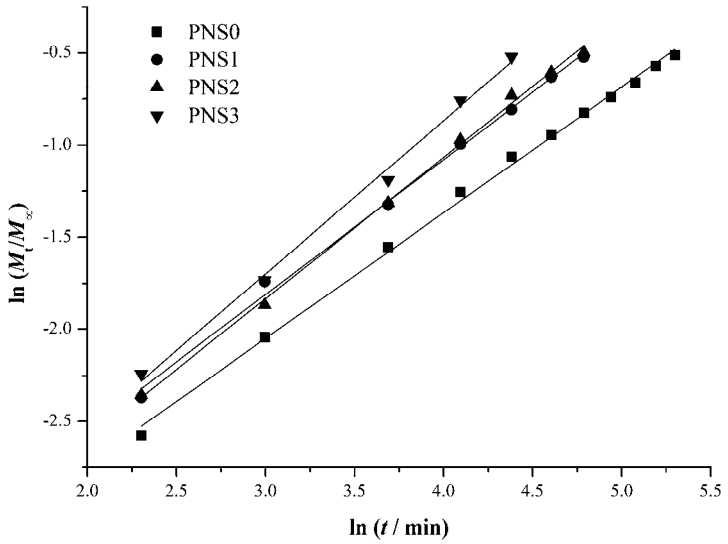

Fig. 7. Fitting of swelling kinetics for hydrogels in deionized water at 25 °C.

TABLE II. Diffusional exponents and deswelling constants for swelling and deswelling kinetics

Sample	Equation (3)		Equation (4)	
	n	R^2	k / min^{-1}	R^2
PNS0	0.68	0.99749	0.00274	0.97955
PNS1	0.73	0.99599	0.03164	0.98486
PNS2	0.76	0.99799	0.04196	0.96967
PNS3	0.83	0.99446	0.04527	0.97621

swollen hydrogel is transferred into higher temperature deionized water, the temperature rises first on the hydrogel surface; hence, if the initial temperature was below and the final temperature above the VPTT, the surface PNIPAAm molecules shrink first in the surface, which results in the formation of a dense skin layer on the hydrogel surface. This skin layer can hinder the outward permeation of water molecules from the hydrogel interior.[35] As the shrink continues, the water molecules inside the hydrogels continue to be extruded. As a result, PNS0 deswells slowly and some bubbles on its surface were observed during the deswelling. In an earlier study,[27] hydrogels containing soy protein were shown to have a higher deswelling rate than that of a PNIPAAm hydrogel, which indicates that soy protein on the hydrogel surface could reduce the density of the skin layer, resulting in relatively high deswelling rates. In the present case, the proposed hydrogels have highly porous structures on the surface and in the interior of the hydrogels. The porous effect is greater than the soy protein effect on the skin layer, and consequently the dense skin layer has little effect on PNS1, PNS2 and PNS3. Therefore, PNS1, PNS2 and PNS3 had faster deswelling rates.

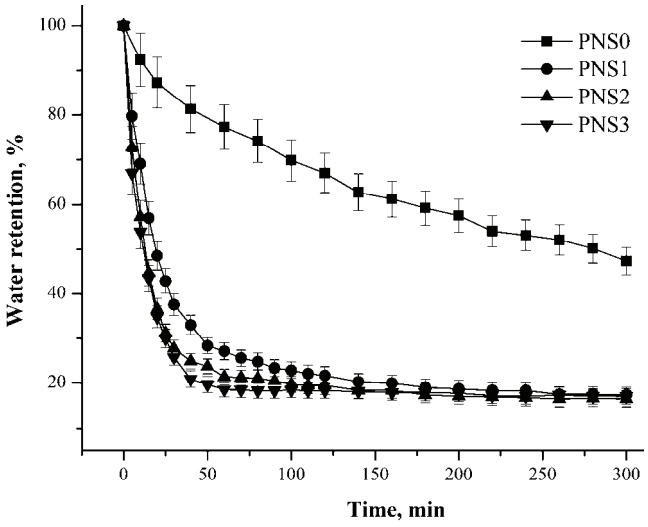

Fig. 8. Deswelling kinetics of hydrogels in deionized water at 37 °C.

To investigate the deswelling kinetics quantitatively, a semi-logarithmic plot of a first-order rate analysis was used to fit the time dependence of the deswelling given by Eq. (4):[36]

$$\ln \frac{M_t - M_\mathrm{d}}{M_\mathrm{e} - M_\mathrm{d}} = -kt \tag{4}$$

where k is the deswelling constant and t is time. A larger k means a faster deswelling process. The value of k obtained from the slope of the plot of ln $((M_t - M_d)/(M_e - M_d))$ *versus* t (Fig. 9) are given in Table II. As shown in Table II, the value of k for PNS3 is 16 times greater than that for PNS0. Moreover, the value

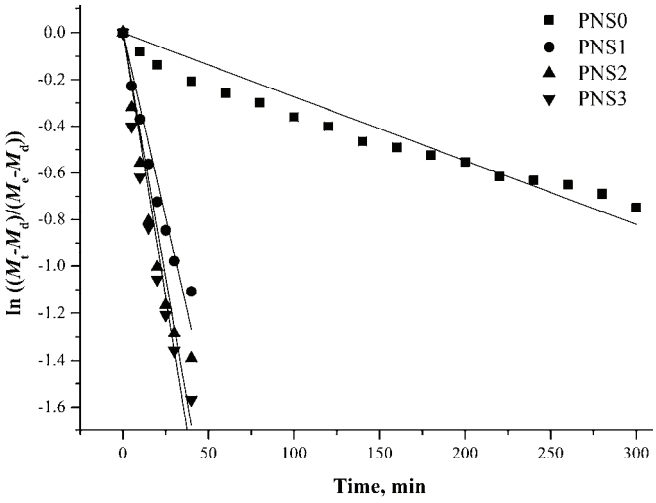

Fig. 9. Deswelling rate analysis of hydrogels in deionized water at 37 °C.

of k increases with increasing mass of $NaHCO_3$ in the polymerization medium (Fig. 10), which further confirms the analyses above.

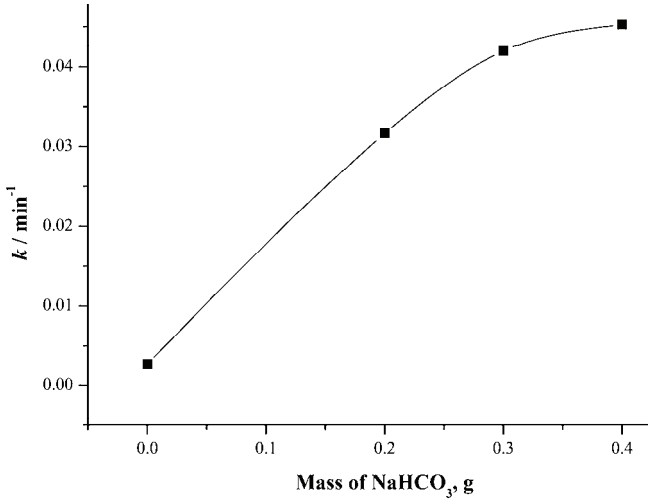

Fig. 10. Dependence of slope k on mass of $NaHCO_3$ in the feed.

CONCLUSIONS

Fast temperature-responsive soy protein/PNIPAAm IPN hydrogels were successfully prepared using the phase separation and foaming agent technologies. All the proposed hydrogels showed good miscibility and thermo-response, and thermal stability. The hydrogels prepared in $NaHCO_3$ solutions had a highly porous structure and showed fast swelling and deswelling rates.

Acknowledgement. This work was financially supported by the Natural Science Foundation of Guangdong Province (Grant Nos. 2012040007710 and 10151022501000033).

ИЗВОД

ДОБИЈАЊЕ И СВОЈСТВА ТЕМПЕРАТУРНО-ОСЕТЉИВИХ ХИДРОГЕЛОВА НА БАЗИ ПРОТЕИНА СОЈЕ/PNIPAAm IPN СА БРЗИМ ОДГОВОРОМ

YONG LIU[1], YINGDE CUI[2], GUOJIE WU[2] и MIAOCHAN LIAO[3]

[1]*School of Chemistry and Chemical Engineering, Zhaoqing University, Zhaoqing 526061, P.R. China,* [2]*Institute of Green Chemical Engineering, Zhongkai University of Agriculture and Engineering, Guangzhou 510225, P.R. China u* [3]*Department of Logistics Management, Zhaoqing University, Zhaoqing 526061, P.R. China*

Интерпенетрирајуће полимерне мреже, IPN, температурно осетљивих хидрогелова на бази протеина соје и поли(*N*-изопропилакриламида) успешно су синтетисане у раствору натријум-хидрогенкарбоната ($NaHCO_3$). Структура и својства синтетисаних IPN хидрогелова су окарактерисани инфрацрвеном спектроскопијом, скенирајућом електронском спектроскопијом, диференцијалном скенирајућом калориметријом и термогравиметријском анализом. Кинетика процеса бубрења и дехидратације хидрогелова, праћена преко промене степена бубрења, детаљно је приказана. У раду је показано да синтетисани хидрогелови поседују порозну структуру, добру мешљивост компоненти

полимерне смеше, термичку стабилност, као и брз температурни одговор. Присуство порогена, $NaHCO_3$, у реакционој смеши незнатно је утицало на температуру запреминског псеудо-фазног прелаза (VPTT) (око 32 °C). У поређењу са конвенционалним хидрогеловима, синтетисани IPN хидрогелови са порознијом структуром показују веће брзине бубрења и дехидратације. Процес бубрења хидрогелова се може описати не-фиковским законом дифузије. Синтетисани хидрогелови са брзим температурним одговором могу наћи потенцијалну примену у области биомедицинских материјала.

(Примљено 19. фебруара, ревидирано 25. априла 2013)

REFERENCES

1. Y. Liu, Y. Cui, G. Yin, L. Luo, *J. Biobased Mater. Bioenergy* **3** (2009) 437
2. A. Sionkowska, *Prog. Polym. Sci.* **36** (2011) 1254
3. J. Stojkovska, J. Zvicer, Ž. Jovanović, V. Mišković-Stanković, B. Obradović, *J. Serb. Chem. Soc.* **77** (2012) 1709
4. A. C. Vega-Lugo, L. T. Lim, *J. Biobased Mater. Bioenergy* **2** (2008) 223
5. K. Y. Lee, S. H. Yuk, *Prog. Polym. Sci.* **32** (2007) 669
6. N. Gupta, A. K. Srivastava, *Polym. Int.* **35** (1994) 109
7. Y. S. Lipatov, *Prog. Polym. Sci.* **27** (2002) 1721
8. X. Y. Li, W. H. Wu, W. Q. Liu, *Carbohydr. Polym.* **71** (2008) 394
9. X. Chen, H. Song, T. Fang, J. Bai, J. Xiong, H. Ying, *J. Appl. Polym. Sci.* **116** (2010) 1342
10. E. S. Gil, S. M. Hudson, *Biomacromolecules* **8** (2007) 258
11. M. Hamcerencu, J. Desbrieres, M. Popa, G. Riess, *Biomacromolecules* **10** (2009) 1911
12. L. Y. Chen, G. Remondetto, M. Rouabhia, M. Subirade, *Biomaterials* **29** (2008) 3750
13. C. M. Vaz, P. F. N. M. van-Doeveren, R. L. Reis, A. M. Cunha, *Polymer* **44** (2003) 5983
14. H. Zheng, Z. Y. Zhou, Y. Chen, J. Huang, F. L. Xiong, *J. Appl. Polym. Sci.* **106** (2007) 1034
15. R. Snyders, K. I. Shingel, O. Zabeida, C. Roberge, M. P. Faure, L. Martinu, *J. Biomed. Mater. Res., A* **83** (2007) 88
16. R. Yoshida, K. Uchida, Y. Kaneko, K. Sakai, A. Kikuchi, Y. Sakurai, T. Okano, *Nature* **374** (1995) 240
17. J. Zhang, R. Xie, S. B. Zhang, C. J. Cheng, X. J. Ju, L. Y. Chu, *Polymer* **50** (2009) 2516
18. J. P. K. Tan, K. C. Tam, *J. Controlled Release* **118** (2007) 87
19. E. Kohli, H. Y. Han, A. D. Zeman, S. V. Vinogradov, *J. Controlled Release* **121** (2007) 19
20. L. L. Yue, R. Xie, J. Wei, X. J. Ju, W. Wang, L. Y. Chu, *J. Colloid Interface Sci.* **377** (2012) 137
21. T. Caykara, S. Kiper, G. Demirel, S. Demirci, C. Cakanyıldırım, *Polym. Int.* **56** (2007) 275
22. X. Z. Zhang, Y. Y. Yang, T. S. Chung, K. X. Ma, *Langmuir* **17 (**2001) 6094
23. F. A. Dorkoosh, M. P. M. Stokkel, D. Blokc, G. Borcharda, M. Rafiee-Tehrania, J. C. Verhoef, H. E. Junginger, *J. Controlled Release* **99** (2004) 199
24. L. C. Yin, L. K. Fei, F. Y. Cui, C. Tang, C. H. Yin, *Biomaterials* **28** (2007) 1258
25. H. L. A. E. Mohdy, A. Safrany, *Radiat. Phys. Chem.* **77** (2008) 273
26. X. Z. Zhang, R. X. Zhuo, *Mater. Lett.* **52** (2002) 5
27. Y. Liu, Y. Cui, *Polym. Int.* **60** (2011) 1117
28. A. Lozsan, *Colloid Polym. Sci.* **290** (2012) 1561
29. O. Okay, *Prog. Polym. Sci.* **25** (2000) 711
30. N. Kato, Y. Sakai, S. Shibata, *Macromolecules* **36** (2003) 961

31. N. M. Franson, N. A. Peppas, *J. Appl. Polym. Sci.* **28** (1983) 1299
32. R. W. Korsmeyer, E. V. Meerwall, N. A. Peppas, *J. Polym Sci., B* **24** (1986) 409
33. S. Gunasekaran, S. Ko, L. Xiao, *J. Food. Eng.* **83** (2007) 31
34. F. Ganji, S. Vasheghani-Farahani, E. Vasheghani-Farahani, *Iran. Polym. J.* **19** (2010) 375
35. Y. Kaneko, R. Yoshida, K. Sakai, Y. Sakurai, T. Okano, *J. Membrane. Sci.* **101** (1995) 13
36. T. Serizawa, K. Wakita, M. Akashi, *Macromolecules* **35** (2002) 10.

Journal of the Serbian Chemical Society
JSCS-info@shd.org.rs • www.shd.org.rs/JSCS
J. Serb. Chem. Soc. *79* (2) 225–239 (2014)
JSCS–4578
UDC 546.723+547.313.2'131+547.261–145.2:532.13
Original scientific paper

Solution behaviour of (*N*,*N*′-ethylenebis(salicylideneiminato))-iron(III) chloride in aqueous methanol at 298.15, 303.15 and 313.15 K

DHIRAJ BRAHMAN and BISWAJIT SINHA*

Department of Chemistry, University of North Bengal, Darjeeling-734013, India

(Received 14 April, revised 19 July 2013)

Abstract: In this study partial molar volumes (φ_V^0) and viscosity *B*-coefficients of (*N*,*N*′-ethylene-bis(salicylideneiminato))iron(III) chloride, abbreviated as Fe^{III}(salen)Cl, in different aqueous methanolic solutions were determined from solution density and viscosity measurements at the temperatures 298.15, 303.15, and 313.15 K under ambient pressure. The apparent molar volumes (φ_V) and densities (ρ) were used to calculate the apparent molar expansibilities (φ_E), the partial molar expansibilities (φ_E^0) and the temperature dependence of the partial molar expansibilities (φ_E^0) at constant pressure, $(\partial\varphi_E^0 / \partial T)_p$ of Fe^{III}(salen)Cl solutions to reveal the nature of different interactions in the ternary solutions. The transition state theory was applied to analyze the viscosity *B*-coefficients based on the activation parameters of viscous flow. The overall results indicated strong solute–solvent interactions between Fe^{III}(salen)Cl and the solvent molecules, preferentially with water molecules and that Fe^{III}(salen)Cl acts as a net structure promoter in the ternary solutions. The UV–Vis absorption spectra of the ternary solutions stand in support of the obtained results.

Keywords: partial molar volumes; viscosity *B*-coefficients; (*N*,*N*′-ethylene-bis(salicylideneiminato))iron(III) chloride; aqueous methanol.

INTRODUCTION

Many natural products contain structural units similar to those of metal heterocyclic compounds that could be used as targets for synthetic, methodological, and biological applications.[1] Schiff base metal complexes belong to class of the many potential materials that deserve extensive studies and, amongst the traditional metal complexes, salen-type Schiff base ligands or their derivatives are of great importance in coordination chemistry and homogeneous catalysis.[2] They can also be regarded as models of reaction centres for metalloenzymes[3] and

* Corresponding author. E-mail: biswachem@gmail.com
doi: 10.2298/JSC170413082B

nonlinear optical materials.[4] According to Groves *et al.*,[5–7] simple iron(III) porphyrins can be used as models for the reaction site of cytochrome P-450. In this regard, metal complexes of the salen ligand are also of great interest to synthetic chemists, since they share features in common with metalloporphyrins as far as their electronic structure and catalytic activities are concerned. Interestingly, Fe^{III}(salen)Cl and Fe^{III} porphyrins have some structural and chemical similarities.[8,9] Like Fe^{III} porphyrins, the iron atom of Fe^{III}(salen)Cl has a penta-coordinated pyramidal geometry wherein the tetradentate salen ligand is in a square planar coordination and the chloride ligand is attached at an apical position. The complex has an open sixth coordination site and salen forms some complexes that mimic porphyrin chemistry.[10] Moreover, Fe^{III}(salen)Cl has an affinity for oxygen molecules and is capable of forming oxo-species as do Fe^{III} porphyrin derivatives.[8,9] Amongst the conventional solvents, methanol is used in numerous chemical processes and it is has a structure analogous to water but with a $–CH_3$ group in place of a proton. This substitution affects the liquid structure and causes significant differences between methanol and water. Hence it is important to understand how solutes such as Fe^{III}(salen)Cl behave in these mixed methanol–water solvents, because an understanding of such behaviour could throw light on the effects of solute concentration on the hydrogen-bonded network, solvation structure and solute dynamics, *etc*.[11]

However, such studies on Fe^{III}(salen)Cl in various pure and mixed solvents are still rare in the literature. To the best of our knowledge, only one report on the solvent effects on the electrochemical behaviour of Fe^{III}(salen)Cl is available in the literature.[12] Hence in this work, the solution behaviour of Fe^{III}(salen)Cl in different aqueous methanol solutions were studied at 298.15, 303.15 and 313.15 K under ambient pressure and the results are discussed in terms of solute–solute and solute–solvent interactions.

EXPERIMENTAL

Materials

Analytical reagent (AR) grade ferric chloride, $FeCl_3 \cdot 6H_2O$ (s), 1,2-ethylenediamine (l), and salicylaldehyde (l), each of purity > 99 %, were purchased from Merck, India. These chemicals were used as received. Spectroscopic grade methanol (minimum assay, GC, purity > 99.8 %) with 0.05 % of water was purchased from Merck, India and used as received. Doubly distilled de-ionized water with a specific conductance of 1×10^{-6} S cm^{-1} at 298.15 K was used for preparing the mixed solvents. Various binary solvents were prepared by mass, with necessary adjustments by volume, to achieve the exact mass fraction of methanol (w_1 = = 0.60, 0.70, 0.80 and 0.90) at 298.15 K. The relative error in solvent composition was estimated to be about 1 %. The physical properties of different solvent/solvent mixtures at the experimental temperatures are reported in Table S-I of the Supplementary material to this paper and compared against available literature values.[13-16]

Fe^{III}(salen)Cl was prepared by a known method[17] taking $FeCl_3 \cdot 6H_2O$(s) and the Schiff base, salenH_2(s) in ethanol (in a 1:1 molar ratio). SalenH_2 (*N*,*N*′-ethylenebis(salicylidene-

amine)) was obtained from an ethanolic solution of 1,2-ethylenediamine and salicylaldehyde (in a 1:2 molar ratio) for 1 h. The bright yellow crystalline solid (m.p. 128 °C) was filtered and washed with ethanol several times and dried under vacuum. Metallation was realized by refluxing an ethanolic solution containing $FeCl_3 \cdot 6H_2O$ (s) (1.08 g, 4 mmol) and salenH_2 (1.07 g, 4 mmol) with little triethylamine (NEt_3) for 30 min at 60 °C. Fe^{III}(salen)Cl was obtained as a deep brown microcrystalline solid from the mixture and was dried under vacuum at 50–60 °C and then recrystallized from ethanol. It was kept in a vacuum desiccator over anhydrous $CaCl_2$. The purity of the complex was checked by elemental analysis (Calcd.: C, 53.74; H, 3.95; N, 7.84; Cl, 9.91; Fe, 15.63 %. Found: C, 53.64; H, 4.01; N, 7.94; Cl, 9.85; Fe, 15.60 %) and IR spectroscopy. Elemental micro-analyses were realised with the aid of a Perkin–Elmer (Model 240C) instrument. The IR spectra ware recorded on a Perkin–Elmer FT-IR spectrophotometer. Characteristic IR bands for the prepared complex (KBr, cm^{-1}) are 585.76, 617.44, 757.92, 795.02, 904.87, 1445.82, 1544.35, 1629.76, 3448.17. The magnetic moment (measured with a Sherwood Scientific magnetic balance) was found to be 5.31 μ_B (5.29 μ_B[18]) at room temperature. The molecular structures of the ligand salenH_2, the complex Fe^{III}(salen)Cl and its dimer $[Fe^{III}(salen)Cl]_2$ are illustrated in Fig. S-1 of the Supplementary material. The IR spectra of the ligand salenH_2 and Fe^{III}(salen)Cl are shown in Fig. S-2 of the Supplementary material.

Stock solutions of the complex in different aqueous methanol solutions were prepared by mass and the working solutions were prepared by mass dilution. Solute molalities (*m*) were converted into molarities (*c*) using experimental density values. All solutions were prepared fresh and degassed with dry nitrogen before use. The uncertainty in the molarity of Fe^{III}(salen)Cl solutions was evaluated to be ±0.0001 mol dm^{-3}.

Methods

The mass measurements were performed on a digital electronic analytical balance (Mettler, AG 285, Switzerland) with a precision of ±0.01 mg. The densities were measured with a vibrating-tube density meter (Anton Paar, DMA 4500M), which was calibrated at the experimental temperatures with doubly distilled, degassed water and dry air at atmospheric pressure. The temperature was automatically kept constant with an accuracy of $\pm 1\times10^{-3}$ K using a built-in Peltier device. The stated repeatability and accuracy of the densities were $\pm 1\times10^{-5}$ and $\pm 5\times10^{-5}$ g cm^{-3}, respectively. However, when the accuracy of the measured densities was checked with the density of an aqueous NaCl solution of known molality based on the data given by Pitzer,[19] the uncertainty of the measured densities for most of the solutions was estimated to be $\pm 1\times10^{-5}$ g cm^{-3}. The viscosity was measured by means of a suspended Ubbelohde (Canon-type) viscometer thoroughly cleaned, dried and calibrated at the experimental temperatures with triply distilled, degassed water and purified methanol.[20-22] It was filled with experimental solution and placed vertically in a glass sided thermostat (maintained constant to ± 0.01 K) with the aid of wooden clumps. Sufficient time was allowed for the attainment of thermal equilibrium and the flow times of the solutions were recorded with a digital stopwatch (correct to ± 0.01 s). In all determinations, adequate precautions were taken to minimize evaporation losses and at least three repetitions of each data (reproducible to ±0.02 s) were taken as the average of the flow times. The uncertainty in viscosity measurements was estimated to be within $\pm 4\times10^{-4}$ mPa s. The absorption spectra of Fe^{III}(salen)Cl (5×10^{-5} mol dm^{-3}) in different aqueous methanol solutions at 298.15 K were recorded on Jasco V-530 double beam UV–Vis spectrophotometer (coupled with a thermostatic arrangement). A quartz cell with a path length of 1 cm was used and the reference solvent was spectroscopic grade methanol for all the spectroscopic measurements.

RESULTS AND DISCUSSION

Molalities (m), densities (ρ) viscosities (η) and the apparent molar volumes (φ_V) for the experimental solutions of Fe^{III}(salen)Cl in different aqueous methanol solutions at various temperatures are given in Table S-II of the Supplementary material. The apparent molar volumes (φ_V) of Fe^{III}(salen)Cl in different aqueous methanol solutions were determined from the solution densities by using the following equation:

$$\varphi_V = (M / \rho_1) - 1000(\rho - \rho_1) / (m\rho\rho_1) \quad (1)$$

where M is the molar mass of Fe^{III}(salen)Cl, m is the molality of the solution, ρ_1 and ρ are the densities of the solvent and solution, respectively. When the φ_V values were plotted against the square root of molal concentrations ($\sqrt{m}$), a linear dependence was observed. Hence the partial molar volumes (φ_V^0) at infinite dilution and the experimental slopes (S_V) were determined using the least squares fitting of φ_V values to the Masson Equation:[23]

$$\varphi_V = \varphi_V^0 + S_V^* \sqrt{m} \quad (2)$$

The φ_V^0 and S_V^* values are reported in Table I, which shows that the φ_V^0 values are positive and increase as the amount of water in the mixtures increases

TABLE I. Partial molar volumes (φ_V^0) and the slopes (S_V^*) of Eq. (2) with the corresponding standard deviations (σ) for Fe^{III}(Salen)Cl in different aqueous methanol solutions at different temperatures (standard errors are given in parenthesis); w_1 – mass fraction of methanol

T / K	$\varphi_V^0 \times 10^6$ / m^3 mol^{-1}	$S_V^* \times 10^6$ / m^3 kg$^{1/2}$ mol$^{-3/2}$	$\sigma \times 10^6$ / m^3 mol^{-1}
		w_1 = 1.00	
298.15	247.37 (±4.65)	–1537.95 (±56.44)	3.10
303.15	228.45 (±4.26)	–1400.29 (±51.76)	2.84
313.15	216.30 (±5.18)	–1335.03 (±62.88)	3.45
		w_1 = 0.90	
298.15	257.09 (±5.83)	–1659.90 (±72.09)	3.86
303.15	243.14 (±3.17)	–1554.86 (±39.15)	2.10
313.15	232.10 (±4.65)	–1524.93 (±57.44)	3.08
		w_1 = 0.80	
298.15	260.72 (±4.47)	–1779.20 (±56.26)	2.96
303.15	253.03 (±0.02)	–1734.17 (±50.46)	2.66
313.15	244.78 (±3.02)	–1672.77 (±38.05)	2.00
		w_1 = 0.70	
298.15	262.39(±3.59)	–1830.54 (±45.76)	2.39
303.15	257.29 (±3.95)	–1799.56 (±50.35)	2.63
313.15	256.91 (±3.95)	–1826.92 (±50.39)	2.63
		w_1 = 0.60	
298.15	264.36 (±5.07)	–1912.71 (±65.74)	3.40
303.15	261.07 (±6.86)	–1917.72 (±88.93)	4.60
313.15	261.20 (±4.89)	–1931.27 (±63.41)	3.28

but decrease with increasing temperature. This indicates the presence of strong solute–solvent interactions[22,24] and these interactions were further strengthened at higher contents of water but weakened at higher temperatures. The dependences of the φ_V^0 values on the solvent composition and temperature are shown in Fig. 1. Fe^{III}(salen)Cl can exist either as dimer or monomer in the solid state. Its behaviour in the solid state depends on the nature of the solvent used in its recrystallization. However, the two forms can be distinguished by their magnetic moments and IR spectra (shown in Fig. S-2 of the Supplementary material). For monomeric complexes, the range of the magnetic moment is 5.29–6.06 μ_B. A value of 5.31 μ_B was obtained for the complex Fe^{III}(salen)Cl and the IR spectra are devoid of any band near 850 cm^{-1}. Thus, the complex was in monomeric form[25] rather than in the dimeric form and hence, it contains a d^5 high spin electronic configuration[26,27] with a square planar geometry around Fe^{3+} at the centre and an apical chlorine atom as coordinated to the fifth coordination site. Thus, solvent molecules can coordinate to the unoccupied sixth position of the coordination site. In this regard, the donor power of individual solvents plays a crucial role. Aqueous methanol solutions are characterized by hydrophobic and hydrophilic interactions. Both computer simulation[28] and experimental studies[29–34] revealed that water strongly interacts with methanol to form complexes. Recent spectroscopic and high performance liquid chromatographic studies revealed that methanol forms a number of complexes with a number of water molecules at low methanol but at high methanol content, it forms a 1:1 complex.[29–34] According to Zhang and Wu,[35] the two critical solvent compositions are H_2O:$CH_3OH \approx 5:1$ and $\approx 1:1$. Thus, as the methanol concentration decreases, more water molecules become free in the bulk solvent mixtures. Hence methanol and water molecules may coordinate for the sixth vacant coordination site of Fe^{III}(salen)Cl *via* O···Fe interactions. Moreover, methanol/water may also interact with Fe^{III}(salen)Cl *via* hydrogen bond interactions with ONNO sites of the complex and thereby affecting its spin-equilibrium in solution. No doubt, H_2O will have comparatively more such hydrogen bond interactions than CH_3OH and because of the fact that methanol (with an effective hard sphere diameter 0.364 nm[36]) is more bulky than water (with effective hard sphere diameter 0.284 nm[36]), the increase in the φ_V values as well as the concomitant increase in the φ_V^0 values with increasing water content in the mixtures may be attributed to preferential coordination of the unoccupied sixth position of Fe^{III}(salen)Cl by water molecules or preferential solvation of Fe^{III}(salen)Cl by water molecules due to stronger electrostatic interaction and comparatively more donor strength of water than methanol.[37] Again, as the φ_V^0 values for the ternary systems increase with more water or polarity of the solvent mixture (the order of relative permittivity of the solvent mixtures:[24] 31.5, 35.7, 40.1, 45.0 and 50.1 for w_1 = 1.00, 0.90, 0.80, 0.70 and 0.60, respectively), the complex most probably remains in its monomeric form in the

solution phase, because the Fe-atom is comparatively more available to the solvent molecules for O···Fe interactions in the monomeric form[18] than in the dimeric form. However, the decrease in the φ_V^0 values with rising temperature indicates disruption of hydrogen bonds and O···Fe interactions at elevated temperatures. The slight increase in the φ_V^0 values at 303.15 and 313.15 K for solvent mixtures with w_1 = 0.60 may probably arise from a delicate balance between the loosely bound dimer and the monomer in this solvent compositions.[25,27] The parameter S_V^* is a volumetric viral coefficient and characterizes the pair-wise interactions between solvated species[38,39] in solution. Its sign is determined by the interactions between solute species (solute–solute interactions). The negative values of S_V^* and their trend opposite to that of the φ_V^0 values indicate weak solute–solute interactions for Fe^{III}(salen)Cl in the studied experimental aqueous methanol solutions.

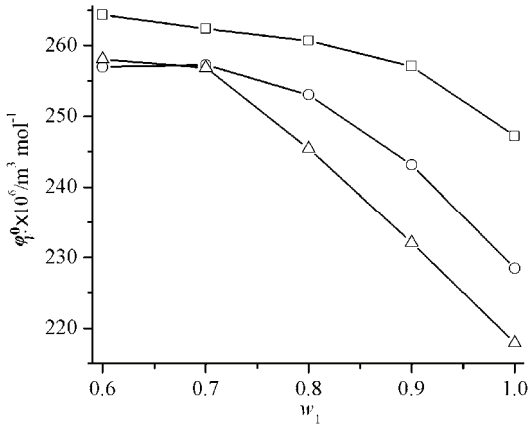

Fig. 1. Dependence of partial molar volume (φ_V^0) on the mass fraction of methanol (w_1) in the aqueous methanol solutions at different temperatures. Symbols: T = 298.15 K, □; T = 303.15 K, ○; T = 313.15 K, Δ.

These results are reflected in the UV–Vis absorption spectra of the studied solutions. The absorption spectra of the Schiff base, salenH_2 in methanol and various aqueous methanol solutions at 298.15 K are shown in Fig. 2. The spectrum of salenH_2 in methanol is characterized by the presence of two strong peaks at 254 and 316 nm and a weak peak at 404 nm, which were discussed previously.[22] Interestingly, when water was introduced, the peak at 404 nm of salenH_2 gradually disappeared and a valley was formed as the concentration of water increased in the ternary solutions and thus, the position of the weak peak at 404 nm varies with the polarity of the aqueous methanol solutions. In addition, the 316 nm peak underwent hypochromic shifts on addition of water. The absorption spectra of Fe^{III}(salen)Cl in methanol and various aqueous methanol solutions at 298.15 K are shown in Fig. 3, which shows that the 404 nm peak of the Schiff base disappeared in methanol as well as in all the aqueous methanol solutions due to coordination of solvent molecules to Fe(III). Simultaneously, an additional

peak at around 500 nm appeared and suffered hypsochromic shifts, indicating coordination or solvation by solvent molecules.[40] The peak at 258 nm did not change appreciably but a new peak at around 320 nm appeared as the amount of water in the ternary systems increased.[27]

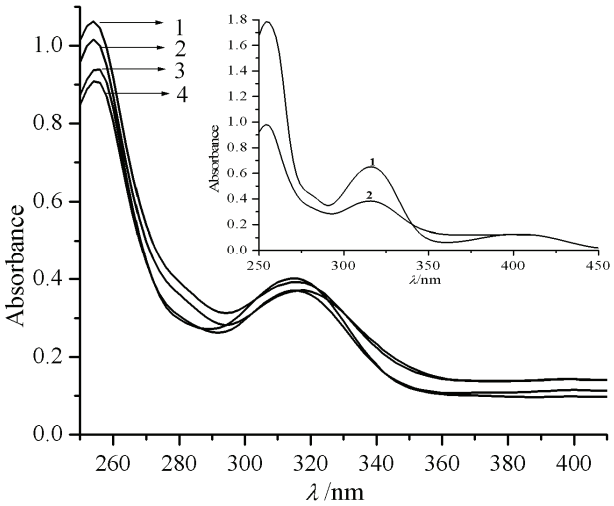

Fig. 2. Changes in the UV–Vis absorption spectra of salenH_2 solutions in different aqueous methanol solutions at 298.15 K for w_1: 1, 0.70; 2, 0.60; 3, 0.90; 4, 0.80. w_1 is the mass fraction of methanol in the aqueous methanol solutions. Inset: 1, salenH_2 in methanol; 2, average absorption spectra in aqueous methanol mixtures at 298.15 K.

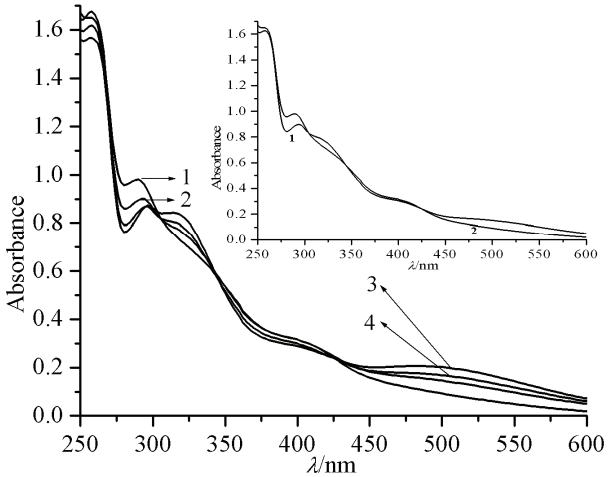

Fig. 3. Changes in the UV–Vis absorption spectra of Fe^{III}(salen)Cl solutions in different aqueous methanol solutions at 298.15 K for w_1: 1, 1.00; 2, 0.90; 3, 0.70; 4, 0.80. w_1 is the mass fraction of methanol in the aqueous methanol solutions. Inset: 1, Fe^{III}(salen)Cl in methanol; 2, average absorption spectra in aqueous methanol mixtures at 298.15 K.

The apparent molar volumes (φ_V) and densities (ρ) were used to derive the apparent molar expansibilities (φ_E) of Fe^{III}(salen)Cl solutions by using the relation:[24]

$$\varphi_E = \alpha\varphi_V + 1000(\alpha - \alpha_0)/(m\rho_0) \quad (3)$$

where α and α_0 are the coefficients of isobaric thermal expansion of the solvent and solution, respectively, and the other symbols have their usual significances; α and α_0 are defined as: $\alpha = -\rho_0^{-1}(\delta\rho_0/\delta T)_p$ and $\alpha = -\rho^{-1}(\delta\rho/\delta T)_p$, respectively. The uncertainty of the α and α_0 values was $\pm 6\times10^{-6}$ K^{-1} and the uncertainty in the φ_E values was within $\pm(0.006–0.061)\times10^{-6}$ m^3 mol^{-1} K^{-1}. The partial molar expansibilities (φ_V^0) were determined from the relation:[24]

$$\varphi_E = \varphi_E^0 + S_E\sqrt{m} \quad (4)$$

The φ_E^0 values for the different experimental solutions at different temperatures are listed in Table S-III of the Supplementary material. The Table reveals that the φ_E^0 values are negative and decrease further as the temperature increases but increase with increasing content of H_2O for all the solutions. These facts may be attributed to structural perturbation influenced by the gradual appearance or disappearance of the caging/packing effect[41] as the water content increases in the ternary solutions or as the temperature of the solutions increases, respectively.

According to Hepler,[42] the sign of $(\delta\varphi_E^0/\delta T)_P$ is a better criterion in characterizing the long-range structure making or breaking ability of a solute in the solution phase. If the $(\delta\varphi_E^0/\delta T)_P$ values are small negative or positive, the solute acts as a structure maker, otherwise it acts as a structure breaker. The $(\delta\varphi_E^0/\delta T)_P$ values were obtained from the slope of a linear fit of the φ_E^0 values against the experimental temperature (T). The correlation coefficients (R^2) values were within the range (0.97210–0.99552). The $(\delta\varphi_E^0/\delta T)_P$ values for different ternary solutions are given in Table S-III of the Supplementary material and Fe^{III}(salen)Cl was found to act as a net structure promoter in the aqueous methanol solutions.

It is reported[43] that Fe^{III}(salen)Cl can produce a stable $[Fe^{III}(salen)]^+$ cation but the experimental solutions did not respond to the $AgNO_3$ test for free Cl^-. Hence, the solution viscosities (η) were analysed with a modified Jones–Dole equation:[44]

$$\eta/\eta_1 = \eta_r = 1 + Bc \quad (5)$$

where $\eta_r = \eta/\eta_1$ is the relative viscosity; η_1 and η are the viscosities of solvent and solution, respectively. The adjustable parameter B, referred to as the viscosity B-coefficient, was obtained by least squares analysis and the obtained values are reported in Table II. Similar to φ_V^0, the viscosity B-coefficient[45,46] provides another avenue to the effects of solute–solvent interactions based on the solution viscosity. Table II shows that the viscosity B-coefficients for Fe^{III}(salen)Cl in the

studied solvent systems were positive but their temperature dependence was negative. A solute that has positive viscosity *B*-coefficients with a negative dependence on temperature is generally considered as a structure maker. Accordingly Fe^{III}(salen)Cl can be considered as a structure maker for the present solvent systems studied. However, the viscosity *B*-coefficients decreased on the introduction of water (w_1 from 1.00 to 0.90), but after that the viscosity *B*-coefficients increased monotonically with further addition of water to the ternary solutions. This is probably due to a sudden perturbation of the arrangement of methanol molecules in the bulk methanol structure arising from strong solvent–solvent interactions in the solvent mixture with w_1 = 0.90. However, for the remaining solvent compositions, solute–solvent interaction seems to dominate in the characterisation of the solution viscosities and the viscosity *B*-coefficients.

TABLE II. Viscosity *B*-coefficients with standard deviations (σ) for Fe^{III}(salen)Cl in different aqueous methanol solutions for linear regression of Eq. (5) at different temperatures (standard errors are given in parenthesis); w_1 – mass fraction of methanol

Parameter	*T* / K		
	298.15	303.15	313.15
	w_1 = 1.00		
$B\times10^3$ / m^3 mol^{-1}	8.424 (±0.254)	8.255 (±0.161)	8.124 (±0.143)
R^2	0.99459	0.99772	0.99815
$\sigma\times10^3$	0.002	0.001	0.001
	w_1 = 0.90		
$B\times10^3$ / m^3 mol^{-1}	7.295 (±0.156)	6.941 (±0.265)	6.706 (±0.124)
R^2	0.99725	0.99131	0.99794
$\sigma\times10^3$	0.001	0.002	0.001
	w_1 = 0.80		
$B\times10^3$ / m^3 mol^{-1}	7.649(±0.180)	7.123 (±0.244)	6.887 (±0.199)
R^2	0.99667	0.99302	0.99502
$\sigma\times10^3$	0.001	0.002	0.001
	w_1 = 0.70		
$B\times10^3$ / m^3 mol^{-1}	7.883 (±0.364)	7.193 (±0.004)	6.991 (±0.079)
R^2	0.98738	0.99999	0.99922
$\sigma\times10^3$	0.002	0.001	0.001
	w_1 = 0.60		
$B\times10^3$ / m^3 mol^{-1}	7.891 (±0.231)	7.439 (±0.261)	7.133 (±0.298)
R^2	0.99490	0.99265	0.98962
$\sigma\times10^3$	0.002	0.002	0.002

According to Eyring and co-workers,[46] the application of statistical thermodynamics to the hole model of viscous flow based on the absolute reaction rate theory yielded the following relation for the free energy of activation for viscous flow per mole of the solvent/solvent mixture ($\Delta\mu_1^{\ominus *}$):

$$\Delta\mu_1^{\ominus *} = \Delta G_1^{\ominus *} = RT \ln\left(\frac{\eta_1 \varphi_{V,1}^0}{hN_A}\right) \tag{6}$$

where N_A and $\varphi_{V,1}^0$ are the Avogadro number and the partial molar volumes of the solvent, respectively. Other symbols have their usual meanings.[45] The above relation was also used for liquid mixtures[45,46] and when rearranged this relation can be expressed as:

$$RT \ln\left(\frac{\eta_1 \varphi_{V,1}^0}{hN_A}\right) = -\left(\frac{\Delta S_1^{\ominus *}}{R}\right) + \left(\frac{\Delta H_1^{\ominus *}}{R}\right)\left(\frac{1}{T}\right) \tag{7}$$

Hence, the values of $\Delta H_1^{\ominus *}$ and $\Delta S_1^{\ominus *}$ were obtained from a linear regression treatment of Eq. (7) with correlation coefficient (R^2) values within the range 0.99866–0.99961. Plots of ln ($\eta_1 \varphi_{V,1}^0 / hN_A$,) against ($10^3/T$) are shown in Fig. S-3 of the Supplementary material. A correlation between viscosity *B*-coefficients and the deviation between the contribution per mole of a solute to the free energy of activation for viscous flow of the solution ($\Delta\mu_2^{\ominus *}$) and the free energy of activation of viscous flow per mole of the pure solvent or solvent mixture ($\Delta\mu_1^{\ominus *}$) was suggested by Feakins *et al.*,[47] in the form of the following relation:

$$B = \left(v\varphi_{V,1}^0 - \varphi_{V,2}^0\right) + \varphi_{V,1}^0 \frac{\left(\Delta\mu_2^{\ominus *} - v\Delta\mu_1^{\ominus *}\right)}{RT} \tag{8}$$

where the coefficient *v* is 1 for an undissociated uncharged solute and $\varphi_{V,2}^0$ is the partial molar volume of the solute. Thus, the ($\Delta\mu_2^{\ominus *} - \Delta\mu_1^{\ominus *}$) values were calculated using relation (8) and the *B*-coefficient values were obtained from Eq. (5). Again, the ($\Delta\mu_2^{\ominus *} - \Delta\mu_1^{\ominus *}$) values can also be expressed as:

$$\frac{\left(\Delta\mu_2^{\ominus *} - \Delta\mu_1^{\ominus *}\right)}{RT} = -\frac{\left(\Delta S_2^{\ominus *} - \Delta S^{\ominus}\right)}{R} + \left[\frac{\left(\Delta H_2^{\ominus *} - \Delta H_1^{\ominus *}\right)}{R}\right]\left(\frac{1}{T}\right) \tag{9}$$

where $\Delta S_i^{\ominus *}$ and $\Delta H_i^{\ominus *}$ are the standard partial molar entropy and enthalpy, respectively, of activation for viscous flow per mole of i^{th} component in the solution. Hence, a linear regression treatment of Eq. (9), with the correlation coefficient (R^2) values within the range 0.81698–0.96863, provided the values of ($\Delta S_2^{\ominus *} - \Delta S_1^{\ominus *}$) and ($\Delta H_2^{\ominus *} - \Delta H_1^{\ominus *}$) from the corresponding slopes and intercept. The parameters $\Delta\mu_1^{\ominus *}$ and ($\Delta\mu_2^{\ominus *} - \Delta\mu_1^{\ominus *}$) are reported in Table III. $\Delta H_1^{\ominus *}$, ($\Delta H_2^{\ominus *} - \Delta H_1^{\ominus *}$), $\Delta S_1^{\ominus *}$ and ($\Delta S_2^{\ominus *} - \Delta S_1^{\ominus *}$) are reported in Table IV. Plots of ($\Delta\mu_2^{\ominus *} - \Delta\mu_1^{\ominus *}$) / *RT* against ($10^3/T$) are shown in Fig. S-4 of the Supplementary material.

TABLE III. The free energy of activation for viscous flow per mole of the solvent–solvent mixture, $\Delta\mu_1^{\ominus *}$, its deviation from the free energy of activation for viscous flow per mole of the solute, $\Delta\mu_2^{\ominus *}$, and $(\Delta\mu_2^{\ominus *} - \Delta\mu_1^{\ominus *})$ for Fe^{III}(salen)Cl in different aqueous methanol solutions at different temperatures (standard errors are given in parenthesis); w_1 – mass fraction of methanol

T / K	$\Delta\mu_1^{\ominus *}$ / kJ mol^{-1}	$(\Delta\mu_2^{\ominus *} - \Delta\mu_1^{\ominus *})$ / kJ mol^{-1}
	w_1 = 1.00	
298.15	9.97 (±0.01)	525.22 (±0.26)
303.15	9.97 (±0.01)	519.26 (±0.17)
313.15	10.00 (±0.01)	521.15 (±0.15)
	w_1 = 0.90	
298.15	10.52 (±0.01)	511.29 (±0.16)
303.15	10.53 (±0.01)	491.39 (±0.27)
313.15	10.61 (±0.01)	484.95 (±0.13)
	w_1 = 0.80	
298.15	10.95 (±0.01)	593.23 (±0.18)
303.15	11.04 (±0.01)	559.14 (±0.25)
313.15	11.22 (±0.01)	553.04 (±0.20)
	w_1 = 0.70	
298.15	11.12 (±0.01)	671.90 (±0.37)
303.15	11.23 (±0.01)	621.36 (±0.01)
313.15	11.43 (±0.01)	618.75 (±0.08)
	w_1 = 0.60	
298.15	11.33 (±0.01)	734.73 (±0.24)
303.15	11.47 (±0.01)	701.61 (±0.27)
313.15	11.73 (±0.01)	689.83 (±0.30)

TABLE IV. The standard partial molar enthalpy of activation for viscous flow of a solvent–solvent mixtures, $\Delta H_1^{\ominus *}$, and its deviation from the standard partial molar enthalpy of activation for viscous flow of the solute, $\Delta H_2^{\ominus *}$, $(\Delta H_2^{\ominus *} - \Delta H_1^{\ominus *})$, along with the standard partial molar entropy of activation for viscous flow of a solvent–solvent mixture, $\Delta S_1^{\ominus *}$, and its deviation from the standard partial molar entropy of activation for viscous flow of the solute, $\Delta S_2^{\ominus *}$, $(\Delta S_2^{\ominus *} - \Delta S_1^{\ominus *})$, for Fe^{III}(salen)Cl in different aqueous methanol solutions; w_1 – mass fraction of methanol

w_1	$\Delta H_1^{\ominus *}$ kJ mol^{-1}	$(\Delta H_2^{\ominus *} - \Delta H_1^{\ominus *})$ kJ mol^{-1}	$\Delta S_1^{\ominus *}$ J mol^{-1}K^{-1}	$(\Delta S_2^{\ominus *} - \Delta S_1^{\ominus *})$ J mol^{-1}K^{-1}
1.00	9.28 (±0.01)	587.17 (±7.34)	–2.31 (±0.04)	214.20 (±4.09)
0.90	8.56 (±0.02)	988.83 (±7.72)	–6.54 (±0.07)	1617.19 (±6.17)
0.80	5.62 (±0.01)	1307.11 (±4.45)	–17.89 (±0.03)	2423.24 (±8.32)
0.70	4.95 (±0.01)	1592.97 (±3.39)	–20.72 (±0.03)	3135.12 (±6.59)
0.60	3.37 (±0.01)	1552.35 (±4.52)	–26.70 (±0.02)	2767.67 (±7.28)

Table III shows that the $\Delta\mu_1^{\ominus *}$ values are almost invariant of the solvent composition and temperature, implying that $\Delta\mu_2^{\ominus *}$ is dependent mainly on the viscosity *B*-coefficients and the $(\varphi_{V,2}^0 - \varphi_{V,1}^0)$ terms. The values $\Delta\mu_2^{\ominus *}$ contain the change in the free energy of activation of solute molecules in presence of

solvent as well as the contribution from the movement of solute molecules. The $\Delta\mu_2^{\ominus *}$ values were positive at all the experimental temperatures and decreased as the temperature increased and increased as the content of water in the ternary solutions (except for those with w_1= 0.90) increased. Such a trend of the $\Delta\mu_2^{\ominus *}$ values suggest that the viscous flow becomes easier at higher temperatures but becomes more difficult with increased amount of water in the ternary solutions, *i.e.*, the formation of the transition state becomes less favourable with increased amounts of water but higher temperature favour its formation.[45]

According to Feakins *et al.*,[47] a solute molecule interacts with every solvent molecule and the sum of these interactions for all solute and solvent molecules is collectively defined as the solute–solvent interaction. A solute molecule interacts with all the solvent molecules in solution including any solvent molecule in its transition state. Thus the effect of the solute on the activation free energy of the solvent molecule is the difference between the solvation energies of the solute in the ground state solvent and the transition state solvent or free energy of transfer, $\Delta G_2^{\ominus *}(1 \rightarrow 1')$ between them. The second contribution to $\Delta\mu_2^{\ominus *}$ comes from the movement of the solute through its own viscous transition state, $\Delta G_2^{\ominus *}$ $(2 \rightarrow 2')$. Hence, the term $\Delta\mu_2^{\ominus *}$ can also expressed as:

$$\Delta\mu_2^{\ominus *} = \Delta G_2^{\ominus *}(1 \rightarrow 1') + \Delta G_2^{\ominus *}(2 \rightarrow 2') \qquad (10)$$

The values of $\Delta G_2^{\ominus *}(2 \rightarrow 2')$ can be approximated with the $\Delta\mu_1^{\ominus *}$ values and the values of $\Delta G_2^{\ominus *}(1 \rightarrow 1')$ simply become equal to the $(\Delta\mu_2^{\ominus *} - \Delta\mu_1^{\ominus *})$ values.

Thus, the quantity $(\Delta\mu_2^{\ominus *} - \Delta\mu_1^{\ominus *})$ is the change in the activation energy per mole of solute on replacing one mole of solvent by one mole of solute at infinite dilution. The obtained values of $(\Delta\mu_2^{\ominus *} - \Delta\mu_1^{\ominus *})$ are positive for all the solvent mixtures and the values decrease almost linearly as the temperature increases for all the solvent mixtures, but they increase with further addition of water in the ternary solutions (except for those with w_1 = 0.90). The positive $(\Delta\mu_2^{\ominus *} - \Delta\mu_1^{\ominus *})$ values and their negative temperature dependence with a similar trend in the viscosity *B*-coefficients for Fe^{III}(salen)Cl indicated the structure making ability of the solute and transfer of solute molecules from the ground state solvent to the transition state solvent is thermodynamically hindered.

Table IV shows that the $\Delta H_2^{\ominus *}$ values are positive for all the solvent systems and thus indicate rupture and distortion of the solvation bonds or intermolecular forces in the activated state of viscous flow and that the viscous process is endothermic. Thus, the viscous flow will be accompanied by a decrease in order and thus positive $\Delta S_2^{\ominus *}$ values were obtained for all the studied solutions. However, the negative $\Delta S_1^{\ominus *}$ values for all the solvent mixtures may be attributed to the negative entropy of mixing of the solutions over the entire range of concentration for aqueous methanol; such a negative entropy of mixing originates from the strong association between the solvent molecules at low methanol contents[35]

and the tendency of the solvent molecules to segregate and form clusters[48–50] in aqueous methanol solutions, which dominate the thermodynamics of aqueous methanol solutions.[51,52]

CONCLUSIONS

In the present study, derived parameters such as partial molar volumes (φ_V^0), partial molar expansibilities (φ_E^0), viscosity *B*-coefficients and various activation parameters for viscous flow for the under investigation Fe^{III}(salen)Cl indicate the presence of strong solute–solvent interactions and these interactions are further strengthened at higher content of water in the ternaries but decrease at higher temperatures. The results further show that Fe^{III}(salen)Cl is preferentially more solvated by water than methanol and it acts as a net structure promoter in the studied ternary solutions. The UV–Vis absorption spectra of the ternary solutions support of the obtained results. A transition state theory treatment of viscosity *B*-coefficients revealed that the transfer of the solute molecules from ground state solvent to transition state solvent is thermodynamically hindered and the viscous process is endothermic.

SUPPLEMENTARY MATERIAL

The physical properties of different aqueous methanol solutions and experimental densities, viscosities of Fe^{III}(salen)Cl solutions along with derived parameters at the experimental temperatures and their dependence on solvent composition and temperatures, *etc*. (listed in Tables S-I–S-III and Figs. S-1–S-4) are available electronically from http://www.shd.org.rs/JSCS/ or from the authors on request.

Acknowledgements. The authors are grateful to the Departmental Special Assistance Scheme under the University Grants Commission, New Delhi (SAP-DRS-III, No. F540/12/DRS/2013) for financial support. One of the authors (D. B) is also thankful to UGC, India for granting him a UGC BSR Research Fellowship in Science [Ref. No. 4-1/2008 (BSR)].

ИЗВОД

ПОНАШАЊЕ РАСТВОРА КОЈИ САДРЖИ (*N*,*N*′-БИС(САЛИЦИЛИДЕН)-ЕТИЛЕНДИАМИНАТО)ГВОЖЂЕ(III)-ХЛОРИД У СМЕШИ ВОДЕ И МЕТАНОЛА НА 298,15; 303,15 И 313,15 K

DHIRAJ BRAHMAN и BISWAJIT SINHA

Department of Chemistry, University of North Bengal, Darjeeling-734013, India

У овом раду су одређене парцијалне моларне запремине (φ_V^0) и *B*-коефицијенти Jones–Dole једначине (*N*,*N*′-бис(салицилиден)етилендиаминато)гвожђе(III)-хлорида, скраћено Fe^{III}(salen)Cl, у растворима смеше растварача воде и метанола мерењем густине и вискозности раствора на температурама 298,15; 303,15 и 313,15 K под атмосферским притиском. Привидне моларне запремине (φ_V) и густине (ρ) су коришћене за прорачун промена привидних моларних запремина од температуре (φ_E)и парцијалних моларних запремина од температуре (φ_E^0) као и одређивање облика температурне зависности при константном притиску $(\partial\varphi_E^0 / \partial T)_p$ у растворима Fe^{III}(salen)Cl са циљем да се

откриje природа различитих интеракција у тернарним растворима . Теорија прелазног стања је примењена у анализи *B* коефицијената на основу активационих параметара вискозног тока. Свеукупни резултати указују на јаке интеракције растворак–растварач између Fe^{III}(salen)Cl и молекула растварача, превасходно молекула воде као и да се Fe^{III}(salen)Cl понаша као компонента која стабилизује структуру тернарних раствора. UV-Vis апсорпциони спектри тернарних раствора потврђују добијене резултате.

(Примљено 14. априла, ревидирано 19. јула 2013)

REFERENCES

1. M. J. Garson, *Chem. Rev*. **93** (1993) 1699
2. T. Katsuki, *Coord. Chem. Rev*. **140** (1995) 189
3. M. F. Summers, L. G. Marzilli, N. B. Pahor, L. Randaccio, *J. Am. Chem. Soc.* **106** (1984) 4478
4. P. G. Lacroix, *Eur. J. Inorg. Chem.* (2001) 339
5. J. T. Groves, T. E. Nemo, R. S. Myers, *J. Am. Chem. Soc.* **101** (1979) 1032
6. J. T. Groves, T. E. Nemo, *J. Am. Chem. Soc.* **105** (1983) 5786
7. J. T. Groves, Y. Watanabe, *J. Am. Chem. Soc.* **110** (1988) 8443
8. A. Böttcher, M. W. Grinstaff, J. A. Labinger, H. B. Gray, *J. Mol. Catal., A* **113** (1996) 191
9. Y. W. Liou, C. M. Wang, *J. Electroanal. Chem.* **481** (2000) 102
10. F. L. Lindoy, *The Chemistry of Macrocyclic Ligand Complexes*, Cambridge University Press, Cambridge, 1989
11. Y. Zhong, G. L. Warren, S. Patel, *J. Comput. Chem.* **29** (2008) 1142
12. D. Ranchet, J. B. Tommasino, O. Vittori, P. L. Fabre, *J. Solution Chem.* **27** (1988) 979
13. G. E. Papanastasiou, I. L. Zlogas, *J. Chem. Eng. Data* **37** (1992) 167
14. C. Carr, J. A. Riddick, *Ind. Eng. Chem.* **43** (1951) 692
15. J. Timmermans, *Physico-Chemical Constants of Pure organic Compounds*, Elsevier, New York, 1950
16. S. Ismadji, H. Djojoputro, *J. Chem. Eng. Data* **50** (2005) 1343
17. M. R. Ganjali, P. Norouzi, M. Golmohammadi, M. Rezapour, M Salavati-Niasari, *Electroanalysis* **16** (2004) 910
18. T. Matsushita, H. Kono, M. Nishino, T. Shono, *Bull. Chem. Soc. Jpn.* **55** (1982) 2581
19. K. S. Pitzer, J. C. Peiper, R. H. Busey, *J. Phys. Chem. Ref. Data* **13** (1984) 1
20. K. N. Marsh, *Recommended reference materials for the realization of physicochemical properties*, Blackwell Scientific Publications, Oxford, 1987
21. J. A. Dean, *Lange's handbook of chemistry*, 11th ed., McGraw-Hill, New York, 1973
22. D. Brahman, B. Sinha, *J. Chem. Eng. Data* **56** (2011) 3073
23. A. K. Covington, T. Dickinson, *Physical chemistry of organic solvent systems*, Plenum, New York, 1973
24. H. S. Harned, B. B. Owen, *The Physical Chemistry of Electrolytic Solutions*, 3rd ed., Reinhold Publishing Corporation, New York, 1964
25. G. M. Bancroft, A. G. Maddock, R. P. Randl, *J. Chem. Soc., A* (1968) 2939
26. M. Gerloch, J. Lewis, F. E. Mabbs, A. Richards, *J. Chem. Soc., A* (1968) 112
27. M. Gullotti, L. Casella, A. Pasini, R. Ugo, *J. Chem. Soc., Dalton Trans.* (1977) 339
28. W. L. Jorgensen, J. Cao, C. Ravimohan, *J. Phys. Chem.* **89** (1985) 3470
29. E. D. Katz, C. H. Lochmuller, R. P. Scott, *Anal. Chem.* **61** (1989) 349
30. Z. Zhao, E. R. Malinowski, *Anal. Chem.* **71** (1999) 602

31. A. Wakisaka, H. A. Carime, Y. Yamamoto, Y. Kiyozumi, *J. Chem. Soc., Faraday. Trans.* **94** (1998) 369
32. T. Sato, A. Chiba, R. Nazaki, *J. Chem. Phys.* **112** (2000) 2924
33. G. Onori, *J. Chem. Phys.* **87** (1987) 1251
34. A. K. Soper, J. L. Finney. *Phys. Rev. Lett.* **71** (1993) 4346
35. G. Zhang, C. Wu, *J. Am. Chem. Soc.* **123** (2001) 1376
36. L. A. Woolf, *Pure Appl. Chem.* **57** (1985) 1083
37. I. Persson, *Pure Appl. Chem.* **58** (1986) 1153
38. R. K. Wadi, P. Ramasami, *J. Chem. Soc., Faraday Trans.* **93** (1997) 243
39. K. Belibagli, E. Agranci, *J. Solution Chem.* **19** (1990) 867
40. W. R. Cordoba, J. S. Zugazagoitia, E. C. Fregoso, J. Peon, *J. Phys. Chem., A* **111** (2007) 6241
41. F. J. Millero, *The partial molal volumes of electrolytes in aqueous solutions*, in *Water and Aqueous Solutions: Structure, Thermodynamics, and Transport Processes*, R. A. Horne, Ed., Wiley-Interscience, New York, 1972, p. 519
42. L. G. Hepler, *Can. J. Chem.* **47** (1969) 4617
43. F. Lloret, J. Moratal, J. Faus, *J. Chem. Soc. Dalton Trans.* (1983) 1743
44. W. Devine, B. M. Lowe, *J. Chem. Soc., A* (1971) 2113
45. D. Feakins, D. J. Freemantle, *J. Chem. Soc., Faraday Trans. I* **70** (1974) 795
46. S. Glasstone, K. Laidler, H. Eyring, *The Theory of Rate Processes*, McGraw-Hill, New York, 1941
47. D. Feakins, F. M. Bates, W. E. Waghorne, K. G. Lawrence, *J. Chem. Soc., Faraday Trans.* **89** (1993) 3381
48. T. D. Pascal, W. A. Goddard, *J. Phys. Chem., B* **116** (2012) 13905
49. S. Dixit, J. Crain, W. C. K. Poon, J. L. Finney, A. K. Soper, *Nature* **416** (2002) 829
50. A. K. Soper, L. Dougan, J. Crain, J. L. Finney, *J. Phys. Chem., B* **110** (2005) 3472
51. J. A. V. Butler, D. W. Thomson, W. H. MacLennan, *J. Chem. Soc.* (1933) 674
52. R. F. Lama, B. C. Y. Lu, *J. Chem. Eng. Data* **10** (1965) 216.

Journal of the Serbian Chemical Society
JSCS@tmf.bg.ac.rs • www.shd.org.rs/JSCS
J. Serb. Chem. Soc. 79 (2) S27–S32 (2014) *Supplementary material*

SUPPLEMENTARY MATERIAL TO

Solution behaviour of (*N*,*N*′-ethylenebis(salicylideneiminato))-iron(III) chloride in aqueous methanol at 298.15, 303.15 and 313.15 K

DHIRAJ BRAHMAN and BISWAJIT SINHA*

Department of Chemistry, University of North Bengal, Darjeeling-734013, India

J. Serb. Chem. Soc. 79 (2) (2014) 225–239

TABLE S-I. Densities (ρ) and viscosities (η) of different aqueous methanol solutions at different temperatures; w_1 – mass fraction of methanol

w_1	T / K	$\rho\times10^{-3}$ / kg m^{-3}		η / mPa s	
		Exp.	Lit.	Exp.	Lit.
1.00	298.15	0.78662	0.78645[1]	0.5469	0.542[1]
	303.15	0.78188	0.7819[2]	0.5092	0.510[2]
	313.15	0.77280	0.7720[3]	0.4488	0.4470[3]
0.90	298.15	0.81582	0.8158[4]	0.7619	0.7885[4]
	303.15	0.81084	0.8108[4]	0.7112	–
	313.15	0.80236	0.8023[4]	0.6344	–
0.80	298.15	0.84237	0.8424[4]	1.0036	1.0241[4]
	303.15	0.83769	0.8378[4]	0.9634	–
	313.15	0.82961	0.8294[4]	0.8871	–
0.70	298.15	0.86761	0.8675[4]	1.1849	1.2335[4]
	303.15	0.86310	0.8630[4]	1.1430	–
	313.15	0.85532	0.8550[4]	1.0620	–
0.60	298.15	0.89113	0.8910[4]	1.4091	1.4264[4]
	303.15	0.88649	0.8864[4]	1.3689	–
	313.15	0.87885	0.8787[4]	1.3017	–

TABLE S-II. Molalities (m), densities (ρ), viscosities (η), and apparent molar volumes (φ_V) of Fe^{III}(salen)Cl in different aqueous methanol solutions at different temperatures; w_1 – mass fraction of methanol

m / mol kg^{-1}	$\rho\times10^{-3}$ / kg m^{-3}	η / mPa s	$\varphi_V \times 10^6$/m^3 mol^{-1}
w_1 = 1.00			
T = 298.15 K			
0.0025	0.78706	0.5539	170.12
0.0036	0.78728	0.5575	158.24

* Corresponding author. E-mail: biswachem@gmail.com

TABLE S-II. Continued

m / mol kg^{-1}	$\rho \times 10^{-3}$ / kg m^{-3}	η / mPa s	$\varphi_V \times 10^6$/m^3 mol^{-1}
		w_1 = 1.00	
		T = 298.15 K	
0.0056	0.78774	0.5638	131.25
0.0076	0.78825	0.5710	107.82
0.0097	0.78876	0.5781	97.84
0.0117	0.78931	0.5879	82.80
		T = 303.15 K	
0.0025	0.78234	0.5164	156.34
0.0036	0.78256	0.5209	148.30
0.0056	0.78302	0.5272	124.24
0.0076	0.78353	0.5327	102.06
0.0097	0.78405	0.5399	91.22
0.0117	0.78459	0.5472	78.26
		T = 313.15 K	
0.0025	0.77327	0.4551	147.90
0.0036	0.77349	0.4595	141.73
0.0056	0.77397	0.4650	112.78
0.0076	0.77446	0.4705	96.85
0.0097	0.77498	0.4761	86.23
0.0117	0.77552	0.4815	73.26
		w_1 = 0.90	
		T = 298.15 K	
0.0025	0.81625	0.7659	179.86
0.0034	0.81646	0.7697	155.44
0.0054	0.81692	0.7772	132.14
0.0074	0.81741	0.7884	115.32
0.0093	0.81794	0.7961	95.63
0.0113	0.81849	0.8055	83.10
		T = 303.15 K	
0.0025	0.81129	0.7151	167.20
0.0034	0.81149	0.7189	150.17
0.0054	0.81195	0.7246	128.25
0.0074	0.81244	0.7321	111.99
0.0093	0.81298	0.7415	90.84
0.0113	0.81353	0.7509	78.73
		T = 313.15 K	
0.0025	0.80282	0.6383	159.83
0.0034	0.80303	0.6428	139.52
0.0054	0.80350	0.6494	117.64
0.0074	0.80399	0.6559	103.37
0.0093	0.80453	0.6625	83.07
0.0113	0.80508	0.6692	71.60

TABLE S-II. Continued

m / mol kg^{-1}	$\rho \times 10^{-3}$ / kg m^{-3}	η / mPa s	$\varphi_V \times 10^6$/m^3 mol^{-1}
		$w_1 = 0.80$	
		$T = 298.15$ K	
0.0024	0.84279	1.0096	177.85
0.0033	0.84300	1.0126	155.41
0.0052	0.84346	1.0251	128.99
0.0071	0.84395	1.0377	110.74
0.0090	0.84448	1.0503	93.93
0.0109	0.84507	1.0639	75.24
		$T = 303.15$ K	
0.0024	0.83812	0.9693	171.52
0.0033	0.83833	0.9732	150.45
0.0052	0.83879	0.9820	125.32
0.0071	0.83928	0.9926	107.60
0.0090	0.83981	1.0051	91.02
0.0109	0.84041	1.0178	71.09
		$T = 313.15$ K	
0.0024	0.83005	0.8948	164.63
0.0033	0.83025	0.8987	149.19
0.0052	0.83072	0.9064	120.78
0.0071	0.83121	0.9169	103.47
0.0090	0.83175	0.9266	85.39
0.0109	0.83230	0.9381	72.29
		$w_1 = 0.70$	
		$T = 298.15$ K	
0.0023	0.86802	1.1921	175.32
0.0032	0.86822	1.1961	158.86
0.0051	0.86869	1.2081	130.73
0.0069	0.86919	1.2240	107.82
0.0088	0.86971	1.2389	94.96
0.0106	0.87032	1.2597	72.35
		$T = 303.15$ K	
0.0023	0.86352	1.1470	169.15
0.0032	0.86371	1.1536	158.36
0.0051	0.86419	1.1667	127.30
0.0069	0.86468	1.1799	106.78
0.0088	0.86521	1.1930	92.27
0.0106	0.86582	1.2054	69.69
		$T = 313.15$ K	
0.0023	0.85574	1.0651	168.44
0.0032	0.85593	1.0708	157.45
0.0051	0.85642	1.0820	123.15
0.0069	0.85691	1.0938	102.96
0.0088	0.85745	1.1066	87.06

TABLE S-II. Continued

m / mol kg^{-1}	$\rho\times10^{-3}$ / kg m^{-3}	η / mPa s	$\varphi_V \times 10^6$/m^3 mol^{-1}
		w_1 = 0.80	
		T = 313.15 K	
0.0106	0.85802	1.1176	69.74
		w_1 = 0.60	
		T = 298.15 K	
0.0022	0.89153	1.4105	172.30
0.0031	0.89172	1.4197	161.56
0.0049	0.89219	1.4321	128.77
0.0067	0.89270	1.4523	106.06
0.0085	0.89321	1.4707	92.97
0.0103	0.89386	1.4912	67.36
		T = 303.15 K	
0.0022	0.88688	1.3734	177.78
0.0031	0.88711	1.3795	148.83
0.0049	0.88756	1.3938	125.41
0.0067	0.88808	1.4091	101.27
0.0085	0.88863	1.4263	82.87
0.0103	0.88918	1.4477	70.89
		T = 313.15 K	
0.0022	0.87925	1.3061	171.46
0.0031	0.87945	1.3121	156.25
0.0049	0.87992	1.3243	124.07
0.0067	0.88045	1.3385	97.58
0.0085	0.88097	1.3537	83.82
0.0103	0.88154	1.3736	68.60

TABLE S-III. Limiting partial molar expansibilities (φ_E^0) for Fe^{III}(salen)Cl in different aqueous methanol solutions at different temperatures; w_1 – mass fraction of methanol

w_1	$\varphi_E^0\times10^{-3}$ / m^3 mol^{-1} K^{-1}			$S_E\times10^{-3}$ / m^3 kg$^{1/2}$ mol^{-1} K^{-1}			$(\delta\varphi_E^0/\delta T)_p\times10^{-5}$ m^3 mol^{-1} K^{-2}
	298.15 K	303.15 K	313.15 K	298.15 K	303.15 K	313.15 K	
1.00	–2.158	–2.208	–2.278	13.809	14.152	14.584	–0.785
	(±0.203)	(±0.206)	(±0.214)	(±2.468)	(±2.502)	(±2.600)	(±0.044)
0.90	–1.804	–1.844	–1.898	9.623	9.868	10.130	–0.612
	(±0.085)	(±0.091)	(±0.091)	(±1.060)	(±1.121)	(±1.120)	(±0.035)
0.80	–1.252	–1.277	–1.313	8.491	8.641	8.890	–0.389
	(±0.262)	(±0.265)	(±0.274)	(±1.299)	(±1.33)	(±1.449)	(±0.015)
0.70	–0.550	–0.562	–0.575	1.504	1.558	1.576	–0.160
	(±0.261)	(±0.265)	(±0.272)	(±0.326)	(±0.379)	(±0.347)	(±0.015)
0.60	–0.409	–0.418	–0.427	0.496	0.506	0.518	–0.115
	(±0.319)	(±0.329)	(±0.334)	(±0.146)	(±0.265)	(±0.333)	(±0.011)

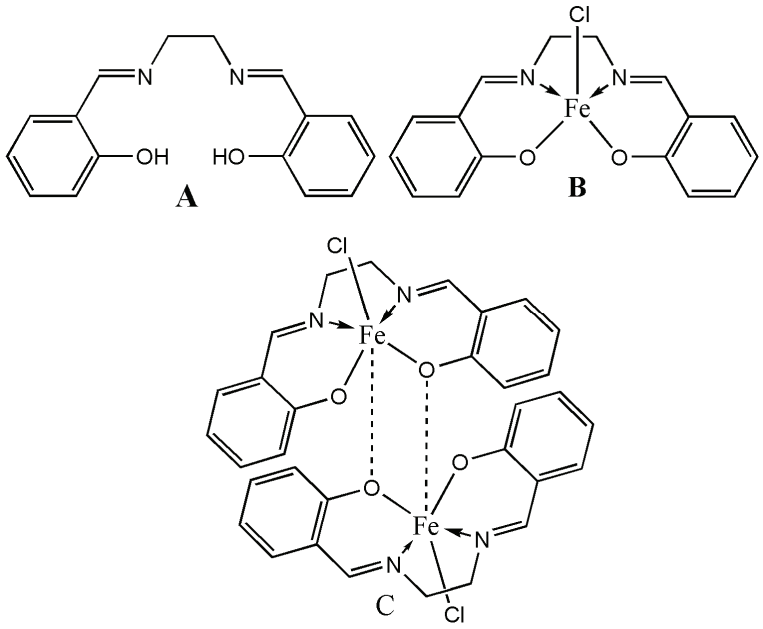

Fig. S-1. Molecular structures of A) salenH$_2$, B) Fe^{III}(salen)Cl and C) [Fe^{III}(salen)Cl]$_2$.

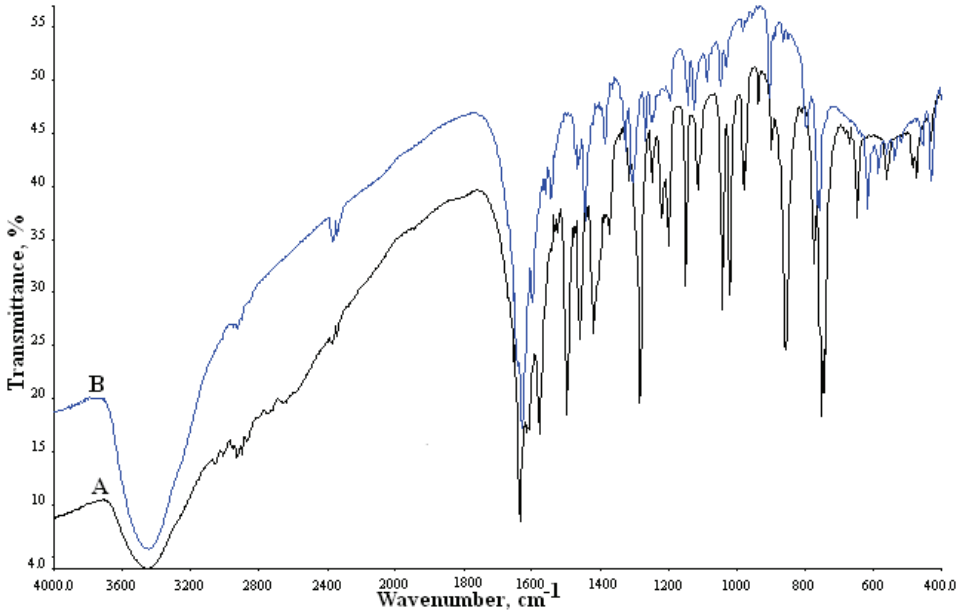

Fig. S-2. IR spectra of A) salenH$_2$ and B) Fe^{III}(salen)Cl in KBr pellets.

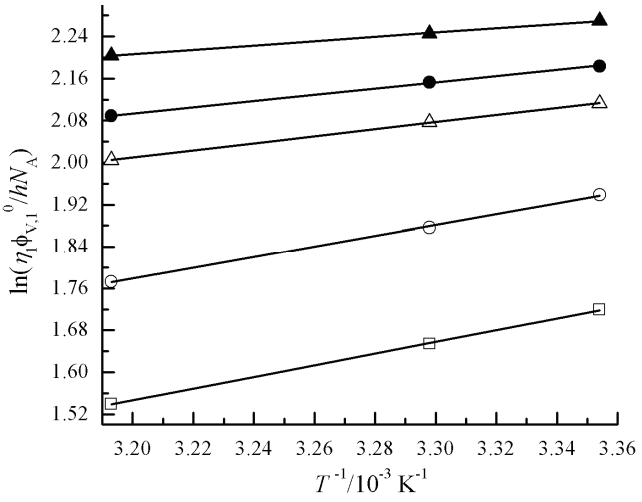

Fig. S-3. Plots of $\ln(\eta_1\varphi_{V,1}^{0}/hN_A)$ against T^{-1} for Fe^{III}(salen)Cl in aqueous methanol mixtures. Symbols: w_1 = 1.00, □; w_1 = 0.90, ○; w_1 = 0.80, Δ; w_1 = 0.70, ●; w_1 = 0.60, ▲; w_1 is the mass fraction of methanol in the aqueous methanol solutions.

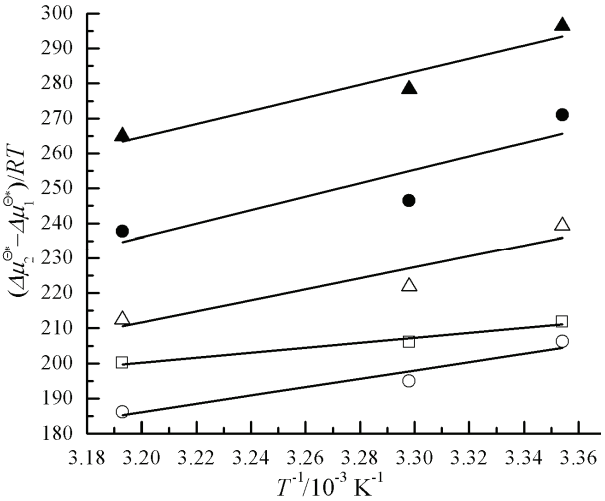

Fig. S-4. Plots of $(\Delta\mu_2^{\ominus *}-\Delta\mu_1^{\ominus *})/RT$ against T^{-1} for Fe^{III}(salen)Cl in aqueous methanol-water mixtures. Symbols: w_1 = 1.00, □; w_1 = 0.90, ○; w_1 = 0.80, Δ; w_1 = 0.70, ●; w_1 = 0.60, ▲; w_1 is the mass fraction of methanol in the aqueous methanol solutions.

REFERENCES

1. G. E. Papanastasiou, I. L. Zlogas, *J. Chem. Eng. Data* **37** (1992) 167
2. J. Timmermans, *Physico-Chemical Constants of Pure organic Compounds*, Elsevier, New York, 1950
3. S. Ismadji, H. Djojoputro, *J. Chem. Eng. Data* **50** (2005) 1343
4. C. Carr, J. A. Riddick, *Ind. Eng. Chem.* **43** (1951) 692.

Journal of the Serbian Chemical Society
JSCS-info@shd.org.rs • www.shd.org.rs/JSCS
J. Serb. Chem. Soc. 79 (2) 241–251 (2014)
JSCS–4579
UDC 532.135:665.33+631.8.022.3:537.872
Original scientific paper

Rheological behaviour of castor oil mixed with different pyromellitic esters

SORINA BORAN and ANDRA TAMAS*

CAICON Department, Faculty of Industrial Chemistry and Environmental Engineering, "Politehnica" University of Timisoara, Vasile Parvan Blv. 6, RO-300223 Timisoara, Romania

(Received 29 January, revised 29 April 2013)

Abstract: The paper presents the rheological behaviour study of castor oil mixed with different pyromellitic esters. The pyromellitic tetra-esters used were obtained through the esterification of pyromellitic anhydride with a special alcohol with a complex alkyl–aryl structure (2-phenoxy-ethanol) in conjunction with linear aliphatic alcohols with variable length (*n*-butanol, *n*-decanol). The influences of the structure and concentration of the pyromellitic esters as well as that of temperature, on the rheological behaviour were determined from the dependence between the shear stress τ and the shear rate $\dot{\gamma}$. An analysis of the dependence between τ and $\dot{\gamma}$ demonstrated that the studied solutions exhibited Newtonian behaviour. The evolution of the viscosity of the samples with temperature was characterized by Arrhenius type equations, the values of activation energy of viscous flow, E_a, were established. This constant can be correlated with the effect of friction reduction in the presence of additives. Characterization of the annulus of fluids flow under the effect of rotational motion was also realized by the calculation of the values of the Taylor–Reynolds number (Ta_{Re}).

Keywords: flow activation energy; Newtonian behaviour; oil additives; viscosity.

INTRODUCTION

The use of lubricants dates back over 3000 years when animal or vegetable fats were used to anoint wood or to facilitate transport processes. The main functions of a lubricant is to reduce friction and wear, to dissipate heat, to disperse deposits and to inhibit corrosion and rusting, while the main properties of a base oil are a relatively constant viscosity, low solidification temperature, low deposit formation, low volatility, good thermal-oxidative and hydrolytic stability, and biodegradablity.[1] The performance and features of lubricants differ from one another. Their only common point is that of composition that includes a main

* Corresponding author. E-mail: andra.tamas@upt.ro
doi: 10.2298/JSC130129062B

element called “the basis lubricant” (base oil) in proportion of 75 to 92 mass % and various additives.[2,3] Mineral base oils are a mixture of paraffinic, aromatic and naphthenic hydrocarbons extracted from crude oil. Their physico-chemical characteristics depend on the oil source and quality, as well as on the employed processing method.[1]

Semi-synthetic lubricants are a mixture of mineral and synthetic oils, designed to maintain their viscosity grades. Additives are designed to improve the performance of lubricants and/or give them new properties. Today, practically all types of lubricating oil contain at least one additive, and some oils contain additives of several different types. The amount of additive used varies from a few hundredths of a percent to 30 % or more.[4] They are designed to protect surfaces (decrease friction and implicit wear, increase resistance to high pressure and inhibit corrosion), to meliorate some properties of the base oil (improvement of the pour point and/or viscosity index, de-emulsifier) or to protect it (inhibit oxidetion and foaming).[5,6]

Along with the need to protect the environment, the use of vegetable oil--based lubricants has become an important alternative in tribology. The basic materials suitable for producing ecological lubricants are vegetable oils because of their high biodegradability, regeneration capacity, low toxicity and wide variety of sources.[7] Unlike mineral oil-based lubricants, those based on vegetable oils are rapidly and completely biodegradable, without having a negative effect on the ecosystem. However, their thermal and hydrolytic stability are lower than those of synthetic oils and require improvement through a variety of measures.[8–10]

The vegetable oils used for this purpose can be both edible (sunflower, soybean, coconut, peanut, palm and rapeseed) and inedible (castor oil).[11,12] The lubricating properties of castor oil were studied and were reported to be similar or better than those of the commonly used vegetable oils.[9,13]

Pyromellitic structures are known for their thermal resistance and polyfunctionality. In order to vary the properties of these esters, aliphatic alcohols of variable length in conjunction with a special alcohol of a complex alkyl–aryl structure (2-phenoxyethanol) were used. The special alcohol has an etheric bridge the influence of which can be expressed by the effect of increased flexibility.

In terms of using aliphatic alcohols with a very long chain, the length of alkyl chain enables fluids of high performance in terms of thermal and tribological properties to be obtained, which could be useful in metalworking or as valuable lubricants.

The existence of the pyromellitic structure ensures the maintenance of thermal resistance while the amount of the special alcohol with a mixed aliphatic––aromatic structure can increase this resistance and, respectively, ensures a wide range of viscosity values, a determinant aspect for their use in tribology.

Viscosity is one of the main properties of the employed oil and its value should vary as little as possible in operation, under all engine-operating conditions. It is desirable that any additive added to a base oil to improve its lubricating qualities should not have a negative influence on its rheological properties.

In this study, castor oil was used as the base vegetable oil with as auxiliary materials, paraffin oil and two pyromellitic esters, the synthesis and characterization of which were previously published.[14,15]

The aim of this work was to analyze the rheological behaviour of castor oil mixed with different pyromellitic esters. The influence of the structure and concentration of the pyromellitic esters, as well as that of temperature, on the rheological behaviour were followed. In addition, rheological relations $\tau = f(\dot{\gamma})$ were established and the activation energies, E_a, of flow were determined.[16–18]

EXPERIMENTAL

Materials

The preparation of the mixed esters is realized by reacting pyromellitic anhydride with 2-phenoxyethanol and *n*-butanol or *n*-decanol, using *p*-toluenesulphonic acid as catalyst. The formed water was extracted azeotropically by means of toluene.[6,16] These two esters are illustrated in the following general structure:

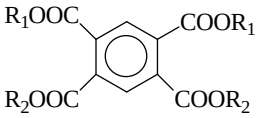

where R_1 = 2-phenoxyethyl and R_2 = *n*-butyl or *n*-decyl.

The two esters differ in the number of carbon atoms from the aliphatic alcohol used in the esterification of pyromellitic anhydride: 4 for PE1 ester (coming from *n*-butanol) and 10 for PE2 ester (coming from *n*-decanol). In both cases, the mole ratio between the residues 2-phenoxyethyl and *n*-butyl or *n*-decyl was 2:2.

The thus-prepared esters were analyzed in terms of tribological properties.[19]

The main characteristics of the pyromellitic esters (PE1 and PE2) are given in Table I and those of the castor oil and paraffin oil are given in Table II. Both oils were supplied by Fluka.

TABLE I. The properties of the pyromellitic esters at 20 °C

Ester	Formula	M / g mol^{-1}	ρ / kg m^{-3}	n_D	Saponification index, mg KOH g^{-1}	
					Theoretical	Analytical
PE1	$C_{34}H_{38}O_{10}$	606	1169.6	1.5373	370.36	369.51
PE2	$C_{46}H_{62}O_{10}$	774	1067.6	1.5135	289.97	292.32

Methods

The samples preparation was realized at room temperature (25 °C) by dispersing the pyromellitic ester, under intense stirring, in the oil mixtures. The composition of the samples

with the esters content is presented in Table III. Castor oil was used as the standard (sample C0). The samples were analyzed after one day of preparation.

TABLE II. The properties of the castor oil and paraffin oil

Property	Castor oil	Paraffin oil
Composition	Ricinoleic acid, min. 85 mass %; oleic acid, min. 2 mass %; linoleic acid, min. 1 mass %	–
Boiling point, °C	313	–
Pour point (by ASTM D97 method), °C	–33	–
ρ^{20} / kg m^{-3}	960	860
n_D^{20}	1.479	1.473
η^{20} / mPa s	903.3	1000

TABLE III. The composition of the samples

Sample	Composition, wt. %			Sample	Composition, wt. %		
	PE1	Paraffin oil	Castor oil		PE2	Paraffin oil	Castor oil
C1	2	5	93	D1	2	5	93
C2	3.5	3.5		D2	3.5	3.5	
C3	5	2		D3	5	2	
C4	7	0		D4	7	0	

The rheological characterization of the samples was performed under thermostatic conditions (temperature range 50–80 °C), using a Rheotest-2 rotation viscometer with the system vat-drum S/S$_1$ suitable for the viscosity range of these fluids and high sensitivity. The device allows the measurement of the torsion moment appearing thanks to the ring-shaped substance layer placed between a fixed cylinder and one rotating at a known revolution. The torsion moment was correlated with the shear stress. The revolution and the thickness of the ring-shaped layer determine the shear rate.

Shear rate values were changed in the range 9–1312 s^{-1}.

RESULTS AND DISCUSSION

The influence of ester type used as an additive on the rheological behaviour of castor oil was studied for different concentrations of additive, at three temperature values. In Fig. 1, the $\tau = f(\dot{\gamma})$ dependence is shown for an ester concentration of 5 % by weight.

The rheological equations corresponding to these dependencies are given in Table IV.

It was registered that for these pyromellitic esters, increasing the number of carbon atoms of the aliphatic alcohol used for the esterification did not change the viscosity of the oil significantly and did not modify its Newtonian behaviour. Increasing the temperature led to a decrease in the viscosity of the samples but without change of the Newtonian behaviour.

In addition, the influence of the additive concentration on the rheological behaviour of castor oil was studied. Thus, the $\tau = f(\dot{\gamma})$ dependence at a tempe-

rature of 50 °C when using the pyromellitic ester PE1 as an additive is shown in Fig. 2.

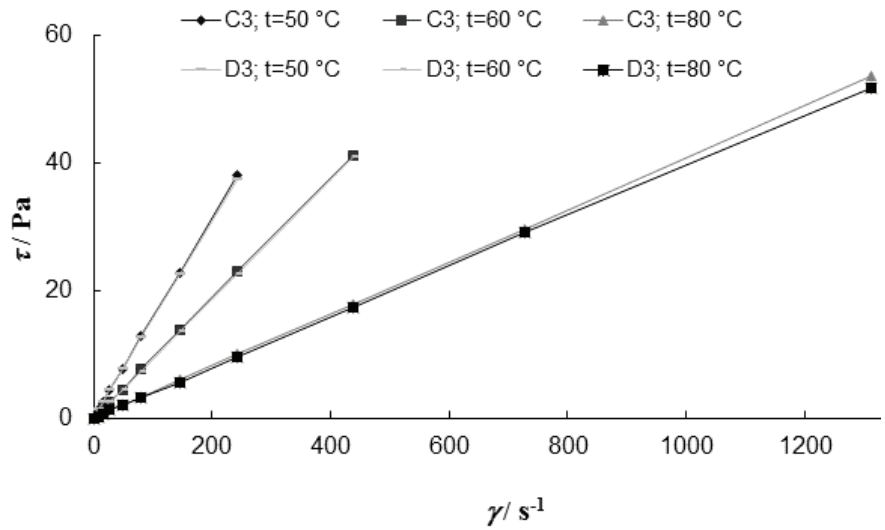

Fig. 1. Shear stress *vs.* shear rate for samples C3 and D3 at different temperatures.

TABLE IV. Rheological equations for samples C3 and D3

t / °C	Eq. ($\tau = \eta\dot{\gamma}$)		Viscosity decreasing[a], %
	C3	D3	
50	$\tau = 0.1565\dot{\gamma}$	$\tau = 0.1538\dot{\gamma}$	1.725
60	$\tau = 0.0939\dot{\gamma}$	$\tau = 0.0937\dot{\gamma}$	0.213
80	$\tau = 0.0407\dot{\gamma}$	$\tau = 0.0405\dot{\gamma}$	0.490

[a]Sample D3 compared with sample C3

From the slopes of the obtained straight lines, it was observed that the addition of a pyromellitic ester leads to a decrease of in the viscosity of the samples in comparison with the viscosity of oil without additives. The viscosity decrease is relatively small (about 15 %), the most pronounced decrease corresponds to an additive content of 2 mass %, followed by its increase with increasing the ester content, but without reaching the corresponding value of the pure oil. A similar situation occurs when PE2 pyromellitic ester was added to the oil. The obtained viscosity values are presented in Table V.

The exponential decrease of the samples viscosity with temperature is described by an Arrhenius-type equation:

$$\eta = A\exp\left(\frac{E_a}{RT}\right) \quad (1)$$

where E_a is the activation energy of flow, J mol^{-1}, R is the universal gas constant, J mol^{-1} K^{-1}, T is the absolute temperature and A represents a material constant, Pa s.

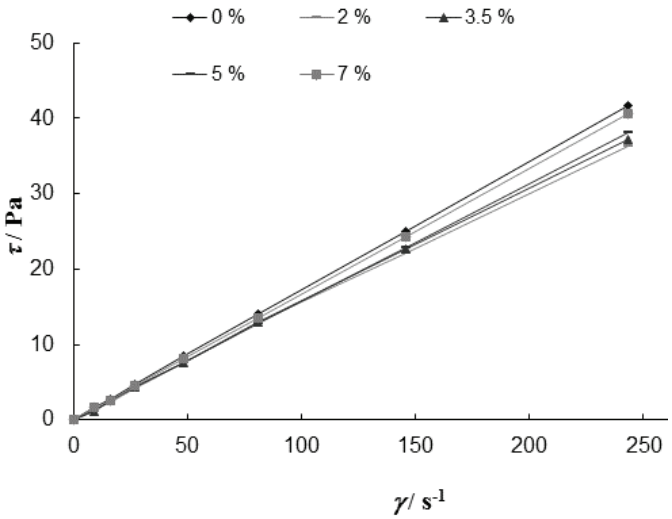

Fig. 2. Shear stress *vs.* shear rate for samples C0–C4 at 50 °C.

TABLE V. Dynamic viscosities of the samples

Sample	η / mPa s			Sample	η / mPa s		
	50 °C	60 °C	80 °C		50 °C	60 °C	80 °C
C0	171.4	103.6	43.5	D1	149.4	87.2	36.0
C1	149.7	88.2	37.6	D2	150.5	92.5	39.5
C2	153.4	90.4	39.2	D3	153.8	93.7	40.5
C3	156.5	93.9	40.7	D4	167.2	101.2	42.8
C4	167.1	98.3	42.3				

Through the measurements at different temperatures, it was possible to establish the dependence ln $\eta = f(1/T)$ and to calculate the E_a values. Particular expressions of Eq. (1) for the castor oil with the two types of pyromellitic esters additives are given in Table VI.

It was found that for the same type of ester, the variation of the activation energy of flow with the concentration of additive was insignificant. Moreover, this finding was valid even when the type of additive was changed, although they were of very different molecular weights.

Using particular expressions of the ln $\eta = f(1/T)$ dependence, the values of the dynamic viscosity of the samples was determined in the temperature range 20–100 °C. Thus, for pure castor oil (C0) and samples C3 and C4, the evolution of the viscosity is shown in Fig. 3.

TABLE VI. Arrhenius-type equations for samples C0–C4 and D1–D4

Sample	Eq. ($\eta = A\times10^5 \exp(E_a/RT)$)	E_a / kJ mol^{-1}
C0	$\eta = 1.70\exp(5212/T)$	43.3
C1	$\eta = 1.35\exp(5237/T)$	43.5
C2	$\eta = 1.70\exp(5167/T)$	42.9
C3	$\eta = 2.10\exp(5108/T)$	42.5
C4	$\eta = 1.65\exp(5204/T)$	43.2
D1	$\eta = 0.80\exp(5398/T)$	44.9
D2	$\eta = 1.75\exp(5160/T)$	42.9
D3	$\eta = 2.10\exp(5096/T)$	42.3
D4	$\eta = 1.80\exp(5178/T)$	43.0

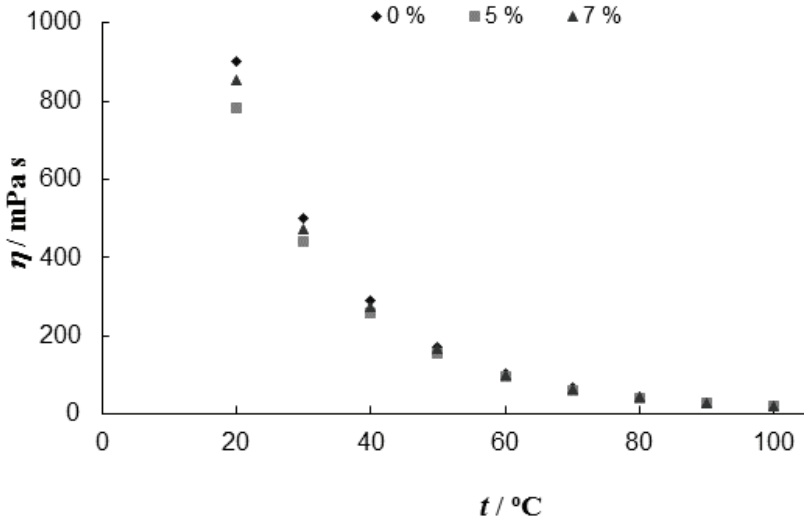

Fig. 3. Dynamic viscosity *vs.* temperature for samples C0, C3 and C4.

It is found that with increasing temperature, the values of the dynamic viscosity of the samples became more similar, regardless of the percentage of additive used.

Rotation in the annulus bounded by the concentric cylinders consisted of the relative flow of successive fluid layers. Changes in the additive process could be quantified by measuring the shear stress of the fluid layers when they were subjected to a controlled rotational motion. This change is reflected on the viscosity of the liquid.[20,21]

Since lubrication is usually used in rotating systems (bearings, gears, *etc*.), the dynamic characteristics (speed, dynamic pressure and shear stress) are expressed in terms of Taylor–Reynolds number (Ta_{Re}) specific to this type of motion. This criterion is also used to characterize fluids flow in the annulus under

the effect of rotational motion and allows all the changes that appear in the flow layers through the gradual increase in revolution to be highlighted.

The values of Ta_{Re} number were calculated using relation (2), taking into account the radii of the inner and outer cylinder (r_i and r_o), the inner cylinder revolution number, n, and the fluid properties (viscosity η and density ρ):[18]

$$Ta_{Re} = \frac{2\pi n r_i (r_o - r_i)\rho}{\eta} \quad (2)$$

Increasing the hydrodynamic regime (characterized by the Ta_{Re} number) leads to a pronounced decrease of the ratio between shear stress τ (experimentally determined) and dynamic pressure P_{dyn} calculated with the maximum speed.

By analogy with fluids flow through straight pipes, the dynamic pressure of the fluid in motion in ring-shaped spaces is calculated by:

$$P_{dyn} = \frac{\rho w_{max}^2}{2} \quad (3)$$

$$w_{max} = \pi d_i n \quad (4)$$

where w_{max} is the speed of fluid laminar layer placed next to the moving wall (inner cylinder) and d_i is the inner diameter of the ring-shaped space.

The variation of the τ/P_{dyn} ratio *vs.* Ta_{Re} for the samples C0, D2 and D4 at a constant temperature (50 °C) is shown in Fig. 4. The variation of the same ratio for sample D2 as a function of temperature is shown in Fig. 5.

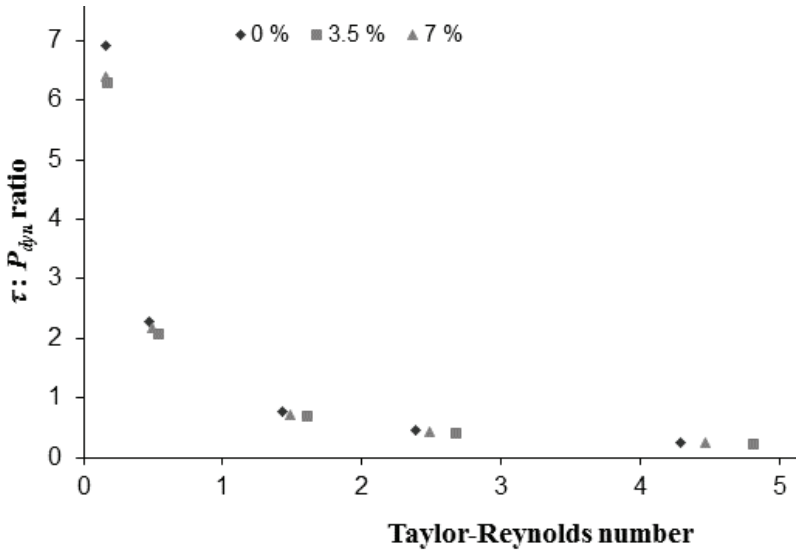

Fig. 4. Ratio τ:P_{dyn} *vs.* Ta_{Re} at 50 °C for samples C0, D2 and D4.

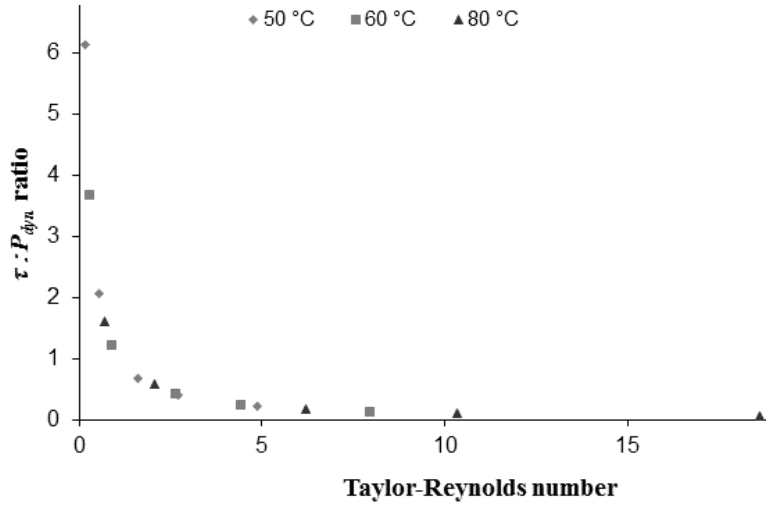

Fig. 5. The influence of temperature on the dependence of the τ:P_{dyn} ratio on Ta_{Re} for sample D2.

It can be seen from Figs. 4 and 5 that that neither the additive concentration nor the temperature have a significant effect on the dependence of the τ/P_{dyn} ratio on the Ta_{Re} number. The profile of both dependencies shows an accentuated decrease with increasing hydrodynamic flow regime.

By analogy, for circular motion of the fluid in stirring processes,[22] the ratio τ/P_{dyn} is correlated with Ta_{Re} number by a relationship of the type:

$$\tau / P_{dyn} = C Ta_{Re}^{m} \tag{5}$$

or in the linear logarithmic form:

$$\ln(\tau / P_{dyn}) = \ln C + m \ln(Ta_{Re}) \tag{5a}$$

The linear forms of the relationship, Eq. (5a), determined for sample D2 at different temperatures and for C0, D2 and D4 at 50 °C are given in Tables VII and VIII, respectively.

TABLE VII. Linear forms of Eq. (5a) for sample D2

t / °C	Eq. ($\ln(\tau/P_{dyn}) = \ln C + m \ln Ta_{Re}$)	C
50	$\ln(\tau/P_{dyn}) = 0.1004 - 1.0102 \ln Ta_{Re}$	1.105
60	$\ln(\tau/P_{dyn}) = 0.0824 - 1.002 \ln Ta_{Re}$	1.086
80	$\ln(\tau/P_{dyn}) = 0.1256 - 1.013 \ln Ta_{Re}$	1.134

Considering that the shear stress τ is equivalent to the friction pressure drop, it could be assumed that the ratio of the two quantities is equal to the friction coefficient, λ, which in the laminar flow regime has a value of $64Re^{-1}$.

TABLE VIII. Particular forms of Eq. (5a) for samples C0, D2 and D4, at 50 °C

Sample	Eq. ($\ln(\tau/P_{dyn}) = \ln C + m \ln Ta_{Re}$)	C
C0	$\ln(\tau/P_{dyn}) = 0.0850 - 1.0055 \ln Ta_{Re}$	1.089
D2	$\ln(\tau/P_{dyn}) = 0.1004 - 1.0102 \ln Ta_{Re}$	1.105
D4	$\ln(\tau/P_{dyn}) = 0.1735 - 1.0247 \ln Ta_{Re}$	1.189

This assumption was confirmed from two directions: on the one hand, the Ta_{Re} values lower than 60, which is the critical value that separates the laminar from the turbulent regime, for fluids flow in annulus.[21,23,24] On the other hand, from the equations presented in Tables VII and VIII, it could be seen that the values of the *m* coefficient are very close to the value –1, similar to the Reynolds exponent from the expression of the friction coefficient, and the values of the *C* coefficient increase slightly with increasing additive content.

CONCLUSIONS

The rheological behaviour of castor oil mixed with was studied, whereby the influence of the type and concentration of the pyromellitic ester and of temperature were monitored.

For each analyzed sample, a linear dependence between shear stress and the shear rate, without a yield point, was found, which shows Newtonian behaviour.

The addition of castor oil led to a slight decrease in viscosity, the most pronounced decrease corresponding to an additive content of 2 mass %. This finding was independent of the nature of the additive used and the temperature. Moreover, increasing the number of carbon atoms of the aliphatic alcohol had an insignificant influence on the viscosity of the castor oil and did not change its Newtonian behaviour.

The viscosity of the samples decreased exponentially with temperature in an Arrhenius-type manner, which enabled the calculation of the activation energy of flow. It is found that these values are insignificantly influenced by changing the type and concentration of the additive.

For the studied system, the dependence between the rheological parameters and the Taylor–Reynolds number (Ta_{Re}) was established. From graphical representations of this dependence, it could be concluded that circular motion of the fluid occurred in the laminar regime.

ИЗВОД

РЕОЛОШКО ПОНАШАЊЕ РИЦИНУСОВОГ УЉА ПОМЕШАНОГ СА РАЗЛИЧИТИМ ПИРОМЕЛИТИЧКИМ ЕСТРИМА

SORINA BORAN и ANDRA TAMAS*

CAICON Department, Faculty of Industrial Chemistry and Environmental Engineering, "Politehnica" University of Timisoara, Vasile Parvan Blv. 6, RO-300223 Timisoara, Romania

Овај рад представља испитивање реолошког понашања рицинусовог уља помешаног са различитим пиромелитичким естрима. Коришћени пиромелитички тетраестри су

добијени естирификацијом пиромелитичког анхидрида специјалним алкохолом сложене алкил–арил структуре (2-фенилетанол), заједно са линеарним алифатичким алкохолом промењиве дужине (*n*-бутанол и *n*-деканол). Утврђен је утицај струцтуре и концентрације пиромелитичких естара, као и температуре, на реолошко понашање, постављањем зависности између напона смицања, τ, и брзине смицања, $\dot{\gamma}$. Анализа зависности између τ и $\dot{\gamma}$ показује да испитивани раствори имају Њутновско понашање. Промена вискозности узорака са температуром је карактерисана једначином Аренијусовог типа, уз успостављање вредности активационе енергије вискозног тока, E_a. Ова константа може да се доведе у корелацију са ефектом смањења трења у присуству адитива. Такође је извршена карактеризација ануларног тока флуида при ефектима ротационог кретања, уз израчунавање вредности Таулор–Реунолдсовог броја (Ta_{Re}).

(Примљено 29. јануара, ревидирано 29. априла 2013)

REFERENCES

1. S. Z. Erhan, *Vegetables oils as lubricants, hydraulic fluids and inks - Bailey's Industrial Oil and Fat Products*, 6th ed., Wiley, Hoboken, NJ, 2005, p. 259
2. http://www.yacco-lub.ro/compozitie.html (28.12.2012)
3. http://www.lubrizol.com/Our-Company/Business-Segments/Lubrizol-Additives.html (28.12.2012)
4. N. S. Ahmed, A. M. Nassar, in *Tribology-Lubricants and Lubrication,* 1st ed., InTech, Rijeka, 2011, p. 249
5. S. Q. A. Rizvi, *A Comprehensive Review of Lubricant Chemistry, Technology, Selection, and Design*, ASTM International, West Conshohocken, PN, 2009, pp. 8–46, 100–211
6. L. E. Mirci, D. Resiga, V. Pode, *Lubr. Sci.* **22** (2010) 341
7. R. L. Goyan, R. E. Melley, P. A. Wissner, W. C. Ong, *Lubr. Eng*. **54** (1998) 10
8. I. Lesiga, M. Picek, K. Nahal, *J. Synth. Lubr.* **13** (1997) 347
9. S. Asadauskas, J. M. Perez, J. Duda, *Lubr. Eng*. **53** (1997) 35
10. R. Becker, A. Knots, *Lubr. Sci*. **8** (1996) 295
11. O. N. Anand, C. V. Kumar, *J. Synth. Lubr*. **23** (2006) 91
12. P. V. Joseph, D. Saxena, D. K. Sharma, *J. Synth. Lubr*. **24** (2007) 181
13. Y. Gerbig, S. I. Ahmed, F. A. Gerbig, H. Haefke, *J. Synth. Lubr*. **21** (2004) 177
14. L. E. Mirci, S. Terescu (Boran), G. Istratuca, *Mat. Plast*. **36** (1999) 13
15. L. E. Mirci, Patent RO 111760 (1996)
16. L. E. Mirci, S. Boran, V. Pode, D. Resiga, *J. Synth. Lubr*. **24** (2007) 51
17. A. Tamas, M. Vincze, *Studia UBB Chemia* **56** (2011) 85
18. A. Tamas, M. Vincze, *Studia UBB Chemia* **56** (2011) 247
19. L. E. Mirci, J. Herdan, *Tribol. Lett*. **4** (1998) 293
20. N. Bors, *PhD Thesis*, Politehnica Univ. of Timisoara, Timisoara, 2010, pp. 80–100 (in Romanian)
21. A. Tamas, N. Bors, R. Minea, *Petroleum-Gas Univ. of Ploiesti Bull., Techn. Ser.* **LX** (2008) 105
22. K. F. Pavlov, P. G. Romankov, A. A. Noskov, *Chemical engineering processes and devices*, Tehnica, Bucuresti, 1981, p. 112 (in Romanian)
23. N. Bors, A. Tamas, Z. Gropsian, *Chem. Bull. Politehnica Univ. Timisoara* **53** (2008) 16
24. N. Bors, A. Tamas, *Sci. Bull. Politehnica Univ. Timisoara-Transactions on Mechanics* **1** (2010) 81.

Journal of the Serbian Chemical Society
JSCS-info@shd.org.rs • www.shd.org.rs/JSCS
J. Serb. Chem. Soc. 79 (2) 253–263 (2014) UDC 666.32–039.7+661.183:628.193+620.266.1
JSCS–4580 *Original scientific paper*

Organobentonites as multifunctional adsorbents of organic and inorganic water pollutants

NATAŠA JOVIĆ-JOVIČIĆ[1]*, ALEKSANDRA MILUTINOVIĆ-NIKOLIĆ[1#], MARIJA ŽUNIĆ[1], ZORICA MOJOVIĆ[1], PREDRAG BANKOVIĆ[1], BILJANA DOJČINOVIĆ[2], ANA IVANOVIĆ-ŠAŠIĆ[1] and DUŠAN JOVANOVIĆ[1]

[1]*University of Belgrade, Institute of Chemistry, Technology and Metallurgy, Center for Catalysis and Chemical Engineering, Njegoševa 12, 11000 Belgrade, Serbia and* [2]*University of Belgrade, Institute of Chemistry, Technology and Metallurgy, Center for Chemistry Njegoševa 12, 11000 Belgrade, Serbia*

(Received 13 January, revised 12 June 2013)

Abstract: The aim of this study was to find a low cost, easy to synthesize and efficient adsorbent for the simultaneous adsorption of both organic and inorganic pollutants (including textile dyes, toxic metals, *etc.*). The starting material, domestic bentonite clay from Bogovina, was modified with amounts of hexadecyltrimethylammonium cations corresponding to 0.5 and 1.0 times the value of the cation exchange capacity. The organobentonites were tested as adsorbents in a three-dye-containing solution, a three-component solution of Pb^{2+}, Cd^{2+} and Ni^{2+} and a hexa-component solution containing all the investigated dyes and toxic metal cations. The used adsorbents showed the highest affinity toward acid yellow 99 and Ni^{2+}. Dye adsorption was enhanced in the presence of toxic metal cations, while the adsorption of all toxic cations from the hexa-component solution was lower than from the three-component solution containing only toxic cations. The synthesized hexadecyltrimethylammonium bentonite could be regarded as an efficient multifunctional adsorbent for the investigated types of water pollutants.

Keywords: simultaneous adsorption; multi-component solutions; dyes; toxic metals; adsorption affinity.

INTRODUCTION

The treatment of soil and water contaminated with mixtures of organic and inorganic pollutants is a challenging task since inorganic and organic contaminants have different transport mechanisms and fate in the environment.[1]

Naturally occurring bentonite clays are able to adsorb toxic metal cations from their aqueous solutions. In general, there are two mechanisms of adsorption:

* Corresponding author. E-mail: natasha@nanosys.ihtm.bg.ac.rs
# Serbian Chemical Society member.
doi: 10.2298/JSC130125065J

ion exchange in the interlamellar region and adsorption on the surface by complexation and precipitation. Ion exchange involves interlamellar cations in smectites.[2,3] The second mechanism is pH dependent. Surface complexation and precipitation occur at surface sites (hydroxyl groups on the external layers and edges).[4,5] By organomodification, bentonite clays obtain the ability to adsorb organic contaminants (non-polar organic compounds, toxic organic dyes, *etc*.).[6,7] The adsorption of inorganic compounds on these materials was also studied.[8,9] The earlier approach was to study independently metal uptake by bentonite[10] and the uptake of organic contaminants by organobentonites.[11] However, the most current and potential uses of organoclays, *i.e*., as landfill additives and reactive barriers, demand the simultaneous removal of organic and inorganic contaminants. The simultaneous adsorption of non-polar organic compounds and toxic metal cations on organoclays was studied[8,12] but there is a lack of data on the simultaneous adsorption of polar organic compounds and toxic metals cations from their solutions.

In previous studies,[13,14] organobentonites with partially substituted exchangeable cations were synthesized. The obtained materials exhibited simultaneously organophilicity and hydrophilicity. Therefore, these materials showed adsorption ability for the simultaneous adsorption of dye acid orange 10 and Pb^{2+},[14] as well as reactive black 5 and Pb^{2+}.[15] According to these results, two hexadecyltrimethylammonium bentonites (HDTMA-B) were chosen to be tested as multifunctional adsorbents for both organic and inorganic water pollutants. The 0.5 HDTMA-B and 1.0 HDTMA-B, obtained by ion exchange with amounts of hexadecyltrimethylammonium cation ($HDTMA^+$) corresponding to 0.5 and 1.0 times of the cation exchange capacity (*CEC*) value, respectively, were tested. The selected adsorbents differed in the composition of the interlamellar region and, therefore, expressed different affinities toward the adsorption of organic and inorganic pollutants.[15]

In this paper, adsorption from different solutions was investigated. The investigated solutions contained either the three selected organic dyes or the three selected toxic metals and finally all six chosen pollutants. The aim of this study was to show whether the investigated organobentonites are potential multifunctional adsorbents for the treatment of complex wastewaters.

EXPERIMENTAL

Adsorbates

Three commercial dyes, namely acid orange 10 (AO10), acid yellow 99 (AY99) and reactive black 5 (RB5) were selected as organic pollutants in this study (Fig. 1). These dyes are widely used in the dyeing of wool, leather, silk, paper and polyamide textiles. All dyes were purchased from Sigma–Aldrich. Toxic metal cations (Pb^{2+}, Cd^{2+} and Ni^{2+}) as nitrate salts were used as test models of inorganic pollutants. Lead (II) nitrate ($Pb(NO_3)_2$) with the purity of 99.99 %, was supplied by the Aldrich Chemical Company, cadmium (II) nitrate

($Cd(NO_3)_2$) with the purity of >99 % was purchased from Carlo Erba and nickel (II) nitrate ($Ni(NO_3)_2$) with the purity of 99.8 % was purchased from Kemika, All compounds were used as received.

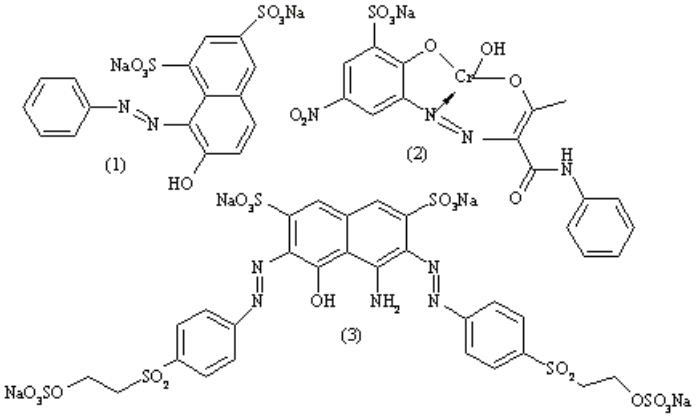

Fig. 1. The chemical structure of the investigated dyes: AO10 (1); AY99 (2); RB5 (3).

Adsorbents

Bentonite was obtained from the Bogovina Coal and Bentonite Mine in Serbia. It was crushed, ground and sieved through a 74-μm sieve. The chemical composition was reported previously.[16]

Na-enriched bentonite (Na-B) and partially exchanged organobentonites were synthesized using previously described procedures.[11,13,14] The organobentonites (OBs) were obtained by the modification of Na-B with hexadecyltrimethylammonium (HDTMA) bromide (supplied by the Alfa-Aesar Chemical Company with purity of 98 %). For this study, the OBs with HDTMA/bentonite ratios of 0.317 and 0.633 corresponding to 0.5 and 1.0 times the value of *CEC* of the clay were chosen. The samples were denoted as 0.5 HDTMA-B and 1.0 HDTMA-B. Detailed characterization of these samples was reported previously.[11,13,14]

Methods

The aqueous adsorbate solutions used in the adsorption study were: *i*) a three-component solution containing AO10, AY99 and RB5 dyes, *ii*) a three-component solution of Pb^{2+}, Cd^{2+} and Ni^{2+} toxic cations and *iii*) a hexa-component solution containing all the investigated dyes and toxic cations (AO10, AY99, RB5, Pb^{2+}, Cd^{2+} and Ni^{2+}). The initial concentration of each adsorbate in all solutions was 50 mg dm^{-3}. The initial pH value was unadjusted (5.5±0.5).[15]

The adsorption was investigated with respect to the contact time (10, 20, 60, 90, 120, 180, 1440 and 2880 min). The experiments were realized at room temperature (25 °C) and using equal volumes of adsorbate solutions, V =50.0 cm^3. The mass of adsorbent (m_{ads}) in all the adsorption studies was 10.0 mg. The adsorption experiments were performed in a thermostated shaker (Memmert WNE 14 and SV 1422). The samples were withdrawn from the shaker at predetermined times and the removed suspension was centrifuged (model Heittech Eva 21) at 17000 rpm for 10 min.

The amount of adsorbed pollutant after time t (q_t / mg g^{-1} or mmol g^{-1}), was calculated using the following mass balance relationship:

$$q_t = \frac{(c_0 - c_t)V}{m_{\text{ads}}} \quad (1)$$

where c_0 and c_t are concentrations of adsorbate at the initial and at time t, respectively. An equilibrium time of 24 h was taken for all the investigated processes, although for some experiments, equilibrium was reached after significantly shorter times. The equilibrium--adsorbed amount was denoted as q_e.

The absorbance of supernatant solution was measured. The spectra of dyes were obtained using a Thermo Electron Nicolet Evolution 500 UV–Vis spectrophotometer.

In preliminary research, it was confirmed that the presence of the investigated toxic metal cations affected neither the position nor the intensity of the dye absorption band at the applied concentrations of the investigated pollutants.

The content of Pb^{2+}, Cd^{2+} and Ni^{2+} in the supernatant solutions was determined by inductively coupled plasma optical emission spectrometry (ICP–OES). The ICP–OES measurements were performed using a Thermo Scientific iCAP 6500 Duo ICP instrument (Thermo Fisher Scientific, Cambridge, UK). For each run, the ICP–OES measurements were performed in triplet. The emission lines Pb II at 220.353 nm, Cd I at 228.802 nm and Ni II at 231.604 nm were employed.

Calculation of the concentrations of the dyes. The determination of concentrations of each dye in the three- and hexa-component solutions was based on the Lambert–Beer Law, where the absorbance is considered as being proportional to the concentration in the lower concentration range, and the additive property of absorbance (Eqs. (2)–(4)). Prior to the concentration determination, calibration curves for each investigated wavelength and dye were plotted. In each case, a linear relationship between the absorbance and the dye concentration was obtained (correlation coefficients ≥0.999 within the concentration range 0–75 mg dm^{-3}).

The UV–Vis spectra of each investigated dye together with spectrum of three-component solution of all the investigated dyes are presented in Fig. 2.

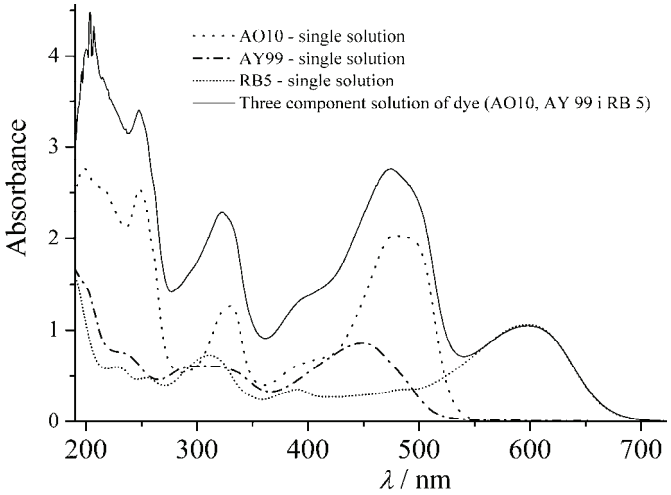

Fig. 2. UV–Vis spectra of the single component solutions of AO10, AY99, RB5 and their three-component solution.

In the solutions that contained the three dyes (AO10, AY99 and RB5), the calculations were performed using the absorbance at the wavelengths 478, 449 and 599 nm. Consequently, the measured absorbances were denoted A_{478}, A_{448} and A_{599}. These wavelengths were chosen since they represent the maximum absorption peaks for each of the investigated dyes. The concentration of each investigated dye was determined using the following equations:[17]

$$A_{478} = c_{AO10}0.0414^{*} + c_{AY99}0.0109 + c_{RB5}0.0076 \quad (2)$$

$$A_{449} = c_{AO10}0.0266 + c_{AY99}0.0163^{*} + c_{RB5}0.0065 \quad (3)$$

$$A_{599} = c_{RB5}0.0243^{*} \quad (4)$$

where c_{AO10}, c_{AY99} and c_{RB5} are the concentrations of AO10, AY99 and RB5, respectively. The symbol * indicates the calibration constants at the wavelength of maximum absorption peaks of each dye.

RESULTS AND DISCUSSION

Adsorption from the three-component solution of the selected dyes

The influences of the adsorption time on percent of the dyes removed are presented in Fig. 3a and b for the as adsorbents 0.5 HDTMA-B and 1.0 HDTMA-

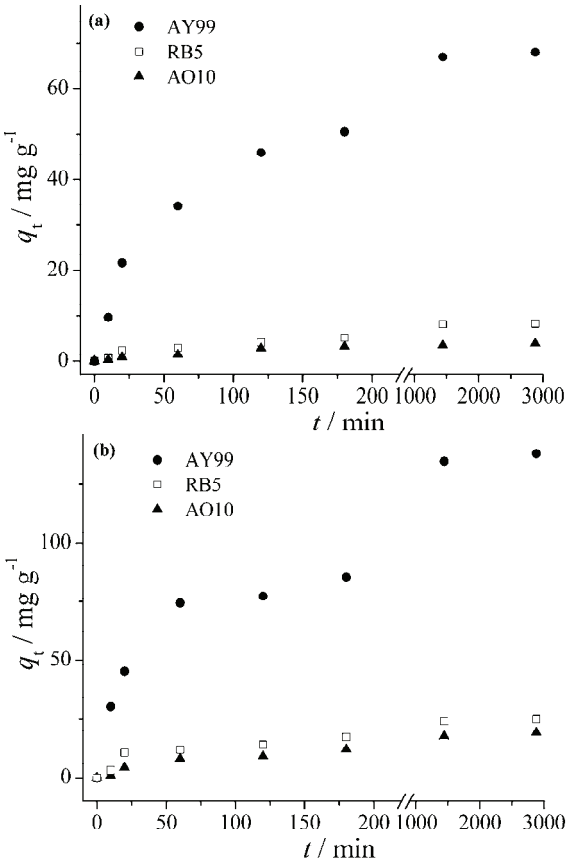

Fig. 3. Adsorption of AO10, AY99 and RB5 onto: a) 0.5 HDTMA-B and b) 1.0 HDTMA-B.

-B, respectively. The obtained values of the equilibrium-adsorbed amounts for each dye are given in Table I. For the sake of comparison, previously published q_e values obtained for adsorption from single dye solutions are also provided in Table I.

TABLE I. The q_e (mg g^{-1}) values for the dyes from the single-component and the three--component solutions

Adsorbent	Three-component solution			Single-component solution		
	Dye					
	AY99	AO10	RB5	AY99	AO10[14]	RB5[15]
0.5 HDTMA-B	68.12	8.26	3.97	103.53	9.16	11.9
1.0 HDTMA-B	138.26	19.12	25.00	142.25	22.83	54.67

The adsorption from three-component solution is slow and equilibrium was reached after 1440 min. Further extension of the adsorption time up to 2880 min did not lead to additional adsorption. Therefore, 1440 min was defined as equilibrium time. Both 0.5 HDTMA-B and 1.0 HDTMA-B had the highest affinity toward AY99. By analyzing the structure of the investigated dyes (Fig. 1), some possible explanations of the greater affinity of the adsorbents for AY99 in comparison to other two dyes can be given. Among the investigated dyes, AY99 has only one $-SO_3^-$, while the others have more than one. This somewhat reduced molecule polarity might be the reason for the enhanced affinity of AY99 toward the organic interlamelar layers. In addition, only AY99 has coordinatively bonded chromium, while AO10 and RB5 have no metallic cation in their structure. In order to explain the influence of presence of chromium in dye structure on the adsorption, additional investigations should be conducted. On the other hand, the adsorption efficiencies of AO10 and RB5 depend on the organophilicity of the adsorbents. The AO10 was better adsorbed on 0.5 HDTMA-B, while 1.0 HDTMA-B was more efficient in the adsorption of RB5. It is possible that the larger RB5 molecule is could be adsorbed more easily on the more organophilic 1.0 HDTMA-B due to the larger interlamelar spacing.[15]

Undoubtedly, it was shown that the adsorption of all dyes was more efficient on the more organophilic adsorbent, namely on 1.0 HDTMA-B. The q_e values for AY99 and AO10 adsorption onto 1.0 HDTMA-B were approximately doubled those on 0.5 HDTMA-B. This effect was even more pronounced for the adsorption of RB5, since the q_e was more than six times higher onto 1.0 HDTMA-B. Such trend was expected since it was already confirmed for different single component dye solutions.[14,15,18] The adsorption of each dye is more pronounced from single component solutions than from three-component solution. These results were expected since competitive adsorption from the three-component solutions was expected to occur (each dye competing for the same organophilic sites).

Adsorption from the three-component solution of the selected toxic metal cations

The adsorption of selected toxic cations: Pb^{2+}, Cd^{2+} and Ni^{2+} from their three-component solution onto 0.5 HDTMA-B and 1.0 HDTMA-B was investigated (Fig. 4a and b, respectively). The obtained q_e values for these adsorption processes are given in Table II.

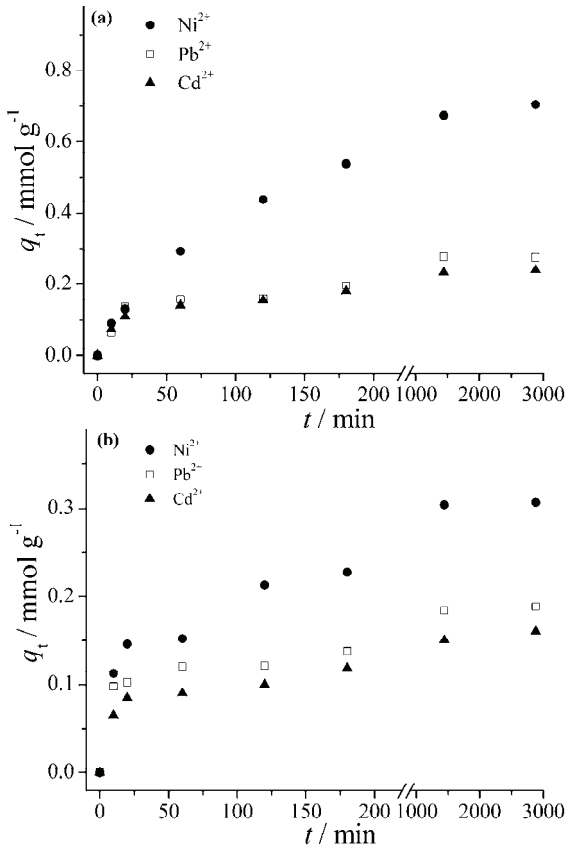

Fig. 4. Adsorption of Pb^{2+}, Ni^{2+} and Cd^{2+} onto: a) 0.5 HDTMA-B and b) 1.0 HDTMA-B.

TABLE II. The q_e (mmol g^{-1}) values for the toxic metals from the single component and the three-component solutions

Adsorbent	Three-component solution			Single-component solution[14]
	Metal			
	Ni^{2+}	Cd^{2+}	Pb^{2+}	Pb^{2+}
0.5 HDTMA-B	0.70	0.24	0.27	0.13
1.0 HDTMA-B	0.31	0.16	0.19	0.09

The adsorption of inorganic cations was the most efficient on unmodified clay (sodium-bentonite) and further decreased with the increase of organophilicity of adsorbents.[14] Thus, the amount of adsorbed toxic cations was higher onto

0.5 HDTMA-B than onto 1.0 HDTMA-B. Corresponding q_e values for the adsorption on 1.0 HDTMA-B were approx. 30 % lower for Cd^{2+} and Pb^{2+} (Table II). The adsorption of Ni^{2+} on 1.0 HDTMA-B although still higher than adsorption of Cd^{2+} and Pb^{2+} was more than two time lower than on 0.5 HDTMA-B.

It was observed that 0.5 HDTMA-B and 1.0 HDTMA-B showed the same selectivity for the investigated toxic metals: $Ni^{2+} > Pb^{2+} \geq Cd^{2+}$. The higher adsorption of Ni^{2+} in comparison to Cd^{2+} and Pb^{2+} onto both investigated adsorbents could be explained by the strong tendency of Ni^{2+} cations to form mixed hydroxo-Ni precipitates at the edges of phyllosilicate particles.[19] Moreover, the observed slightly more pronounced adsorption of Pb^{2+} in comparison to Cd^{2+} is in accordance with literature data.[20–22] Despite the organophilicity of the 0.5 HDTMA-B and 1.0 HDTMA-B adsorbents, the obtained q_e values for all the investigated toxic metal cations were higher than for some hydrophilic adsorbents reported in the literature.[23]

After 180 min (Fig. 4a and b), an increase in the q_t values for all investigated cations was observed. It is assumed that for shorter adsorption times (up to 180 min), the main adsorption mechanism was cation exchange, while the mechanisms of surface complexation and precipitation were more pronounced for longer adsorption times.

Adsorption from the hexa-component solution

The above-obtained results showed that both adsorbents (0.5 HDTMA-B and 1.0 HDTMA-B) were able to adsorb textile dyes and toxic metal cations, and that they could be used as multifunctional adsorbents. However, since the 1.0 HDTMA-B possessed a more organophilic surface, it is more appropriate for effluents with a higher content of organic pollutants and a lower concentration of toxic cations, such as textile wastewaters.[24,25] Therefore, in this study, only 1.0 HDTMA-B was used as adsorbent for the purification of the hexa-component solution from all the investigated dyes (AO10, AY 99 and RB5) and toxic metals (Pb^{2+}, Ni^{2+} and Cd^{2+}). The obtained results are presented in Fig. 5a and b and Table III.

The affinity of 1.0 HDTMA-B toward each of the investigated textile dyes from their three- component solution (Table I) and from the hexa-component solution (Table III) followed the same trend AY99 > RB5 > AO10. Comparing the q_e values for the adsorption of the dyes from the hexa-component solution with those from the three-component solution of the dyes, it was observed that the q_e values were higher for the hexa-component solution. Therefore, the adsorption of the dyes was more efficient from the hexa-component solution. This almost unexpected result could be explained through the adsorption mechanism in the presence of cations. The adsorption textile dyes occurs on organophilic sites,[18] while the adsorption of toxic metal cation occurs on hydrophilic

sites.[5,20,26] The toxic cations adsorbed by the surface complexation mechanism[4,20] could be considered as new adsorption sites for the adsorption of textile dyes *via* electrostatic interaction of the toxic cations with the $-SO_3^-$ groups of the dyes (Fig. 1).

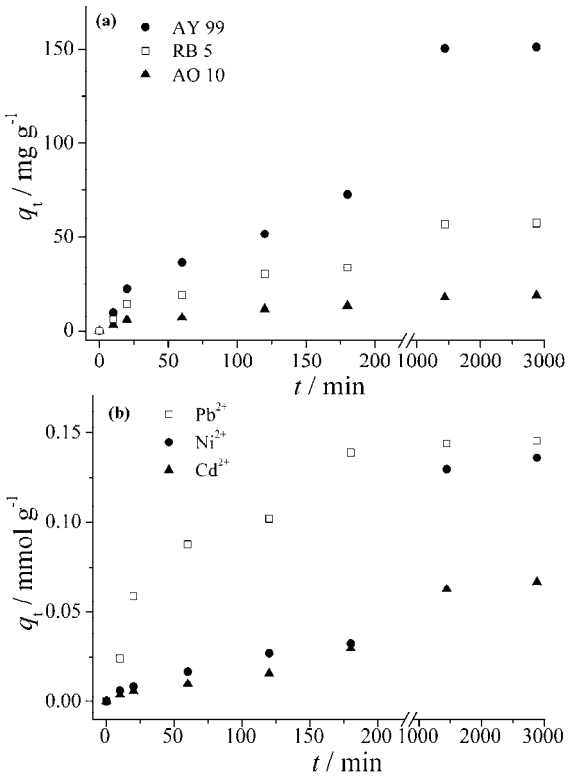

Fig. 5. Adsorption from the hexa-component solution by 1.0 HDTMA-B of: a) AO10, AY99 and RB5, and b) Pb^{2+}, Ni^{2+} and Cd^{2+}.

TABLE III. The q_e values for the dyes and toxic metals from the hexa-component solution

Adsorbent	q_e / mg g^{-1}			q_e / mmol g^{-1}		
	AY99	AO10	RB5	Ni^{2+}	Cd^{2+}	Pb^{2+}
1.0 HDTMA-B	151.18	18.96	57.16	0.13	0.07	0.15

Generally, the adsorption of all toxic cations from the hexa-component solution (Table III) was lower than from the three-component solution containing only toxic cations (Table II). This effect was very pronounced in the case of Ni^{2+} and Cd^{2+}, while it was less expressed in the case of Pb^{2+}. It appears that the presence of adsorbed dyes acts as an obstacle for toxic metal cations, perhaps due to the large dimensions of the dye molecules.

CONCLUSIONS

Two organobentonites were obtained by modification of sodium bentonite with the hexadecyltrimethylammonium (HDTMA) cation. The bentonite/HDTMA ratio used for modification corresponded to 0.5 and 1.0 times of the value of the cation exchange capacity. The obtained adsorbents were denoted as 0.5 HDTMA-B and 1.0 HDTMA-B. Three different solutions were used for the adsorption studies at room temperature: a) a three-component solutions of the dyes (AO10, AY99 and RB5), b) a three-component solution of the toxic metal cations (Pb^{2+}, Ni^{2+} and Cd^{2+}) and c) a hexa-component solution of all the selected organic and inorganic pollutants. Both 0.5 HDTMA-B and 1.0 HDTMA-B showed the highest affinity toward AY99 and Ni^{2+}. The amount of adsorbed dyes was higher on the more organophilic adsorbent (1.0 HDTMA-B). The adsorption of the toxic cations was the reverse. The adsorption from the hexa-component solution (AO10, AY99, RB5, Pb^{2+}, Ni^{2+} and Cd^{2+}) was performed only on the multifunctional adsorbent with a higher affinity toward organic dyes (1.0 HDTMA-B), which are the main type of contaminant in textile industry wastewaters. A synergistic effect of the simultaneous adsorption of dyes from hexa-component solution was observed. Dye adsorption was enhanced in the presence of the toxic metal cations. It was assumed that the previously adsorbed metal cations acted as new adsorption sites for dye adsorption. On the other hand, the adsorption of all toxic cations from the hexa-component solution was lower than from the three-component solution containing only toxic cations.

Acknowledgment. This work was supported by the Ministry of Education, Science and Technological Development of the Republic of Serbia through Project III 45001.

И З В О Д

ОРГАНОБЕНТОНИТИ КАО ВИШЕФУНКЦИОНАЛНИ АДСОРБЕНТИ ОРГАНСКИХ И НЕОРГАНСКИХ ЗАГАЂИВАЧА ВОДЕ

НАТАША ЈОВИЋ-ЈОВИЧИЋ[1], АЛЕКСАНДРА МИЛУТИНОВИЋ-НИКОЛИЋ[1*], МАРИЈА ЖУНИЋ[1], ЗОРИЦА МОЈОВИЋ[1], ПРЕДРАГ БАНКОВИЋ[1], БИЉАНА ДОЈЧИНОВИЋ[2], АНА ИВАНОВИЋ-ШАШИЋ[1] и ДУШАН ЈОВАНОВИЋ[1]

[1]*Универзитет у Београду, Институт за хемију, технологију и металургију, Центар за катализу и хемијско инжењерство, Његошева 12, 11000 Београд и* [2]*Универзитет у Београду, Институт за хемију, технологију и металургију, Центар за хемију, Његошева 12, 11000 Београд*

Циљ овог рада је био добијање јефтиног и ефикасног адсорбенса који може да се користи за симултану адсорпцију органских и неорганских загађивача (укључујући текстилне боје, токсичне метале и др.). Полазни материјал је домаћа бентонитна глина из рудника Боговина. која је модификована хексадецилтриметиламонијум катјонима ($HDTMA^+$). Количина $HDTMA^+$ коришћена за модификацију одговарала је половини и целој вредности капацитета катјонске измене полазне глине. Овако добијени органобентонити су тестирани као адсорбенси трокомпонентне смеше текстилних боја, трокомпонентне смеше метала (Pb^{2+}, Cd^{2+} и Ni^{2+}) и шестокомпонентне смеше која је садржавала све испитиване боје и катјоне токсичних метала. Коришћени адсорбенси пока-

зују највећи афинитет према боји acid yellow 99 и јонима Ni^{2+}. Адсорпција боја је била поспешена присуством катјона токсичних метала, док је адсорпција свих токсичних катјона била нижа из шест-компонентног него из три-компонентног раствора токсичних катјона. Синтетисани хексадецилтриметиламонијум-бентонити могу бити ефикасни мултифункционалани адсорбенси за испитане типове загађивача вода.

(Примљено 13. јануара, ревидирано 12. јуна 2013)

REFERENCES

1. D. Sparks, *Environmental Soil Chemistry*, Academic Press, San Diego, CA, 1995
2. E. Alvarez-Ayuso, A. Garcia-Sanchez, *Clay Clay Miner.* **51** (2003) 475
3. R. Donat, A. Akdogan, E. Erdem, H. Cetsli, *J. Colloid Interface Sci.* **286** (2005) 43
4. M. H. Bradbury, B. Baeyens, *Geochim. Cosmochim. Acta* **63** (1999) 325
5. F. Barbier, G. Duc, M. Petit-Ramel, *Colloids Surfaces, A* **166** (2003) 153
6. I. Man-Chi Lo, L. Cheng-Hao, H. M. Liljestrand, *Water Sci. Technol.* **34** (1996) 319
7. K. R. Ramakrishna, T. Viraraghavan, *Water Sci. Technol.* **36** (1997) 189
8. V. A. Oyanedel-Craver, M. Fuller, J. A. Smith, *J. Colloid Interface Sci.* **309** (2007) 485
9. Y. F. He, F. R. Li, R. M. Wang, F. Y. Li, Y. Wang, Z. H. Zhang, *Water Sci. Technol.* **61** (2010) 1235
10. N. Karapinar, R. Donat, *Desalination* **249** (2009) 123
11. N. Jović-Jovičić, A. Milutinović-Nikolić, I. Gržetić, D. Jovanović, *Chem. Eng. Technol.* **31** (2008) 567
12. T. Lee, J. Choi, J. W. Park, *Chemosphere* **49** (2002) 1309
13. N. Jović-Jovičić, A. Milutinović-Nikolić, P. Banković, B. Dojčinović, B. Nedić, I. Gržetić, D. Jovanović, *Acta Phys. Pol., A* **117** (2010) 849
14. N. Jović-Jovičić, A. Milutinović-Nikolić, P. Banković, Z. Mojović, M. Žunić, I. Gržetić, D. Jovanović, *Appl. Clay Sci.* **47** (2010) 452
15. N. Jović-Jovičić, A. Milutinović-Nikolić, M. Žunić, Z. Mojović, P. Banković, I. Gržetić, D. Jovanović, *J. Contam. Hydrol.* **150** (2013) 1
16. Z. Vuković, A. Milutinović-Nikolić, Lj. Rožić, Z. Nedić, D. Jovanović, *Clay Clay Miner.* **54** (2006) 697
17. Q. Shizhang, H. Qiuhong, H. Fouad, H. Xijun, L. Gao Qing, *Sep. Purif. Technol.* **67** (2009) 218
18. J. Ma, B. Cui, J. Dai, D. Li, *J. Hazard. Mater.* **186** (2011) 1758
19. A. M. Scheidegger, D. L. Sparks, *Soil Sci.* **161** (1996) 813
20. *Handbook of Clay Science, Developments in Clay Science*, Vol. 1, F. Bergaya, B. K. G. Theng, G. Lagaly, Eds., Elsevier, Amsterdam, 2006
21. V. A. Oyanedel-Craver, J. A. Smith, *J. Hazard. Mater., B* **137** (2006) 1102
22. C. Ouellet-Plamondon, R. J. Lynch, A. Al-Tabbaa, *Appl. Clay Sci.* **67** (2012) 91
23. J. Ming-Qin, J. Xiao-Ying, L. Xiao-Qiao, C. Zu-Liang, *Desalination* 252 (2010) 33
24. Y. Fu, T. Viraraghavan, *Water Qual. Res. J. Can.* **35** (2000) 95
25. X. R. Xu, H. B. Li, W. H. Wang, J. D. Gu, *Chemosphere* **59** (2005) 893
26. H. B. Bradl, *J. Colloid Interface Sci.* **277** (2004) 1.

Journal of the Serbian Chemical Society
JSCS-info@shd.org.rs • www.shd.org.rs/JSCS
J. Serb. Chem. Soc. 79 (2) 265–276 (2014)
JSCS–4581
UDC 546.3+66–914+551.578.4+
625.712.2:551.321.7(497.113)
Original scientific paper

Multivariate analysis of the contents of metals in urban snow near traffic lanes in Novi Sad, Serbia

ALEKSANDRA MIHAILOVIĆ[1]*, MILICA VUČINIĆ VASIĆ[1], JORDANA NINKOV[2#], SUZANA ERIĆ[3], NEBOJŠA M. RALEVIĆ[1], TOMAS NEMEŠ[1] and ALEKSANDAR ANTIĆ[1]

[1]*Faculty of Technical Sciences, University of Novi Sad, Trg Dositeja Obradovića 6, 21000 Novi Sad, Serbia,* [2]*Institute of Field and Vegetable Crops, Maksima Gorkog 30, 21000, Novi Sad, Serbia and* [3]*Faculty of Mining and Geology, University of Belgrade, Đušina 7, 11000 Belgrade, Serbia*

(Received 11 March, revised 13 May 2013)

Abstract: During December 2009, snow was collected at twenty two locations across the urban area of Novi Sad, directly from roads and from traffic islands near crossroads. The total metal concentration was determined for each of ten metals (Al, Ca, Cu, Fe, K, Mn, Na, Ni, Pb and Zn) using the ICP-OES analytical technique. Ni was found to have the lowest concentration (0.0265 mg dm^{-3}). Na was the metal with the highest concentration (10786 mg dm^{-3}), which was the consequence of sodium chloride being used as a de-icing salt on the roads. The metal with the second highest concentration at all locations was Ca; this was most likely the result of soil dust. The Spearman rank correlation coefficients between analyzed metals were calculated to determine how the concentrations of the metals were related. Cluster analysis was performed on the obtained data sets, using both the hierarchical and partitioning methods in order to identify associations among metals and/or locations. It was shown that traffic density was not the most important factor that caused the differences between the concentrations of the metals in the samples.

Keywords: metal concentration; snow; traffic; correlation; cluster analysis.

INTRODUCTION

There has been an interest in investigating the chemistry of urban snow in recent years.[1–4] Road runoff after the melting of snow presents a significant source of pollution in the environment. Snow melting usually exerts an acute impact on waters receiving road runoff. Snow on the road contains high concentrations of pollutants from both natural and anthropogenic sources including

* Corresponding author. E-mail: zandra@uns.ac.rs
# Serbian Chemical Society member.
doi: 10.2298/JSC130311052M

heavy metals.[1,5,6] A part of this snow is ploughed to the roadside and therefore is a contributing factor in the pollution of urban land in the vicinity of the roads, especially traffic islands.

The natural sources of road snow pollutants are materials from surrounding soils (windblown soil dust), particles from atmospheric deposition and biological materials from vegetation.[7,8] Road-deposited particulate matter can be attributed to anthropogenic sources, such as emissions from industrial plant processes, vehicle exhaust emissions and wear of automobile parts.[9–11] Traffic intensity is one of the most important factors influencing pollution in road runoff.[12,13]

Significant differences in the levels of pollutants in urban snow have been found in studies performed in different regions, thus indicating the need for local data. This is caused by differences in climate, surrounding land-type and land--use, vehicular traffic density, neighbouring industrial plants, *etc*.[14] Pollutant load is very high during snow melting in regions where snow cover lasts several months.[6] In northern countries, various efforts have been made to address this problem, but little is known about the pollution of urban snow in the Balkan region. In regions where the snow cover does not remain for longer periods, the environmental impact of snowmelt is not as acute but it should be investigated. The present case study was performed in the city of Novi Sad (Serbia). In regions such as Serbia, snow has a short lifespan and usually does not remain for longer than ten days. The intention of the study was to determine whether there was any significant pollution in urban road/roadside snow.

The melt water with all its pollutants is often directly discharged without treatment into the receiving water. In all urban areas in the city of Novi Sad, water that enters the sewage system discharges into the Danube River without any chemical or mechanical treatment. During snowmelt, pollutants are usually rapidly released from snow piles[6] and the pollutant load can rise suddenly thus having a significant impact on the receiving watercourses.[3] The toxicity of metal pollutants in receiving waters is mostly connected to the dissolved fraction, but knowledge about total metal concentration is also very important.[15–17]

In this study, two statistical techniques: descriptive statistics and multivariate analysis of experimental data were employed. Correlation analysis is often performed to estimate the extent of a relationship between any pair of variables, *e.g.*, in a group of selected metals.[18,19] Cluster analysis, a multivariate statistical technique, has been widely used to interpret complex data and to identify sources of pollution.[20,21]

The objectives of the work presented in this paper were: to analyze the metal concentration in snow collected: *i*) directly from the road near crossroads and *ii*) from traffic islands in the urban area of Novi Sad and to identify pollution sources using statistical analysis of the data.

EXPERIMENTAL

Novi Sad is the second largest city in Serbia, located on the Danube River in the southern part of The Pannonian Plain. The urban area of the city is 129.7 km². The population was estimated to be 370,000 at the end of 2009. Novi Sad has a moderate continental climate, with an average of 22 days of complete sub-zero temperatures. January is the coldest month, with an average temperature of −1.9 °C.

From December 20 until December 22, 2009, snow was collected at twenty-two locations across Novi Sad. The snowfall started on December 15 and continued intermittently until December 23. The snow cover persisted for ten days due to cold weather, with temperatures constantly below 0 °C. The snow depth was in the range of 18–25 cm. Sampling locations are shown on the map of Novi Sad presented in Fig. 1.

Fig. 1. Sampling locations on the map of the city of Novi Sad.

Fourteen of the sampling points were situated directly on roads near crossroads and were divided into two subgroups. For subgroup one, “high traffic”, the average traffic volume at the crossroads was in the range of 400–800 vehicles per hour, while for the second, “low traffic”, it was 30–150 vehicles per hour. Seven sampling points were located on traffic islands separating lanes of opposing traffic. Sampling locations in the high traffic subgroup, low traffic subgroup and traffic island subgroup are denoted by H1–H7, L8–L14 and TI1–TI7, respectively. The reference sampling point is R15.

Samples were collected using polyethylene (PE) bags, PE trowels and PE gloves. Prior to sampling, the trowels were cleaned with nitric acid and rinsed with distilled water. One–two

litres of snow were collected at each sampling site, except at the reference site where fifteen litres of snow was collected.

Before analysis, samples were allowed to melt slowly. To avoid potential problems with detection limits, only the reference sample was 50-fold pre-concentrated. Pre-concentration was realized by non-boiling evaporation. The melted samples were acidified with nitric acid to a pH of less than 2. Sub-samples of 100 mL, taken from homogenized acidified samples, were acid digested with nitric acid. Prior to analysis, the sub-samples were filtrated through a blue ribbon filter (Whatman) with an average retention 2–4 μm. The filtrates were used for measurements. The total concentration of metals was measured using ICP-OES (Vista-Pro, Axial; Varian) in accordance with the US EPA method 200.7:2001. Quality assurance and quality control (QA/QC) were conducted by performing laboratory blanks and NIST standard reference material 1643e (trace elements in water). Deviations from the obtained results were within ±10 % of the certified value. The limits of detection for the examined metals were: 15 (Al), 1 (Ca), 6 (Cu), 4 (Fe), 5 (K), 0.5 (Mn), 1.5 (Na), 3 (Ni), 15 (Pb) and 3 μg dm^{-3} (Zn).

All statistical analyses were performed using the software package Statistica 10.[22] Non-parametric correlation analysis was performed due to the non-normal distribution of some parameters and because non-parametric correlation analysis is less sensitive to outliers. The Spearman rank correlation coefficients between the analyzed variables were calculated. Only correlation coefficients significant at the 0.05 level are discussed within this paper. A cluster analysis was also performed on the obtained data sets, using both hierarchical and partitioning methods by minimizing the squared Euclidean distances.

RESULTS AND DISCUSSION

Basic statistical parameters of the data are given in Table I. Concentrations of metals at reference site were: 2.6 (Al), 545 (Ca), 1.5 (Cu), 11 (Fe), 129 (K), 1.6 (Mn), 603 (Na), 0.7 (Ni), 1.3 (Pb) and 14 μg dm^{-3} (Zn). Concentrations of all metals investigated from locations H1–H7, L8–L14 and TI1–TI7 were several

TABLE I. Results of multi-element analysis

Parameter	Element									
	Al	Ca	Cu	Fe	K	Mn	Na	Ni	Pb	Zn
Low traffic										
c_{min} / mg dm^{-3}	0.61	102.70	0.10	4.68	3.23	0.27	233.80	0.030	0.06	0.34
c_{max} / mg dm^{-3}	2.96	586.50	0.26	29.39	19.24	2.01	5104.50	0.058	0.49	1.39
c_{mean} / mg dm^{-3}	1.86	347.43	0.18	17.09	10.66	1.10	1924.30	0.042	0.27	0.92
SD / mg dm^{-3}	0.94	164.48	0.06	8.57	5.49	0.52	1676.18	0.011	0.13	0.32
High traffic										
c_{min} / mg dm^{-3}	1.27	192.90	0.14	9.81	5.67	0.52	1149.80	0.027	0.20	0.45
c_{max} / mg dm^{-3}	6.14	849.40	0.32	30.82	34.25	1.99	10786.00	0.086	1.37	2.37
c_{mean} / mg dm^{-3}	2.38	453.34	0.20	15.97	11.96	0.95	3494.91	0.045	0.46	0.94
SD / mg dm^{-3}	1.70	273.62	0.06	7.01	9.96	0.48	3393.07	0.024	0.41	0.64
Traffic islands										
c_{min} / mg dm^{-3}	0.22	34.85	0.04	1.78	0.88	0.10	235.30	–	0.05	0.12
c_{max} / mg dm^{-3}	0.74	116.30	0.09	5.72	3.20	0.30	2174.50	–	0.23	0.43
c_{mean} / mg dm^{-3}	0.35	59.34	0.05	3.01	1.92	0.15	983.31	–	0.10	0.19
SD / mg dm^{-3}	0.18	26.65	0.02	1.35	0.73	0.07	624.20	–	0.06	0.11

orders of magnitude higher than ambient background levels measured at the reference site. Reference sampling point (R15) was located in a residential area in Novi Sad near the Danube River away from roads and industrial plants. Therefore, the reference sample was believed not to be directly polluted by traffic or human activities, but affected only by atmospheric pollutants. The lowest metal concentration was found for Ni (0.0265 mg dm^{-3}) while, as expected, the highest was for Na (10786 mg dm^{-3}). The high concentration of Na, which exceeds the other concentrations by orders of magnitude, is a consequence of sodium chloride being used as a de-icing agent on roads during winter. Sodium chloride has only been considered a pollutant since 2001.[23] The metals, in descending order of mean concentration were Na > Ca > Fe > K > Al > Mn > Zn > Pb > Cu > Ni. This order was the same for both high traffic and low traffic locations. The order was the same for traffic islands, but the Ni concentration was below the limit of detection. This indicates only small variations in the composition of the snow at the selected locations in urban areas of Novi Sad. It also indicates that the samples were in general impacted by the same source(s). It is considered that the main pollution sources in the area studied in this work may be traffic, oil refining and combusting for home heating in some parts of the city. The only large facility is the oil refinery located in the northeast part of the city. The second highest concentration of Ca at all locations was, most probably, due to contribution from soil particles containing minerals. Soil dust is the most likely source of this high level of Ca as well as of K. Another source of Ca and K was the de-icing salt. Namely, according to its Quality and Safety Certificate, the de-icing salt used by the Public Utilities Company of the city of Novi Sad contained 0.281 Ca, 0.040 Mg and 0.012 % K. The salt was imported from Ukraine (produced in salt mines in Soledar).

The calculated ratio between mean values of metal concentration at high and low traffic locations, shown in Fig. 2a, indicates the impact of traffic volume. The most significant differences in concentrations of elements that mainly originate from anthropogenic sources at locations near the high and the low traffic crossroads were for Na (1.73) and Pb (1.58). For a number of years, only unleaded petrol has been in use in many countries, but in Serbia, leaded petrol was still in use at the time of sample taking. Therefore, it was assumed that the lead content was mostly a result of traffic pollution. Considering de-icing salt as the main source of Na, it is evident that more salt was applied at high traffic locations.

The main source of metals at traffic island locations was snow ploughed from the roads. As expected, the mean concentration of metals at traffic islands was considerably lower compared with those at high traffic density locations. The ratio between mean values of metal concentration at traffic islands and high traffic locations was not significantly different, as can be seen in Fig. 2b.

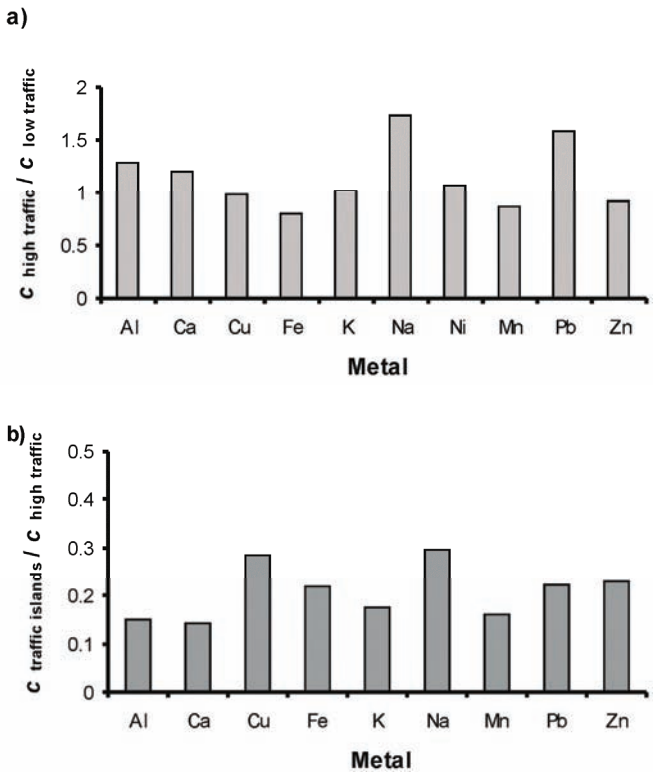

Fig. 2. Ratio between the mean values of the metal concentrations at: a) high and low traffic locations and b) traffic islands and high traffic locations.

The results of this study were compared with the results of the total metal concentrations in urban snow reported for Cu, Zn and Pb,[3] as well as for Al, Ca, Cu, Fe, Na, Pb and Zn.[1] Concerning Cu, Zn and Pb, the results of this study were in the same range as those reported in the literature.[3] Mean values of Cu and Zn were of the same order of magnitude but lower than the values measured in Innsbruck[3] for both high and low traffic locations. The mean Pb concentration at low traffic locations was approximately the same, while at high traffic locations the result of this study was higher than that reported by Engelhard *et al.*[3] The results of this study were compared with the values reported by Glen and Sansalone[1] for snow collected on highways in Cincinnati, OH (USA). The maximum concentrations for Cu, Al, Fe and Zn were one order of magnitude lower that the corresponding concentrations reported in the literature.[1] The smallest difference between the results reported here and in the literature[1] concerns Ca and Pb. The highest concentration level obtained for Na was one order of magnitude greater than that reported by Glen and Sansalone.[1]

Correlation analysis was performed to estimate the extent of the relationship between any two variables in the group of investigated metals. The Spearman rank correlation coefficient values were calculated for high and low traffic loca-

tions data and the results are given in Table II. Interestingly, all correlation coefficients significant at the 0.05 level were positive. The correlation analysis results showed the absence of significant correlations between the concentration of Na and any other metal considered in the study. This result is consistent with the fact that the total metal concentration was measured. An observation on polluted snow from other studies[23,24] was that increased values of dissolved metal concentrations are correlated with greater levels of de-icing salt concentrations. The chloride ion is highly mobile and causes the washout of pollutants, such as heavy metals, from deposited sediments.[25–27]

TABLE II. Spearman rank correlation coefficient values between the measured parameters for combined data: high + low traffic locations; * – values significant at the 0.05 level

	Ca	Cu	Fe	K	Mn	Na	Ni	Pb	Zn
Al	0.45	0.81*	0.86*	0.30	0.52	–0.03	0.87*	0.67*	0.45
Ca		0.39	0.32	0.68*	0.68	0.52	0.57*	0.85*	0.60*
Cu			0.67*	0.23	0.28	–0.28	0.73*	0.56*	0.25
Fe				0.28	0.70	–0.05	0.83*	0.51	0.64*
K					0.56	0.46	0.36	0.43	0.56*
Mn						0.28	0.64*	0.64*	0.88*
Na							0.09	0.30	0.36
Ni								0.66*	0.67*
Pb									0.51

In agreement with expectations, metals originating predominantly from natural sources were strongly correlated (at the 0.05 significance level), *e.g.*, strong positive correlations were found between Ca and K. Furthermore, the results indicated a strong positive correlation between the Fe and Ni concentrations, which could be a result of attrition of steel parts. The strong positive correlation between Cu and Ni could be a consequence of the emission of these two metals from brake-lining wear, and metal plating parts.[16,28] This was also the case for Ni and Zn, for which a strong statistically significant positive correlation was found. Potential sources of Zn are tire wear and motor oil.[10] The statistically significant positive correlation between Al–Ni, Al–Fe, Al–Cu, Fe–Cu, Fe–Zn is consistent with the fact that the traffic related emission sources contribute to the levels of these elements in the environment.[9,25]

Interestingly, a very strong, statistically significant, positive correlation was found between Ca and Pb, which means that there could be some kind of relationship between them. This result is not consistent with the mentioned assumption that the main source of lead was vehicle exhausts. As already stated, the main source of Ca at all locations was probably minerals from soil dust particles.

Cluster analysis is a very efficient tool for the identification of metal sources.[29] The main purpose of cluster analysis is to split a number of variables into groups that have similar characteristics or behaviour.[30,31] Cluster analysis

can be performed either by clustering variables or samples. In multi-element analysis, obtained concentration levels are usually very different. Therefore, the data must be "prepared" for cluster analysis by using appropriate standardization techniques. The Z-scale standardization was used in this analysis. Although some cluster analysis procedures do not require the data to be normally distributed, the Box–Cox transformation[32] was performed as well. In this study, the most common approach, hierarchical clustering, was used to cluster variables. Hierarchical clustering was first performed on the data from the high and low traffic locations using the Ward method[33] with squared Euclidean distances as a measure of similarity. This approach resulted in grouping the metals into two clusters with significant differences between them. The dendrogram of the hierarchical cluster analysis of total metal concentrations at the high and low traffic locations is shown in Fig. 3. The first cluster consists of Al, Cu, Fe and Ni, divided into two sub-clusters: Al–Cu and Fe–Ni according to the degree of association between the metals. As mentioned in the subsection concerning correlation analysis, very strong statistically significant correlation coefficient values were found for pairs of metals within this group. These metals are typical road run-off pollutants and many sources for all of them are traffic related: moving engine parts and brake-lining attrition, auto body rust and wire corrosion.[25,34] The second cluster contained K, Ca, Pb, Mn, Zn and Na. Such a groupation in the second cluster was unexpected because of the close linkage between Ca and Pb, and between Mn and Zn. It is assumed that Ca and Mn mainly originated from natural geochemical sources (soil erosion products, windblown soil dust) while Pb and Zn may have derived mostly from traffic pollution (leaded gasoline, tire wear, motor oil). While interpreting the results, it was born in mind that sampling locations with high (low) anthropogenic input could additionally be influenced by high (low) natural input. In other words, high anthropogenic input does not exclude high natural input.

When hierarchical clustering was performed for all data, including those from traffic island locations, three distinct clusters were obtained. Fig. 4 displays the hierarchical dendrogram for high traffic + low traffic + traffic island data. Ni was not detected on traffic island locations and therefore was not included in the analysis. As could be seen in Fig. 4, cluster 1 contained Al, Cu and Fe; cluster 2 K, Ca, Pb, Mn, and Zn, while cluster 3 contained only Na. As already mentioned, the main source of Na is de-icing salt and the results of the multivariate statistical analysis are consistent with this fact.

The partitioning method was used to cluster sampling locations. In contrast to the hierarchical method, this method requires the number of clusters to be predetermined. Considering the vehicular traffic density as one of the primary variables that influences metal concentration, a hypothesis that all samples could be divided into two groups was proposed. The idea was to check how the

samples would cluster if there was the possibility to separate them into two groups. The *K*-means algorithm with a predetermined number of clusters was used. The partitioning method was initially performed on data for both high and low traffic metal concentration values, then traffic density data (an additional variable) was added. The results were the same. One of the clusters included locations L2, L4, H5 and H7. The other included L1, L3, L5, L6, L7, H1–H4, and H6. Each cluster comprised sampling locations from both high and low traffic locations. Thus, the results showed that traffic density was neither the only nor the most important factor that divided the samples into two groups.

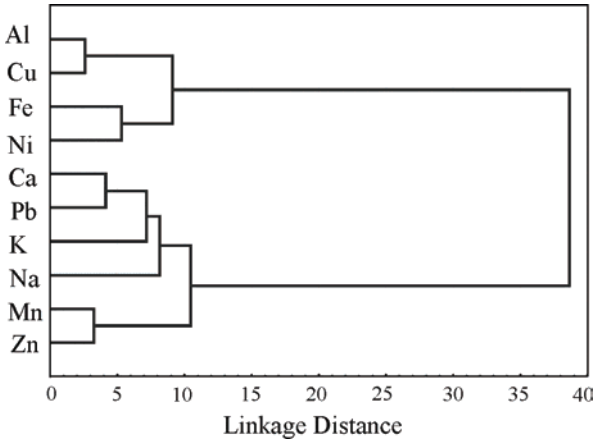

Fig. 3. The dendrogram of the hierarchical cluster analysis of the total metal concentrations for combined data: high traffic locations + low traffic locations.

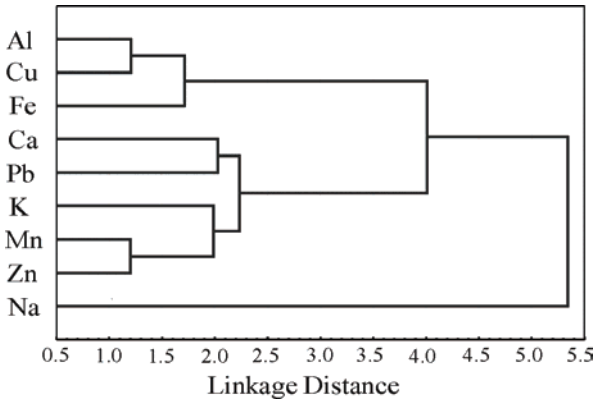

Fig. 4. The dendrogram of the hierarchical cluster analysis of total metal concentrations for combined data: high traffic locations + low traffic locations + traffic islands.

CONCLUSIONS

The metal contents of twenty-two snow samples taken directly from the roads and traffic islands in the urban area of Novi Sad were determined using the ICP-OES analytical technique. The small variation in the composition of snow at the selected locations indicates that the samples were, in general, impacted by the same source(s).

The hierarchical clustering applied to the variables (metals) for samples taken directly from the roads comprised two distinct groups of metals according to the degree of their association. The results of metal clustering were consistent with the fact that very strong statistically significant correlation coefficient values were obtained between pairs of metals within both groups. The partitioning method of cluster analysis was also performed on sampling locations. The results showed that the traffic density was neither the only nor the most important factor that divided the samples into two groups.

The results of non-parametric correlation analysis and multivariate statistical analysis revealed that common sources (most likely traffic related) mainly contribute to the contents of Al, Cu, Fe and Ni. Associations between some investigated elements (Ca, K, Mn, Pb and Zn) may suggest inputs from both anthropogenic activities and natural geochemical sources. Considering all of the analyses conducted in this study, no categorical conclusion concerning the pollution sources could be made.

Acknowledgment. The Ministry of Education, Science and Technological Development of the Republic of Serbia financially supported this work, projects No. III45015 and 34014.

И З В О Д

МУЛТИВАРИЈАЦИОНА АНАЛИЗА САДРЖАЈА МЕТАЛА У СНЕГУ СА УРБАНОГ ПОДРУЧЈА ГРАДА НОВОГ САДА

АЛЕКСАНДРА МИХАИЛОВИЋ[1], МИЛИЦА ВУЧИНИЋ ВАСИЋ[1], ЈОРДАНА НИНКОВ[2], СУЗАНА ЕРИЋ[3], НЕБОЈША М. РАЛЕВИЋ[1], ТОМАС НЕМЕШ[1] и АЛЕКСАНДАР АНТИЋ[1]

[1]*Факултет техничких наука, Универзитет у Новом Саду, Трг Доситеја Обрадовића 6, 21000 Нови Сад,* [2]*Институт за ратарство и повртарство, Максима Горког 30, 21000 Нови Сад и* [3]*Рударско–геолошки факултет, Универзитет у Београду, Ђушина 7, 11000 Београд*

Током децембра 2009. године сакупљен је снег на двадесет и две локације на подручју града Новог Сада и то директно са асфалтних путева и са пешачких острва. Методом ICP-OES спектроскопије одређена је укупна концентрација следећих метала: Al, Ca, Cu, Fe, K, Mn, Na, Ni, Pb и Zn. Најмања и највећа концентрација метала у испитиваним узорцима утврђене су за никл и натријум, редом. Други по опадајућем редоследу концентрација био је калцијум и то на свим локацијама. У циљу одређивања повезаности метала израчунате су вредности Спирмановог (Spearman) корелационог коефицијента за парове метала. Такође, да би се утврдила повезаност између самих метала као и између метала и локација извршена је и кластер анализа добијених података и то користећи хијерархијски и партициони метод. На основу извршених анализа утврђено је да

густина саобраћаја није најбитнији фактор који је узроковао разлике у концентрацијама метала у испитиваним узорцима.

(Примљено 11. марта, ревидирано 13. маја 2013)

REFERENCES

1. D. W. Glenn, J. J. Sansalone, *J. Environ. Eng.* **128** (2002) 167 2
2. K. Reinosdotter, M. Viklander, *Water Air Soil Pollut.* **167** (2005) 3
3. C. Engelhard, S. De Toffol, I. Lek, W. Rauch, R. Dallinger, *Sci. Tot. Environ.* **382** (2007) 286
4. S. Levshina, *Water Air Soil Pollut*. **223** (2012**)** 3553
5. L. Herngren, A. Goonetilleke, G. A. Ayoko, *Anal. Chim. Acta* **571** (2006) 270
6. C. Westerlund, M. Viklander, *Sci. Tot. Environ.* **362** (2006) 143
7. T. Hinkley, F. Pertsiger, L. Zavjalova, *Geophys. Res. Lett.* **24** (1997) 1607
8. Z. Cong, S. Kang, D. Qin, *J. Environ. Sci. (China)* **21 (**2009) 914
9. V. Novotny, in Proceedings of the NATO Advanced Research Workshop on Regional Approaches to Water Pollution in the Environment, Byšice, Czech Republic, 1995, p. 33
10. W. F. Rogge, L. M. Hildemann, M. A. Mazurek, G. R. Cass, B. R. T. Simoneit, *Environ. Sci. Technol.* **27** (1993) 1892
11. A. Veysseyre, K. Moutard, C. Ferrari, K. Van de Velde, C. Barbante, G. Cozzi, G. Capodaglio, C. Boutron, *Atmos. Environ.* **3** (2001) 415
12. H. Lee, S. L. Lau, M. Kayhanian, M. K. Stenstrom, *Water Res.* **38** (2004) 4153
13. B. Crabtree, F. Moy, M. Whitehead, A. Roe, *Water Environ. J.* **20** (2006) 287
14. B. L. Brezonik, T. H. Stadelmann, *Water Res.* **36** (2002) 1743
15. J. J. Sansalone, S. G. Buchberger, S. R. Al Abed, *Sci. Tot. Environ.* **190** (1996) 371
16. Phase I: Preliminary Environmental Investigation of Heavy Metals in Highway Runoff, http://depts.washington.edu/trac/bulkdisk/pdf/661.1.pdf (11.02.2013)
17. H. Preciado, L. Li, *Water Air Soil Pollut.* **172** (2006) 81
18. M. Biasoli, H. Grčman, T. Kralj, F. Madrid, E. Diaz-Barrientos, F. Ajmone-Marsan, *J. Environ. Qual.* **36** (2007) 70
19. B. Helmreich, R. Hilliges, A. Schriewer, H. Horn, *Chemosphere* **80** (2010) 991
20. M. N. Shah, N. Shaheen, *J. Hazard. Mat.* **147**(2007) 759
21. P. Thavamani, M. Megharaj, R. Naidu, *Environ. Monit. Assess.* **184** (2012) 3875
22. Statistica 10, http://www.statsoft.com/products/statistica-10-new-features (20.12.2012)
23. O. Ruth, *Water Sci. Technol.* **48** (2003) 33 9
24. M. Vučinić Vasić, A. Mihailović, U. Kozmidis-Luburić, T. Nemeš, J. Ninkov, T. Zeremski-Škorić, B. Antić, *Chemosphere* **86** (2012) 585
25. C. Amrhein, J. E. Strong, P. A. Mosher, *Environ. Sci. Technol.* **26** (1992) 703
26. M. Bäckström, U. Nilsson, K. Hakansson, B. Allard, S. Karlsson, *Water Air Soil Pollut.* **147** (2003) 343
27. J. Marsalek, *Water Sci. Technol.* **48** (2003) 61
28. *Typical pollutants in stormwater runoff*, http://lakes.chebucto.org/SWT/pollutants.html (26.01.2013.)
29. M. De Luca, F. Oliverio, D. Ioele, G.-P. Husson, G. Ragno, *Inter. J. Environ. Anal. Chem*. **88** (2008) 1087
30. B. S. Everitt, G. Dunn, *Applied Multivariate Data Analysis*, Oxford University Press, Oxford, 2001, p. 131
31. S. Ražić, Đ. Čokeša, S. Sremac, *J. Serb. Chem. Soc.* **72** (2007) 1487
32. G. E. P. Box, D. R. Cox, *J. Roy. Stat. Soc., B* **26** (1964) 211

33. J. H. Ward, *Am. Stat. Ass. J.* **58** (1963) 236
34. L. Ritter, K. Solomon, P. Sibley, K. Hall, P. Keen, G. Mattu, B. Linton, *J. Toxicol. Environ. Health, A* **65** (2002) 1.